

Wireless Communications and Mobile Computing

Communications and Networking for Connected Vehicles

Lead Guest Editor: Li Zhu

Guest Editors: Richard Yu, Victor Leung, Hongwei Wang, Cesar Briso,
and Yan Zhang





Communications and Networking for Connected Vehicles

Wireless Communications and Mobile Computing

Communications and Networking for Connected Vehicles

Lead Guest Editor: Li Zhu

Guest Editors: Richard Yu, Victor Leung, Hongwei Wang,
Cesar Briso, and Yan Zhang



Copyright © 2018 Hindawi. All rights reserved.

This is a special issue published in “Wireless Communications and Mobile Computing.” All articles are open access articles distributed under the Creative Commons Attribution License, which permits unrestricted use, distribution, and reproduction in any medium, provided the original work is properly cited.

Editorial Board

- Javier Aguiar, Spain
Wessam Ajib, Canada
Muhammad Alam, China
Eva Antonino-Daviu, Spain
Shlomi Arnon, Israel
Leyre Azpilicueta, Mexico
Paolo Barsocchi, Italy
Alessandro Bazzi, Italy
Zdenek Becvar, Czech Republic
Francesco Benedetto, Italy
Olivier Berder, France
Ana M. Bernardos, Spain
Mauro Biagi, Italy
Dario Bruneo, Italy
Jun Cai, Canada
Zhipeng Cai, USA
Claudia Campolo, Italy
Gerardo Canfora, Italy
Rolando Carrasco, UK
Vicente Casares-Giner, Spain
Dajana Cassioli, Italy
Luis Castedo, Spain
Ioannis Chatzigiannakis, Greece
Lin Chen, France
Yu Chen, USA
Hui Cheng, UK
Luca Chiaraviglio, Italy
Ernestina Cianca, Italy
Riccardo Colella, Italy
Mario Collotta, Italy
Massimo Condoluci, Sweden
Bernard Cousin, France
Telmo Reis Cunha, Portugal
Igor Curcio, Finland
Laurie Cuthbert, Macau
Donatella Darsena, Italy
Pham Tien Dat, Japan
André de Almeida, Brazil
Antonio De Domenico, France
Antonio de la Oliva, Spain
Gianluca De Marco, Italy
Luca De Nardis, Italy
Alessandra De Paola, Italy
Liang Dong, USA
- Trung Q. Duong, Sweden
Mohammed El-Hajjar, UK
Oscar Esparza, Spain
Maria Fazio, Italy
Mauro Femminella, Italy
Manuel Fernandez-Veiga, Spain
Gianluigi Ferrari, Italy
Ilario Filippini, Italy
Jesus Fontecha, Spain
Luca Foschini, Italy
A. G. Fragkiadakis, Greece
Sabrina Gaito, Italy
Óscar García, Spain
Manuel García Sánchez, Spain
L. J. García Villalba, Spain
José A. García-Naya, Spain
Miguel Garcia-Pineda, Spain
A.-J. García-Sánchez, Spain
Piedad Garrido, Spain
Vincent Gauthier, France
Carlo Giannelli, Italy
Carles Gomez, Spain
Juan A. Gomez-Pulido, Spain
Ke Guan, China
Daojing He, China
Paul Honeine, France
Sergio Ilarri, Spain
Antonio Jara, Switzerland
Xiaohong Jiang, Japan
Minho Jo, Republic of Korea
Shigeru Kashihara, Japan
Dimitrios Katsaros, Greece
Minseok Kim, Japan
Mario Kolberg, UK
Nikos Komninos, UK
Juan A. L. Riquelme, Spain
Pavlos I. Lazaridis, UK
Tuan Anh Le, UK
Xianfu Lei, China
Hoa Le-Minh, UK
Miguel López-Benítez, UK
Martín López-Nores, Spain
Javier D. S. Lorente, Spain
Tony T. Luo, Singapore
- Maode Ma, Singapore
Imadeldin Mahgoub, USA
Pietro Manzoni, Spain
Álvaro Marco, Spain
Gustavo Marfia, Italy
Francisco J. Martinez, Spain
Davide Mattera, Italy
Michael McGuire, Canada
Nathalie Mitton, France
Klaus Moessner, UK
Antonella Molinaro, Italy
Simone Morosi, Italy
Kumudu S. Munasinghe, Australia
Enrico Natalizio, France
Keivan Navaie, UK
Thomas Newe, Ireland
Wing Kwan Ng, Australia
Tuan M. Nguyen, Vietnam
Petros Nicolaitidis, Greece
Giovanni Pau, Italy
Rafael Pérez-Jiménez, Spain
Matteo Petracca, Italy
Nada Y. Philip, UK
Marco Picone, Italy
Daniele Pinchera, Italy
Giuseppe Piro, Italy
Vicent Pla, Spain
Javier Prieto, Spain
Rüdiger C. Prys, Germany
Junaid Qadir, Pakistan
Sujan Rajbhandari, UK
Rajib Rana, Australia
Luca Reggiani, Italy
Daniel G. Reina, Spain
Abusayeed Saifullah, USA
Jose Santa, Spain
Stefano Savazzi, Italy
Hans Schotten, Germany
Patrick Seeling, USA
Muhammad Z. Shakir, UK
Mohammad Shojafar, Italy
Giovanni Stea, Italy
Enrique Stevens-Navarro, Mexico
Zhou Su, Japan



Luis Suarez, Russia
Ville Syrjälä, Finland
Hwee Pink Tan, Singapore
Pierre-Martin Tardif, Canada
Mauro Tortonesi, Italy

Reza Monir Vaghefi, USA
Juan F. Valenzuela-Valdés, Spain
Aline C. Viana, France
Enrico M. Vitucci, Italy
Honggang Wang, USA

Jie Yang, USA
Sherali Zeadally, USA
Jie Zhang, UK
Meiling Zhu, UK

Contents

Communications and Networking for Connected Vehicles

Li Zhu , Fei Richard Yu, Victor C. M. Leung , Hongwei Wang, Cesar Briso-Rodríguez , and Yan Zhang

Editorial (4 pages), Article ID 5612785, Volume 2018 (2018)

Study on Formal Modeling and Safety Verification of Train-to-Train Communication

Haonan Feng 

Research Article (9 pages), Article ID 2406968, Volume 2018 (2018)

A Novel Approach to Enhance the Physical Layer Channel Security of Wireless Cooperative Vehicular Communication Using Decode-and-Forward Best Relaying Selection

Esraa M. Ghourab , Mohamed Azab, Mohamed F. Feteiha, and Hesham El-Sayed

Research Article (15 pages), Article ID 9624856, Volume 2018 (2018)

Comprehensive Analysis on Heterogeneous Wireless Network in High-Speed Scenarios

Yuyang Zhang, Tao Zheng , Ping Dong , Hongbin Luo, and Zhibo Pang 

Research Article (12 pages), Article ID 4259510, Volume 2018 (2018)

An Efficient Traffic Congestion Monitoring System on Internet of Vehicles

Duc-Binh Nguyen , Chyi-Ren Dow , and Shioh-Fen Hwang

Research Article (17 pages), Article ID 9136813, Volume 2018 (2018)

A Progressive Extended Kalman Filter Method for Freeway Traffic State Estimation Integrating Multisource Data

Yingshun Liu, Shanglu He , Bin Ran , and Yang Cheng 

Research Article (10 pages), Article ID 6745726, Volume 2018 (2018)

QoS-Aware Resource Allocation for Network Virtualization in an Integrated Train Ground Communication System

Li Zhu , Fei Wang, and Hongli Zhao

Research Article (12 pages), Article ID 2653405, Volume 2018 (2018)

Wideband Channel Modeling for mm-Wave inside Trains for 5G-Related Applications

Juan Moreno García-Loygorri , César Briso-Rodríguez , Israel Arnedo , César Calvo ,

Miguel A. G. Laso , Danping He, Florentino Jiménez, and Vicente González Posadas

Research Article (11 pages), Article ID 6916954, Volume 2018 (2018)

An Operation Control Strategy for the Connected Maglev Trains Based on Vehicle-Borne Battery Condition Monitoring

Wenjing Zhang , Wenjun Wei, Yifan Yang, and Nan Nan

Research Article (10 pages), Article ID 5698910, Volume 2018 (2018)

Adaptive Equalizer Design for Unmanned Aircraft Vehicle Image Transmission over Relay Channels

Huang Wenqian  and Ding Wenrui

Research Article (10 pages), Article ID 5497926, Volume 2018 (2018)

A New Movement Authority Based on Vehicle-Centric Communication

Tuo Shen  and Haifeng Song 

Research Article (10 pages), Article ID 7451361, Volume 2018 (2018)

The QoS Indicators Analysis of Integrated EUHT Wireless Communication System Based on Urban Rail Transit in High-Speed Scenario

Xiaoxuan Wang , Hailin Jiang, Tao Tang, and Hongli Zhao

Research Article (9 pages), Article ID 2359810, Volume 2018 (2018)

Propagation at mmW Band in Metropolitan Railway Tunnels

Ana González-Plaza , César Calvo-Ramírez, César Briso-Rodríguez , Juan Moreno García-Loygorri, David Oliva, and José I. Alonso

Research Article (10 pages), Article ID 7350494, Volume 2018 (2018)

Modeling and Analysis of Safety Messages Propagation in Platoon-Based Vehicular Cyber-Physical Systems

Liqiang Qiao, Yan Shi , Shanzhi Chen, and Wei Gao

Research Article (12 pages), Article ID 5641258, Volume 2018 (2018)

A Road Layout Based Broadcast Mechanism for Urban Vehicular Ad Hoc Networks

Yoonyoung Sung  and Meejeong Lee 

Research Article (21 pages), Article ID 1565363, Volume 2018 (2018)

Editorial

Communications and Networking for Connected Vehicles

Li Zhu ¹, **Fei Richard Yu**,² **Victor C. M. Leung** ³, **Hongwei Wang**,¹
Cesar Briso-Rodríguez ⁴ and **Yan Zhang**⁵

¹State Key Laboratory of Rail Traffic Control and Safety, Beijing Jiaotong University, Beijing, China

²Department of Systems and Computer Engineering, Carleton University, Ottawa, ON, Canada

³Department of Electrical and Computer Engineering, The University of British Columbia, Vancouver, BC, Canada

⁴Technical University of Madrid, Madrid, Spain

⁵University of Oslo, Oslo, Norway

Correspondence should be addressed to Li Zhu; zhulibjtu@gmail.com

Received 13 May 2018; Accepted 15 May 2018; Published 13 June 2018

Copyright © 2018 Li Zhu et al. This is an open access article distributed under the Creative Commons Attribution License, which permits unrestricted use, distribution, and reproduction in any medium, provided the original work is properly cited.

New wave of urbanization, ever more stringent emission standards, and high pressure on improving efficiency of private and public transport have made the development of more sustainable transportation systems one of the fundamental societal challenges of the next decade. Connected vehicles have been envisioned to provide enabling key technologies to enhance transportation efficiency, reduce incidents, improve safety, and mitigate the impacts of traffic congestion. The seamless integration and convergence of vehicular communication networks, information and transportation systems, and mobile devices and networks will face a number of technical, economic, and regulatory challenges. It is of paramount importance to (i) design vehicular communication systems that enable road users and other actors to exchange information in real time with high reliability, (ii) enable pervasive sensing to monitor the status of vehicles and the surroundings, (iii) develop data analytics tools for processing large amounts of data generated by the connected vehicles, and (iv) develop middleware platforms for data management and sharing.

In this context, we present a collection of high-quality research papers on recent developments, current research challenges, and future directions in the use of control, communications, and emerging technologies to realize communications and networking for connected vehicles that are safer and more efficient.

Bin Ran and his research fellows aim to integrate the traffic features extracted from the wireless communication

records and the measurements from the microwave sensors for the state estimation. A state-space model and a Progressive Extended Kalman Filter (PEKF) method are proposed. The results from the field test exhibit that the proposed method efficiently fuses the heterogeneous multisource data as well as adaptively tracking the variation of traffic conditions. The proposed method is satisfactory and promising for future development and implementation.

Safety messages propagation is the major task for Vehicular Cyber-Physical Systems in order to improve the safety of roads and passengers. However, reducing traffic and car accidents can only be achieved by disseminating safety messages in a timely manner with high reliability. Although mathematical modeling of the delay of safety messages is extremely beneficial, analyzing the safety messages propagation is considerably complex due to the high dynamics of vehicles. Moreover, most of previous works assume that vehicles drive independently and the interaction between vehicles is not taken into consideration. The authors in Beijing University of Posts and Telecommunications propose an analytical model to describe the performance of safety messages propagation in the VCPSSs under platoon-based driving pattern. Infrastructure-less and RSU-supported scenarios are evaluated independently. The analytical model also takes into account different transmission situations and various system parameters, such as communication range, traffic flow, and platoon size. The effectiveness of the analytical model is verified through simulation and the impacts

of different parameters on the expected transmission delay are investigated. The results will help determine the system design parameters to satisfy the delay requirement for safety applications in VCPSs.

Urban rail transit plays an increasingly important role in urbanization processes. Communications-Based Train Control (CBTC) systems, Passenger Information Systems (PIS), and Closed Circuit Television (CCTV) are key applications of urban rail transit to ensure its normal operation. In existing urban rail transit systems, different applications are deployed with independent train ground communication systems. When the train ground communication systems are built repeatedly, limited wireless spectrum will be wasted, and the maintenance work will also become complicated. Researchers in Beijing Jiaotong University design a network virtualization based integrated train ground communication system, in which all the applications in urban rail transit can share the same physical infrastructure. In order to better satisfy the Quality of Service (QoS) requirement of each application, the authors propose a virtual resource allocation algorithm based on QoS guarantee, base station load balance, and application station fairness. Moreover, with the latest achievement of distributed convex optimization, they exploit a novel distributed optimization method based on alternating direction method of multipliers (ADMM) to solve the virtual resource allocation problem. Extensive simulation results indicate that the QoS of the designed integrated train ground communication system can be improved significantly using the proposed algorithm. X. Wang et al. in Beijing Jiaotong University set up an Enhanced Ultra-High Throughput (EUHT) wireless communication system for urban rail transit in high-speed scenario integrating all the traffics of it. An outdoor testing environment in Beijing-Tianjin high-speed railway is set up to measure the performance of integrated EUHT wireless communication system based on urban rail transit. The communication delay, handoff latency, and throughput of this system are analyzed. Extensive testing results show that the Quality of Service (QoS) of the designed integrated EUHT wireless communication system satisfies the requirements of urban rail transit system in high-speed scenario.

Safety services of Vehicular Ad Hoc Network (VANET) require reliable broadcasts. Urban road characteristics such as frequent intersections, high traffic density, and traffic concentration caused by wait traffic signals are not carefully taken into account. Inaccuracy of beacon information due to losses of beacons caused by high traffic density or by the signal attenuation at intersections may result in choosing suboptimal forwarding vehicles and lead to broadcast collisions or unnecessary broadcasts. In particular, the inaccuracy of information tends to aggravate the broadcast inefficiency more seriously when traffic is heavily concentrated. Therefore, Y. Sung and M. Lee propose "VANET Broadcasting for Urban areas based on Road Layout (VBURL)," which minimizes the dependency on information that may become inaccurate in order to maximize the efficiency of broadcast. VBURL takes into account the road layout information accessible from the digital map and only the real-time information obtained from the broadcast messages or beacons instead of leveraging the holding information from beacons

or implicit guess about the status of neighboring vehicles. VBURL basically makes the vehicle that is farthest from the current forwarding vehicle take the role of next forwarding vehicle. Furthermore, VBURL makes an additional broadcast happen at the intersections in addition to the one made by the farthest vehicle as long as there exists a vehicle hearing the broadcast at the intersection or else at least there exist one or more vehicles that are moving toward the intersection with that intersection within their transmission range. Through a course of simulations, the performance of VBURL is compared with that of the legacy schemes proposed for reliable broadcast on urban roads. The simulation results verified that VBURL achieves the same high performance as that of the compared schemes in terms of reliability with much higher efficiency.

E. M. Ghourab et al. in Alexandria University propose a novel approach to enhance wireless vehicle-to-vehicle channel-secrecy capacity by imposing signal transmission diversity. This work exploits cooperative vehicular relaying to extract the associated underlying multipath and Doppler diversity using precoding techniques. We evaluated the capacity and diversity gain for the presented approach to ensure its effectiveness and efficiency. The abundance of moving vehicles, operating in an ad hoc fashion, can eliminate the need to establish a dedicated relaying infrastructure. A relay selection scheme is deployed taking advantage of the potentially large number of available relaying vehicles. Further, they derive a closed-form mathematical expression for the channel-secrecy capacity, diversity order gain, and the intercept probability. We used the direct transmission scenario as a reference to assess our analysis. Our analytical and simulation results for the presented model showed that channel-secrecy capacity and performance-indicators improved significantly.

The next generation of mobile communications, 5G, will provide a wideband network based on microwave and millimeter-waves (mmW) communication radio links with the goal of fulfilling the strict and severe requirements of the future test cases. In particular, D. Oliva et al. in University of Madrid focus on mmW bands in metropolitan railway tunnels. For that purpose, a propagation measurement campaign is performed at 24 GHz band in a passenger train on a realist subway environment and these results were combined with ad hoc simulations for tunnels and a theoretical modal propagation model. Narrowband and wideband study have been conducted with the aim of obtaining the path loss, fading, power-delay profile, and angle of arrival, all of this taking into consideration a horizontal and vertical polarization in the receiving and transmitting antennas. This validation can be used to design and deploy wideband mobile communication networks at mmW bands in railway scenarios. Passenger trains and especially metro trains have been identified as one of the key scenarios for 5G deployments. The wireless channel inside a train car is reported in the frequency range between 26.5 GHz and 40 GHz. These bands have received a lot of interest for high-density scenarios with a high-traffic demand, two of the most relevant aspects of a 5G network. C. Calvo et al. provide a full description of the wideband channel estimating power-delay

profiles (PDP), Saleh-Valenzuela model parameters, time-of-arrival (TOA) ranging, and path-loss results. Moreover, the performance of an automatic clustering algorithm is evaluated. The results show a remarkable degree of coherence and general conclusions are obtained.

The communication system presently applied in the European Train Control System can only support data exchange between vehicles and ground, but the direct vehicle-to-vehicle communication is not available. The details of interlocking information and other vehicles' movements are invisible to drivers who are the last defense to prevent unsafe scenarios. As connected vehicles have been envisioned to enhance transportation efficiency and improve safety, the direct vehicle-to-vehicle communication network is involved to increase the safety critical needs of railway transport. T. Shen and H. Song propose a new train movement authority (MA+). Apart from a wireless communication unit, this system does not require any other infrastructure. With the assistance of vehicle-centric communication technology, MA+ can detect the condition of switches and trains within a certain scope. Additionally, different implementation scenarios are also discussed. The detection range is estimated and validated based on mathematical calculation and experimental equations. An application demo of the MA+ is presented on the Driver Machine Interface of the onboard equipment. The results indicate that MA+ can be a flexible and scalable system for furthering the improvement of railway safety.

Greater demands are being placed on the access bandwidth, stability, and delay of network because of the quickening rhythm of life and work, especially in mobile scenario. In order to obtain a stable network with low latency and high bandwidth in mobile scenario, taking advantage of the wireless heterogeneous network in parallel is a good choice. Nowadays, people are increasingly concerned about the network quality under the mobile scenario. Some scholars have done the relevant measurements. However, all of those measurements mainly investigate part of the network parameters or part of mobile scenarios. T. et al. in Beijing Jiaotong University make the following contributions. Firstly, in high-speed mobile scenario, the wireless network qualities of different vendors are measured synthetically. Secondly, they analyze the benefits of taking advantage of the different vendors. Thirdly, they deploy the replication link mechanism in high-speed mobile scenario and propose an algorithm to remove the duplicate packet in high-speed mobile scenario. And the algorithm can also be used in other multipath schedule algorithms to improve the reliability.

Existing intelligent transport systems (ITS) do not fully consider and resolve accuracy, instantaneity, and compatibility challenges while resolving traffic congestion in Internet of Vehicles (IoV) environments. D.-B. Nguyen et al. in Feng Chia University propose a traffic congestion monitoring system, which includes data collection, segmented structure establishment, traffic-flow modeling, local segment traffic congestion prediction, and origin-destination traffic congestion service for drivers. Macroscopic model-based traffic-flow factors were formalized on the basis of the analysis results. Fuzzy rules-based local segment traffic congestion

prediction was performed to determine the traffic congestion state. To enhance prediction efficiency, they present a verification process for minimizing false predictions, which is based on the Rankine-Hugoniot condition and an origin-destination traffic congestion service is also provided. To verify the feasibility of the proposed system, a prototype was implemented. The experimental results demonstrate that the proposed scheme can effectively monitor traffic congestion in terms of accuracy and system response time.

VBTC (Vehicle-to-Vehicle Communications-Based Train Control) has gradually become an important research trend in the field of rail transit. This has resulted in advantages of decreasing the amount of wayside equipment and improving the efficiency of real-time system communication. Characteristics and mechanism of train-to-train communication, as key implementation technology of safety critical system, are discussed by H. Feng in China Academy of Railway Sciences. A new method, based on the LTS (labelled transition system) model checking, is proposed for verifying the safety properties in the communication procedure. The LTS method is adapted to model system behaviours and analysis and safety verification is checked by means of LTSA (labelled transition system analyzer) software. The results show that it is an efficient method to verify safety properties and to assist the complex system's design and development.

H. Wenqian and D. Wenrui in Beihang University propose a novel length adaptive method for time domain equalizer by taking the channel attenuation ratio between different multipath components into account in UAV-UAV and UAV-ground channels. Then, considering received image quality, the minimum bit error ratio (MBER) criterion is exploited to design adaptive equalizers for both amplify-and-forward (AF) and decode-and-forward (DF) relaying systems by the proposed length adaptive method. Results show that proposed MBER adaptive equalizers outperform the traditional ones in both AF and DF relaying as channel attenuation ratio in UAV-ground channel increases. Moreover, DF outperforms AF as channel attenuation ratio in UAV-UAV channel increases. Furthermore, bit error ratio (BER) and peak signal-to-noise ratio (PSNR) performances in both AF and DF are evaluated to show the enhancement by the proposed MBER adaptive equalizers.

Vehicle-borne battery condition is an important factor affecting the efficiency of the Maglev train operation and other connected ones. To effectively eliminate the influence of the battery condition and improve the operation efficiency of the connected Maglev trains, an operation control strategy is proposed to guarantee train operation safety by W. Zhang et al. in Beijing Jiaotong University. Based on Internet of Things, a sensor network is designed to monitor vehicle-borne battery condition in each vehicle of the train. The train Operation Control System collects battery data of all vehicles in a Maglev train by Train Communication Network. All connected Maglev trains share the battery data via a 38 GHz directional Radio Communication System and adjust operation control strategy accordingly. Simulation results indicate that the proposed strategy can guarantee the operation safety of the connected Maglev trains.

Overall, it is imperative that we continue to progress in our search for appropriate models, which can adequately and faithfully improve the safety and performance of communications and networking for connected vehicles. The progress reported in this special issue suggests that, in the future, achieving these aims might be a distant prospect but an unattainable one.

Li Zhu
Fei Richard Yu
Victor C. M. Leung
Hongwei Wang
Cesar Briso-Rodríguez
Yan Zhang

Research Article

Study on Formal Modeling and Safety Verification of Train-to-Train Communication

Haonan Feng ^{1,2}

¹Signal and Communication Research Institute, China Academy of Railway Sciences, Beijing 10081, China

²The Center of National Railway Intelligent Transportation System Engineering and Technology, Beijing 10081, China

Correspondence should be addressed to Haonan Feng; fhn02212005@163.com

Received 6 December 2017; Revised 20 March 2018; Accepted 23 April 2018; Published 4 June 2018

Academic Editor: Li Zhu

Copyright © 2018 Haonan Feng. This is an open access article distributed under the Creative Commons Attribution License, which permits unrestricted use, distribution, and reproduction in any medium, provided the original work is properly cited.

VBTC (vehicle-to-vehicle communication based train control) has gradually become an important research trend in the field of rail transit. This has resulted in advantages of decreasing the number of pieces of wayside equipment and improving the efficiency of real-time system communication. Characteristics and mechanism of train-to-train communication, as key implementation technology of safety critical system, are given and discussed. A new method, based on the LTS (labelled transition system) model checking, is proposed for verifying the safety properties in the communication procedure. The LTS method is adapted to model system behaviours; analysis and safety verification are checked by means of LTSA (labelled transition system analyzer) software. The results show that it is an efficient method to verify safety properties, as well as to assist the complex system's design and development.

1. Introduction

With rapid development of urbanization, demands from increased living standards and travel lead to requirement of rapid development of urban transit transport. Signal system, as an important role of traffic safety, is to ensure traffic safety, shorten the operation interval, and improve traffic efficiency [1]. CBTC (communication based on train control) system adding wireless communication technology into traditional ground interlocking control system, which makes moving block operation mode under double protection of ground ATP (automatic train protection) and vehicle ATP, provides protective speed based on real-time speed from vehicle [2, 3]. CBTC system has a great advantage in terms of transportation capacity and system safety, and its great development in urban transit signalling system contributes to lower the urban traffic pressure [4, 5].

The next generation of train control system welcomes a new research field that follows on from the mature development of CBTC system and modern communication technology. VBTC system is a good example in attractive research trend [6]. The system is designed to improve train automotive control, reduce system coupling for better efficiency, and lower cost [7]. Train-to-train communication is the main

supporting architecture in VBTC, whose simple structure has the advantage of decreasing equipment number and lowering construction and maintenance cost. Direct communication among trains in real time should decrease the impact from delay caused by undirected wireless communication and improve overall system efficiency [8, 9].

Although VBTC brings out innovative results by optimizing communication methods, it originally belongs to safety critical system, which requires design phase needed to be verified carefully to the extent of safety and security. Formal modeling is the process of converting the natural description language into a formal description language during the system's requirement design phase, which can improve the completeness and consistency of the system design. According to the description of the system characteristics, it can be divided into two categories: one is used to describe the system sequence characteristics based on mathematical analysis methods, such as Z method [10], B method [11], and VDM method [12]; the other method is preferable to describe concurrent characteristics of system, such as Petri net [13–15], finite automata [16, 17], and LTS [18].

Different from other formal methods, LTS has the unique ability to analyze the countably infinite set of states and actions of system and infinite interactive branching, so it is

appropriate for reactive and concurrent system behaviour. It provides method to trace state transit behaviour, identify observable states, and evaluate sequence of performed actions. As an ideal tool to verify concurrent and complex system, it gains a great achievement in the application of verifying safety protocol RSSP-1 [19] and needs of ERTMS/ETCS system [20]. This paper focuses on formal modeling and verification based on LTS method for train-to-train communication logic in the architecture of VBTC.

In the rest of this paper, we firstly define and describe new architecture of VBTC and make comparison with CBTC in Section 2. In Section 3, LTS and its auxiliary analysis tool LTSA software are introduced and adopted to model the behaviours of train-to-train communication. Safety property of train-to-train communication is verified in Section 4. Comparisons in the aspect of application and performance are listed using LTS method and traditional human checking method in Section 5. Finally, the conclusions are presented in Section 6.

2. The Architecture of VBTC

VBTC system is shown in Figure 1. Its five cardinal parts are central ITS (intelligent train supervision system), TMC (train management center), OC (object controller) belonging to wayside systems, IVOBC (intelligent vehicle on board controller) installed in vehicle, and DCS (data communication system), which provides data transmission link between static equipment and moving train. Main functions of each system are illustrated as follows.

Central ITS is in charge of train operation schedule, monitoring all the conditions of other systems, and processing safety related events. All the trains on line should interact with central ITS based on periodic and reliable communication. Central ITS checks status of every section to make sure safety of the whole line operation. It will provide all the necessary information required for trains to identify what trains are in front or behind.

TMC is responsible for the storage and distribution of electronic map, system configuration data, and temporary speed limits. Its communication mode should be aperiodic or passive response.

OC is a new kind of wayside equipment control unit. It collects and sends status of control objects in response to request of trains and central ITS; at the same time, it receives control information as operation input. Passive communication is interactive mode of this type of unit.

IVOBC is the core of VBTC system. It inherits all the features of ATP (automatic train protection) and ATO (automatic train operation) and V2I (vehicle-to-infrastructure) communication in CBTC system; IVOBC also develops the new functions of route plan, route safety protection, and moving authority calculation.

DCS should support multiple communication protocols as an important bridge link for IVOBC and other systems, for communication standards should vary adaptively with distance parameters in the adjacent trains. For instance, a train should communicate with other trains by the communication

form of LTE-V2X in long range, and it chooses direct-to-direct communication form when range is less than 1km.

The property differences between VBTC and CBTC system are compared in the five aspects of system components, train-to-train communication mode, train control mode, wayside equipment, and daily maintenance (see Table 1).

3. Formal Modeling and Verification Methodology Based on LTS

The communication cooperation among trains has the characteristics of complex concurrency and logic synchronization. Therefore, LTS method is selected by the advantage of accurate description of system behaviour in real time and concurrency. The train-to-train communication cooperation strategy in VBTC is modeled by LTS method, which provides a basis for subsequent simulation and verification analysis.

3.1. Formal Definition of LTS. Let S represent the universal set of states including a designated error state π . L is the universal set of labels and acts as $D = L \cup \{\tau\}$, where τ denotes an internal actions that cannot be observed by the environment of an LTS.

An LTS of a process P is a quadruple $\langle Q, A, T, q_0 \rangle$, where

- (1) Q is a countable finite and nonempty set of states,
- (2) A is a countable set of labels $A = \alpha P \cup \{\tau\}$, where αP denotes the alphabet of P , and $\alpha P \subseteq L$,
- (3) $T \subseteq Q - \{\pi\} \times A \times Q$ denotes a transition relation that maps from a state and an action onto another state,
- (4) $q_0 \in Q$ indicates the initial state of P .

The only LTS that is allowed to have the error state π as its initial state is $\langle \{\pi\}, D, \{\}, \pi \rangle$, named E . The alphabet of this process $\alpha E = L$.

An LTS $P = \langle Q, A, T, q_0 \rangle$ transits with action $a \in A$ into P' , denoted as $P \xrightarrow{a} P'$, if

- (1) $P' = \langle Q, A, T, q'_0 \rangle$, where $q'_0 \neq \pi$ and $(q, a, q'_0) \in T$,
- (2) $P' = E$, and $(q, a, \pi) \in T$.

$P \xrightarrow{a}$ means that $\exists P'$ such that $P \xrightarrow{a} P'$.

End states $Z \subseteq S$ such that an LTS $P = \langle Q, A, T, q_0 \rangle$ is terminating if there is a state $e \in Z$ and $\exists (e, a, q) \in T$ for all $a \in A$.

LTSA software, as an auxiliary analysis tool based on LTS, can animate and check the behaviour of the overall system before it is implemented. It focuses on the aspect of concurrency, provides methods to model animation to visualize system behaviour, and gives mechanical verification of system properties including safety and progress. LTSA program supports process algebra notation, such as FSP (finite state process), for concise description of system component behaviour [21].

3.2. Train-to-Train Communication Mechanism. Train-to-train communication can be broken down into a set of

TABLE I: Comparison between VBTC and CBTC system.

Property	VBTC	CBTC
System components	Central ITS TMC IVOBC DCS OC	Central ATS (automatic train supervision) DSU (digital storage unit) VOBC (vehicle on board controller) DCS ZC (zone controller) CI (computer interlocking)
Train to train communication mode	Direct radio communication between trains	Indirect communication between trains, interactive information needs to be relayed by wayside equipment
Train control mode	IVOBC is center of system, ground only provides auxiliary functions, such as schedule plan, emergency procedure	Train operation is controlled by ATP from ground and vehicle
Wayside equipment	Little wayside equipment, only balises, switch controller	Amount of axle counting, balises, semaphores
Daily maintenance	less maintenance data mainly involving of train	Amount of maintenance data including train, wayside equipment

simpler activities, its mechanism should include at least three basic functions: (a) identification of train in front, (b) communication status management between train and the train in front, and (c) communication status management between train and the following train. These activities are not executed one after the other in a strictly fixed order in the physical world. In fact, it is noticing that these activities are permitted to overlap or occur concurrently in certain scenarios.

(a) *Identification of Train in Front.* It is accessible to get numbers ID information of other trains when a train enters recognizable region in touch with central ITS. After a train confirms all the trains in the same region in the mode of calling and answering, it begins to identify and confirm the train in front. The procedure of this stage is shown in Figure 2.

(b) *Communication Status Management between Train and the Train in Front.* Implementation of the stage should be divided into four steps as follows:

- (1) Get the train ID in front and check tracing condition requirements.
- (2) Send the tracing establishment request message when tracing condition is satisfied.
- (3) Wait and receive tracing establishment reply from train in front; the communication between train and the front should be closed if communication time is over the designed parameter of time gate.
- (4) It is successful to enter tracing mode after train accepts reply from the train in front; otherwise the train should resend tracing establishment request message in the case that communication between train and the front status is still valid, or the train rebuild tracing link from the beginning if communication time is over the designed parameter time gate.

The procedure of this stage is shown in Figure 3.

(c) *Communication Status Management between Train and the Following Train.* It is similar to the previous stage. The tracing mode is triggered by the following train; confirmation message is sent by the train in response to the tracing request of the following train. Train will check condition after receiving message. The procedure of this stage is shown in Figure 4.

3.3. *Simulation and Verification.* Designed to be easily machine readable, FSP is a simple algebraic notation to describe process models; each description of state in LTS has a corresponding FSP description. The semantics of basic FSP can be easily defined in terms of LTS, and LTSA software has the function of depicting the LTS by FSP language as a graph. In the following, their correspondence is defined by the function in

$$lts : E \longrightarrow \xi \quad (1)$$

where E is the set of FSP process expressions and ξ represents the set of LTSs. The function lts is defined inductively on the structure of FSP process expressions.

After analyzing train-to-train communication workflow in the Section 3.2, action sets of system behaviour are illustrated by alphabet sets A , while system process S and intermediate transition process variables $M_i, (i=1,2,\dots,9)$ should be defined in FSP language as follows.

$$A = \{ inichk, inisysOK, inisysBad, sndReqTrain, rcvFdReqTrain, checkTrainID, rcvReqTrain, reqTraintimeout, trainAlarm, sndITS, isTrainPos, trainisFront, trainisBack, sndBldTracReq, bldTracReqTimeout, rcvBldTracAns, checkTracCond, tracCondisOK, tracCondNotOK, setTracMode, selfFixBlock, selfTracingMode, sndDismissTracReq, dismissTracReqtimeout \}$$

$$S = M_1,$$

$$M_1 = (inichk \rightarrow inisysOK \rightarrow M_2 \\ | inichk \rightarrow inisysBad \rightarrow M_3),$$

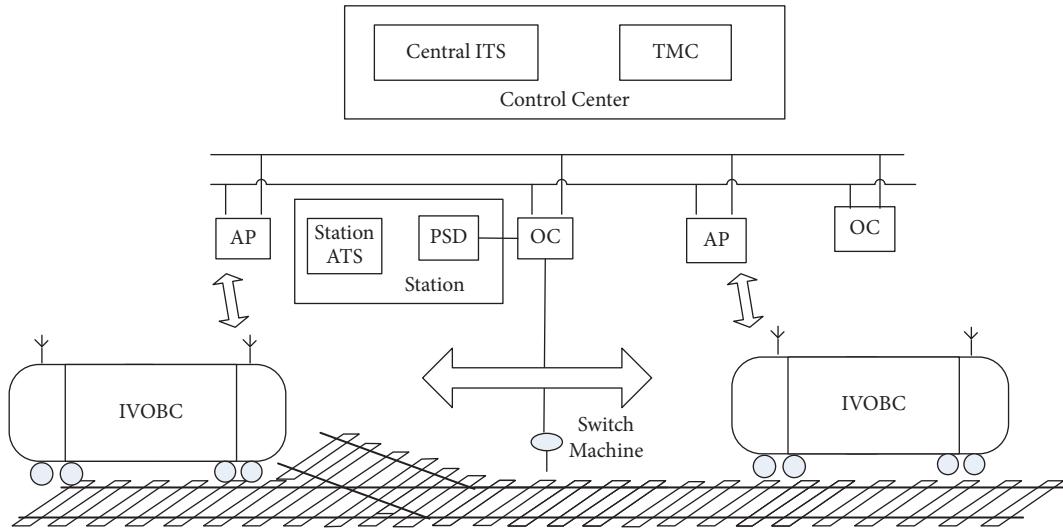


FIGURE 1: Architecture of train-to-train based train control system.

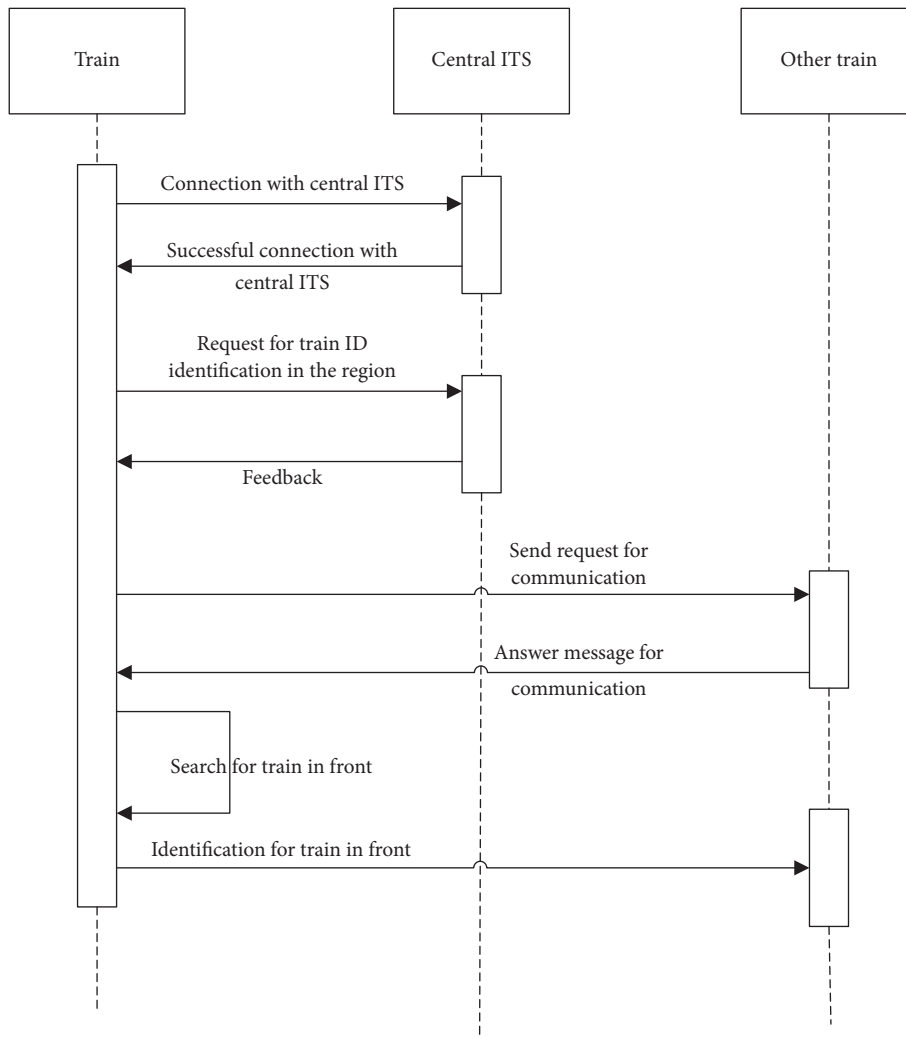


FIGURE 2: Time sequence of train in front identification.

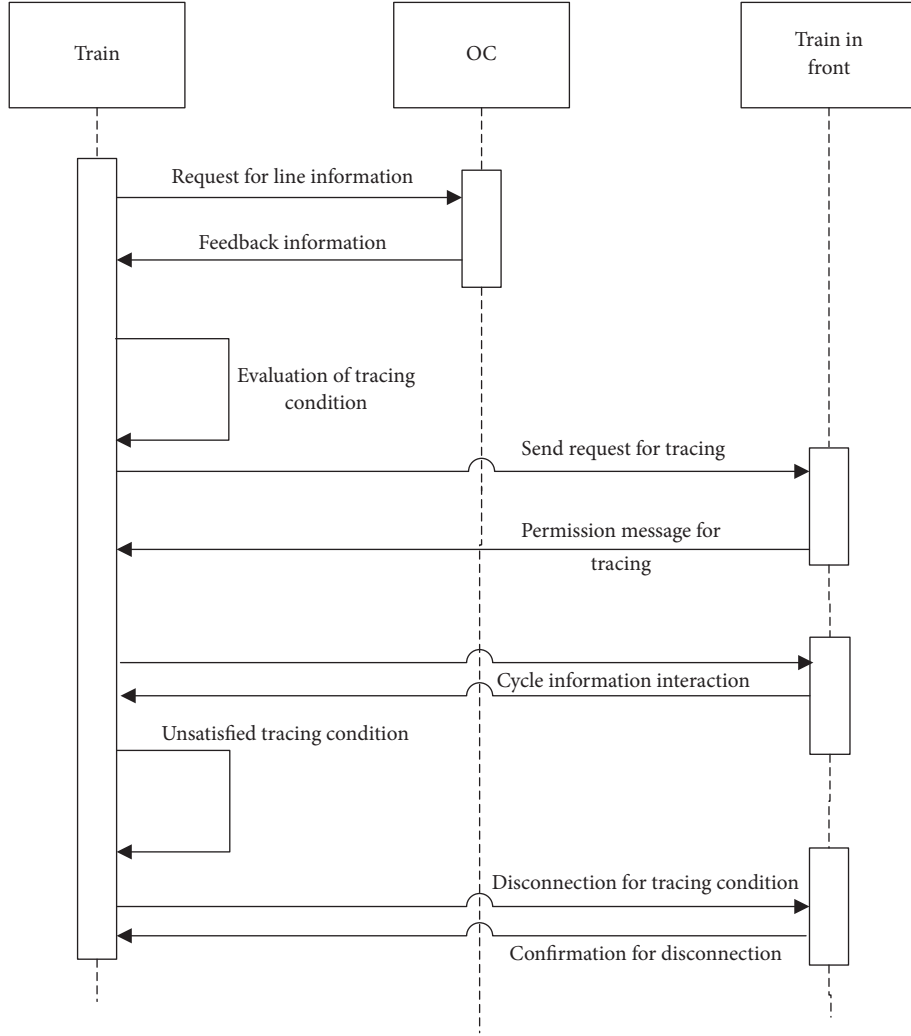


FIGURE 3: Holding process of tracing mode.

$$\begin{aligned}
 M_2 &= (\text{sndReqTrain} \rightarrow \text{rcvFdReqTrain} \rightarrow \text{checkTrainID} \rightarrow M_4 \mid \text{rcvReqTrain} \rightarrow \text{checkTrainID} \rightarrow M_4 \\
 &\quad \mid \text{sndReqTrain} \rightarrow \text{reqTracTimeout} \rightarrow M_3), \\
 M_3 &= (\text{trainAlarm} \rightarrow \text{sndITS} \rightarrow M_1), \\
 M_4 &= (\text{isTrainPos} \rightarrow \text{trainisFront} \rightarrow M_5 \\
 &\quad \mid \text{isTrainPos} \rightarrow \text{trainisBack} \rightarrow M_6), \\
 M_5 &= (\text{sndBldTracReq} \rightarrow M_6 \\
 &\quad \mid \text{sndBldTracReq} \rightarrow \text{bldTracReqTimeout} \rightarrow M_3), \\
 M_6 &= (\text{rcvBldTracAns} \rightarrow M_8), \\
 M_7 &= (\text{checkTracCond} \rightarrow \text{tracCondisOK} \rightarrow M_8 \\
 &\quad \mid \text{checkTracCond} \rightarrow \text{tracCondNotOK} \rightarrow M_9), \\
 M_8 &= (\text{setTracMode} \rightarrow \text{selfFixBlock} \rightarrow M_2 \\
 &\quad \mid \text{setTracMode} \rightarrow \text{selfTracingMode} \rightarrow M_5), \\
 M_9 &= (\text{sndDismissTracReq} \rightarrow \text{rcvDismissTracAns} \rightarrow M_8 \\
 &\quad \mid \text{sndDismissTracReq} \rightarrow \text{dismissTracReqTimeout} \rightarrow M_3).
 \end{aligned}$$

Detailed explanations of actions in FSP language are shown in Table 2.

By means of LTSA software, the graphic transition actions and processes of train-to-train communication model are shown in Figure 5. The nodes in the Figure 5 represent states of the system, and transitions are depicted by connecting edges. It is noticed that no error label -1 is shown in these model checking result. The verification results by LTSA in Figure 6 give that there is no deadlock or logic violations in 19 states before the model is implemented into executable codes.

4. Safety Verification

In the design phase of VBTC, there exist some dangerous situations that should never not be allowed to occur. Designers and programmers should take careful and thoughtful actions to these dangerous situations. Fault-oriented safety principle is convention in the engineering field of rail transit. The prohibited system requirements should be listed and fulfilled in the final implementation of system.

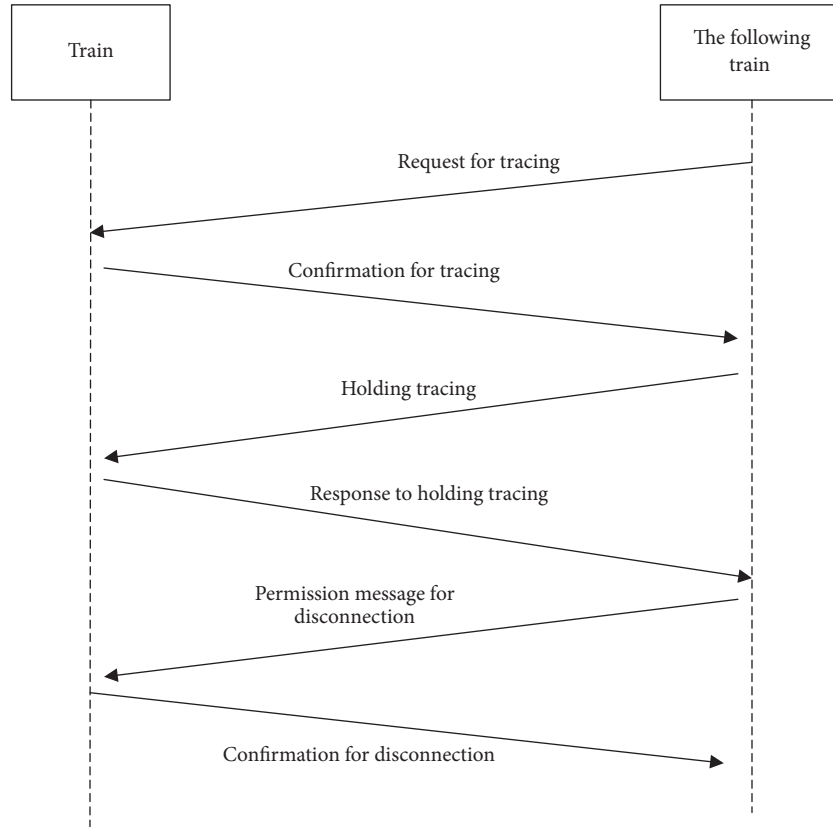


FIGURE 4: Holding process of tracing mode between train and following train.

The following actions are prohibited; the safety aspects should be verified strictly as safety property in the system model.

- (1) Send request message to other train when the initialization check of self system fails.
- (2) Send request message to other train when train alarms for error.
- (3) Send build tracing request message to other train in the case of timeout for request message.
- (4) Tracing condition should not be satisfied in the case of timeout for built tracing request.
- (5) The mode is not allowed to be set tracing mode in the case of timeout for tracing request message.
- (6) The mode is not allowed to be set tracing mode when tracing condition is unsatisfied.

The safety property in these unacceptable behaviours above modeled by FSP language is follows:

```

property TrainSafety = Safe,
Safe =(inisyBad -> sndReqTrain -> Safe
|trainAlarm-> sndReqTrain -> Safe
|reqTraintimeout -> sndBldTrackReq -> Safe
|bldTrackReqTimeout -> trackCondisOK-> Safe

```

```

|dismissTrackReqtimeout -> selfTracingMode ->
Safe
|trackCondNotOK -> selfTracingMode-> Safe).

```

It appears a mistake state labelled ‘-1’ in the system in Figure 7, which means that, in all transition traces begun from initial state, there are no exceptional transition lists from (1) to (6). It can be confirmed that the model of system satisfies the safety requirements.

5. Application and Performance

The formal modeling and verification method presented above is used in the deployment of train-to-train communication program. In order to evaluate the efficiency of the LTS modeling method, two independent developing teams with the same labour and similar technical experience are assigned to fulfill the program.

Both teams start the task simultaneously, and eight hours is their work time in one day. The entire developed procedure is divided into two stages, developing phase and testing phase. The main task of the first phase is to convert executable code from model based on the system requirement; testers in the second phase focus on errors occurring in the executable code, analysis, and classification of their reason. Operating time and categorized bugs are recorded in summary as important evaluation parameters in Table 3.

- EURASIP Journal on Wireless Communications and Networking*, vol. 2012, no. 1, pp. 1–16, 2012.
- [6] J. K. Xu, “Analysis of novel CBTC system based on train to train communication,” *Railway Signaling and Communication*, vol. 50, no. 6, pp. 78–80, 2014.
- [7] C. Li, *Research on Train Communication Cooperation under V2V Communication Environment based on State Machine*, Beijing Jiaotong University Master Degree, 2017.
- [8] H. Du, J. G. Sun, and Q. Zhang, “A new generation of CBTC system without CI and ZC,” *Urban Rapid Rail Transit*, vol. 30, no. 4, pp. 91–95, 2017.
- [9] D. Briginshaw, “Alstrom’s simplified CBTC technology to debut in lille,” *International Railway Journal*, vol. 53, no. 1, pp. 23–24, 2013.
- [10] N. Zafar, “Formal dynamic operational model of RIS components,” *International Journal of Computer Science and Network Security*, vol. 11, pp. 91–97, 2011.
- [11] H. D. Tong, B. Ning, and H. F. Wang, “Research on event-B based modelling and verification of interlocking route control,” *Railway Computer Application*, vol. 22, no. 6, pp. 57–61, 2013.
- [12] N. A. Zafar, “Formal model for moving block railway interlocking system based on un-directed topology,” in *Proceedings of the 2nd Annual International Conference on Emerging Technologies 2006, ICET 2006*, pp. 217–223, Peshawar, Pakistan, November 2006.
- [13] H. Song and E. Schnieder, “Validation, verification and evaluation of a train to train distance measurement system by means of colored petri nets,” *Reliability Engineering & System Safety*, vol. 164, pp. 10–23, 2017.
- [14] E. Schnieder, L. Schnieder, and J. Müller, “Conceptual foundation of dependable systems modelling,” *2nd IFAC Workshop on Dependable Control of Discrete Systems*, vol. 42, no. 5, pp. 198–202, 2009.
- [15] M. M. Zu Hörste and E. Schnieder, “Modelling and simulation of train control systems using petri nets,” in *FMRail Workshop*, 1999.
- [16] Y. Dong and X. J. Gao, “Method for generating formal interlocking software model based on scenario,” *Computer Science*, vol. 42, no. 1, pp. 193–195, 2015.
- [17] X. Y. Zhao, R. J. Cheng, and Y. Cheng, “Formal modeling and parameter analysis method for train control system based on hybrid unified modeling language,” *Journal of the China Railway Society*, vol. 38, no. 11, pp. 80–87, 2016.
- [18] X. Wang, Z. W. Xu, and M. Mei, “A software safety verification method based on model checking,” *Journal of Wuhan University (Natural Science Edition)*, vol. 56, no. 2, pp. 156–160, 2010.
- [19] M. Meng, X. Zhongwei, W. Xi, and W. Yongbing, “Model checking-based safety verification for railway signal safety protocol-I,” *International Journal of Computer Applications in Technology*, vol. 46, no. 3, pp. 195–202, 2013.
- [20] M. Ghazel, “Formalizing a subset of ERTMS/ETCS specifications for verification purposes,” *Transportation Research Part C: Emerging Technologies*, vol. 42, pp. 60–75, 2014.
- [21] J. Magee and J. Kramer, *Concurrency State Models and Java Programs*, John Wiley Sons Ltd, Chichester, England, 1999.

Research Article

A Novel Approach to Enhance the Physical Layer Channel Security of Wireless Cooperative Vehicular Communication Using Decode-and-Forward Best Relaying Selection

Esraa M. Ghourab ¹, Mohamed Azab,^{2,3} Mohamed F. Feteiha,^{2,4,5} and Hesham El-Sayed⁶

¹Electrical Engineering Department, Alexandria University, Alexandria, Egypt

²Informatics Research Institute, The City of Scientific Research and Technological Applications, Alexandria, Egypt

³ACIS, Electrical and Computer Engineering, University of Florida, Gainesville, FL, USA

⁴Electrical and Computer Engineering Department, Faculty of Engineering, University of Waterloo, Waterloo, Ontario, Canada

⁵Systems Design Engineering Department, Smart-Nations Technology Development Inc., Ontario, Canada

⁶Computer and Network Engineering Department, United Arab Emirates University, Al-Ain, UAE

Correspondence should be addressed to Esraa M. Ghourab; esraa.m.ghourab@mena.vt.edu

Received 24 October 2017; Revised 30 January 2018; Accepted 15 April 2018; Published 28 May 2018

Academic Editor: Hongwei Wang

Copyright © 2018 Esraa M. Ghourab et al. This is an open access article distributed under the Creative Commons Attribution License, which permits unrestricted use, distribution, and reproduction in any medium, provided the original work is properly cited.

This paper proposes a novel approach to enhance wireless vehicle-to-vehicle channel-secrecy capacity by imposing signal transmission diversity. This work exploits cooperative vehicular relaying to extract the associated underlying multipath and Doppler diversity using precoding techniques. We evaluated the capacity and diversity gain for the presented approach to ensure its effectiveness and efficiency. The abundance of moving vehicles, operating in an ad hoc fashion, can eliminate the need to establish a dedicated relaying infrastructure. A relay selection scheme is deployed, taking advantage of the potentially large number of available relaying vehicles. Further, we derive a closed-form mathematical expression for the channel-secrecy capacity, diversity order gain, and the intercept probability. We used the direct transmission scenario as a reference to assess our analysis. Our analytical and simulation results for the presented model showed that channel-secrecy capacity and performance-indicators improved significantly.

1. Introduction

In large cities, the complex network of diverse people and the exponentially increasing service demands urge leading telecommunication networking to improve the communication capabilities.

In the search for ways to enhance network performance and security, researchers and practitioners started to consider offloading such heavy burden to road-traveling vehicles. The abundant on-vehicle computing resources may be underutilized by the traditional vehicular applications. Many wireless communication technologies are available for “Vehicular Ad hoc Networks (VANETs)” communications, including traditional wireless technologies or technologies specifically introduced for the vehicular environment.

In most practical scenarios, due to the broadcast nature of the system, legal user’s data can be easily overheard, altered, or blocked by malicious parties (eavesdropping attacks). VANETs physical layer designs need to cope with tremendous security challenges. However, the conventional physical layer security technique depends mainly on the replication for reliability and encryption for security [1–6]. Antenna diversity is used to address the aforementioned challenges by enhancing signal quality, such as MIMO and cooperative diversity using replication.

Additionally, researchers proved that, even with computationally expensive resources, eavesdropper can still decrypt heavily encrypted data [7]. In [8, 9], Wyner presented the concept of channel secrecy as an indication of data transmission security. Channel secrecy is defined as the

relation between the channel capacity of the main link (from source to destination) and the wire-tap link (from source to eavesdropper). Channel-secrecy capacity was evaluated in Gaussian wire-tap channel as the difference between the channel capacity of the main link and that of the wire-tap link [9].

Cooperative communication has the ability to improve the overall channel-secrecy capacity for any given set of bandwidths [10, 11], with the appropriate relay selection.

In [12], authors presented the effect of Decode-and-Forward (DF) relay selection mechanisms on channel secrecy and intercept probability without a direct link. They presented the optimal and traditional (Max-Min) relay selection mechanisms.

Authors presented in [6] performance comparison between both cooperative diversity protocols Amplify-and-Forward (AF) and Decode-and-Forward (DF) for ergodic channel-secrecy capacity and intercept probability. They proved that AF cooperative protocol has better intercept probability than DF protocol. Furthermore, in [11], authors presented the ergodic channel-secrecy capacity for DF cooperative protocol in case of a direct link. Their analysis was derived from Independent Nonidentical Distribution (i.n.i.d) cooperative link, assuming Maximal Likelihood (ML) scenario at the destination node. They proved that the (i.n.i.d) DF cooperative protocol with the existence of direct link has low intercept probability.

In this paper, we adopted the model presented in [13, 14] to devise an enhanced version towards more secure vehicular networks. Additionally, we present a vehicle-to-vehicle communication model assessment using intercept probability and channel secrecy as an indication of how secure the system can be in the presence of attackers.

Authors in [13] presented precoded multihop vehicular transmission with cooperative DF relaying to forward the signal from a source vehicle to a destination vehicle in the absence of a direct link. Moreover, they determined the analytical tight upper bound expressions for the Pairwise Error Probability (PEP) and diversity gain. Their performance analysis through PEP showed that, via proper precoding, the proposed system is able to extract the maximum available diversity in multiple dimensions. These dimensions can be summarized as follows: time dimension (through Doppler diversity), frequency dimension (through multipath diversity), and space dimension (through best relaying vehicle selection).

In this paper, we use the above-mentioned modified system [13], considering that there is a direct link between vehicles. We exploit direct transmission and cooperative terminals links to increase the channel-secrecy capacity of VANETs system without increasing the bandwidth.

However, our vehicle model assumes that vehicles are traveling on a highway with a fixed speed. Given the fact that our presented model relies mainly on moving vehicles with no presence of roadside units, considering the vehicle speed in this scenario is not applicable. Our future work will consider vehicle speed among other communication characteristics in totally different scenarios to be presented in our sequel papers.

The main contributions of this paper can be summarized as follows:

- (i) Derive a closed form for the optimal channel-secrecy capacity and intercept probability for both direct and DF cooperative links. We rely on a precoded cooperative transmission technique to extract the underlying rich multipath-Doppler-spatial diversity.
- (ii) Evaluate the proposed best relay selection scheme in presence of eavesdropper among large number of moving vehicle relays.
- (iii) Derive a mathematical closed-form expression for diversity order by combining direct and cooperative links diversity.
- (iv) Derive closed form for the outage probability of our proposed model, showing the benefits of combining direct and cooperative links in the vehicular diversity model.

The paper is organized as follows: Section 2 describes the proposed two-phase dual-hop cooperative system model, with best relay selection. Section 3 presents the derivation of channel-secrecy capacity and intercept probability closed-form expressions. Section 4 presents numerical results to confirm the analytical derivations. Finally, we conclude the paper in Section 5.

2. System Model

In this section, we explain an overview of the system model from a communication point of view and provide a description of how the presented approach improves the system performance. Secondly, we explain the system model in the presence of an eavesdropper and provide description of security improvement. Finally, we discuss the optimal relay selection technique to improve the secrecy capacity.

2.1. Base System Model. In this section, we explain the idea of the overall system from the communication and security points of view. We propose an efficient cooperative vehicular transmission technique to create advanced heterogeneous telecommunication networks in an approach for increasing the networking capabilities of heavily populated urban areas. Our transmission scheme is built by making use of on-road vehicles equipped with low-elevation antennas as well as short- and medium-range wireless communication technologies.

Vehicular networks are expected to offer reasonable throughput, lower operational cost, and more flexible configuration. The realization of cooperative vehicular relaying entails many challenges, all of which require dynamic and real-time remedies. The full potential for expanding any network of this scale entails complexities referring to a reliable communication link, optimized transmission schemes, and eventually information extraction.

We remark that there are mainly two approaches to handle this type of high communication mobility. The first approach involves adaptive transmission in which one or more transmission parameters (coding, modulation, power,

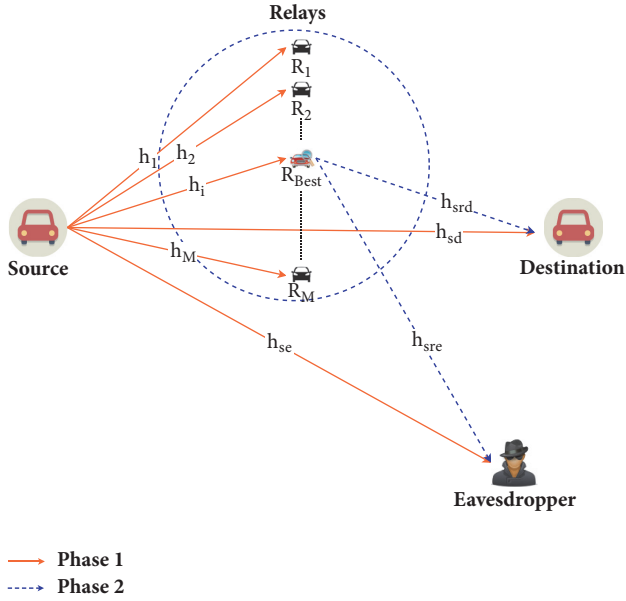


FIGURE 1: System model of cooperative relay communication in the presence of an eavesdropper node with existing direct link.

etc.) are varied according to the channel conditions. This builds on closed-loop implementation in which a feedback from the receiver to the transmitter is required. The second approach is based on using either outer coding or precoding. This approach is open-loop implementation and does not require any feedback from the transmitter. Such techniques are particularly useful over time-varying channels, where reliable feedback is difficult to obtain.

Considering the time-selective nature of the vehicular system under consideration in this paper, we used the linear constellation precoding (LCP) approach [15]. Taking this into consideration, we built our communication scheme over orthogonal transmission protocols, cooperative relaying, and linear signal precoding.

2.2. Proposed Model. This paper proposes a cooperative communication scenario shown in Figure 1, which consists of one source, one destination, and a set of M Decode-and-Forward (DF) trusted relays that help to prevent passive/active eavesdropper attacks. Specifically, the source node communicates directly with the destination node and indirectly through relaying vehicles $R_i \mid i = 1, 2, \dots, M$, which serve as a best selected relaying terminal. All terminals are assumed to be equipped with a single transmit-and-receive antenna and operate in half-duplex mode.

Such cooperative system consists of two phases [13, 15, 16] as illustrated in Figure 2. In the broadcasting phase (phase 1), the source transmits its precoded signal to all relaying vehicles and to a destination node in the presence of an active/passive eavesdropper. In the relaying phase (phase 2), the best-selected relay is engaged in forwarding the received signal only if it was decoded correctly; otherwise, the relay remains silent. The relay decodes and then forwards a fresh decoded copy of the precoded signal to the destination. The

destination makes its decision based on the two received signals over the broadcasting and relaying phases. The distances between nodes are arbitrary and identical. Additionally, the signal experiences independent relay fading. As a result, the composite channel becomes independent and identically distributed (i.i.d.).

Figure 3 illustrates that, in the presence of an active/passive eavesdropper, the system model consists of two channels: the main channel from source to destination and the wire-tap channel between source and an eavesdropper. The source node transmits a signal $(S(n))$ to destination and to vehicle relays during the broadcast phase in the presence of an eavesdropper.

The time-sampled OFDM signal $s(n)$ is converted into the frequency domain by implementing a Discrete Fourier Transform (DFT) [13, 15, 16]. DFT renders a discrete finite sequence of complex coefficients, which are given by

$$S(n) = \sum_{q=0}^Q s(n) e^{-jw_q}, \quad (1)$$

where $w_q = 2\pi(q - Q/2)/N_t$ is the finite Fourier basis that captures the time variation.

From (1), the Basis Expansion Model (BEM) can be used to represent a discrete-time base-band equivalent channel for the vehicular doubly selective channel under consideration and is given by

$$h_B(\iota; l) = \sum_{q=0}^Q h_q(n; l) e^{j2w_q \iota}, \quad \iota \in [0, L], \quad (2)$$

where $h_q(n; l)$ is zero-mean complex Gaussian.

ι , denotes the serial index for the input data symbols. The block index is given by $[n = \iota/N_t]$.

The block diagram of the proposed cooperative scheme is shown in Figure 4. The input data blocks (generated from an M-QAM constellation) of length N_t are divided into shorter subblocks of length $N_s \mid (N_s \leq N_t)$. Let each of these subblocks be denoted by $s(n)$ which are the input to a linear precoder Θ of size $N_s \times N_t$.

We assumed that eavesdropper used the same cooperative schemes shown in Figure 4(d), with the same precoder length and the same number of resolvable multipath components [15, 16].

The aggregate channel model of this paper takes into account both small-scale fading and path loss [15]. Path loss is proportional to d^a , where a is the path loss coefficient and d is the propagation distance. The path loss, associated with the distance $d_{sr,d}$ from the source node to the destination node, is modeled as

$$\Omega(d) = 10^{\beta_{sd}}, \quad (3)$$

where

- (i) $\beta_{sd} = 128.1 - 36.7 \times \log_{10}(d_{sr,d})/10$,
- (ii) d_{sd} denotes the distance from source to destination,
- (iii) $d_{(sr_i)}$ and $d_{(r_i,d)}$ are the distances from source to relays (R_i) and from relays (R_i) to destination, respectively.

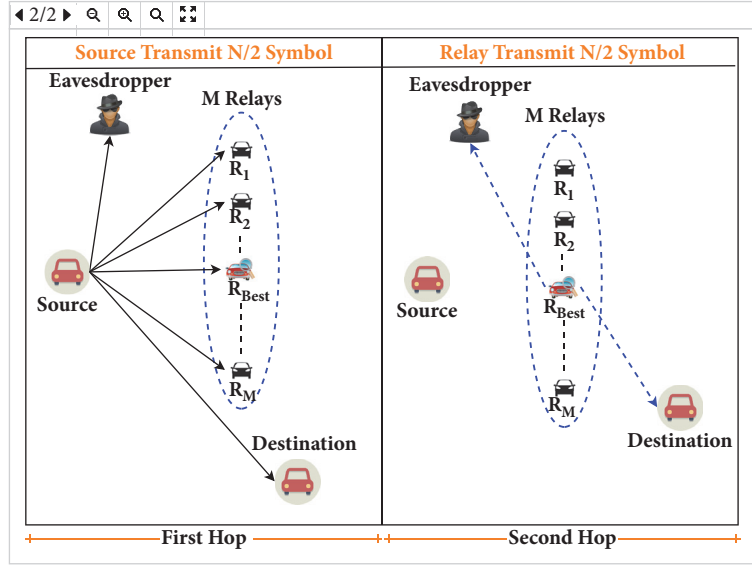


FIGURE 2: Half-duplex dual-hop VANET cooperative communication scenario.

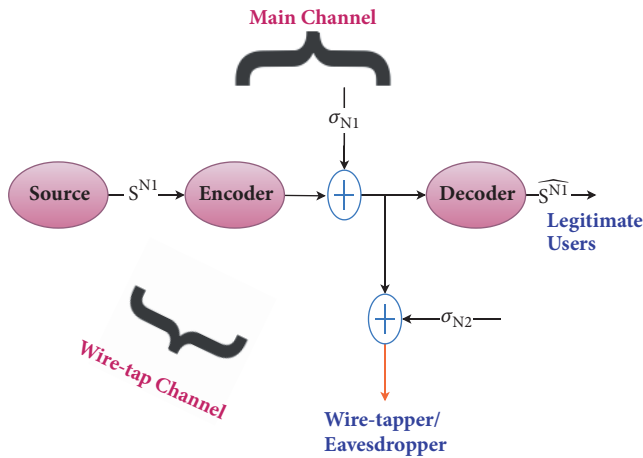


FIGURE 3: The block diagram of the Gaussian wire-tap channel (including the channel from source to destination in the presence of active/passive eavesdropper).

The relative geometrical gains are defined as

$$(i) G_{(sr_i)} = (d_{sd}/d_{sr_i})^\alpha. G_{(r,d)} = (d_{sd}/d_{r,d})^\alpha.$$

2.3. System Model Strategy Equations. In this section, we introduce an equation derivation in case of direct transmission and dual-hop relays (broadcasting and relaying phases) transmission.

2.3.1. Direct Transmission

(i) Received Signal at Destination

$$y_{sd}^{\text{direct}}(n) = \sqrt{P_t} h_{sd}(n) s(n) + n_{sd}(n), \quad (4)$$

where

- (i) $y_{sd}^{\text{direct}}(n)$ is direct transmission between source and destination nodes,
- (ii) $s(n)$ is transmitted signal from source node where, $E(|s(n)|^2) = 1$,
- (iii) P_t is transmitted power,
- (iv) $n_{sd}(n)$ is the Additive White Gaussian Noise (AWGN) from source to destination with zero mean and variance $N_0/2 = \sigma_n^2$,
- (v) $h_{sd}(n)$ are fading coefficients of the channel from source to destination and are modeled as Rayleigh fading, which corresponds to an ideal OFDM sub-channel,
- (vi) $\sigma_{sd}^2 = E(|h_{sd}|^2)$ is the variance of main channel fading coefficients.

(ii) *Received Signal at Eavesdropper.* Due to the broadcast nature of the wireless cooperative system model, the eavesdropper attempts to overhear the transmitted signal.

$$y_{se}^{\text{direct}}(n) = \sqrt{P_t} h_{se}(n) s(n) + n_{se}(n), \quad (5)$$

where

- (i) $y_{se}^{\text{direct}}(n)$ is direct transmission between source and eavesdropper nodes,
- (ii) $n_{se}(n)$ is AWGN from source to eavesdropper with zero mean and variance $N_0/2 = \sigma_n^2$,
- (iii) $h_{se}(n)$ are fading coefficients of the channel from source to eavesdropper; they are modeled as Rayleigh fading, which corresponds to an ideal OFDM sub-channel,
- (iv) $\sigma_{se}^2 = E(|h_{se}|^2)$ is the variance of wire-tap channel fading coefficients.

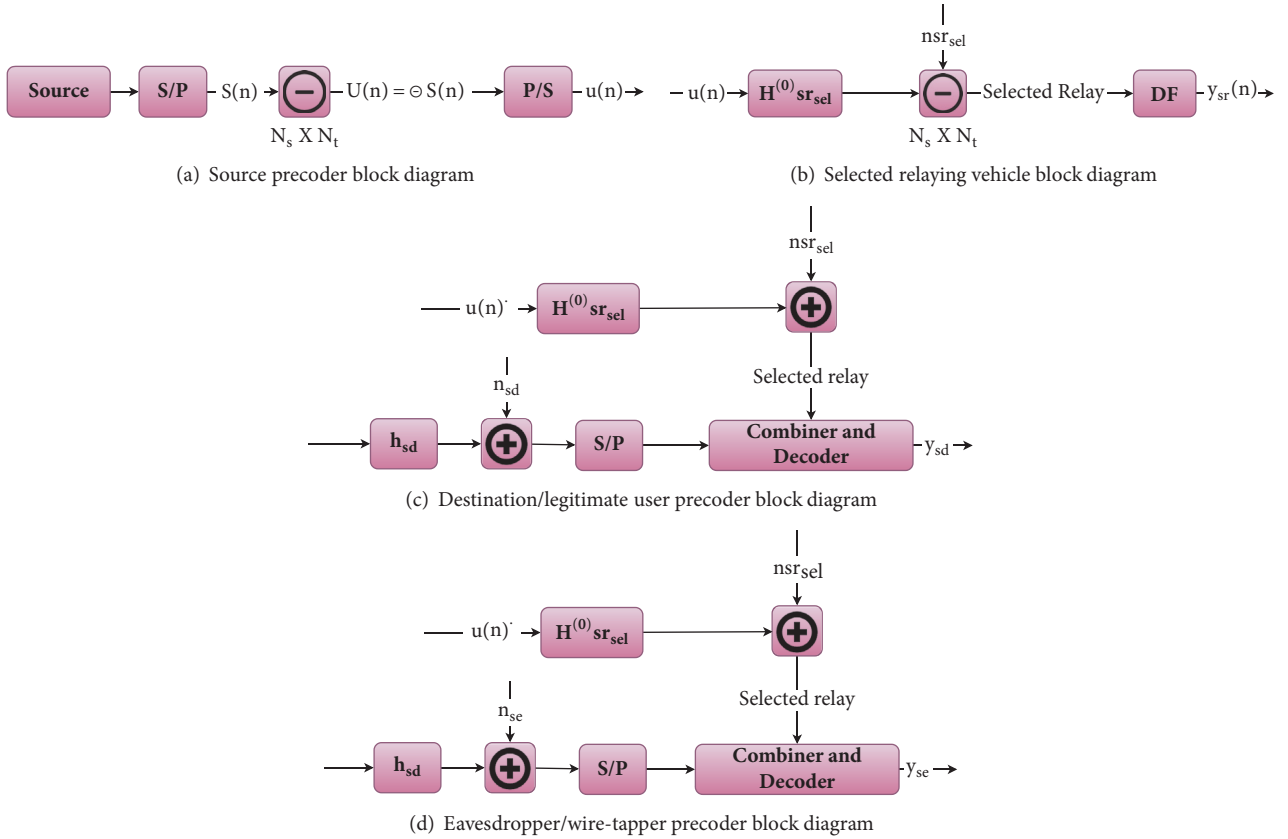


FIGURE 4: Precoder block diagram of the proposed DF cooperative scheme for an eavesdropper wire-tapper.

2.3.2. Dual-Hop DF Relays Transmission

During Broadcast Phase

(i) Received Signal at Destination

$$y_{sd}^{\text{DF}}(n) = \sqrt{\frac{P_t}{2}} h_{sd}(n) s(n) + n_{sd}(n). \quad (6)$$

(ii) Received Signal at Relays

$$y_{sr}^{\text{DF}}(n) = \sqrt{\frac{P_t G_{sr}}{2}} h_{sr}(n) s(n) + n_{sr}(n), \quad (7)$$

where

- (i) h_{sr} are fading coefficients of the channel from source to relays,
- (ii) n_{sr} is AWGN from source to relays with zero mean and variance $N_0/2 = \sigma_n^2$.

(iii) *Received Signal at Eavesdropper.* Meanwhile, due to the broadcast nature of wireless transmission, the eavesdropper also receives a copy of the source signal $s(n)$ and the corresponding received signal is written as

$$y_{se}^{\text{DF}}(n) = \sqrt{\frac{P_t}{2}} h_{se}(n) s(n) + n_{se}(n), \quad (8)$$

where

- (i) h_{se} are fading coefficients of the channel from source to eavesdropper,
- (ii) $|h_{sd}|^2$ and $|h_{se}|^2$ are independent and exponentially distributed with variances σ_{sd}^2 and σ_{se}^2 , respectively.

During Relaying Phase. Without loss of generality, consider that R_i is selected as the optimal relay to reencode and forward its decoded signal to the destination. In DF relaying protocol, relays first decode their received signal from the source and then they transmit the decoded outcome version to the destination node. Considering equal power allocation, to make a fair comparison with the direct transmission, we obtain the transmitted power at the source and relay nodes as $P_t/2$.

Therefore, the received signal at destination via R_i is given by

$$y_{rd}^{\text{DF}}(n) = \sqrt{\frac{P_t G_{rd}}{2}} h_{rd}(n) s(n) + n_{rd}(n). \quad (9)$$

Similarly, considering that R_i is selected as the optimal relay, the eavesdropper is able to overhear this optimal selected relay. An eavesdropper is located randomly around the source and relay nodes (R_i). In our model, we consider the worst-case scenario, where the eavesdropper overhears

the transmissions of both the source and relay nodes and attempts to decode the transmitted signal.

$$y_{re}^{DF}(n) = \sqrt{\frac{P_t}{2}} h_{re}(n) s(n) + n_{re}(n). \quad (10)$$

In the next section, we introduce the ergodic channel-secrecy capacity concept in the proposed vehicle cooperative system to evaluate the system security. Additionally, from the security evaluation, we deduct the optimal conditions to achieve the maximum secrecy capacity and the lowest intercept probability.

3. Security Assessment Analysis

Traditional security techniques fail to retain the overall system security. Currently, researchers focus on improving the security of the physical layers instead of the higher layers. Their work tries to provide perfect transmission security from source to the legal receivers of the physical layer [17].

The channel-secrecy capacity is the difference between main and wire-tap channels as described in the following equation: $C_s = C_m - C_{mw}$ on the condition that $C_m > C_{mw} \rightarrow C_s > 0$.

Furthermore, the Shannon coding theorem explains the conditions for an efficient secure data transmission. It proved that the legitimate receiver does not recover the transmitted data if the main channel capacity (C_m) is less than the effective transmission rate (R) (i.e., $C_m < R$). However, the eavesdropper is still able to intercept the transmitted data even when the secrecy capacity falls below zero ($P_{\text{intercept}} = P(C_s < 0)$).

3.1. Ergodic Channel-Secrecy Capacity Derivation. In this section, we derive a closed-form equation for ergodic channel-secrecy capacity with the existence of a direct link. We assume that the destination node receives two different signals during the two phases (i.e., broadcast and relay phases) on different orthogonal time slots. Therefore, the main channel consists of two different components: the first component is from source to destination (direct link) and the second component is from source to vehicle relays (cooperative link). Additionally, as we consider the worst-case scenario, the wire-tap channel consists of two-link component. The eavesdropper is able either to overhear data from the source directly during the broadcast phase or to overhear during the vehicle relays from the selected best relay.

3.1.1. Direct Transmission. The direct channel-secrecy capacity is the difference between the main and wire-tap links. Therefore, the channel-secrecy equation of the direct transmission is defined as

$$C_{sd}^{\text{direct}} = C_m - C_{mw}. \quad (11)$$

Assuming that the optimal Gaussian codebook is used at the source, the maximal achievable rate (also known

as channel capacity) of direct transmission from source to destination is obtained from (5) as follows:

$$C_{sd}^{\text{direct}} = \log_2 \left(1 + \frac{|h_{sd}|^2 P_t}{\sigma_n^2} \right). \quad (12)$$

Similarly, from (6), wire-tap capacity link from source to eavesdropper during direct transmission is given by

$$C_{se}^{\text{direct}} = \log_2 \left(1 + \frac{|h_{se}|^2 P_t}{\sigma_n^2} \right). \quad (13)$$

h_{sd} and h_{se} represent the fading coefficient of the channel from source to destination and from source to eavesdropper, respectively.

3.1.2. Dual-Hop DF Relays Transmission. The capacity of dual-hop DF relaying transmission is the minimum of both capacities from source to relays and that from relays to destination [2]. This means that the dual-hop DF transmission results in failure when either source-relays link or relays-destination link is in failure. Therefore, considering R_i is the optimal relay, we can obtain the capacity of dual-hop DF transmission as

$$C_{srd}^{DF} = \min(C_{sr}, C_{rd}), \quad (14)$$

where C_{sr} and C_{rd} are the channel capacities from source to R_i and from R_i to a destination, respectively. These capacities can be given by

$$C_{sr} = \log_2 \left(1 + \frac{|h_{sr}|^2 P_t G_{sr}}{2\sigma_n^2} \right), \quad (15)$$

$$C_{rd} = \log_2 \left(1 + \frac{|h_{rd}|^2 P_t G_{rd}}{2\sigma_n^2} \right). \quad (16)$$

Based on our proposed model, the destination node is capable of decoding the transmitted signal even when the relays are silent. Additionally, when at least one of the relaying vehicles succeeds in decoding the transmitted signal, the destination node will select the maximum capacity of both received signals. Specifically, using the selection diversity combining, the destination-secrecy capacity with help of the optimal relay selection scheme is the highest of C_{sd}^{DF} and C_{srd}^{DF} yielding to

$$\begin{aligned} C_m^{DF} &= \max(C_{sd}^{DF}, C_{srd}^{DF}) \\ &= \log_2 \left(1 + \frac{\max(|h_{sd}|^2, \min(|h_{sr}|^2, |h_{rd}|^2)) P_t}{2\sigma_n^2} \right). \end{aligned} \quad (17)$$

Similarly, due to the broadcast nature, the eavesdropper attempts to decode the transmitted signal either from the source node or from the best relay selected (if any). This means that even if the relays fail to decode the transmitted signal, the eavesdropper might still decode the transmitted signal from the source node.

Moreover, if at least one relay succeeds in decoding the transmitted signal, eavesdropper overhears the transmissions of both source and selected vehicle relay. Specifically, using the selection diversity combining, the eavesdropper-secrecy capacity with optimal relay selection scheme is the highest one of C_{se}^{DF} and C_{sre}^{DF} , yielding to

$$C_{mw}^{DF} = \max(C_{se}^{DF}, C_{sre}^{DF}), \quad (18)$$

where C_{se}^{DF} and the C_{sre}^{DF} are the secrecy capacity from the source to an eavesdropper directly and from source to eavesdropper via R_i , respectively.

The secrecy capacity C_{sre}^{DF} is the minimum of both capacities from source to relays and from relays to eavesdropper [2]. Therefore, considering that R_i is the optimal relay, we can obtain the capacity of dual-hop DF transmission as follows:

$$C_{sre}^{DF} = \min(C_{sr}, C_{re}), \quad (19)$$

where C_{re} is the channel capacity from R_i to eavesdropper. It can be given by

$$C_{re} = \log_2 \left(1 + \frac{|h_{re}|^2 P_t G_{re}}{2\sigma_n^2} \right). \quad (20)$$

Therefore, the wire-tap channel-secrecy capacity can be obtained as

$$\begin{aligned} C_{mw}^{DF} &= \log_2 \left(1 + \frac{\max(|h_{se}|^2, \min(|h_{sr}|^2, |h_{re}|^2)) P_t}{2\sigma_n^2} \right). \end{aligned} \quad (21)$$

Combining (17) and (21), the secrecy capacity of dual-hop DF relaying transmission via R_i is given by

$$\begin{aligned} C_r^{DF} &= \log_2 \left(1 + \frac{\max(|h_{sd}|^2, \min(|h_{sr}|^2, |h_{rd}|^2)) P_t}{2\sigma_n^2} \right) \\ &\quad - \log_2 \left(1 + \frac{\max(|h_{se}|^2, \min(|h_{sr}|^2, |h_{re}|^2)) P_t}{2\sigma_n^2} \right). \end{aligned} \quad (22)$$

3.1.3. Relay Selection Technique. This section presents a defined relay selection equation that may be applied to enhance the physical layer security of vehicle relay communication in presence of an active/passive eavesdropper node with the existence of a direct link. Several best relay selection techniques are used to effectively overcome the eavesdropper attacks and maintain the whole system physical layer security.

As mentioned in Figure 2, in Phase 1, the source transmits its precoded signal to the M relay vehicles and to the destination. In Phase 2, relays are engaged in forwarding the received signal only if it was decoded correctly; otherwise,

relays remain silent. These relay nodes, which succeed in perfectly decoding the source signal, forward a fresh decoded copy of the precoded signal to the destination. After that, destination makes its decision based on the two received signals over the broadcasting and relaying phases.

Successive decoding relays are represented by the successful decoding set Δ . Given M relay nodes, there are 2^M possible *Source – Relays* pairs.

Therefore, the resultant successful decoding set Δ is given by the following equation:

$$\Delta = \{\phi, \Delta_1, \Delta_2, \dots, \Delta_n, \dots, \Delta_{2^M-1}\}, \quad (23)$$

where ϕ is the empty set, meaning that no relay node succeeds in perfectly decoding the transmitting signal $s(n)$, while Δ_n is a nonempty set of M relays node, meaning that a specific relay will be selected to forward its decoded signal to the destination node.

Specifically, the selection techniques are based on the channel state information (CSI) to perform single best relay selection mechanism accurately. In case the CSI of wire-tap link is available, the proposed relay selection will be considered; then, by minimizing C_{mw}^{DF} , the channel secrecy will be maximized (C_s) [6].

In contrast, traditional relay selection will be used to maximize C_m , when only the CSI of the main link is known [18].

3.1.4. Proposed Relay Selection Mechanism. In this section, we consider the relay that maximizes the channel-secrecy capacity of the dual-hop DF relaying transmission as the optimal relay. The optimal relay selection requires the global CSI for both main and wire-tap links. Therefore, the proposed relay of DF relaying based on optimal relay selection can be obtained from (22) as follows:

$$\begin{aligned} \text{optimal relay} &= \arg \max_{r \in R} C_r^{DF} \\ &= \arg \max_{r \in R} \left(\frac{\max(|h_{sd}|^2, \chi_{srd}) P_t + 2\sigma_n^2}{\max(|h_{se}|^2, \chi_{sre}) P_t + 2\sigma_n^2} \right), \end{aligned} \quad (24)$$

where $\chi_{srd} = \min(|h_{sr}|^2, |h_{rd}|^2)$ and $\chi_{sre} = \min(|h_{sr}|^2, |h_{re}|^2)$.

3.1.5. Traditional Relay Selection Mechanism. In this section, we consider the relay that maximizes the capacity of DF relaying transmission as the traditional relay. The traditional relay selection requires only the CSI of the main link without considering that of wire-tap link. Therefore, the traditional relay of DF relaying based on optimal relay selection can be obtained from (17) as follows:

$$\begin{aligned} \text{optimal relay} &= \arg \max_{r \in R} C_m^{DF} \\ &= \arg \max_{r \in R} \max(|h_{sd}|^2, \min(|h_{sr}|^2, |h_{rd}|^2)). \end{aligned} \quad (25)$$

Additionally, the ergodic channel-secrecy capacity can be obtained by averaging the instantaneous secrecy capacity $C_r^{\text{DF}+}$ over the fading channels coefficient [19], where

$$C_r^{\text{DF}+} = \text{mean} \left(\max \left(C_r^{\text{DF}}, 0 \right) \right). \quad (26)$$

3.2. Intercept Probability Derivation. In this section, we extract a closed form for the intercept probability based on the calculated channel-secrecy capacity equations. Wyner mentioned that [8] when the channel secrecy falls below zero ($C_m < C_{me} \rightarrow C_s < 0$), the eavesdropper will succeed in attacking the transmitted data and receive a copy of the transmitted signal.

3.2.1. Direct Transmission. In this section, we analyze the intercept probability of the direct link transmission as a benchmark for comparison purpose. Therefore, based on (11), the intercept probability equation can be written as follows:

$$\begin{aligned} P_{\text{intercept}}^{\text{direct}} &= P_r \left(C_{sd}^{\text{direct}} < C_{se}^{\text{direct}} \right) = P_r \left(|h_{sd}|^2 < |h_{se}|^2 \right) \\ &= \frac{\sigma_{se}^2}{\sigma_{sd}^2 + \sigma_{se}^2}. \end{aligned} \quad (27)$$

Notice that the following random variables $|h_{sd}|^2$ and $|h_{se}|^2$ follow exponential distribution with means $\sigma_{sd}^2 = E(|h_{sd}|^2)$ and $\sigma_{se}^2 = E(|h_{se}|^2)$, respectively. For simplicity, we assumed that the main link $|h_{sd}|^2$ and wire-tap link $|h_{se}|^2$ are independent and identically distributed (i.i.d.) random variables.

In this paper, we denote the ratio of the channel gain of the main link to that of the wire-tap link by $\lambda_{me} = \sigma_{sd}^2 / \sigma_{se}^2$. Throughout this paper, we refer to λ_{me} as the main-to-eavesdropper ratio (MER). Thereof, we can simplify (27) as follows:

$$P_{\text{intercept}}^{\text{direct}} = \frac{1}{1 + \lambda_{me}}. \quad (28)$$

Equation (28) shows that the intercept probability is independent of the transmitted power P_t ; then the security level cannot improve by adjusting the power. This motivates

the employment of optimal relay selection scheme for the security improvements in the cooperative vehicle systems.

3.2.2. Dual-Hop DF Relays Transmission

(i) Proposed Relay Selection Mechanism. This section drives a closed form for the intercept probability expression for the proposed relay selection. Based on the definition of the intercept event occurrence, the intercept probability of the proposed relay selection is obtained from Eq. (24) as

$$\begin{aligned} P_{\text{intercept}}^{\text{DF}} &= P_r \left(\max_{r \in R} C_r^{\text{DF}} < 0 \right) \\ &= \prod_{r=1}^M P_r \left\{ \max \left(|h_{sd}|^2, \min \left(|h_{sr}|^2, |h_{rd}|^2 \right) \right) \right. \\ &\quad \left. < \max \left(|h_{se}|^2, \min \left(|h_{sr}|^2, |h_{re}|^2 \right) \right) \right\}. \end{aligned} \quad (29)$$

Denote

- (i) $X = \min(|h_{sr}|^2, |h_{rd}|^2)$,
- (ii) $Y = \min(|h_{sr}|^2, |h_{re}|^2)$,
- (iii) $Z = \max(|h_{sd}|^2, X)$,
- (iv) $W = \max(|h_{se}|^2, Y)$.

We can easily obtain the Cumulative Distribution Function (CDF) of X , Y , Z , and W , respectively, as

$$P_X(X < x) = 1 - e^{-((x/\sigma_{sr}^2) + (x/\sigma_{rd}^2))}, \quad (30a)$$

$$P_Y(Y < x) = 1 - e^{-((x/\sigma_{sr}^2) + (x/\sigma_{re}^2))}, \quad (30b)$$

$$\begin{aligned} P_Z(Z < x) &= P \left(|h_{sd}|^2 < x \right) P(X < x) \\ &= \left(1 - e^{-x/\sigma_{sd}^2} \right) \left(1 - e^{-((x/\sigma_{sr}^2) + (x/\sigma_{rd}^2))} \right), \end{aligned} \quad (30c)$$

$$\begin{aligned} P_W(W < x) &= P \left(|h_{se}|^2 < x \right) P(Y < x) \\ &= \left(1 - e^{-x/\sigma_{se}^2} \right) \left(1 - e^{-((x/\sigma_{sr}^2) + (x/\sigma_{re}^2))} \right), \end{aligned} \quad (30d)$$

where $x \geq 0$. Starting from (29), we can get (31) as follows:

$$\begin{aligned} P_{\text{intercept}}^{\text{DF}} &= \prod_{r=1}^M P_r \left\{ \max \left(|h_{sd}|^2, \min \left(|h_{sr}|^2, |h_{rd}|^2 \right) \right) < \max \left(|h_{se}|^2, \min \left(|h_{sr}|^2, |h_{re}|^2 \right) \right) \right\} \\ &= \int_0^{\infty} \frac{1}{\sigma_{re}^2} \left[\left(1 - e^{-x/\sigma_{sd}^2} \right) \left(1 - e^{-((x/\sigma_{sr}^2) + (x/\sigma_{rd}^2))} \right) \right] \left[\left(1 - e^{-x/\sigma_{se}^2} \right) \left(1 - e^{-((x/\sigma_{sr}^2) + (x/\sigma_{re}^2))} \right) \right] dx, \quad (31) \\ P_{\text{intercept}}^{\text{DF}} &= \prod_{r=1}^M \left(\frac{\sigma_{sd}^2 \sigma_{rd}^2 \sigma_{se}^2 \sigma_{re}^2 + \sigma_{sd}^2 \sigma_{sr}^2 \sigma_{se}^2 \sigma_{re}^2 + \sigma_{sd}^2 \sigma_{sr}^2 \sigma_{rd}^2 \sigma_{se}^2 + \sigma_{sd}^2 \sigma_{sr}^2 \sigma_{rd}^2 \sigma_{re}^2}{\sigma_{sr}^2 \sigma_{rd}^2 \sigma_{se}^2 \sigma_{re}^2 + \sigma_{sd}^2 \sigma_{rd}^2 \sigma_{se}^2 \sigma_{re}^2 + \sigma_{sd}^2 \sigma_{sr}^2 \sigma_{se}^2 \sigma_{re}^2 + \sigma_{sd}^2 \sigma_{sr}^2 \sigma_{rd}^2 \sigma_{se}^2 + \sigma_{sd}^2 \sigma_{sr}^2 \sigma_{rd}^2 \sigma_{re}^2} \right). \end{aligned}$$

(ii) Traditional Relay Selection Mechanism. This section drives a closed form for the intercept probability expression for the

traditional relay selection in the Rayleigh fading channel. Based on the definition of the intercept event occurrence,

the intercept probability of the proposed relay selection is obtained from (25) as follows:

$$P_{\text{intercept}}^{\text{DF}} = P_r \left(\max_{r \in R} C_m^{\text{DF}} < C_{oe}^{\text{DF}} \right), \quad (32)$$

where C_{oe}^{DF} is the channel-secrecy capacity from the optimal relay to an eavesdropper. Using the law of total probability and the intercept probability of traditional relay selection, the optimal relay selection scheme is obtained as follows:

$$P_{\text{intercept}}^{\text{DF}} = \sum_{i=1}^M \frac{1}{M} P_r \left(\max_{r \in R} \left(\max(|h_{sd}|^2, \min(|h_{sr}|^2, |h_{rd}|^2)) \right) < |h_{ie}|^2 \right). \quad (33)$$

Using (33) and letting $|h_{ie}|^2 = \tau$, we can obtain the traditional intercept probability as in (34). Based on binomial expansion, A_k represents the k -th nonempty subcollection of M relays, and $|A_k|$ is the element's number in set A_k .

$$\begin{aligned} P_{\text{intercept}}^{\text{DF}} &= \sum_{i=1}^M \int_0^\infty \prod_{r=1}^M \left[1 - e^{-((\tau/\sigma_{sr}^2) + (\tau/\sigma_{rd}^2))} \right] \\ &\quad \cdot \left[1 - e^{-\tau/\sigma_{sd}^2} \right] \left[\frac{1}{\sigma_{ie}^2} e^{-\tau/\sigma_{ie}^2} \right] d\tau. \\ &= \sum_{i=1}^M \frac{1}{M} \int_0^\infty \left(1 + \sum_{k=1}^{2^M-1} (-1)^{|A_k|} \exp\left(\frac{\tau}{\sigma_{sd}^2}\right)^{|A_k|} \right. \\ &\quad \cdot \exp\left[-\sum_{r \in A_k} \frac{\tau}{\sigma_{sd}^2} + \frac{\tau}{\sigma_{sr}^2} + \frac{\tau}{\sigma_{rd}^2}\right] \Big) \\ &\quad \cdot \frac{1}{\sigma_{ie}^2} \exp\left(-\frac{\tau}{\sigma_{ie}^2}\right) d\tau \\ &= \sum_{i=1}^M \left(1 + \sum_{k=1}^{2^M-1} (-1)^{|A_k|} \right. \\ &\quad \cdot \left. \left[1 + \frac{1}{\sigma_{sd}^2} \sum_{r \in A_k} \left(\frac{\sigma_{ie}^2}{\sigma_{sd}^2} + \frac{\sigma_{ie}^2}{\sigma_{sr}^2} + \frac{\sigma_{ie}^2}{\sigma_{rd}^2} \right)^{-1} \right] \right) \end{aligned} \quad (34)$$

3.3. Diversity Order Analysis. In this section, we derive the diversity order performance of the direct transmission and the dual-hop DF relaying transmission based on proposed and traditional selection schemes.

The traditional diversity gain order is based on SNR, where SNR is the Signal to Noise Ratio [20], which is given by

$$d = - \lim_{\text{SNR} \rightarrow \infty} \frac{\log P_e(\text{SNR})}{\log \text{SNR}}, \quad (35)$$

where $P_e(\text{SNR})$ is the bit error rate. It is observed from the intercept probability equations that the traditional diversity is not applicable here. Therefore, the generalized diversity gain is given by

$$d_{\text{generalized}} = - \lim_{\lambda_{me} \rightarrow \infty} \frac{\log(P_{\text{intercept}})}{\log(\lambda_{me})}. \quad (36)$$

3.3.1. Direct Transmission. In this section, we analyze the benchmark diversity order gain of the direct transmission. By substituting (28) for (36), the diversity order gain is obtained as follows:

$$d_{\text{direct}} = - \lim_{\lambda_{me} \rightarrow \infty} \frac{\log(1/(1 + \lambda_{me}))}{\log(\lambda_{me})} = 1, \quad (37)$$

meaning that the direct transmission achieves a single diversity order.

3.3.2. Dual-Hop DF Relays Transmission

(i) Proposed Relay Selection Mechanism. This section presents the diversity order gain analysis of the optimal relay selection. Substituting (31) for (36) gives the diversity order gain as follows:

$$d_{\text{Proposed}}^{\text{DF}} = - \lim_{\lambda_{me} \rightarrow \infty} \frac{\log(P_{\text{DF}}^{\text{intercept}})}{\log(\lambda_{me})}. \quad (38)$$

For simplicity, we denote $\sigma_{sr}^2 = \alpha_{sr} \sigma_{sd}^2$, $\sigma_{rd}^2 = \alpha_{rd} \sigma_{sd}^2$, and $\sigma_{re}^2 = \alpha_{re} \sigma_{se}^2$, where α_{sr} , α_{rd} , and α_{re} are constants. The intercept probability can be rewritten as

$$P_{\text{intercept}}^{\text{DF}} = \frac{\alpha_{re} \alpha_{sr}^{-1} + \alpha_{re} \alpha_{rd}^{-1} + (1 + \alpha_{re}) \lambda_{me}}{\alpha_{re} + \alpha_{re} \alpha_{sr}^{-1} + \alpha_{re} \alpha_{rd}^{-1} + (1 + \alpha_{re}) \lambda_{me}}. \quad (39)$$

By substituting (39) for (38), the diversity order will be

$$d_{\text{Proposed}}^{\text{DF}} = M. \quad (40)$$

Equations show that the proposed relay selection transmission achieves the diversity order by M .

(ii) Traditional Relay Selection Mechanism. This section presents the diversity order gain analysis of the traditional relay selection. Substituting (34) for (36) gives the diversity order gain as

$$d_{\text{Traditional}}^{\text{DF}} = - \lim_{\lambda_{me} \rightarrow \infty} \frac{\log(P_{\text{DF}}^{\text{intercept}})}{\log(\lambda_{me})}. \quad (41)$$

For simplicity, we can obtain

$$\begin{aligned} &\left[1 - \exp - \left(\frac{\tau}{\sigma_{sr}^2} + \frac{\tau}{\sigma_{rd}^2} \right) \right] \left[1 - \exp - \left(\frac{\tau}{\sigma_{sd}^2} \right) \right] \\ &= \left[\frac{\tau}{\sigma_{sr}^2} + \frac{\tau}{\sigma_{rd}^2} + \frac{\tau}{\sigma_{sd}^2} \right] \quad \text{for } \lambda \rightarrow \infty. \end{aligned} \quad (42)$$

Using Taylor series expansion and ignoring the higher-order terms, the intercept probability can be rewritten as follows:

$$P_{\text{DF}}^{\text{intercept}} = \sum_{i=1}^M (M-1)! \prod_{r=1}^M \left(\frac{\gamma_{ie}}{\gamma_{sr}} + \frac{\gamma_{ie}}{\gamma_{rd}} + \frac{\gamma_{ie}}{\gamma_{sd}} \right) \times \left(\frac{1}{\lambda_{me}} \right)^M, \quad (43)$$

where $\gamma_{sr} = \sigma_{sr}^2/\sigma_{sd}^2$, $\gamma_{rd} = \sigma_{rd}^2/\sigma_{sd}^2$, and $\gamma_{ie} = \sigma_{ie}^2/\sigma_{sd}^2$. Substituting (43) for (41) gives

$$d_{\text{Traditional}}^{\text{DF}} = M, \quad (44)$$

meaning that the traditional relay selection transmission achieves the diversity order also by M . From (37), (40), and (44), it is obvious that the dual-hop DF optimal relay selection achieves the same diversity order gain M . This means that, at high MER, for $M > 1$, the intercept probabilities of DF relay selection schemes are reduced faster than the direct transmission. This implies that the physical layer improves by using the dual-hop DF optimal relay selection.

3.4. Outage Probability Derivation. In this section, we present the outage probability analysis for our proposed system model. Based on Shannon capacity [21] and Wyner's results [8, 9], eavesdropper fails to decode the transmitted signal when the wire-tap channel is lower than the data rate (R_d). Whenever the wire-tap channel overcomes R_d , eavesdropper may succeed in decoding the transmitting signal; then the intercept probability occurs.

One of the basic solutions for security level improvement is to increase the data rate (R_d). In contrast, as R_d increases, this comes at the cost of transmission reliability degradation, which leads to the decrease of the vehicular cooperative systems throughput.

3.4.1. Reliability Derivation Of Direct Transmission. The outage probability of the main link ($S - D$) increases when R_d increases. Therefore, based on Shannon capacity [21], the outage probability P_{out} of a direct transmission is obtained as follows:

$$P_{\text{out}} = P_r(C_{sd} < R_d) = P_r(|h_{sd}|^2 < R_d) = 1 - \exp\left(-\frac{\delta}{\sigma_{sd}^2}\right), \quad (45)$$

where $\delta = (2^{R_d} - 1)/\gamma$ and $\gamma = P_t/\sigma_n^2$.

3.4.2. Reliability Derivation Of Dual-Hop DF Relays. Figure 1 shows that the destination node is capable of decoding the transmitted signal even when the relay decoding set is empty ($\Delta = \phi$).

Additionally, when at least one of the vehicle relays succeeds in decoding the transmitted signal ($\Delta = \Delta_n$), the destination node will select the maximum capacity of both received signals (from source and R_{best}).

Using the law of total probability [22], the outage probability of the main link is formulated as follows:

$$P_{\text{out}}^{\text{DF}} = P_r(\Delta = \phi) P_r(C_{sd}^{\text{DF}} < R_d) + \sum_{n=1}^{2^M-1} \left[P_r(\Delta = \Delta_n) P_r(C_m^{\text{DF}} < R_d) \right]. \quad (46)$$

The $|h_{sr}|^2$ and $|h_{rd}|^2$ factors of different vehicle relay nodes are independent and follow exponential distribution with a mean of σ_{sr}^2 and σ_{rd}^2 .

The probability of occurrence for the event ($\Delta = \phi$) is obtained from (14):

$$P_r(\Delta = \phi) = \prod_{r=1}^M P_r \left[\log_2 \left(1 + \frac{\min(|h_{sr}|^2, |h_{rd}|^2) P_t}{2\sigma_n^2} \right) < R_d \right] = \prod_{r=1}^M \left[P_r(|h_{sr}|^2 < \Gamma) P_r(|h_{rd}|^2 < \Gamma) \right] = \prod_{r=1}^M \left[1 - \exp\left(-\frac{\Gamma}{\sigma_{sr}^2}\right) - \exp\left(-\frac{\Gamma}{\sigma_{rd}^2}\right) + \exp\left(-\left(\frac{\Gamma}{\sigma_{sr}^2} + \frac{\Gamma}{\sigma_{rd}^2}\right)\right) \right], \quad (47)$$

where M is the number of vehicle relay nodes and $\Gamma = (2^{2R_d} - 1)/\gamma$. For simplicity, we considered i.i.d. as randomly generated variables. The fading coefficients of all main links (i.e., $|h_{sd}|^2$, $|h_{sr}|^2$, and $|h_{rd}|^2$) are independent and have identical channel gain σ_m^2 .

Therefore, the above equation can be simplified as follows:

$$P_r(\Delta = \phi) = \left[1 - 2 \exp\left(-\frac{\Gamma}{\sigma_m^2}\right) + \exp\left(-\frac{2\Gamma}{\sigma_m^2}\right) \right]^M. \quad (48)$$

From (12), with $P_t = P_t/2$, we can obtain $P_r(C_{sd}^{\text{DF}} < R_d)$ as follows:

$$P_r(C_{sd}^{\text{DF}} < R_d) = P_r(|h_{sd}|^2 < \Gamma) = 1 - \exp\left(-\frac{\Gamma}{\sigma_m^2}\right). \quad (49)$$

The probability of occurrence for event ($\Delta = \Delta_n$) can be obtained as follows:

$$P_r(\Delta = \Delta_n) = \begin{cases} P_r(C_{sr,d}^{\text{DF}} > R_d), & R_i \in \Delta_n \\ P_r(C_{sr,d}^{\text{DF}} < R_d), & R_j \in \overline{\Delta_n} \end{cases} \quad (50)$$

where $\overline{\Delta_n} = (R - \Delta_n)$ is the complement of Δ_n , given that Δ is not empty, and a vehicle relay R_i is selected to forward a fresh

decoded copy of the transmitted signal \hat{s} to destination node. When the received signal at destination node is ($\hat{s} = s$), this means that the relays perfectly decode the transmitted signal.

The probability of occurrence for event $\Delta = \Delta_n$ can be obtained from (50) as follows:

$$\begin{aligned}
P_r(\Delta = \Delta_n) &= \prod_{R_i \in \Delta_n} P_r(|h_{sr_i}|^2 > \Gamma) \left(P_r(|h_{r,d}|^2 > \Gamma) \right) \\
&\quad \times \prod_{R_j \in \overline{\Delta_n}} P_r(|h_{sr_j}|^2 > \Gamma) \left(P_r(|h_{r,d}|^2 > \Gamma) \right) \\
&= \prod_{R_i \in \Delta_n} \left[\exp\left(-\frac{\Gamma}{\sigma_{sr_i}^2}\right) \exp\left(-\frac{\Gamma}{\sigma_{r,d}^2}\right) \right] \\
&\quad \times \prod_{R_j \in \overline{\Delta_n}} \left[1 - \exp\left(-\frac{\Gamma}{\sigma_{sr_j}^2}\right) \exp\left(-\frac{\Gamma}{\sigma_{r,d}^2}\right) \right].
\end{aligned} \tag{51}$$

Considering $\sigma_{sr}^2 = \sigma_{rd}^2 = \sigma_{sd}^2 = \sigma_m^2$, we can simplify (51) as follows:

$$\begin{aligned}
P_r(\Delta = \Delta_n) &= \left[\exp\left(-\frac{2\Gamma|\Delta_n|}{\sigma_m^2}\right) \right] \\
&\quad \cdot \left[1 - 2 \exp\left(-\frac{\Gamma}{\sigma_m^2}\right) + \exp\left(-\frac{2\Gamma}{\sigma_m^2}\right) \right]^{|\overline{\Delta_n}|}.
\end{aligned} \tag{52}$$

Finally, based on (17), we can obtain $P_r(C_m^{\text{DF}} < R_d)$ as follows:

$$\begin{aligned}
P_r(C_m^{\text{DF}} < R_d) &= P_r(\max(C_{sd}, C_{srd}) < R_d) \\
&= P_r(|h_{sd}|^2 < \Gamma) P_r\left(\min_{r \in M} (C_{sr}, C_{rd}) < \Gamma\right) \\
&= \left(1 - \exp\left(-\frac{\Gamma}{\sigma_m^2}\right) \right)^2 \\
&\quad \cdot \left(1 - 2 \exp\left(-\frac{\Gamma}{\sigma_m^2}\right) + \exp\left(-\frac{2\Gamma}{\sigma_m^2}\right) \right)^{|\Delta_n|}.
\end{aligned} \tag{53}$$

Therefore, upon substituting (48)–(53) for (46), we can formulate the closed-form outage probability expression of our proposed model in the following equation:

$$\begin{aligned}
P_{\text{out}}^{\text{DF}} &= \left[1 - 2 \exp\left(-\frac{\Gamma}{\sigma_m^2}\right) + \exp\left(-\frac{2\Gamma}{\sigma_m^2}\right) \right]^M \left[1 \right. \\
&\quad \left. - \exp\left(-\frac{\Gamma}{\sigma_m^2}\right) \right] + \sum_{n=1}^{M-1} \left[\left[1 - \exp\left(-\frac{\Gamma}{\sigma_m^2}\right) \right] \right. \\
&\quad \left. \cdot \left[1 - 2 \exp\left(-\frac{\Gamma}{\sigma_m^2}\right) + \exp\left(-\frac{2\Gamma}{\sigma_m^2}\right) \right]^{|\Delta_n|} \right].
\end{aligned}$$

$$\begin{aligned}
&\cdot \left[\exp\left(-\frac{2\Gamma|\Delta_n|}{\sigma_m^2}\right) \right] \\
&\cdot \left[1 - 2 \exp\left(-\frac{\Gamma}{\sigma_m^2}\right) + \exp\left(-\frac{2\Gamma}{\sigma_m^2}\right) \right]^{|\Delta_n|}.
\end{aligned} \tag{54}$$

The simplified closed form of the outage probability expression can be obtained as follows:

$$\begin{aligned}
P_{\text{out}}^{\text{DF}} &= \left[1 - \exp\left(-\frac{\Gamma}{\sigma_m^2}\right) \right] \\
&\quad \cdot \left[1 - 2 \exp\left(-\frac{\Gamma}{\sigma_m^2}\right) + 2 \exp\left(-\frac{2\Gamma}{\sigma_m^2}\right) \right]^M.
\end{aligned} \tag{55}$$

From (55), it is obvious that the outage probability increases as the number of the vehicular relays increases.

4. Numerical Calculation Study

This section shows the numerical study of the channel-secrecy capacity of DF cooperative vehicle schemes. Simulation results show that channel-secrecy capacity of the proposed system model is higher than the traditional system (i.e., without existing direct link).

Moreover, simulation results showed that the channel secrecy of the proposed system model significantly increases when the number of the vehicle relays increases. Therefore, the simulation results show an improvement in the physical layer security when exploiting cooperative relays.

Additionally, the simulation showed the effect of increasing the relays gain (G), assuming that all relays are identical and independently distributed (i.i.d).

The following simulation parameters were considered for all tests:

- (i) G_{srd} (dB) = 0; G_{sre} (dB) = 0. $\sigma_{sd}^2 = 0.5$.
- (ii) $\sigma_{si}^2 = \sigma_{id}^2 = \sigma_{ie}^2 = 1$.
- (iii) $N_t = 9$. SNR = 12 dB.

Figure 5 depicts the ergodic channel-secrecy capacity and intercepts probability comparison between traditional direct transmission and DF cooperative vehicle protocol for both the proposed system model and the traditional system model. Figure 5 shows that the traditional direct transmission is worse than the DF cooperative vehicle protocol regardless of the system model (traditional or proposed) used.

Moreover, when $M \geq 1$, the optimal system model always outperforms the traditional system model. Therefore, regardless of the DF relaying mechanism, whether it was optimal or traditional, the direct transmission and cooperative diversity relay selection constantly performs worse than the traditional and optimal relay selections in terms of both ergodic secrecy capacity and intercept probability.

Figure 5(a) presents ergodic channel-secrecy capacity comparison between direct transmission and DF cooperative vehicle schemes with the traditional and the proposed system models. As shown in Figure 5(a), the proposed system model gives better channel-secrecy capacity

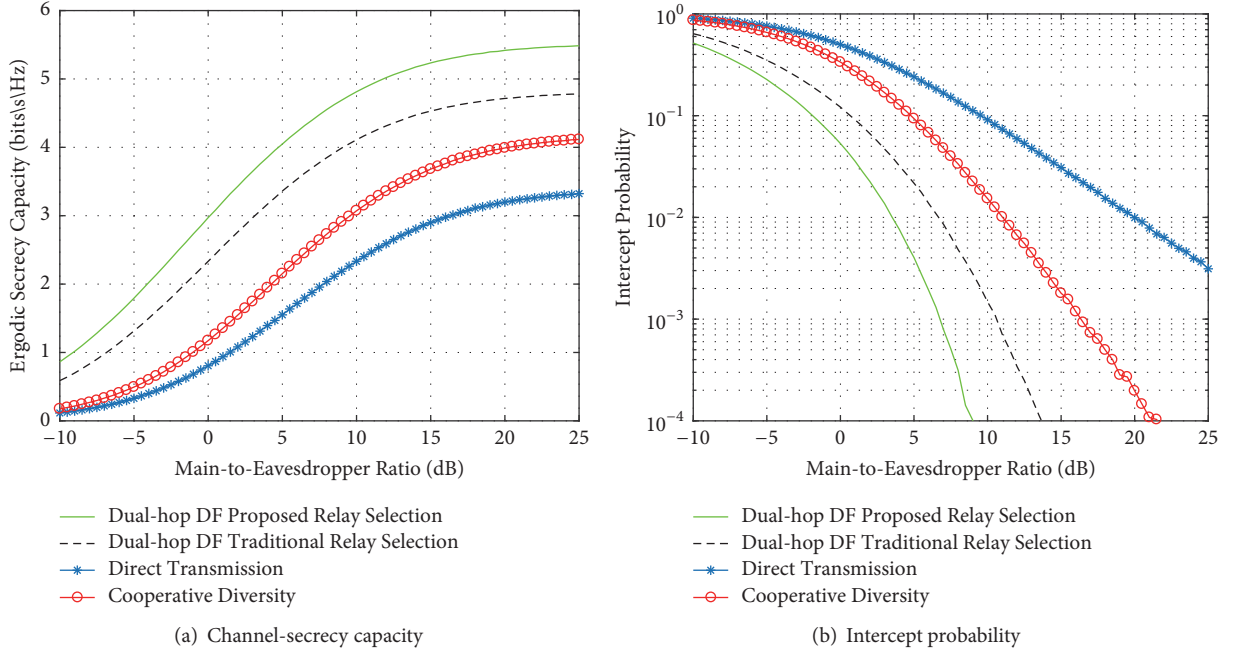


FIGURE 5: C_S and $P_{\text{intercept}}$ probability versus MER for dual-hop DF cooperative vehicles schemes.

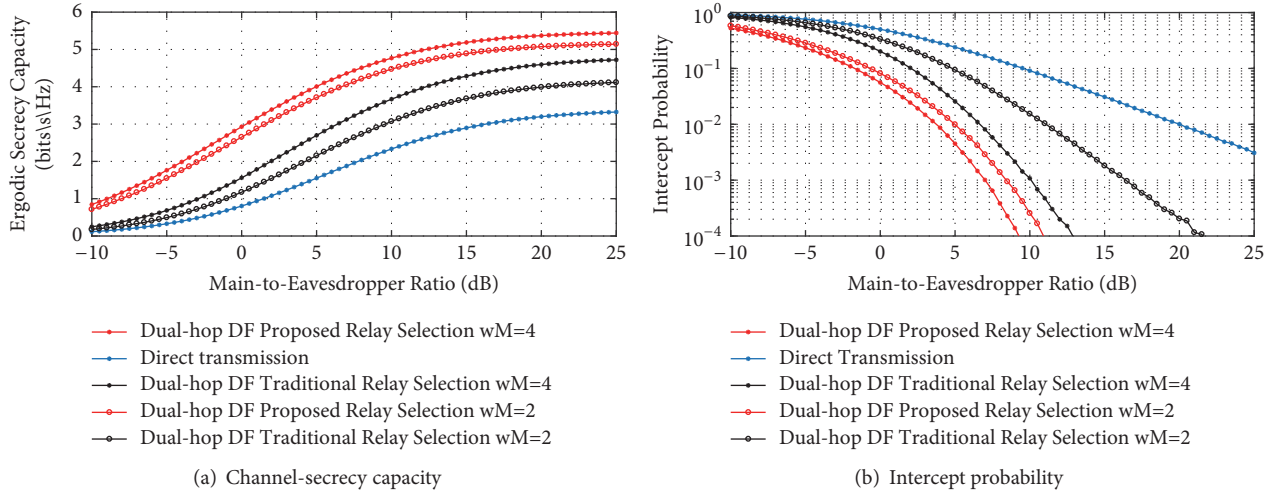


FIGURE 6: C_S and $p_{\text{intercept}}$ versus MER of dual-hop DF cooperative vehicles scheme (proposed and traditional relay selection mechanisms) and direct transmission system models with different number of transmitted relays.

than the traditional system model and the conventional direct transmission. Increasing channel capacity implies that using cooperative relays enhances the overall system security.

Figure 5(b) shows that the best intercept probability performance is given by DF cooperative vehicle scheme using either the proposed or the traditional system model when compared to conventional direct transmission. Moreover, the proposed system model is better than the traditional system model with respect to intercept probability.

Figure 6 shows that as the number of relays between a transmitter and receiver increases ($M = 2$ and 4), the

physical layer security is improving using either our proposed system model or the cooperative system model. Additionally, Figure 6 shows that the proposed system model is strictly higher than that of either the cooperative system model or the conventional transmission.

Figure 6(a) shows that as the number of relays increases, the ergodic channel-secrecy capacity improves. It is obvious that the channel-secrecy capacity of the dual-hop DF proposed and traditional system models with $M = 4$ is higher than the capacity of $M = 2$.

Figure 6(b) shows that the probability of the eavesdropper to listen the transmitted data is decreased in our proposed

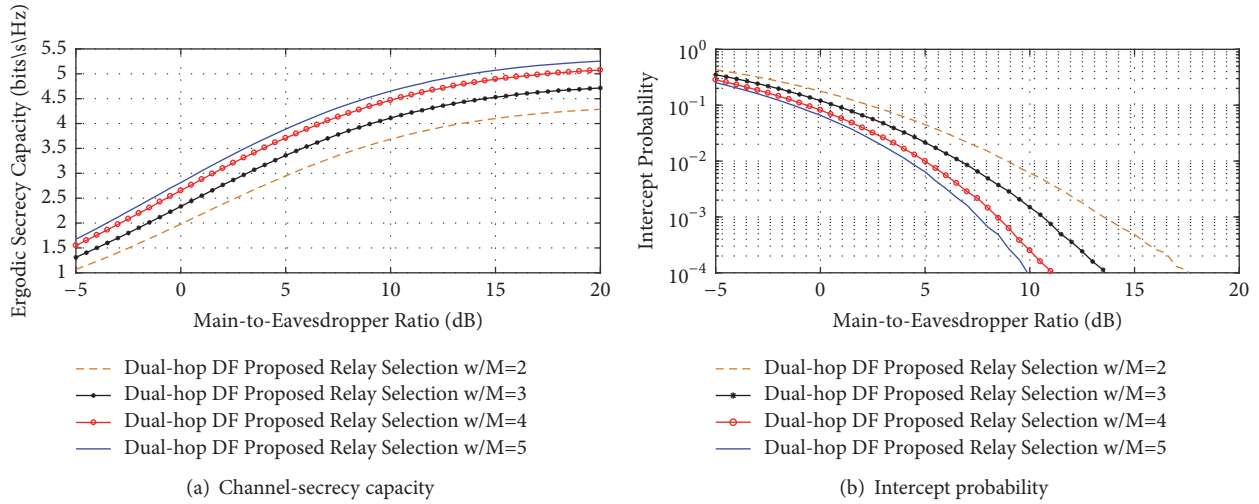


FIGURE 7: C_S and $p_{\text{intercept}}$ versus MER of dual-hop DF cooperative vehicles scheme: comparison of proposed relay selection mechanism with different number of transmitted relays.

system model. Moreover, the intercept probability of the dual-hop DF proposed and traditional system models with $M = 4$ is lower than the intercept probability of $M = 2$. Therefore, the overall physical layer security in the proposed system model is the highest one.

Figure 7 characterizes the effect of varying number of relays when relay's gain is constant for DF cooperative vehicle algorithm. Moreover, Figure 7 presents the channel-secrecy capacity and the intercept probability of the proposed system model for a different number of relays $M = 2, 3, 4, 5$. The channel-secrecy capacity of the proposed dual-hop DF cooperative diversity with $M = 5$ is the highest one.

Figure 7(a) shows significant increase in ergodic-secrecy capacity as the number of relays (M) increases. Therefore, channel-secrecy capacity of $M = 5$ has the highest channel secrecy and the lowest capacity is for $M = 2$.

Moreover, Figure 7(b) proves that the intercept probability of DF cooperative vehicle protocol with our proposed system model is improved by increasing the number of relays between transmitter and receiver. Therefore, DF cooperative vehicle protocol using the proposed system model has the best intercept probability.

Figure 8 depicts the effect of changing the relays locations with a constant number of relays $M = 2$ and constant geometric relays gain for DF cooperative vehicle algorithms.

Figure 8(a) presents the channel-secrecy capacity of DF using the proposed system model. Figure 8(a) shows that channel-secrecy capacity is significantly improved as the relays are closer to the source node. As per the aforementioned figure, the relays are closer to destination node, in which case an active/passive eavesdropper is able to attack the legitimate user data during the broadcast phase.

Figure 8(b) shows the improvement of the intercept probability when relays are closer to the source node. Therefore, by exploiting cooperative relays closer to the source node, the physical layer security will be improved.

Figure 9 presents a comparison of the outage probability in our proposed system model and the traditional cooperative diversity with the direct transmission. It is clearly obvious from Figure 9 that the outage probability increases as MER increases, which is proved in (55). Moreover, Figure 9 shows that the outage probability of our proposed system model is strictly higher than the traditional cooperative diversity and direct transmission.

Figure 10 presents our numerical outage probability results for direct transmission, cooperative diversity relays, and the proposed cooperative vehicle scheme for different data rates. As shown from Figure 10, when the data rate increases from $R_d = 1.5$ to $R_d = 2.5$, the outage probability of our proposed model is strictly lower than the direct transmission and the traditional cooperative diversity at certain MER.

Figure 11 presents the relation between the outage probability and the used data rate R_d from the source node with respect to the number of vehicular relays between the source and destination. As shown in Figure 11, when the data rate R_d increases from $R_d = 1$ to $R_d = 4.5$, the outage probability is significantly reduced. It is also observed in Figure 11 that, for $R_d = 1$ to $R_d = 4.5$, the outage probability of our proposed system model tends to zero, as the number of relays increases from $M = 1$ to $M = 10^3$. This demonstrates that reliability of dual-hop vehicular cooperative model improves upon increasing the number of relays.

5. Conclusion

This paper proposed a novel technique to improve vehicular wireless channel secrecy by enabling precoded cooperative vehicular relaying to contribute towards the formation of an advanced telecommunication network. The goal is to increase network security by enhancing the channel secrecy and reducing the intercept probability. Best relay selection

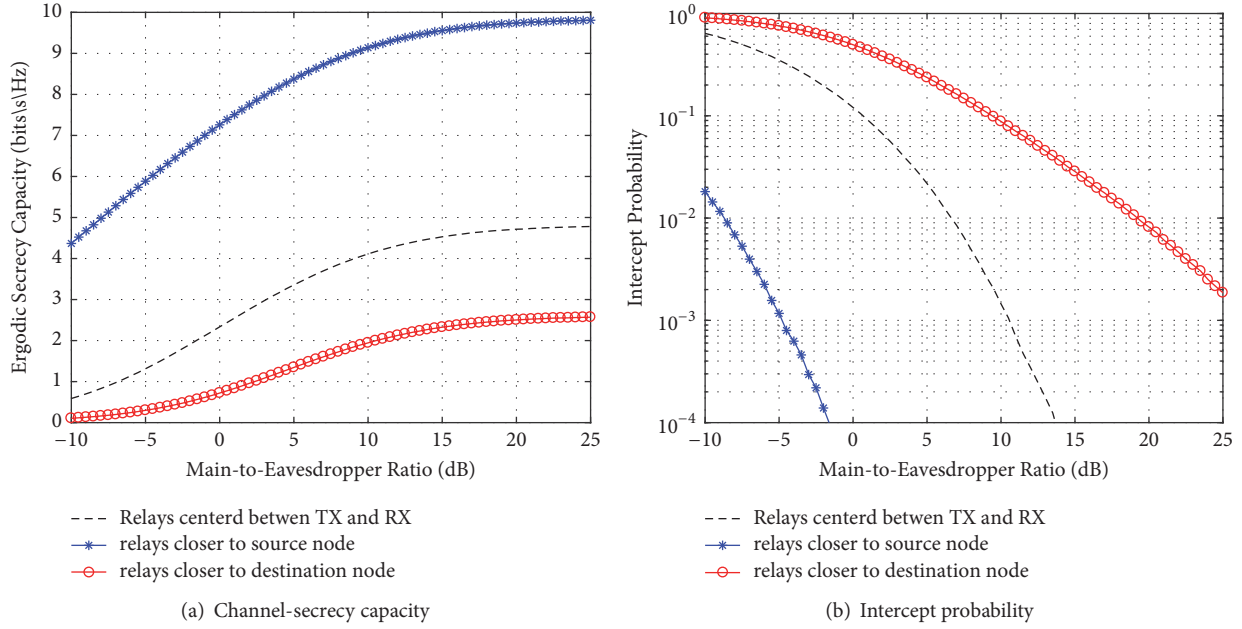


FIGURE 8: C_S and $P_{\text{intercept}}$ versus MER of DF cooperative vehicles scheme: comparison of proposed system model with different relays locations.

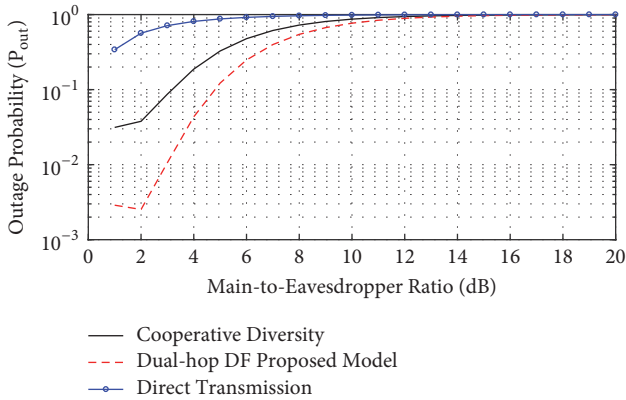


FIGURE 9: Outage probability of the direct transmission, cooperative diversity, and dual-hop DF cooperative vehicular relays versus the MER.

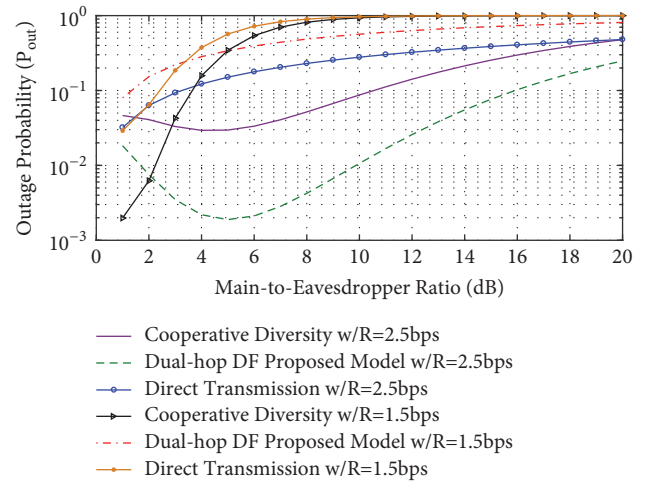


FIGURE 10: Outage probability of the direct transmission, cooperative diversity, and dual-hop DF cooperative vehicular relays versus the MER for different data rates R_d .

mechanism is presented as a base to realize security-through-diversity concepts for cooperative wireless vehicular networks.

This paper demonstrated that using vehicles to construct cooperative relaying in broadband networks not only potentiates reduced levels of power consumption but also provides lower error rates, increases channel security, and promises lower intercept probabilities. We employed a precoded cooperative transmission technique to extract the underlying rich multipath-Doppler-spatial diversity. Analytical and simulation results demonstrated significant increase in the physical layer security with a clear reduction in the required transmitting power compared with traditional transmission schemes.

Our proposed scheme can be particularly useful in heavily populated urban areas.

Our future work will consider vehicle speed among other communication characteristics in various communication scenarios.

Conflicts of Interest

The authors declare that there are no conflicts of interest.

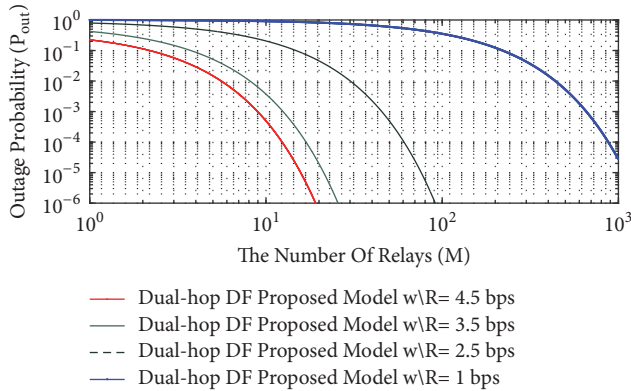


FIGURE 11: Outage probability of direct transmission, cooperative diversity, and dual-hop DF cooperative vehicular relays versus different number of relay nodes associated for different data rates R_d .

Acknowledgments

This research was partially supported by the Roadway, Transportation, and Traffic Safety Research Center (RTT SRC) of the United Arab Emirates University (Grant no. 31R058). The authors would like to express their appreciation for the “IoT and Cyber Security Lab,” SmartCI, Alexandria University, Egypt, for supporting and hosting the activities related to this manuscript.

References

- [1] E. M. Hourab, M. Azab, M. Rizk, and A. Mokhtar, “Security versus reliability study for power-limited mobile IoT devices,” in *Proceedings of the 2017 8th IEEE Annual Information Technology, Electronics and Mobile Communication Conference (IEMCON)*, pp. 430–438, Vancouver, BC, October 2017.
- [2] E. M. Hourab, A. Mansour, M. Azab, M. Rizk, and A. Mokhtar, “Towards physical layer security in Internet of Things based on reconfigurable multiband diversification,” in *Proceedings of the 2017 8th IEEE Annual Information Technology, Electronics and Mobile Communication Conference (IEMCON)*, pp. 446–450, Vancouver, BC, October 2017.
- [3] A. Tulino, A. Lozano, and S. Verdú, “MIMO capacity with channel state information at the transmitter,” in *Proceedings of the Eighth IEEE International Symposium on Spread Spectrum Techniques and Applications - Programme and Book of Abstracts*, pp. 22–26, Sydney, NSW, Australia.
- [4] Y. Zhou and T.-S. Ng, “Performance analysis on MIMO-OFCDM systems with multi-code transmission,” *IEEE Transactions on Wireless Communications*, vol. 8, no. 9, pp. 4426–4433, 2009.
- [5] J. Hu and N. C. Beaulieu, “Performance analysis of decode-and-forward relaying with selection combining,” *IEEE Communications Letters*, vol. 11, no. 6, pp. 489–491, 2007.
- [6] Y. Zou, X. Wang, and W. Shen, “Optimal relay selection for physical-layer security in cooperative wireless networks,” *IEEE Journal on Selected Areas in Communications*, vol. 31, no. 10, pp. 2099–2111, 2013.
- [7] S. V. Kartalopoulos, “A primer on cryptography in communications,” *IEEE Communications Magazine*, vol. 44, no. 4, pp. 146–151, 2006.
- [8] A. D. Wyner, “The wire-tap channel,” *Bell Labs Technical Journal*, vol. 54, no. 8, pp. 1355–1387, 1975.
- [9] S. K. Leung-Yan-Cheong and M. E. Hellman, “The Gaussian wire-tap channel,” *Institute of Electrical and Electronics Engineers Transactions on Information Theory*, vol. 24, no. 4, pp. 451–456, 1978.
- [10] J. N. Laneman, D. N. Tse, and G. . Wornell, “Cooperative diversity in wireless networks: efficient protocols and outage behavior,” *Institute of Electrical and Electronics Engineers Transactions on Information Theory*, vol. 50, no. 12, pp. 3062–3080, 2004.
- [11] E. R. Alotaibi and K. A. Hamdi, “Ergodic secrecy capacity analysis for cooperative communication with relay selection under non-identical distribution,” in *Proceedings of the 2016 IEEE International Conference on Communications, ICC 2016*, Malaysia, May 2016.
- [12] Y. Zou, X. Wang, and W. Shen, “Intercept probability analysis of cooperative wireless networks with best relay selection in the presence of eavesdropping attack,” in *Proceedings of the ICC 2013 - 2013 IEEE International Conference on Communications*, pp. 2183–2187, Budapest, Hungary, June 2013.
- [13] M. F. Feteiha and M. H. Ahmed, “Best-Relay Selection for Multi-Hop Vehicular Communication in Highways,” in *Proceedings of the GLOBECOM 2015 - 2015 IEEE Global Communications Conference*, pp. 1–7, San Diego, CA, USA, December 2015.
- [14] M. Feteiha and H. S. Hassanein, “Decode-and-Forward cooperative vehicular relaying for LTE-A MIMO-downlink,” *Vehicular Communications*, vol. 3, pp. 12–20, 2016.
- [15] M. F. Feteiha and M. Uysal, “On the Performance of MIMO Cooperative Transmission for Broadband Vehicular Networks,” *IEEE Transactions on Vehicular Technology*, vol. 64, no. 6, pp. 2297–2305, 2015.
- [16] M. F. Feteiha and M. Uysal, “Multipath-Doppler Diversity for Broadband Cooperative Vehicular Communications,” in *Proceedings of the ICC 2011 - 2011 IEEE International Conference on Communications*, pp. 1–6, Kyoto, Japan, June 2011.
- [17] T. Chrysikos, T. Dagiuklas, and S. Kotsopoulos, “Wireless Information-Theoretic Security in MANETs,” in *Proceedings of the 2013 IEEE International Conference on Communications (ICC) Workshops*, pp. 692–696, Budapest, June 2013.
- [18] A. Bletsas, A. Khisti, D. P. Reed, and A. Lippman, “A simple cooperative diversity method based on network path selection,” *IEEE Journal on Selected Areas in Communications*, vol. 24, no. 3, pp. 659–672, 2006.
- [19] Y. Zou, J. Zhu, X. Wang, and V. C. M. Leung, “Improving physical-layer security in wireless communications using diversity techniques,” *IEEE Network*, vol. 29, no. 1, pp. 42–48, 2015.
- [20] L. Zheng and D. N. C. Tse, “Diversity and multiplexing: a fundamental tradeoff in multiple-antenna channels,” *IEEE Transactions on Information Theory*, vol. 49, no. 5, pp. 1073–1096, 2003.
- [21] C. E. Shannon, “A mathematical theory of communication,” *Bibliometrics*, vol. 5, no. 1, pp. 3–55, 2001.
- [22] Y. Zou, J. Zhu, B. Zheng, and Y.-D. Yao, “An adaptive cooperation diversity scheme with best-relay selection in cognitive radio networks,” *IEEE Transactions on Signal Processing*, vol. 58, no. 10, pp. 5438–5455, 2010.

Research Article

Comprehensive Analysis on Heterogeneous Wireless Network in High-Speed Scenarios

Yuyang Zhang,¹ Tao Zheng ,¹ Ping Dong ,¹ Hongbin Luo,¹ and Zhibo Pang ²

¹Beijing Jiaotong University, China

²ABB Corporate Research, Sweden

Correspondence should be addressed to Tao Zheng; zhengtao@bjtu.edu.cn

Received 4 November 2017; Accepted 16 April 2018; Published 22 May 2018

Academic Editor: Richard Yu

Copyright © 2018 Yuyang Zhang et al. This is an open access article distributed under the Creative Commons Attribution License, which permits unrestricted use, distribution, and reproduction in any medium, provided the original work is properly cited.

Greater demands are being placed on the access bandwidth, stability, and delay of network because of the quickening rhythm of life and work, especially in mobile scenario. In order to obtain a stable network with low latency and high bandwidth in mobile scenario, taking advantage of the wireless heterogeneous network in parallel is a good choice. Nowadays, people are increasingly concerned about the network quality under the mobile scenario. Some scholars have done the relevant measurements. However, all of those measurements mainly investigate part of the network parameters or part of mobile scenarios. In this paper, we make the following contributions. Firstly, in high-speed mobile scenario, the wireless network qualities of different vendors are measured synthetically. Secondly, we analyze the benefits of taking advantage of the different vendors. Thirdly, we deploy the replication link mechanism in high-speed mobile scenario and propose an algorithm to remove the duplicate packet in high-speed mobile scenario. And the algorithm can also be used in another multipath schedule algorithm to improve the reliability.

1. Introduction

With the rapid development of high-speed rail technologies, high-speed rails have become the main way of daily short or medium distance travels [1]. In China, there are 1.713 billion trips made in 2017 bringing the total cumulative number of trips to 7 billion. Followed by the tremendous passenger flow, greater demands are being placed on mobile scenario [2, 3].

Nowadays, cellular network has become the main way for people to access the Internet [4]. With the development of cellular network, many researchers measure the performance of cellular networks from different aspects in different scenarios. Tan et al. [5] did the research about multiple commercial 3G UMTS networks. They analyzed their latency, throughput, and the performance of different applications. Tso et al. [6] analyze the HSPA network in low-speed mobile scenario. However, all of those measurements mainly investigate the network layer parameters and transport layer parameters. And they miss SNR, an important network parameter in network access layer. Rodriguez-Pineiro J and Martin-Vega pointed out that SNR is an important network parameter

for analyzing the cellular networks in high-speed mobile scenario [7, 8].

In addition, there are some literatures studying the performance of wireless network in high-speed mobile scenario [9, 10]. However, these literatures only focus on the network performance of single vendor in high-speed mobile scenario, and they do not analyze the performance of heterogeneous networks that are created by different vendors. We analyze the relationship for heterogeneous networks at the same time and place in high-speed scenario.

In this paper, we carry out a measurement to study heterogeneous wireless networks performance in high-speed mobile scenarios. We define the high-speed mobile scenario that the speed of receiver relative to base station is 300 Km/h or above. 300 Km/h is the typical velocity of the China Railway High-Speed (CRH), which is the largest commercial high-speed railway network. We did our measurement in the Beijing-Tianjin Intercity Railway. In our experiments, we develop a special measurement tool, which is called Heterogeneous Network Measurement Instrument (HNMI). HNMI can access three heterogeneous wireless networks. In our measurement, we made the HNMI access to the three greatest

vendors CMCC, China Unicom (CU), and China Telecom (CT) at the same time. We choose Iperf [11] as the TCP packet generator and Ali cloud server as the TCP receiver, which is the Chinese biggest cloud service provider. In order to investigate the influence of moving speed on wireless network, we design the measurement in static scenario and low-speed mobile scenario as the reference. Beijing Metro Line 13 is selected as the low-speed mobile scenario, where the running speed of the train is about 50 Km/h. And a playground in Beijing Jiaotong University is selected as the static scenario, where the signal strength of three vendors is excellent. The results show that, in high-speed scenario, a single wireless network is too poor to satisfy the user's demand. And the network is not stabilized in high-speed scenario.

Moreover, it is possible to comprehensively utilize the heterogeneous wireless networks because of abundant wireless network resources along the railway [12]. In this paper, we try to deploy the replication link mechanism in high-speed mobile scenario. The actual measurement results show that the replication link mechanism effectively reduces the network volatility, reduces the overall packet loss rate, and significantly improves the network throughput.

The structure of the paper is organized as follows. Section 2 reviews some related works about wireless network measurement. In Section 3, we describe the measurement methodology of our measurement. In Section 4, we describe our result and analyze the influence of moving speed on network performance for each vendor. In Section 5, we deploy the packet replication mechanism in high-speed mobile scenario.

2. Related Work

Research on the vehicle-ground communication is a hot topic [13]. Studying the performance of wireless networks under different mobile speeds is an important direction of vehicle-ground communication. Many researchers do a lot of measurement for wireless mobile network. These works can be divided into two categories:

(1) Limited Scenarios.

Tso et al. [6] investigated the performance of HSPA networks. They analyze not only the static scenario but also many mobile scenarios including subway, trains, and city bus. However, limited by the commercial network deployment, they only analyze the 3G networks, instead of the 4G networks. Jang et al. [14] measured 3G and 3.5G networks with different vendors in different moving scenarios. References [8, 15] proposed different network channel models of high-speed mobile scenarios. Huang et al. [16] measured low-speed mobile scenario. They find that, in low-speed mobile scenario, the RTT remains stable with small volatility. As their analysis SNR is an important parameter that affects the network throughput, Li et al. [17] investigated the TCP behavior in high-speed mobile scenario. They find that current TCP is not adapted to high-speed mobile scenario. However,

the measurement scenarios for these literatures are limited and there is no comprehensive analysis of the network performance in high-speed mobile scenario.

(2) limited Network Parameters.

Xiao et al. [18] carried out extensive measurements on the 4G LTE networks performance in high-speed scenario. They investigate their RSRP, RTT, jitter, and TCP throughput. However, they do not measure the SNR, which is an important parameter for wireless network. Tan et al. do the research about multiple commercial 3G UMTS networks [5]. They analyze their latency, throughput, and the performance of different applications. Liu et al. [19] measured three different LTE networks in high-speed scenarios. They focus on the parameter of transport layer and they do not analyze the parameters of network access layer. However, these literatures only focus on the network performance of single vendor in high-speed mobile scenario and do not analyze the performance of heterogeneous networks that are created by different vendors.

In this paper, we carry out a measurement to study heterogeneous wireless networks performance in different mobile scenarios. We analyze the influence of high-speed mobile scenario on wireless network. And we explore the method of utilizing the heterogeneous networks along the high-speed rails.

3. Measurement Methodology

In order to explore the actual network quality, we design a set of experiments to measure the network quality in different scenarios. In this section, we describe the contents of our network measurements including the tools, scenarios, and measurement methods. And we analyze the measurement result of network quality in detail.

3.1. Measurement Scenario. In order to measure the impact on the wireless network at different moving speeds, we choose three typical scenarios, namely, static scenario, low-speed mobile scenario, and high-speed mobile scenario.

We select an open area of Beijing Jiaotong University as the static scenario, where the network signals of all the vendors are well. The Beijing Metro Line 13 is selected as the low-speed mobile scenario, where the running speed of the train is about 70 Km/h. We select the Beijing-Tianjin intercity high-speed rail as high-speed mobile scenario, where the running speed of the train is around 300 Km/h.

In China, the wireless cellular network is mainly operated by China Telecom (CT), China Unicom (CU), and China Mobile. We select these top three vendors in China to study the relationship between heterogeneous cellular networks at the same place and time. The names and frequency bands of the three major vendors are shown in the Table 1.

3.2. Measurement Parameters. With reference to the previous works, the network parameters are presented in the Table 2.

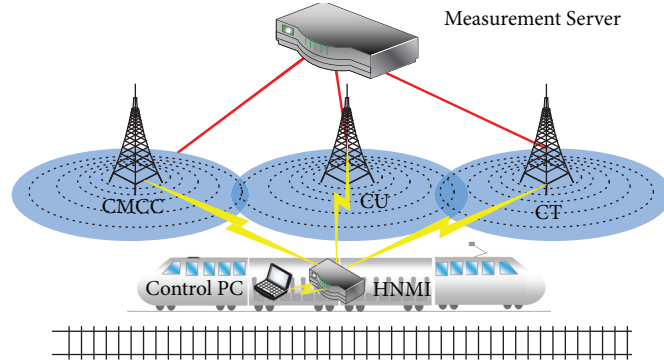


FIGURE 1: Measurement topology.

TABLE 1: Heterogeneous wireless networks for different vendors.

vendor	Uplink Freq	Downlink Freq	mode	
CMCC	890–909	935–954	GSM900	2G
	1710–1725	1805–1820	DCS1800	2G
	2010–2025	2010–2025	TD-SCDMA	3G
	1880–1890	1880–1890		
	2320–2370	2320–2370	TD-LTE	4G
	2575–2635	2575–2635		
CU	909–915	954–960	GSM900	2G
	1940–1955	2130–2145	WCDMA	3G
	1755–1765	1850–1860	FDD-LTE	4G
CT	825–840	870–885	CDMA	2G
	1920–1935	2110–2125	CDMA-2000	3G
	1765–1780	1860–1875	FDD-LTE	4G

We divide all the parameters into three parts according to the TCP/IP Stack. There are a couple of reasons for this: (1) a large number of applications exist on the Internet; (2) the vast majority of traffic is TCP traffic; (3) the throughput of TCP can well reflect the user's network experience. Therefore, we select TCP throughput as the breakthrough point of our measurement. The quality of the network layer impacts the quality of the transport layer. Hence, we analyze the network layer parameters. RTT and jitter are the most popular parameters. The network access layer guarantees the quality of network layer. As the 4G network is widely covered by vendors in China, RSRP is the most important parameter for indicating the strength of network signal. According to [7, 8], SNR is a significant parameter for network transmission model especially in high-speed scenario. The cell ID represent the cellular network base station that we access. The change of cell ID means that the access network has been switched. During the network switch, the mobile devices have to send a series of packets for reregistration, which is bad for transmission.

3.3. Measurement Tools. Most of the traditional measurement tools can only measure one kind of wireless network at the same time. In order to get further study about the network quality in the different mobile scenarios at the same time, we design the network transmission topology shown in Figure 1.

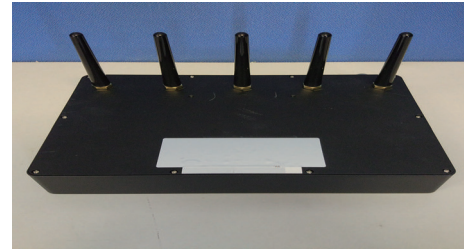


FIGURE 2: Heterogeneous Network Measurement Instrument.

Moreover, the network quality measurement tool we develop is shown in Figure 2.

The topology of the measurement is shown in Figure 1. We purchase Ali cloud services as our server. The reason why we choose Ali cloud is that it is the largest cloud service provider in China and it has enough access bandwidth to those three major mobile vendors. Last but not least, it can reduce the impact of the cable link in the measurement. The client is the dedicated network quality measurement tool shown in Figure 2. It consists of three identical cellular network adapters and a WLAN network adapter. Each cellular network adapter corresponds to a separate cellular network. Therefore, the device can support three major vendors simultaneously. The WLAN network adapter accommodates the control devices in the IEEE 802.11 b/g/n protocol.

As for software, we develop a network parameters monitoring module based on the Linux 3.2.0 kernel. The module can monitor information including RSRP, SNR, access base station information, network delay, TCP throughput, and so on.

3.4. Measurement Procedure. We did the measurement over three different network vendors simultaneously in three different scenarios. We group the parameters by characteristics of four layers of TCP/IP model. Aiming at the network access layer's parameters, we read the network adapter information every 100 ms. At the network layer, we get the information by the way of sending Ping command periodically. The transport layer information is obtained by Iperf that can make the best of the transport layer's resources. Then we calculate the results of transport layer's parameters from the network adapter every 100 ms.

TABLE 2: Measurement parameters.

parameters	division	introduction
RSRP		Reference Signal Received Power (RSRP) is a measurement used to represent the received power level in an LTE cell network.
SNR	Network access Layer	Signal-to-noise ratio is a measurement used in science and engineering that compares the level of a desired signal to the level of background noise.
Mode		Received signal network standard
Cell ID		The ID of cellular network base station. It means that a network switch has occurred when it changes.
RTT	Network Layer	Round-trip time is the length of time it takes for a signal to be sent plus the length of time it takes for an acknowledgment of that signal to be received.
Jitter		Jitter is the variation in packet delay at the receiver of the information.
TCP throughput	Transport Layer	The rate of TCP packets delivery over a transmission channel.

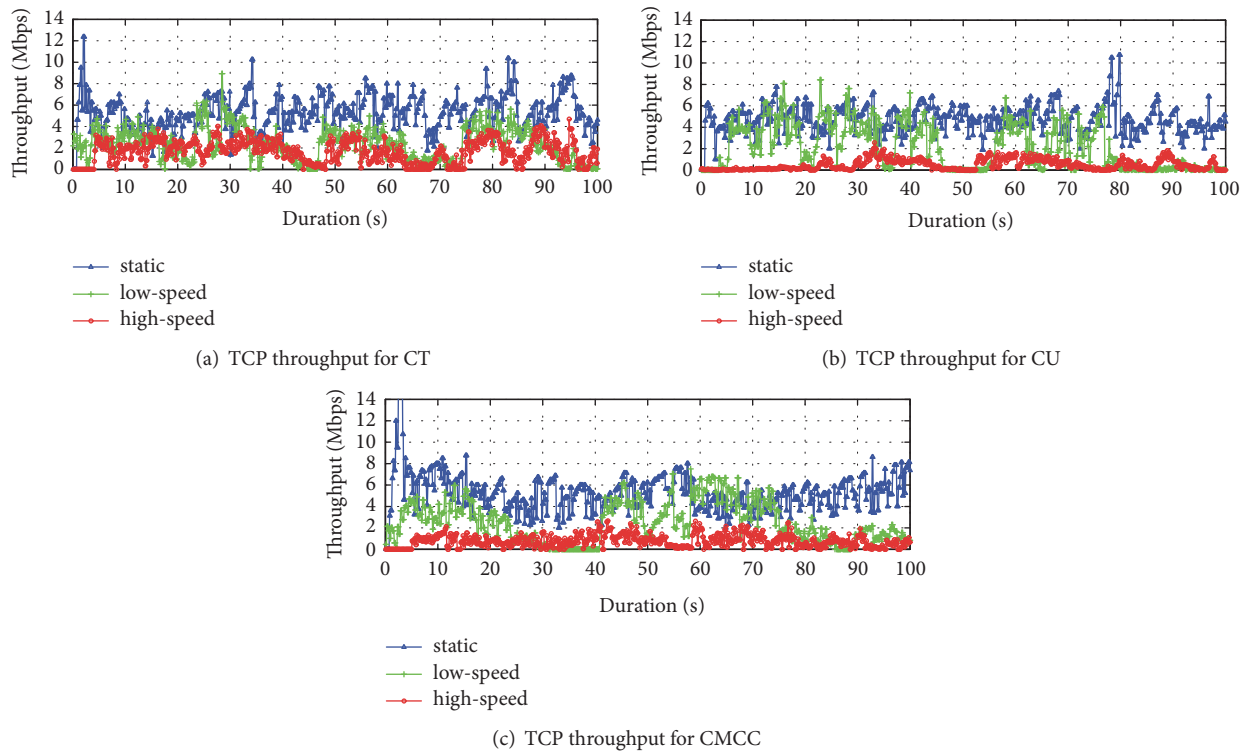


FIGURE 3: TCP throughput in different scenarios.

4. The Advantage of Heterogeneous Network

By actual measurement result, we find that the network performance is not good in high-speed mobile scenario that cannot meet people's demands of accessing the Internet. In this section, we analyze the factors that affect single vendor's network performance in high-speed mobile scenario layer by layer. In addition, we make a further discussion of the advantage of using heterogeneous networks.

4.1. Transport Layer. First of all, let us intuitively observe the performance of the transport layer parameters in high-speed mobile scenario. Figure 3 illustrates the TCP performance in different scenarios. The changing trends of TCP throughput at different speeds are similar to each vendor. In all of three

scenarios, obviously, the performance of TCP throughput in high-speed scenario is the poorest. In high-speed scenario, the average of TCP throughput is the lowest and the TCP throughput's volatility is the most dramatic.

Next, we give the statistic analysis by boxplot and cumulative distribution function (CDF) figure. Figure 4 shows the boxplot of TCP throughput in different scenarios. The pattern that we name the horizontal axis is "vendor_scenario." S means static scenario, L means low-speed mobile scenario, and H means high-speed mobile scenario. For each cellular network, the median ratios of high-speed mobile scenario to static scenario are 33.32%, 6.25%, and 15.9%.

Furthermore, we study the volatility of TCP throughput. Figure 5 is the CDF of the volatility of TCP throughput in 100 ms. The horizontal axis is the ratio of the volatility

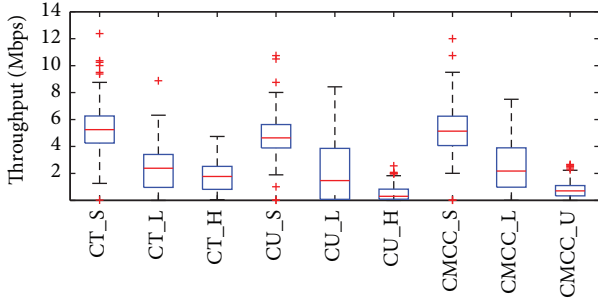


FIGURE 4: TCP throughput boxplot in different scenarios.

of TCP throughput within the 100 ms to the median of results. Vertical axis is the cumulative probability. In high-speed mobile scenario, it is only about 40% possible that the volatility is stable. However, in static scenario, the index is more than 60%. And in high-speed scenario, it is about 40% possible that the volatility of TCP throughput is over 20%. The same index in static scenario is about 20%. In high-speed scenario, such huge volatility in a single network has a great impact on user experience.

Based on the above analysis, we find that, in high-speed mobile scenario, it is difficult to satisfy people's demand for accessing the Internet by single wireless network. Maybe taking advantage of heterogeneous networks can satisfy the people's demand for accessing the Internet. From Figure 3, we find that there is little risk that all the wireless networks perform badly in throughput at the same time. Therefore, as shown in Figure 6, an appropriate algorithm that can utilize heterogeneous networks and achieve bandwidth aggregation can get a relatively reliable network.

4.2. Network Layer. Through the analysis of the transport layer, we can observe that, in high-speed mobile scenario, the network performance of a single wireless network is poor. However, with the heterogeneous networks, the performance of the entire network has a huge room for improvement. Next, we analyze the network layer to find out the advantages of using heterogeneous networks.

Figure 7 shows the RTT in different scenarios for single wireless network. Vertical axis is the RTT value. RTT equal to zero means that the probe packet is lost at this moment. We can observe that, with the increase of moving speed, the average RTT is increasing and sometimes the probe packet is lost.

Next, let us observe the effect of moving on RTT jitter [20]. From Figure 8, we can observe that the RTT jitter in high-speed scenarios is more dramatic. In the CMCC network, it is more than 40% possible that the RTT jitters over 50 ms in high-speed scenario. However, the median RTT is only 131 ms.

Through the above analysis, we find that the trend of RTT is similar. With the increase of moving speed, the packets need more time for delivery and are even lost. This may cause disaster to the applications that are very sensitive to packet delay, such as real-time games. Maybe taking advantage of heterogeneous networks can reduce the transmission delay.

TABLE 3: RSRP level.

level	RSRP (dBm)
Very Good	RSRP > -85 dBm
Good	-85 dBm ≥ RSRP > -95 dBm
Average	-95 dBm ≥ RSRP > -105 dBm
Weak	-105 dBm ≥ RSRP > -115 dBm
Bad	-115 dBm ≥ RSRP

TABLE 4: RSRP level in different scenarios.

	vendor	static	low-speed	high-speed
Very Good	CT	100%	8.0%	2.1%
	CU	100%	10.0%	2.2%
	CMCC	100%	28.0%	2.1%
Good	CT	0	28.2%	15.5%
	CU	0	20.8%	4.3%
	CMCC	0	56.5	3.4%
Average	CT	0	33.8%	39.1%
	CU	0	54.6%	37.2%
	CMCC	0	12.5%	19.2%
Weak	CT	0	22.9%	41.1%
	CU	0	9.0%	50.0
	CMCC	0	3.0%	61.6%
Bad	CT	0	7.1%	2.3%
	CU	0	5.6%	6.4%
	CMCC	0	0	13.8%

Therefore, as shown in Figure 9, an appropriate algorithm shows that each time network selects the fastest link it can get a relatively reliable network.

4.3. Network Access Layer. After the analysis of transport layer and network access layer parameters, we find that the root cause of poor performance in high-speed scenarios is the poor performance of network access layer.

At first, we analyze the signal quality. In our whole measurement, each scenario is covered with 4G networks. RSRP is mainly used in 4G cellular network. Figure 10 shows the RSRP in different scenarios. In our measurement, we divide the RSRP into 5 levels as Table 3 shown. Table 4 is the measurement result. We can see that, in static scenarios, the RSRP is strong enough. However, when the receiver moves, the RSRP is not strong enough and most of the time the RSRP locates in the Average Level. What is more, the RSRP in high-speed scenario is lower than the low-speed scenario's. The SNR is another important parameter for cellular network. Figure 11 shows that SNR in high-speed scenario is lower than SNR in static scenario.

Next, we analyze the signal quality volatility. Figure 12 shows the volatility of RSRP in different scenarios. Figure 13 shows the volatility of SNR in different scenarios. We analyze these parameters together because they have similar characteristics. We can observe that, in static scenario, RSRP is stable and SNR is a little bit volatile. In mobile scenario, RSRP has a certain degree of volatility and the degrees of volatility

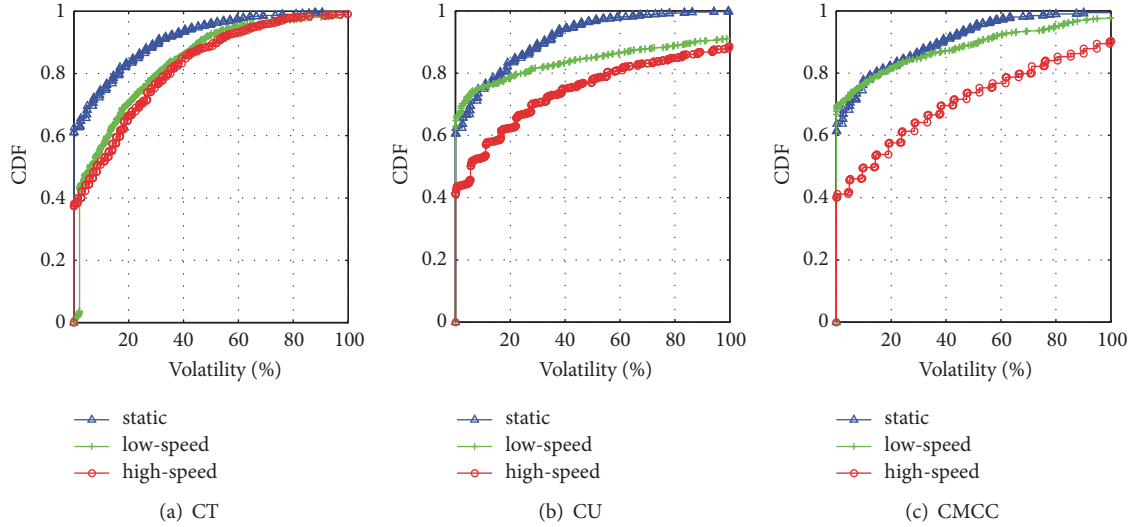


FIGURE 5: TCP throughput volatility CDF in different scenarios.

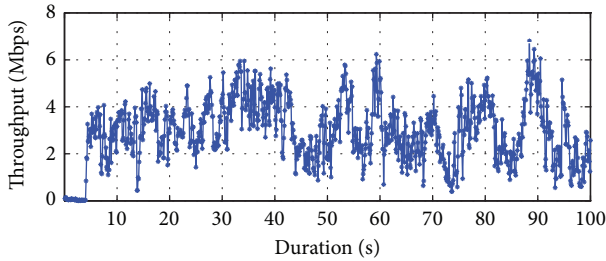


FIGURE 6: TCP throughput performance aggressive in high-speed scenario.

in high-speed scenario and low-speed scenario are closer. In my opinion, there are two reasons for this problem. For low-speed scenario, the measurement scenario is in urban area where the wireless environment is complex and the access to the base station often changes. In high-speed scenario, rapid movement of the receiver leads to changes in the RSRP and SNR. But the base station along the railway is more equally distributed. This is also proved by handoff duration CDF shown in Figure 14. The horizontal axis is the duration of receiver accessing in the same base station. Vertical axis is the cumulative probability. We can observe that although the receiver in high-speed scenario goes far in the same time, the receiver infrequently switched due to the distribution of base station.

Although the performance of the three vendors in high-speed mobile scenario is not very good, their network signals in high-speed mobile scenario are relatively independent. Table 5 is the result of correlation analysis of different vendors in high-speed mobile scenario. The data of the two groups are not correlated where the correlation coefficient is less than 0.3.

We give a further discussion about the handoff of each wireless cellular network under different scenarios. We measured these three wireless cellular networks simultaneously. Concrete analysis on the handoff is shown in one figure as

TABLE 5: Signal Correlation analysis.

	RSRP	SNR
CT vs CU	0.2807	0.1950
CT vs CMCC	0.0175	0.0559
CU vs CMCC	0.0248	0.1034

Figure 15. The horizontal axis is the time. Vertical axis is the different vendors in different scenarios. S means static scenario, L means low-speed scenario, and H means high-speed scenario. In Figure 15, the same color block means that the receiver is accessed to the same base station. In other words, the junction of different color blocks is the time when handoff occurs. We can clearly observe that, in the same scenario, it seldom happens that three cellular wireless network have handoff at the same time. In other word, even in the high-speed scenario, using multiple vendors' network with a suitable schedule algorithm can support a reliable network.

5. Comprehensive Utilization of Heterogeneous Network Resources in High-Speed Mobile Scenario

Section 4 points out that, in high-speed mobile scenario, due to the shielding of vehicle body and wireless cellular network volatility, a single wireless network is difficult to meet the needs of users. However, there are many different wireless networks resources along the railway. The comprehensive utilization of heterogeneous wireless networks along the railway has become an important method to solve the network access in high-speed mobile scenario.

For such a harsh network environment, a simple idea is to copy the data packets, respectively, from different links to send, taking the first arrival of the data packets as useful data packets. And the remaining packets are discarded. At first

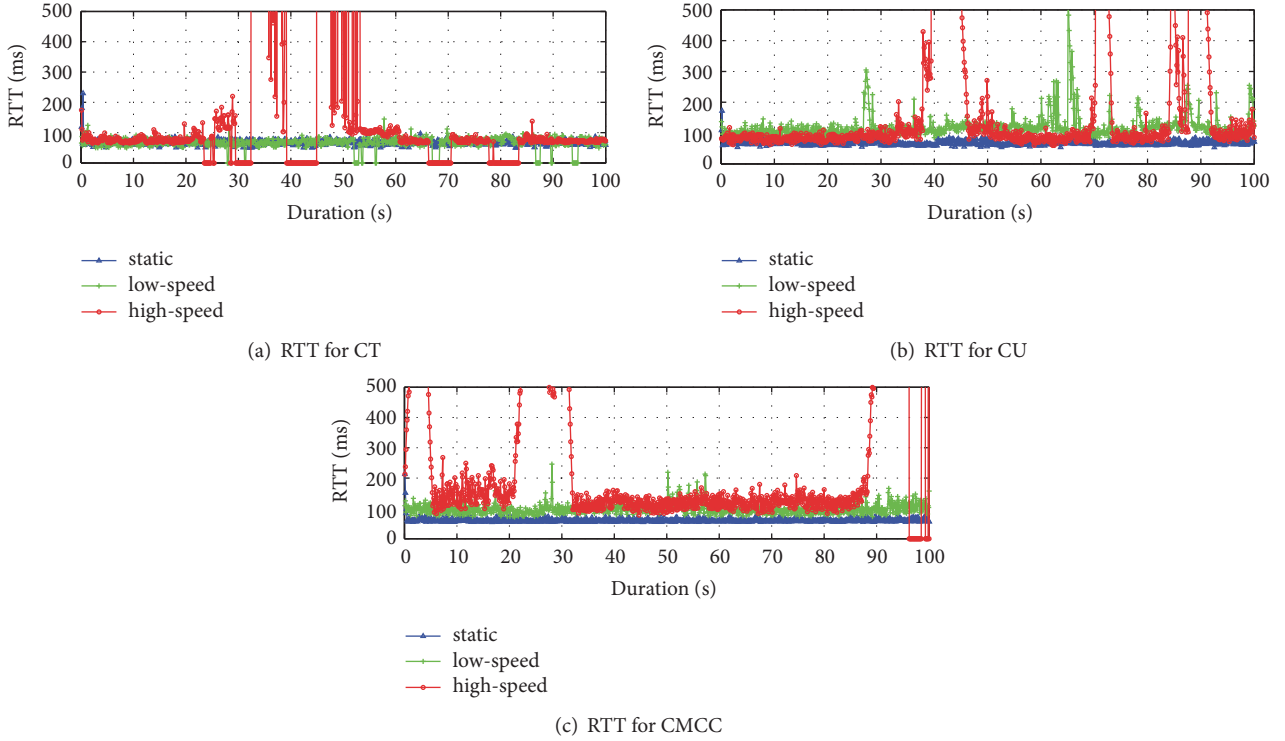


FIGURE 7: RTT in different scenarios.

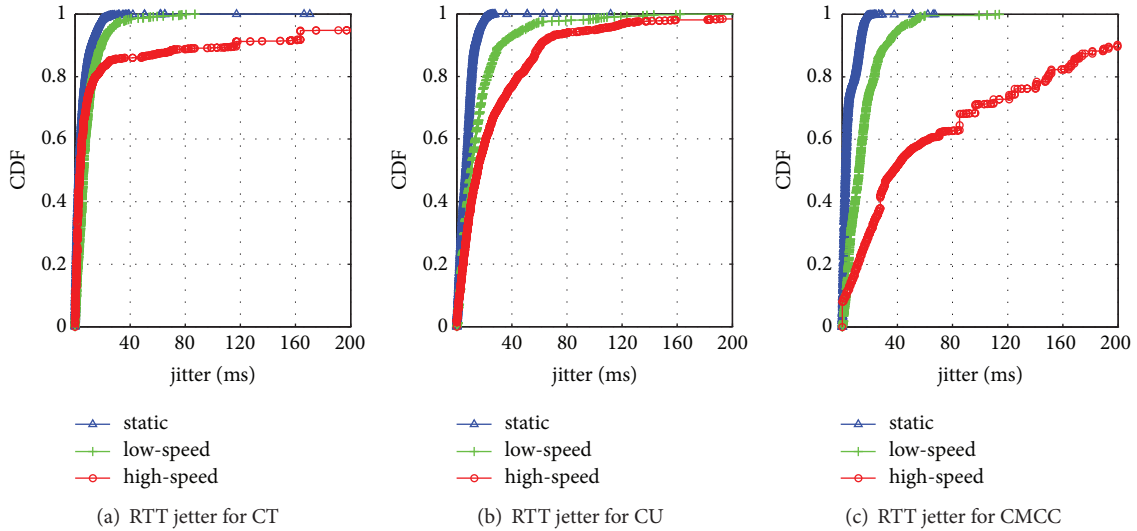


FIGURE 8: RTT jitter CDF in different scenarios.

glance the cost of this idea is very great. However, in such a harsh wireless network environment, due to the wireless link switching, network delay volatility, and packet loss, the TCP protocol designed for reliable wired network is difficult to make full use of the current network resource. In the case of link switching, we find that, in high-speed mobile scenario, the cellular base stations connected by the mobile devices are constantly switching. However, according to the analysis in the previous section, the possibility of the network switching of three vendors is almost no. In terms of network latency, the receiver only receives the first arriving packets.

In other words, this kind of multipath transmission idea can dynamically select the fastest link to transmit. And every choice it makes is absolutely accurate. Moreover, it can reduce the link delay volatility.

$$P_{\text{all}} = 1 - \prod_{i=1}^n P_i \quad (1)$$

In the packet loss, the probability analysis is shown in (1). We can find that the replication link mechanism greatly reduces the packet loss rate. In terms of throughput, the server

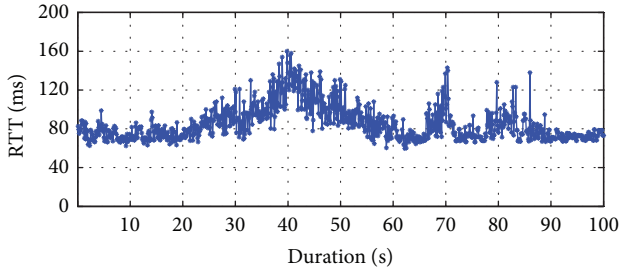


FIGURE 9: Minimum delay.

receives the first arriving packet in any one link. This ensures that, at any given time, throughput is the highest link of the currently available links. In high-speed mobile scenario, the real-time throughput of each link is rapidly fluctuating and the replication link mechanism can select the current optimal link in real-time to ensure the throughput. In addition, multipath transmission in heterogeneous network faces an important issue that is out-of-order packets. According to the design principle of TCP protocol, once the packet is out-of-order, it triggers the retransmission mechanism, which seriously affects the effective throughput of the link. In static scenario, the scholars design a lot of methods to prevent out-of-order packets. However, most of these methods are based on the precise measurement of the link quality based on the system or protocol. These methods, based on the measurement results, make accurate calculations to avoid out-of-order data packets. In high-speed mobile scenario, we find that the quality of the wireless link is very volatile. These methods have difficulty estimating the quality of accurate links and cannot make accurate scheduling decisions. However, the replication link mechanism effectively avoids the problem of out-of-order packet in multipath transmission because the problem of out-of-order packet can be neglected when the packets are transmitted on a single link.

The replication link mechanism is also faced with a lot of problems in design. Among them, removing the duplicate packet is a very important problem [17]. The problem for heterogeneous wireless networks in high-speed mobile scenario is particularly prominent. In the replication link mechanism, the same packets are copied into many copies and send from different links. In these same packets, any packet arrives as a valid packet and the rest of the packets are treated as duplicate packets are discarded. Duplicate ACKs in the packets trigger the congestion control mechanism of TCP, if these duplicate packets send to the receiver. The TCP throughput slows down and the link utilization drops. Therefore, we need to number the packets and remove the duplicate packets. We cannot record all the packet numbers because the computer's storage space is limited. At the same time, how to quickly determine whether a packet has been received is also an important problem. Moreover, in high-speed mobile scenario, the difference of packet sequence number is very large in a short time. Designing a deduplication algorithm in a high-speed mobile scenario faces enormous challenges.

We design a deduplication algorithm for high-speed mobile scenario. This algorithm can be not only deployed

```

(1)  $P_i = \text{AnalyzePacket}()$ 
(2) if  $P_i == 1$  then
(3)    $P_{clear} = 0$ 
(4)    $\text{Buffer.clear}(\text{all})$ 
(5)   return true
(6) end if
(7) if  $P_i < P_{clear}$  then
(8)   return true
(9) end if
(10) if  $\text{Buffer.find}(P_i)$  then
(11)  return true
(12) else
(13)   $\text{Buffer.Add}(P_i)$ 
(14)  if  $\text{Buffer.length}() > \text{MAX}$  then
(15)     $\text{Buffer.clear}(\text{threshold})$ 
(16)  end if
(17)  return false
(18) end if

```

ALGORITHM 1: Deduplication algorithm.

to the replication link mechanism but also used as a fault-tolerant mechanism in other multipath transmission mechanism. The deduplication algorithm is designed as shown in Algorithm 1.

During the execution of the algorithm, the system stores two variables. One is that the last clear packet sequence number records the maximum sequence number of packets cleared each time. The other is a buffer to record the receive packet sequence number. And the received packet sequence number is stored in order and regularly cleaned. The algorithm is used to determine whether the packet is repeated. It indicates that the packet is a duplicate packet if the algorithm returns true. It indicates that the packet is not duplicated if the algorithm returns false. When packets arrive, step 1 analyzes the packet and obtains the packet sequence number. If the packet number is 1, as steps 3 and 4 showed, the algorithm clears the last clear packet sequence number and clears the received packet number buffer. In step 7, when the received packet number is less than the last clear packet number, which means that the same packet has already arrived, the packet is a duplicate packet. And the algorithm returns true. If the received packet number is greater than the last clear packet number, you need to search the received packet number buffer. In step 10, if the packet is found, it indicates that the same packet arrives. The algorithm returns true.

In step 12, if the packet is not found, it means that this packet is the first arrival of the data packet. In this case, the algorithm checks the length of the received packet number buffer. If the length exceeds the maximum length of the buffer. The algorithm clears a part of the buffer and return false. Here, out-of-order packet is a common phenomenon because the network in high-speed mobile scenario is very bad. Therefore, the received packet number buffer cannot be cleared. Otherwise, the out-of-order packets are mistaken for not receiving packets.

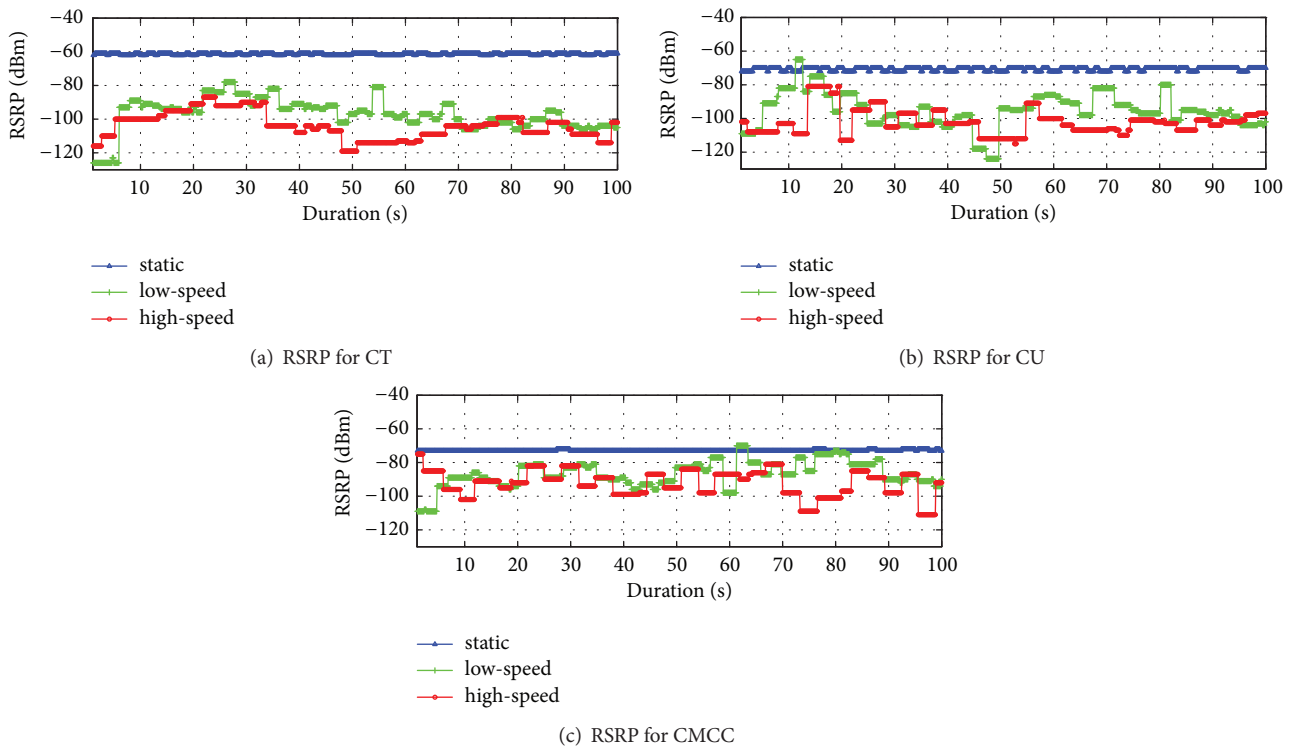


FIGURE 10: RSRP in different scenarios.

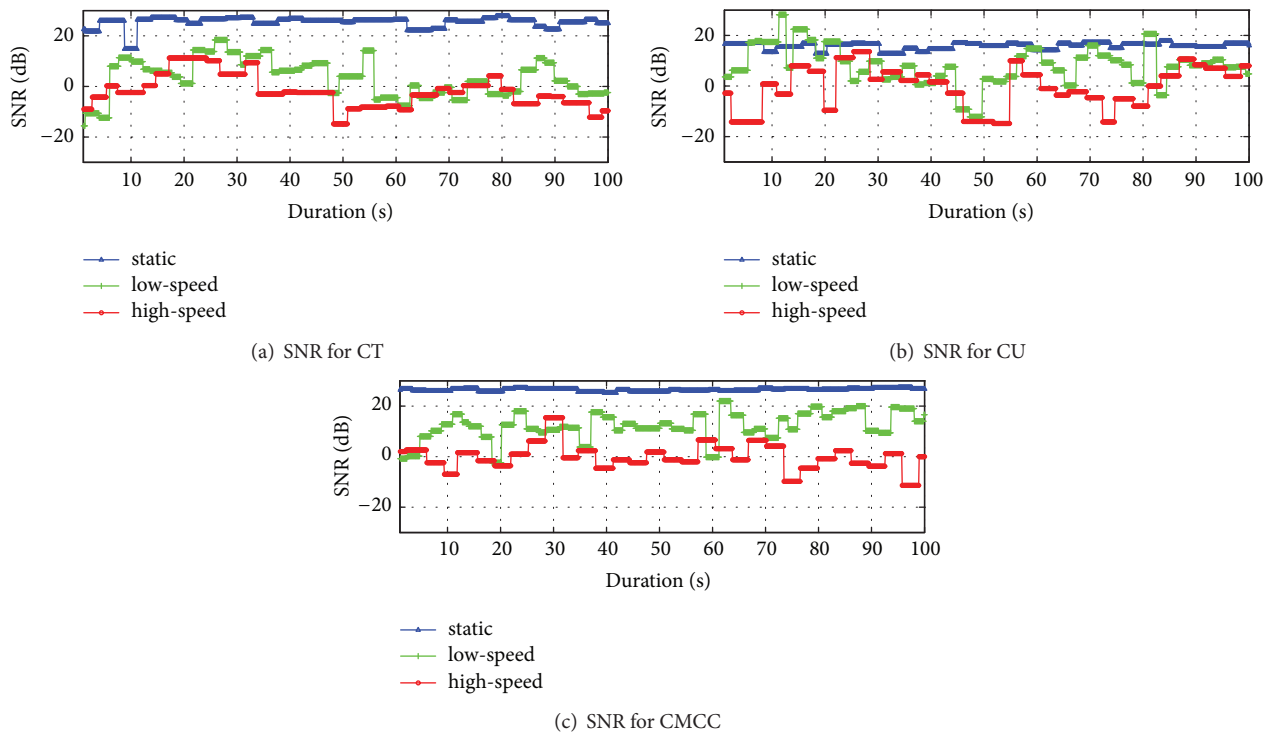


FIGURE 11: SNR in different scenarios.

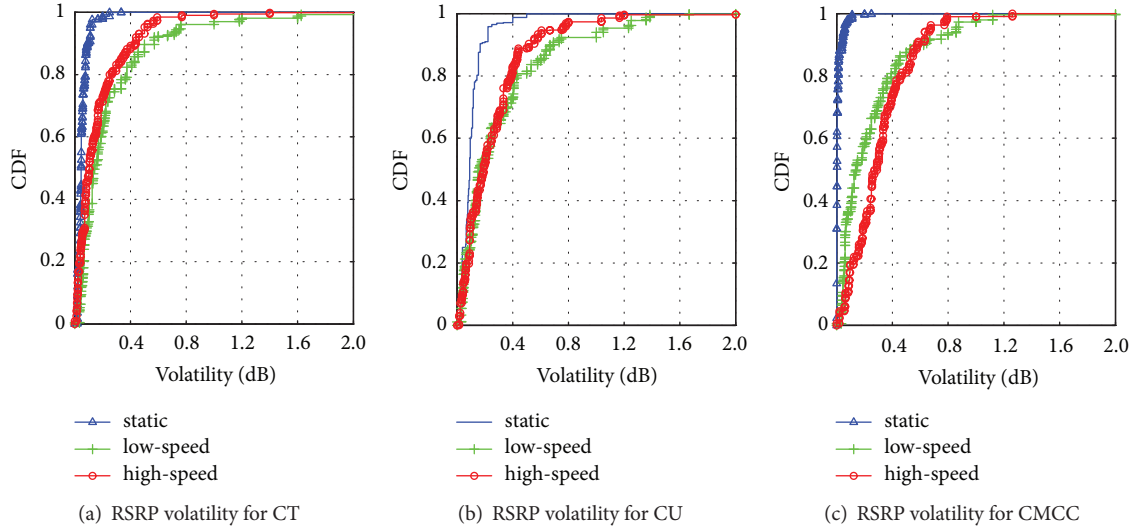


FIGURE 12: RSRP volatility CDF in different scenarios.

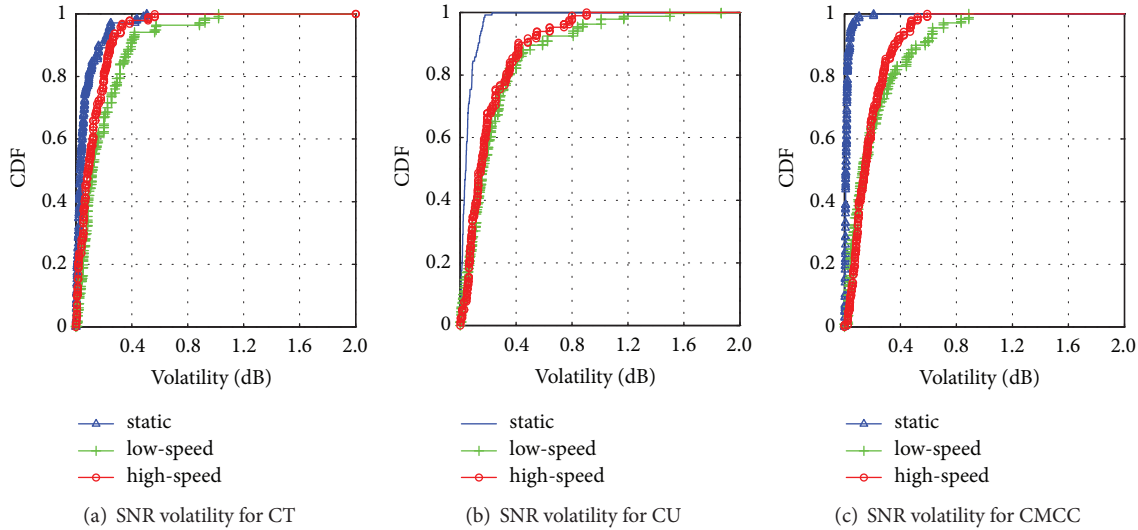


FIGURE 13: SNR volatility CDF in different scenarios.

Figure 16 shows the results of our deployment of the replication link mechanism in high-speed mobile scenario. Compared with Figure 3, we can observe that, in high-speed mobile scenario, the effect of the replication link mechanism is much better than any single wireless network. Compared with Figure 6, we can observe that the replication link mechanism effectively reduces the volatility and packet loss of the network.

6. Conclusion

In this paper, with a lot of actual experimental results, we conduct a comprehensive analysis of heterogeneous wireless networks performance. We design the HNMI to measure different vendors' networks at the same time. We find that, in the high-speed mobile scenario, the single wireless network finds difficulty meeting the needs of accessing the Internet.

The comprehensive use of heterogeneous networks has many advantages. Moreover, we deploy a replication link mechanism in actual high-speed mobile scenario and propose an algorithm to remove the duplicate packet that can also be used in other multipath scheduling algorithms. From the measurement, we find that the replication link mechanism performs better than any single network because it effectively reduces the network volatility and packet loss. In the future, we will continue to explore how to use the heterogeneous networks in the high-speed mobile scenario, to provide users with better network services.

Disclosure

This manuscript was presented in the 5th International Conference on Enterprise Systems 2017 as slides, not a full manuscript.

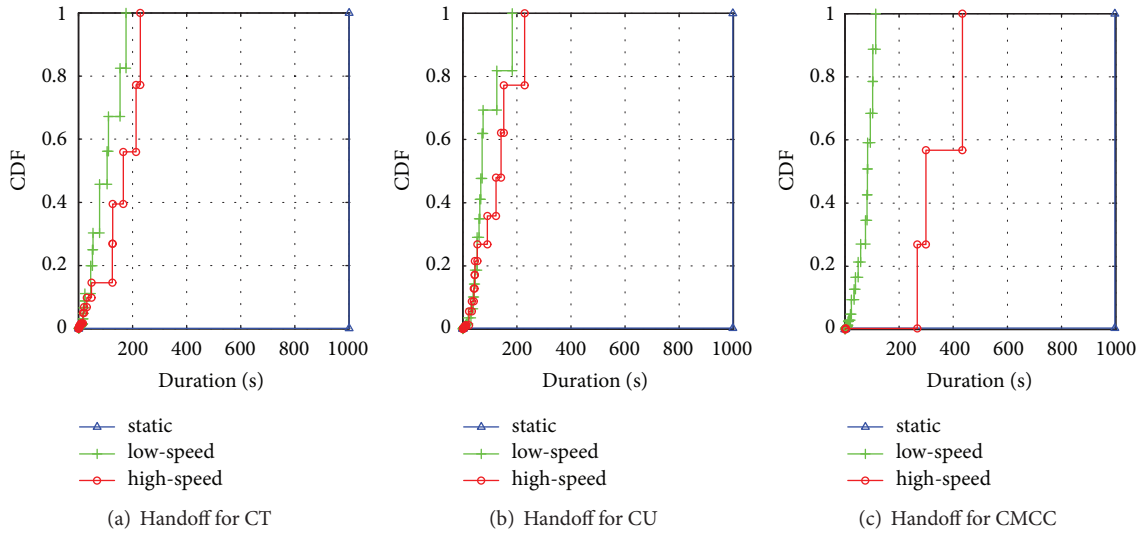


FIGURE 14: Handoff CDF in different scenarios.

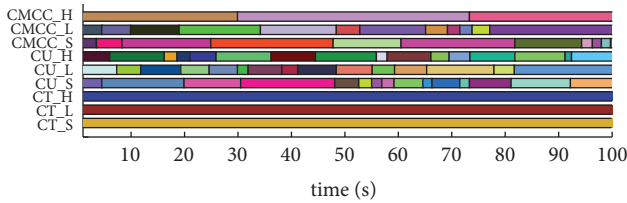


FIGURE 15: SNR in different scenarios.

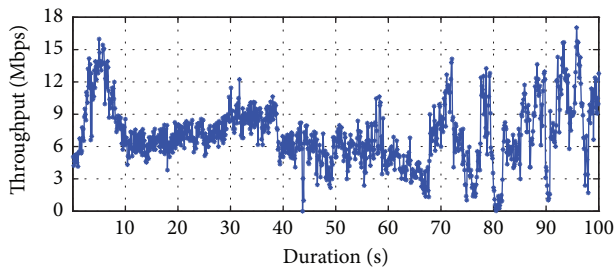


FIGURE 16: Duplicate packet in high-speed mobile scenario.

Conflicts of Interest

The authors declare that there are no conflicts of interest regarding the publication of this paper.

Acknowledgments

This work was supported by the Fundamental Research Funds for the Central Universities (Grant no. 2017JBM018) and the National Basic Research Program of China (973 Program, under Grant no. 2013CB329101).

References

[1] H. Zhang, P. Dong, S. Yu, and J. Song, “A scalable and smart hierarchical wireless communication architecture based

on network/user separation,” *IEEE Wireless Communications Magazine*, vol. 24, no. 1, pp. 18–24, 2017.

[2] L. Li, K. Xu, D. Wang et al., “A Longitudinal Measurement Study of TCP Performance and Behavior in 3G/4G Networks over High Speed Rails,” *IEEE/ACM Transactions on Networking*, vol. 25, no. 4, pp. 2195–2208, 2017.

[3] P. Dong, T. Zheng, S. Yu, H. Zhang, and X. Yan, “Enhancing Vehicular Communication Using 5G-Enabled Smart Collaborative Networking,” *IEEE Wireless Communications Magazine*, vol. 24, no. 6, pp. 72–79, 2017.

[4] P. Dong, B. Song, H. Zhang, and X. Du, “Improving Onboard Internet Services for High-Speed Vehicles by Multipath Transmission in Heterogeneous Wireless Networks,” *IEEE Transactions on Vehicular Technology*, vol. 65, no. 12, pp. 9493–9507, 2016.

[5] W. L. Tan, F. Lam, and W. C. Lau, “An Empirical Study on 3G Network Capacity and Performance,” in *Proceedings of the IEEE INFOCOM 2007 - 26th IEEE International Conference on Computer Communications*, pp. 1514–1522, Anchorage, AK, USA, May 2007.

[6] F. P. Tso, J. Teng, W. Jia, and D. Xuan, “Mobility: A double-edged sword for HSPA networks: A large-scale test on Hong Kong Mobile HSPA networks,” in *Proceedings of the 11th ACM International Symposium on Mobile Ad Hoc Networking and Computing, MobiHoc 2010*, pp. 81–90, usa, September 2010.

[7] P. Rodriguez, R. Chakravorty, J. Chesterfield, I. Pratt, and S. Banerjee, “MAR,” in *Proceedings of the the 2nd international conference*, p. 217, Boston, MA, USA, June 2004.

[8] J. Rodriguez-Pineiro, P. Suarez-Casal, M. Lerch et al., “LTE downlink performance in high speed trains,” in *Proceedings of the 81st IEEE Vehicular Technology Conference, VTC Spring 2015*, gbr, May 2015.

[9] G. Tingting and S. Bin, “A high-speed railway mobile communication system based on LTE,” in *Proceedings of the 2010 International Conference on Electronics and Information Engineering (ICEIE 2010)*, pp. V1-414–V1-417, Kyoto, Japan, August 2010.

[10] M.-S. Pan, T.-M. Lin, and W.-T. Chen, “An enhanced handover scheme for mobile relays in LTE-A high-speed rail networks,” *IEEE Transactions on Vehicular Technology*, vol. 64, no. 2, pp. 743–756, 2015.

- [11] L. M. Surhone, M. T. Tennoe, S. F. Henssonow, and P. Theorem, *Iperf*, Betascript Publishing, 2010.
- [12] M. Li, A. Lukyanenko, Z. Ou et al., "Multipath Transmission for the Internet: A Survey," *IEEE Communications Surveys & Tutorials*, vol. 18, no. 4, pp. 2887–2925, 2016.
- [13] X. Yan, P. Dong, T. Zheng, and H. Zhang, "Fuzzy and utility based network selection for heterogeneous networks in high-speed railway," *Wireless Communications Mobile Computing*, vol. 2017, no. 4, p. 14, 2017.
- [14] K. Jang, M. Han, S. Cho et al., "3G and 3.5G wireless network performance measured from moving cars and high-speed trains," in *Proceedings of the the 1st ACM workshop*, p. 19, Beijing, China, September 2009.
- [15] F. J. Martin-Vega, I. M. Delgado-Luque, F. Blaquez-Casado, G. Gomez, M. C. Aguayo-Torres, and J. T. Entrambasaguas, "LTE Performance over High Speed Railway Channel," in *Proceedings of the 2013 IEEE 78th Vehicular Technology Conference (VTC Fall)*, pp. 1–5, Las Vegas, NV, USA, September 2013.
- [16] J. Huang, F. Qian, A. Gerber, Z. M. Mao, S. Sen, and O. Spatscheck, "A close examination of performance and power characteristics of 4G LTE networks," in *Proceedings of the 10th International Conference on Mobile Systems, Applications, and Services (MobiSys '12)*, pp. 225–238, ACM, June 2012.
- [17] L. Li, K. Xu, D. Wang, C. Peng, Q. Xiao, and R. Mijumbi, "A measurement study on TCP behaviors in HSPA+ networks on high-speed rails," in *Proceedings of the 34th IEEE Annual Conference on Computer Communications and Networks, IEEE INFOCOM 2015*, pp. 2731–2739, Hong Kong, China, May 2015.
- [18] Q. Xiao, K. Xu, D. Wang, L. Li, and Y. Zhong, "TCP Performance over Mobile Networks in High-Speed Mobility Scenarios," in *Proceedings of the 2014 IEEE 22nd International Conference on Network Protocols (ICNP)*, pp. 281–286, October 2014.
- [19] Q. Liu, K. Xu, H. Wang, M. Shen, L. Li, and Q. Xiao, "Measurement, Modeling, and Analysis of TCP in High-Speed Mobility Scenarios," in *Proceedings of the 2016 IEEE 36th International Conference on Distributed Computing Systems (ICDCS)*, pp. 629–638, Nara, Japan, June 2016.
- [20] S. Paul, "'Real-time transport protocol (rtp)," RFC1889, 1998.

Research Article

An Efficient Traffic Congestion Monitoring System on Internet of Vehicles

Duc-Binh Nguyen , Chyi-Ren Dow , and Shioh-Fen Hwang

Department of Information Engineering and Computer Science, Feng Chia University, Taichung, Taiwan

Correspondence should be addressed to Chyi-Ren Dow; crdow@mail.fcu.edu.tw

Received 4 December 2017; Revised 4 March 2018; Accepted 2 April 2018; Published 20 May 2018

Academic Editor: Li Zhu

Copyright © 2018 Duc-Binh Nguyen et al. This is an open access article distributed under the Creative Commons Attribution License, which permits unrestricted use, distribution, and reproduction in any medium, provided the original work is properly cited.

Existing intelligent transport systems (ITS) do not fully consider and resolve accuracy, instantaneity, and compatibility challenges while resolving traffic congestion in Internet of Vehicles (IoV) environments. This paper proposes a traffic congestion monitoring system, which includes data collection, segmented structure establishment, traffic-flow modelling, local segment traffic congestion prediction, and origin-destination traffic congestion service for drivers. Macroscopic model-based traffic-flow factors were formalized on the basis of the analysis results. Fuzzy rules-based local segment traffic congestion prediction was performed to determine the traffic congestion state. To enhance prediction efficiency, this paper presents a verification process for minimizing false predictions which is based on the Rankine-Hugoniot condition and an origin-destination traffic congestion service is also provided. To verify the feasibility of the proposed system, a prototype was implemented. The experimental results demonstrate that the proposed scheme can effectively monitor traffic congestion in terms of accuracy and system response time.

1. Introduction

Over the last few decades, traffic congestion has become a serious problem in cities, which not only negatively affects the daily lives of humans but also impedes stable economic and societal development. Traffic congestion increases air pollution, travel time, and economic losses. Governments increasingly strive to monitor and resolve traffic congestion, but the task is difficult because of the complexity of the problem; specifically, traffic congestion is difficult to predict. The complexity of traffic congestion is also reflected in its dynamic and interrelated characteristics. Traffic congestion can propagate from a congested road segment to neighboring road segments. Because of these complexities, fully automatic analysis of traffic congestion is difficult to achieve.

Currently, two major challenges must be addressed to facilitate traffic congestion estimation and monitoring. The first challenge is formalizing the basic factors for estimating and forecasting traffic congestion on a large-scale road network. Several researchers have proposed solutions to resolve the problem, which can be grouped into two approaches,

namely, traffic congestion forecasting based on infrastructure equipment and traffic congestion forecasting based on Vehicular Ad Hoc Network (VANET) technology. The first approach [1] mainly uses floating car data, namely, data from Global Positioning System- (GPS-) equipped vehicles. Some protocols use data from sensor equipment with the limitation, including loop detectors, video recording devices, and infrared technologies. Although the infrastructure-based approach is the most widespread and features high reliability and accurate formalization, it lacks flexibility. The second approach [2] utilizes vehicle-to-vehicle (V2V) technologies to gather vehicles' traffic data and then formalizes the traffic model characteristics, including speed, density, flow, and travel time. Based on the formalized information, researchers have adopted mathematical prediction algorithms to estimate traffic congestion levels. The advantage to this approach is that it can be implemented without deploying infrastructure sensors and has been demonstrated to operate effectively in various traffic and deployment scenarios. However, the approach is limited by network communication obstacles, including delayed and inaccurate traffic estimates [3], redundant data, bandwidth problems [4], and reliability problems

[5]. These problems may cause insufficient precision or even failure in traffic congestion prediction.

The second challenge is to guarantee the accuracy, instantaneity, and reliability of traffic congestion prediction. Existing systems do not fully address and resolve this challenge. The VANET-based approach involves considerable propagation delays and low reliability, whereas the infrastructure-based approach generally uses GPS data and data from limited number of sensors that lack flexibility. Furthermore, most applications of the infrastructure-equipped approach use HTTP-based protocols for gathering and transferring data between a central computing unit and vehicles and equipment. This not only hinders integration with various types of sensor equipment but may also cause a serious overhead problem if the vehicle number increases markedly in a traffic congestion situation or if the amount of data transferred over a long period of time increases substantially. In contrast, because of the complexities of traffic congestion problems, these systems' mechanisms simply classify traffic congestion levels by analyzing the traffic information on the basis of their own rules without verifying the real-time traffic conditions. This may result in false prediction [6].

Considering the aforementioned problems, this paper proposes a traffic congestion monitoring system using real traffic data based on Message Queue Telemetry Transport (MQTT) for investigating traffic congestion patterns; the proposed system has the advantages of both an infrastructure-based approach and MQTT techniques: the flexibility to support the integration of various types of sensors for traffic-flow observation in low-bandwidth and high-latency vehicular network environments of MQTT and the high reliability and accurate traffic-flow formalization of an infrastructure-based approach. This research also adopted a fuzzy rule-based method to address complex nondeterministic problems such as traffic congestion determination. Furthermore, the proposed system is designed as a distributed system to eliminate computational bottlenecks and to avoid overhead problems, which is especially suitable for traffic congestion situations in which numerous communications are required due to the markedly increased number of vehicles. First, the authors formalized vehicle detector (VD) data provided by Taiwan's government according to a macroscopic traffic-flow model. To provide a road segment-based traffic congestion monitoring service, the geographic map was converted to a segmented structure. Subsequently, the authors established a publish/subscribe platform using the MQTT protocol. Then, the authors defined the traffic congestion monitoring method and designed a mechanism that uses the segmented structure to predict local traffic congestion. The authors also designed and developed a real-time origin-destination traffic congestion service by using MQTT's publish/subscribe feature. Finally, to verify the proposed system's feasibility, the authors implemented a system prototype for both the control center and vehicles to evaluate user interfaces and communications and the system's performance.

The remainder of this paper is organized as follows. Section 2 briefly describes the current relevant research and technology. Section 3 discusses the proposed traffic congestion monitoring method in detail. Section 4 details

the implementation prototype. In Section 5, the experimental results are demonstrated. Finally, Section 6 presents conclusions and future research directions.

2. Related Work

The Internet of Things (IoT) era has opened up as an emerging research trend over recent years. The IoT has originated from the needs of better monitoring, control, and management in various areas, such as healthcare, education, entertainment, energy manager [7], and transportation [8]. The IoV plays as a part of the IoT, but it has distinctive characteristics. In the IoV, the mobility of vehicles is an important topic that needs to be paid attention. The IoV involves the way to gather information regarding sensors [9] on vehicles, roads, and their surroundings onto mobility platforms with the integration of the Internet. Based on collected information, IoV systems can effectively support vehicles by providing numerous services, including entertaining, guiding, surveillance, and protecting from unattended collision. IoV technologies aim to use in intelligent transportation systems (ITS) which deliver intelligent traffic applications as the typical IoT applications in mobility environment. In recent years, the IoV is proposed to provide more convenient services. Yang et al. [10] proposed an abstract IoV network model, which considers various connections of vehicles, roads, environments, and pedestrians. Fu et al. [11] present an effective way to solve the parking problem based on the reservation optimization parking recommendation model in the IoV environment. The model adopts a phased approach to actively recommend to drivers by means of interacting with the considering of evaluation indicators.

With the development trend of the IoV, a huge number of sensors and vehicles tend to continuously connect to the Internet which may constitute the network bandwidth challenge. Due to this reason, it is necessary to develop suitable lightweight protocols for using in IoT/IoV environments. MQTT is one of the best developed candidates for this purpose. MQTT uses publish/subscribe model to get the polling information, and thus it can eliminate unnecessary communications that helps to save the energy consumption and lowers the delay for communication in vehicle environment compared to HTTP. Yokotani and Sasaki [12] proved that the MQTT protocol is more scalable and reliable for applications, which requires very high data transmission frequency as in IoV environments. In a deeper research, Del Campo et al. [13] presented an integrated different-degrees MQTT protocol architecture, which has an ability of effective and reliable distribution of notification messages among different actors. The proposed architecture has been adopted for the home monitoring of patients with dementia. Szabó and Farkas [14] presented a design for smart city application using MQTT publish/subscribe model for communication functions. The design aims to apply to crowd-sourcing based smart applications, such as smart travel planner or smart parking in the cities.

Traffic congestion deals with negative impacts to people's lives. Numerous research studies have highlighted the effect of traffic congestion, such as decreasing productivity and

TABLE 1: Historical VD Data Fields.

Device ID	Longitude, latitude	Date time	Lane order	Vehicle volume	Average speed	Max speed	Travel direction
-----------	---------------------	-----------	------------	----------------	---------------	-----------	------------------

TABLE 2: Real-time vehicle's data fields.

Vehicle ID	Destination	Longitude, latitude	Date time	Speed
------------	-------------	---------------------	-----------	-------

worsening pollution and increasing the transportation cost [15]. The traffic congestion effect can be seen in any country no matter it is a developing country or developed country. Traffic congestion is classified into two categories [16]: recurrent and nonrecurrent. Recurrent traffic congestion is a frequent basis type caused by various factors such as dramatic increases of traffic flow during peak hour [17] or repeated on-ramp and off-ramp road network [18]. Nonrecurrent congestion is an irregular type, which may happen due to road network disruptions such as road accidents and natural disaster [19]. To tackle with the traffic congestion problems, various scenarios have been proposed, which depended on various traffic flow detection techniques. Gholve and Chougule [20] proposed a wireless sensor network-based traffic congestion detection system for highways, which has developed a protocol to guarantee the communication between sensor nodes and was prototyped on an Arduino embedded device. The proposed system used magnetic sensors for vehicle detection through proper signal conditioning and use of data processing. Bhoraskar et al. [21] adopted probe vehicle-based techniques in cooperation with using of nonintrusive method to detect traffic congestion in Mumbai's road network. The proposed system archived promising results in using smart phones sensors for traffic congestion detection.

3. Traffic Congestion Monitoring Scheme

In this section, the authors present the proposed traffic congestion monitoring scheme, particularly VD data collection, traffic-flow modelling, segmented structure establishment, publish/subscribe mechanism according to time and location, local segment traffic congestion prediction, and the origin-destination traffic congestion service for drivers.

3.1. Data Collection. Real data collection and analysis are vital requirements for forming a realistic system. In this subsection, the authors describe the collection of VD data and real-time vehicular data. The collected data are used to formalize fundamental factors according to macroscopic traffic-flow models, establish a segmented structure, and predict traffic congestion.

3.1.1. Vehicle Detector Data Collection. In this study, the authors used VD data to determine traffic conditions. VD data analysis was performed to formalize the fundamental factors according to the macroscopic traffic-flow model that and used to extract information about the distribution of traffic flows. Furthermore, at the beginning of system development, more than 184 million historical VD records concerning traffic on the main roads of Taichung City,

Taiwan, were sorted in ascending order of the recorded time. Table 1 illustrates the data fields.

The device ID is a number unique to each VD device used to identify which device is recording. Longitude and latitude field indicates the location of the VD device. Longitude and latitude are also used to identify the road segment. For roads with more than one lane, lane order is the order number of the lane for which the traffic information has been obtained, and each record represents one lane of the road segment. The date-time field is used to store the time stamp of the recorded traffic event. Historical VD records represent traffic events and were obtained at 5-minute intervals. The vehicle volume field indicates the number of vehicles occupying the current lane of the road segment. The average speed field indicates the average speed of vehicles, which was measured using the VD devices. Speed limit is used to define the maximum allowable speed of the road lane. Travel direction is used to determine lanes whose travel direction is the same.

3.1.2. Real-Time Vehicular Data Collection. The insufficiency of just-in-time information is a major cause of traffic congestion. In this study, to manage traffic congestion problems, real-time movement-related vehicular data are focused. In this system, the authors presume that vehicles play two roles. The first role, vehicles act as normal users that can subscribe to published topics to receive traffic congestion information using the MQTT model. In fact, each vehicle has a distinct origin-destination route. Thus, the proposed system provides vehicles the initiative in their origin-destination traffic congestion information. To handle origin-destination traffic congestion matter, each vehicle maintains a status table as shown in Table 2.

The vehicular ID is the unique vehicle registration plate number. The destination indicates the desired destination of predefined route. Longitude and latitude are used to identify the current road segment where the vehicle is located. The date-time field is used to determine the time when the record was recorded. The speed is the vehicle's current speed, which, in combination with vehicle location, is used for origin-destination traffic congestion service.

A vehicle acts the second role when the vehicle is selected as the header of a segment with a high possibility of congestion to publish information to MQTT topics. Each header is assigned to estimate traffic-flow and predict local traffic within its road segment. This design intends to eliminate communication redundancy and computational bottlenecks. Consequently, the overall performance and computational ability of the system should be improved. In the proposed system, the header vehicles and sensors possess a predefined identification number that helps the control center



FIGURE 1: VD based segmentation.

determine them in advance. Then, the control center can collect the header vehicles' data following the topic structure $\langle \text{DataCollection}/\text{SourceID} \rangle$.

3.2. Segmented Structure. In fact, each segment of a road network exhibits different traffic-flow levels, and traffic congestion usually occurs in high-traffic-flow road segments. Traffic congestion starts at a specified road segment when the vehicle number reaches the capacity of the road segment. Thereafter, traffic congestion may propagate from a congested road segment to neighboring road segments. Because of this characteristic, the authors used historical VD data to investigate road network traffic-flow levels, which benefits local traffic congestion prediction. First, the authors used longitude and latitude information to locate VD devices on a geographical map as shown in Figure 1(a). Each VD device is denoted by a red legend as the location symbol. Based on the recommendation of Taiwan's government and to avoid redundant data in traffic observation, as well as wasted deployment and maintenance costs, a VD device should be recommended to be placed at a suitable location to guarantee that each VD device observes traffic flows on its own predefined road.

Subsequently, the authors divided the geographical map into segments as shown in Figure 1(b). The authors assumed that N is the number of VD devices on a road; then, VD devices were ordered from 1 to N following the numbering rule of the road. Thus, the number of segments on each road depends on the number of VD devices. The determination of each segment of the road follows three rules. First, the first segment can be determined using the following:

$$\begin{aligned} \text{start}_{\text{pos}(\text{VD}_1)} &= (x_{R_0}, y_{R_0}) \\ \text{end}_{\text{pos}(\text{VD}_1)} &= \left\{ (x_{R_1}, y_{R_1}) \mid \text{dist}(x_1, y_1, x_{R_1}, y_{R_1}) \right. \\ &= \left. \text{dist}(x_{R_1}, y_{R_1}, x_2, y_2) \right\}, \end{aligned} \quad (1)$$

where (x_{R_0}, y_{R_0}) denotes the latitude and longitude coordinates of the start point of the road and (x_1, y_1) and (x_2, y_2) denote the latitude and longitude coordinates of VD_1 and VD_2 , respectively.

Second, the last segment can be determined using the following:

$$\begin{aligned} \text{start}_{\text{pos}(\text{VD}_N)} &= \left\{ (x_{R_{N-1}}, y_{R_{N-1}}) \mid \text{dist}(x_{N-1}, y_{N-1}, x_{R_{N-1}}, y_{R_{N-1}}) \right. \\ &= \left. \text{dist}(x_{R_{N-1}}, y_{R_{N-1}}, x_N, y_N) \right\} \\ \text{end}_{\text{pos}(\text{VD}_N)} &= (x_{R_N}, y_{R_N}), \end{aligned} \quad (2)$$

where (x_{R_N}, y_{R_N}) denotes the latitude and longitude coordinates of the last point of the road and (x_{N-1}, y_{N-1}) and (x_N, y_N) denotes the latitude and longitude coordinates of VD_{N-1} and VD_N , respectively. The last rule is used to determine VD_i segments, where $1 < i < N$ defines so-called normal segments. In the proposed system, a segment i where a VD_i device is located can be calculated using the latitude and longitude of the VD_i device and two neighboring VD devices. The formulas for segment determination can be expressed as follows:

$$\begin{aligned} \text{start}_{\text{pos}(\text{VD}_i)} &= \left\{ (x_{R_{i-1}}, y_{R_{i-1}}) \mid \text{dist}(x_{i-1}, y_{i-1}, x_{R_{i-1}}, y_{R_{i-1}}) \right. \\ &= \left. \text{dist}(x_{R_{i-1}}, y_{R_{i-1}}, x_i, y_i) \right\} \\ \text{end}_{\text{pos}(\text{VD}_i)} &= \left\{ (x_{R_i}, y_{R_i}) \mid \text{dist}(x_i, y_i, x_{R_i}, y_{R_i}) \right. \\ &= \left. \text{dist}(x_{R_i}, y_{R_i}, x_{i+1}, y_{i+1}) \right\}, \end{aligned} \quad (3)$$

where (x_i, y_i) denotes the latitude and longitude coordinates of current VD device ordered as VD_i and (x_{i-1}, y_{i-1}) and (x_{i+1}, y_{i+1}) denote the latitude and longitude coordinates of two neighboring VD devices ordered as VD_{i-1} and VD_{i+1} .

Finally, both the control center and vehicles can use MQTT publish/subscribe to exchange traffic congestion information in the model based on a segmented structure.

3.3. Traffic Flow Modelling. Traffic congestion problem management requires an explicit understanding of how traffic flow operates. Thus, many traffic-flow theories have been

investigated over the last 60 years, and three types of traffic-flow models predominate, namely, microscopic, mesoscopic, and macroscopic [22]. Macroscopic models adopt a viewpoint of vehicular flow that is suited to large-scale network applications. Macroscopic models analyze three fundamental factors: velocity v (km/h), density d (vehicles/km), and flow f (vehicles/h). Velocity $v = v(x, t)$ denotes the average velocity of vehicles on road segment x at time t . Density $d = d(x, t)$ denotes the number of vehicles on road segment x at time t . Flow $f = f(x, t)$ denotes the number of vehicles passing road segment x at time t . The relationship between flow, density, and velocity can be expressed as follows:

$$f = dv \quad (4)$$

For traffic flow factor calculation in this study, the authors used the real-time VD data that are shown in Table 1.

The first factor of traffic flow, the velocity of a segment can be calculated as expressed in the following:

$$v = \frac{\sum_{k=1}^m \text{Velocity}_{\text{avglane}k}}{m}, \quad (5)$$

where v denotes the average velocity of the segment, $\text{Velocity}_{\text{avglane}k}$ is the average velocity in lane k , and m is the number of lanes with the same travel direction. Subsequently, the vehicle density is calculated as the number of vehicles per kilometer, which is expressed in the following:

$$d = \frac{\sum_{k=1}^m \text{Vehicle}_{\text{volumelane}k}}{l}. \quad (6)$$

The last factor, the flow reflects the number of vehicles passing through a road segment. On the basis of the relationship

between density, velocity, and flow, as expressed in (4), the flow is calculated as shown in the following:

$$f = \sum_{k=1}^m \text{Velocity}_{\text{avglane}k} * \left(\frac{\text{Vehicle}_{\text{volumelane}k}}{l} \right). \quad (7)$$

3.4. Local Segment Traffic Congestion Prediction. In this section, the authors provide a solution for local traffic congestion or road segment-based traffic congestion. First, the authors analyzed historical VD data to construct an observation table, which is used to identify road segments at a high risk of traffic congestion during specific hours of the day and on specific days of the week. Then, the authors evaluated the current traffic congestion situation of these road segments by using a fuzzy rule-based method on the basis of velocity and density. Finally, the authors performed a verification process, which involved using the remaining flow factors of these road segments and their neighboring road segments.

3.4.1. Traffic Congestion Observation Table. To identify road segments at a high risk of traffic congestion and provide a global view of traffic transition, the authors used historical VD data for traffic analysis to build a traffic congestion observation table. In the past, density and velocity characteristics were used in a simple combination of their value range to determine the traffic congestion condition. For example, traffic congestion is identified in a road, which has a high vehicle density and a low velocity value. However, this strategy has limitations attributable to range value classification, because the range values of density and velocity vary greatly from road to road. This may cause inaccurate estimation and failure in traffic congestion prediction. Because of this problem, the authors propose the traffic congestion coefficient (TCC) concept, which represents the possibility of a traffic congestion condition existing on a large-scale road network. The TCC is calculated as shown in the following:

$$\begin{aligned} \text{TCC} &= \frac{I_d}{I_v} \\ \text{IND} &= \frac{d}{D_{\max}} \\ \text{INV} &= \begin{cases} \frac{v}{V_{\max}}, & \text{if all lanes have the same } V_{\max} \\ \frac{\sum_{k=1}^m (\text{Velocity}_{\text{avglane}k} / V_{\text{Maxlane}k})}{m}, & \text{if each lane have a different } V_{\max}, \end{cases} \end{aligned} \quad (8)$$

where

- I_d is the density performance index;
- I_v is the velocity performance index;
- d is the average density of the road segment;
- v is the average velocity of the road segment;

V_{\max} is the maximum limitation velocity of road segment;

D_{\max} is the maximum recorded density in the road segment;

$\text{Velocity}_{\text{avglane}k}$ is the average velocity of lane k in the road segment;

TABLE 3: Traffic congestion observation table.

Day of week	Time interval	Segment ID	Location	Congestion coefficient value
Sat.	(17-18)	V069320	(24.145285, 120.632205)	1.25
Sat.	(17-18)	V029500	(24.17083, 120.685352)	0.8

$V_{\text{Maxlane}k}$ is the maximum limitation velocity of lane k in the road segment;

l is the road segment length;

m is the number of lanes which have the same travel direction.

Because VD data records are extremely numerous, the records should be effectively analyzed to derive useful information. Thus, the authors divided historical VD records into seven sets, one for each day of the week, and then divided each set into 24 subsets, one for each hour of the day. Once the historical VD data records had been classified, the congestion coefficient value of segments in each set was calculated. The following assumptions are defined to explain the calculation efficiently:

1. $W = \{\text{Mon}, \text{Tue}, \text{Wed}, \text{Thu}, \text{Fri}, \text{Sat}, \text{Sun}\}$ indicates the day of the week of investigation.
2. $TI = \{(0-1), (1-2), \dots, (23-24)\}$ indicates the time interval of investigation.
3. $TD = \{td_0, td_1\}$ indicates the travel direction.
4. $R_{ij} = \{r_1, r_2, \dots, r_u\}$ indicates a set of historical VD records on day of the week $i \in W$ and in time slot $j \in TI$.
5. $RID = \{rid_1, rid_2, \dots, rid_n\}$ indicates the set of road segment IDs.
6. $TCC_{ij}^{rid(td)}$ indicates the TCC of travel direction td of road segment rid on day of the week $i \in W$ and in time slot $j \in T$.
7. $IND_{ij}^{rid(td)}$ indicates the density performance index of travel direction td of road segment rid on day of the week $i \in W$ and in time slot $j \in T$.
8. $INV_{ij}^{rid(td)}$ indicates the velocity performance index of travel direction td of road segment rid on day of the week $i \in W$ and in time slot $j \in T$.
9. $D_{max}^{rid(td)}$ indicates the maximum recorded density of road segment rid .
10. $N_{ij}^{rid(td)}$ indicates the number of historical TCCs of road segment rid on day of the week $i \in W$ and in time slot $j \in T$.

The following TCC calculation algorithm should be executed at the end of the day of the week i and time slot j as shown in Algorithm 1.

1. (Lines (1)–(4)) First, $IND_{ij}^{rid(td)}$, $INV_{ij}^{rid(td)}$, $D_{ij}^{rid(td)}$, and $counter^{rid(td)}$ variables, which are used for TCC calculation for each road segment on day of the week i

and in time slot j are initialized. $IND_{ij}^{rid(td)}$ represents the density performance index value; $INV_{ij}^{rid(td)}$ represents the velocity performance index value; $D_{ij}^{rid(td)}$ represents the density value; $counter^{rid(td)}$ denotes the number of records for each day of the week i and time slot j . At the beginning, variable values are assigned as zero or NULL.

2. (Lines (5)–(11)) Second, each historical VD data record is investigated to extract the speed and volume information of vehicles. The information is classified by road segment. The calculation results are temporarily expressed as the $INV_{ij}^{rid(td)}$ and $D_{ij}^{rid(td)}$ variables of each road segment.
3. (Lines (12)–(15)) Third, the previous values of TCC, number of TCC calculation, and max density are read for TCC calculation.
4. (Lines (16)–(19)) To improve the accuracy of density performance index calculation, the estimated density value of the current session is evaluated by comparing it with the maximum density. If the current density value is greater than the maximum density value, the maximum density value is updated as the current density value.
5. (Lines (20)–(22)) Subsequently, the TCC of each road segment in time slot j and day of the week i is calculated on the basis of (8), (12), and (13), which considers both current session data and previous session data.
6. (Lines (23)–(26)) Finally, the calculated TCC value and the number of TCC calculation session of each road segment are stored in the database for the next TCC calculation session.

The calculation results are maintained as tables in the control center; each table corresponds to a set of historical VD data as illustrated in Table 3. Furthermore, to quantify the TCC values, the authors define two types of road segments on the basis of their correlated range of TCC values: first, a road segment with a high possibility of traffic congestion has a TCC value greater than 1; second, a road segment with a low possibility of traffic congestion has a TCC value equal to or lower than 1. The first type has a high possibility of traffic congestion, whereas the second type is almost traffic congestion free. If a road segment's TCC value equals 1, its density and velocity correlate sufficiently to guarantee stable traffic conditions on the road.

3.4.2. Fuzzy-Based Traffic Congestion Evaluation. Fuzzy rules-based methods are a particularly suitable solution for

TCC Calculation Algorithm

- (1) $IND_{ij}^{rid(td)} = 0$
- (2) $INV_{ij}^{rid(td)} = 0$
- (3) $D_{ij}^{rid(td)} = 0$
- (4) $counter^{rid(td)} = 0$
- (5) **For each** $r_k \in R_{ij}$ **do**
- (6) **If** $r_k.device_id = rid_p$ and $r_k.travel_direction = td_q$ **then**
- (7) $INV_{ij}^{rid_p(td_q)} = INV_{ij}^{rid_p(td_q)} + \frac{r_k.V_{avg}}{r_k.V_{Max}}$
- (8) $D_{ij}^{rid_p(td_q)} = D_{ij}^{rid_p(td_q)} + \frac{r_k.Vehicle_volume}{Length(rid_p)}$
- (9) $counter^{rid_p(td_q)} = counter^{rid_p(td_q)} + 1$
- (10) **End if**
- (11) **End for**
- (12) **For each** traveling direction $td_q \in TD$ of $rid_p \in RID$ **do**
- (13) Read ($TCC_{ij}^{rid_p(td_q)}$)
- (14) Read ($N_{ij}^{rid_p(td_q)}$)
- (15) Read ($D_{ijMax}^{rid_p(td_q)}$)
- (16) **If** $(D_{ij}^{rid_p(td_q)} * rid_p.number_of_lanes) / counter^{rid_p(td_q)} > D_{ijMax}^{rid_p(td_q)}$ **then**
- (17) $D_{ijMax}^{rid_p(td_q)} \leftarrow \frac{D_{ij}^{rid_p(td_q)} * rid_p.number_of_lanes}{counter^{rid_p(td_q)}}$
- (18) Write ($D_{ijMax}^{rid_p(td_q)}$)
- (19) **End if**
- (20) $INV_{ij}^{rid_p(td_q)} = \frac{INV_{ij}^{rid_p(td_q)}}{counter^{rid_p(td_q)}}$
- (21) $IND_{ij}^{rid_p(td_q)} = \frac{D_{ij}^{rid_p(td_q)} * rid_p.number_of_lanes}{counter^{rid_p(td_q)} * D_{ijMax}^{rid_p(td_q)}}$
- (22) $TCC_{ij}^{rid_p(td_q)} = \frac{TCC_{ij}^{rid_p(td_q)} * N_{ij}^{rid_p(td_q)} + IND_{ij}^{rid_p(td_q)} / INV_{ij}^{rid_p(td_q)}}{N_{ij}^{rid_p(td_q)} + 1}$
- (23) $N_{ij}^{rid_k} = N_{ij}^{rid_k} + 1$
- (24) Write ($TCC_{ij}^{rid_p(td_q)}$)
- (25) Write ($TCC_{ij}^{rid_p(td_q)}$)
- (26) **End for**

ALGORITHM 1: Pseudocode of TCC calculation algorithm.

addressing complex nondeterministic problems, including transportation field [23]. In this paper, the authors propose a fuzzy logic-based traffic congestion evaluation method that uses the estimated traffic density and velocity performance index of a road segment as input parameters. The proposed method provides the results of traffic congestion level evaluation. The method is applied to road segments that are at a high risk of traffic congestion as determined using the traffic congestion observation table and from segments discovered to have traffic-flow values higher than

usual. The following assumptions are defined to explain the algorithm.

1. $RO = \{ro_1, ro_2, \dots, ro_z\}$ denotes the set of records in the corresponding traffic congestion observation table of the evaluation.
2. *UpdateIND* denotes an updated density performance index value of a segment.
3. *UpdateINV* denotes an updated velocity performance index value of a segment.

```

Initiation Algorithm of Fuzzy-based Traffic Congestion Evaluation
(1) UpdateIND = 0
(2) UpdateINV = 0
(3) For each  $ro_k \in RO$  do
(4)   If  $ro_k.congestion\_coefficient\_value > 1$  then
(5)     Evaluation( $ro_k$ )
(6)   End if
(7)   Else
(8)     UpdateIND $_{ro_k}$  = Get_update( $ro_k$ , IND)
(9)     UpdateINV $_{ro_k}$  = Get_update( $ro_k$ , INV)
(10)    If UpdateIND $_{ro_k}$ /UpdateINV $_{ro_k}$  >  $ro_k.congestion\_coefficient\_value$  then
(11)      Evaluation( $ro_k$ )
(12)    End if
(13)    Else exit
(14)  End else
(15) End for

```

ALGORITHM 2: Pseudocode of initiation algorithm of fuzzy-based traffic congestion evaluation.

The following initiation algorithm should be executed to start fuzzy rule-based traffic congestion evaluation, as presented in Algorithm 2.

1. (Lines (1)-(2)) First, the *UpdateIND* and *UpdateINV*, which are used to store updated density performance index value and velocity performance index value of a segment, are initialized. At the beginning, variable values are assigned as zero.
2. (Lines (3)-(6)) Second, each record of traffic congestion observation table is investigated to decide which segments need to be evaluated using fuzzy rules-based traffic congestion evaluation. If the current coefficient value is greater than 1, the fuzzy rules-based traffic congestion evaluation is activated on the corresponding segment of the record.
3. (Lines (7)-(15)) Third, if the current coefficient value is smaller than or equal to one, then the density performance index value *UpdateIND* and velocity performance index value *UpdateINV* of the corresponding segment will be updated. Under this circumstance, if division *UpdateIND* by *UpdateINV* is greater than current coefficient value, which may represent an abnormal traffic congestion situation. Subsequently, the fuzzy rules-based traffic congestion evaluation is required to perform on the corresponding segment of the record.

The control center selects the header for each road segment with a high possibility of traffic congestion. Normally, the vehicle that has remained for the longest in each road segment is selected as a header to maximize stability. For example, a bus that has spent the longest time in a particular road segment is selected as the grid header. In rare situations, in which no vehicle is equipped with an onboard smart device for header selection or most vehicles, including the selected header, tend to leave the segment in an extremely short time before the completion of traffic-flow estimation or local

traffic prediction, the control center is assigned to finalize uncompleted tasks to guarantee stability. Consequently, each header subscribes to a VD data topic that is maintained by the control center to track real-time VD data. The real-time VD data are used to estimate the traffic density and velocity performance index of the road segment by using (12) and (13). The estimation results are published to the control center by using the MQTT publish method for maintaining traffic data topic and used as input variables for fuzzy rules-based traffic congestion evaluation.

Traffic congestion situation is directly linked with high values of the density performance index. Consequently, the high category of the density performance index is divided into two further categories, high and very high. Thus, the input variables are divided into fuzzy categories: the fuzzy categories of the density performance index are very high, high, medium, and low. The fuzzy categories of the velocity performance index are low, medium, and high. The partial degrees of membership functions are defined as shown in Figure 2. The output fuzzy categories reflect traffic congestion levels, which are assigned, according to Taichung City Government's traffic congestion classification framework, into four categories: free flow, stable flow, unstable flow, and congested. The fuzzy rules are defined to evaluate output fuzzy categories on the basis of input fuzzy categories, which are shown in Table 4. Finally, the fuzzy rules-based traffic congestion condition is evaluated using the header.

3.4.3. Traffic Congestion Condition Verification. To minimize false predictions, the authors propose traffic congestion condition verification. Whereas traffic congestion predictions involve employing road segment traffic velocity and density characteristics to predict the traffic congestion condition, the traffic congestion verification process entails analyzing the close relationship between a road segment under investigation and neighboring road segments to verify the traffic congestion condition of the road segment.

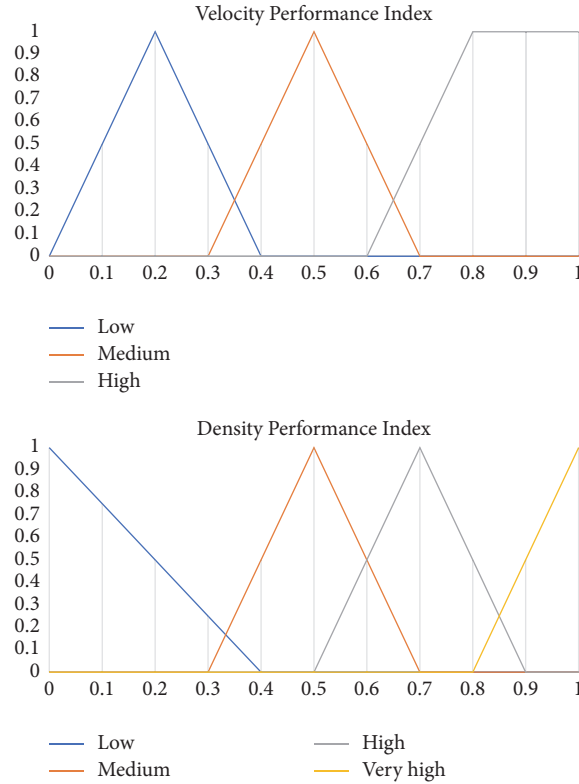


FIGURE 2: Velocity and density performance index membership function.

TABLE 4: Fuzzy rules for traffic congestion evaluation.

	Velocity performance index		
	Low	Medium	High
Density performance index			
Low	Stable flow	Free-flow	Free-flow
Medium	Unstable flow	Stable flow	Free-flow
High	Congested	Unstable flow	Stable flow
Very High	Congested	Unstable flow	Stable flow

This relationship is used in traffic congestion verification because of the shock wave phenomenon, in which each road segment transfers traffic pressure to its neighboring. This phenomenon may cause traffic congestion on neighboring road segments and was first mentioned by Franklin [24]. A shock wave is a type of kinematic wave. A shock wave occurs when two continuous road segments r_1 and r_2 encounter density shock ($[d_r] > 0$, where $[d_r] = d_{r_2} - d_{r_1}$). The velocity V_s of the shock wave can be obtained using the *Rankine-Hugoniot conditions* [25], as shown in the following:

$$V_s = \frac{[f_r]}{[d_r]} = \frac{(f_{r_2} - f_{r_1})}{(d_{r_2} - d_{r_1})}. \quad (9)$$

Obviously, the direction awareness of V_s depends on the sign of the result of subtracting outflow traffic f_{r_2} from inflow traffic f_{r_1} , since outflow traffic f_{r_2} being less than inflow traffic f_{r_1} implies an upstream moving shock ($V_s < 0$), which directly indicates a congested [22].

TABLE 5: Inflow neighbor table.

Segment ID	Inflow neighbor
------------	-----------------

On this basis, the proposed traffic congestion verification proceeds as follows. When a road segment experiences a congestion condition as defined using the fuzzy rules-based method, traffic congestion verification is triggered by the control center. The control center thereafter maintains a traffic-flow topic for each road segment as illustrated in Figure 3, which allows the system to store information on traffic flow and traffic direction for each road segment. Meanwhile, the control center maintains an inflow neighbor table for each road segment for managing inflow, as illustrated in Table 5. The content of the inflow neighbor table is derived from corresponding traffic-flow tables. Using the inflow neighbor table of a particular road segment, the control center selects a header in each road segment. Each header is thereafter

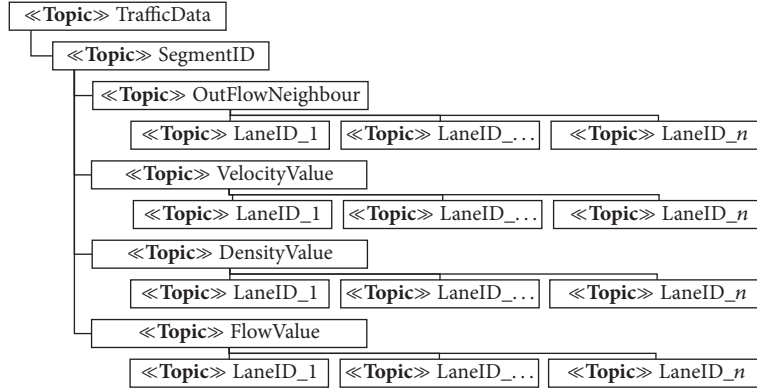


FIGURE 3: Traffic flows MQTT topic.

responsible for traffic data estimation within its road segment. The headers periodically upload flow value and density value information for their road segments. Traffic data estimation follows (6) and (7). Once the traffic data of the road segments have been estimated, the verification process begins, during which the traffic data of road segments under investigation and inflow neighboring road segments, including flow and density values, are collected. The headers transmit the data to the control center for verification by using the MQTT publish method. Subsequently, using the data received from the headers of road segments under investigation and inflow neighboring road segments, the control center examines whether the data fulfil the Rankine-Hugoniot conditions. The Rankine-Hugoniot conditions are evaluated under this circumstance, as expressed in (10). A congested condition is confirmed when $V_s < 0$.

$$V_s = \frac{[f_r]}{[d_r]} = \frac{(f_{r_{\text{sys}}} - \sum f_{r_{\text{inf}}})}{(d_{r_{\text{sys}}} - \sum d_{r_{\text{inf}}})}, \quad (10)$$

where

V_s is the shock wave velocity;

f_r is the flow shock;

d_r is the density shock;

$f_{r_{\text{sys}}}$ is the outflow of the road segment under investigation;

$f_{r_{\text{inf}}}$ is the inflow to the road segment under investigation from the inflow neighboring road segment;

$d_{r_{\text{sys}}}$ is the density of the road segment under investigation;

$d_{r_{\text{inf}}}$ is the inflow to the road segment under investigation from the inflow neighboring road segment.

The following assumptions are defined to explain the congestion verification process:

1. $R = \{r_1, r_2, \dots\}$ indicates a set of road segments.
2. $G = \{g_1, g_2, \dots\}$ indicates a set of grid headers.

The algorithm used for traffic congestion verification is described as shown in Algorithm 3.

3.5. Origin-Destination Traffic Congestion Service for Drivers.

An origin-destination traffic congestion service is proposed to provide on-the-way congestion information for drivers who travel through road segments to their destination. The origin-destination traffic congestion service is used when a traffic congestion condition has been verified on a road segment and the preselected travel route of the vehicle traverses the verified road segment. The workflow of the proposed mechanism is detailed as follows: once a congested condition has been verified on a road segment, the control center establishes the segments order number as 1 to denote the road segment as a level 1 congestion road segment, creates an event ID for the congestion, and changes the road segment's status to 'congested.' Vehicles on the inflow neighboring road segments are then informed of the congested status. Thereafter, each header of inflow neighboring road segments that are classified as level 2 congestion road segments updates the order value by increasing it by 1. This task is repeated sequentially for level three congestion road segments and so on. The task is completed when all interrelated inflow neighboring road segments have updated their congestion status. Once the process has been completed, each vehicle with a unique traveling route that directly passes through the verified congested segment will estimate origin-destination traffic congestion information based on the instant distance to the congested road segment and the velocity of the vehicle, as illustrated in Figure 5.

4. System Prototype and Implementation

To provide traffic congestion monitoring service for drivers, this study designed and implemented a simple prototype system. We describe the framework of this prototype in this section. Figure 4 illustrates the system architecture, which consists of three parts: vehicles, the VD sensors subsystem, and the control center subsystem. In the system, each vehicle is equipped with an onboard smart device. The onboard smart device allows drivers to receive traffic notifications from the system and displays vehicle journey information. The VD sensor subsystem is used to collect traffic data and send the collected data to the control center. The VD sensor subsystem includes VD sensors and a roadside unit (RSU).

```

Traffic Congestion Condition Verification Operation
(1) If (Fuzzy_Based_Evaluation( $r_c$ ) == 'congested') then
(2)    $Verification\_Result = NULL$ 
(3)   For each  $r_i$  do
(4)     If (Exist_Outflow( $lane_j, r_k$ ) == true) then
(5)       Update_Neighbor( $r_j$ ) to inflow neighbor table of  $r_k$ 
(6)     End if
(7)   End For
(8)   For each inflow neighbor  $r_k$  of  $r_c$  do
(9)      $g_{r_k} = Select\_header(r_k)$ 
(10)  End for
(11)  While ( $Verification\_Result = NULL$ ) do
(12)     $g_{r_c}$  performs Update_traffic( $flow, density$ ) to traffic flow table of  $r_c$ 
(13)     $g_{r_c}$  performs Publish( $flow, density, r_c$ ) to the control center
(14)    For each inflow neighbor  $r_k$  of  $r_c$  do
(15)       $g_{r_k}$  performs Update_traffic( $flow, density$ ) to traffic flow table of  $r_k$ 
(16)       $g_{r_k}$  performs Publish( $flow, density, r_k$ ) to the control center
(17)    End For
(18)    do Rankine-Hugoniot_Validation( $r_i, r_{k_1}, r_{k_2}, \dots, r_{k_n}$ )
(19)    If (Rankine-Hugoniot_Validation( $r_i, r_{k_1}, r_{k_2}, \dots, r_{k_n}$ ) < 0) then
(20)       $Verification\_Result == 'Verified'$ 
(21)    Else  $Verification\_Result == 'Failed'$ 
(22)      Fuzzy_Based_Evaluation( $r_c$ ) = 'unstable-flow'
(23)    End while
(24)  End if

```

ALGORITHM 3: Pseudocode of traffic congestion condition verification.

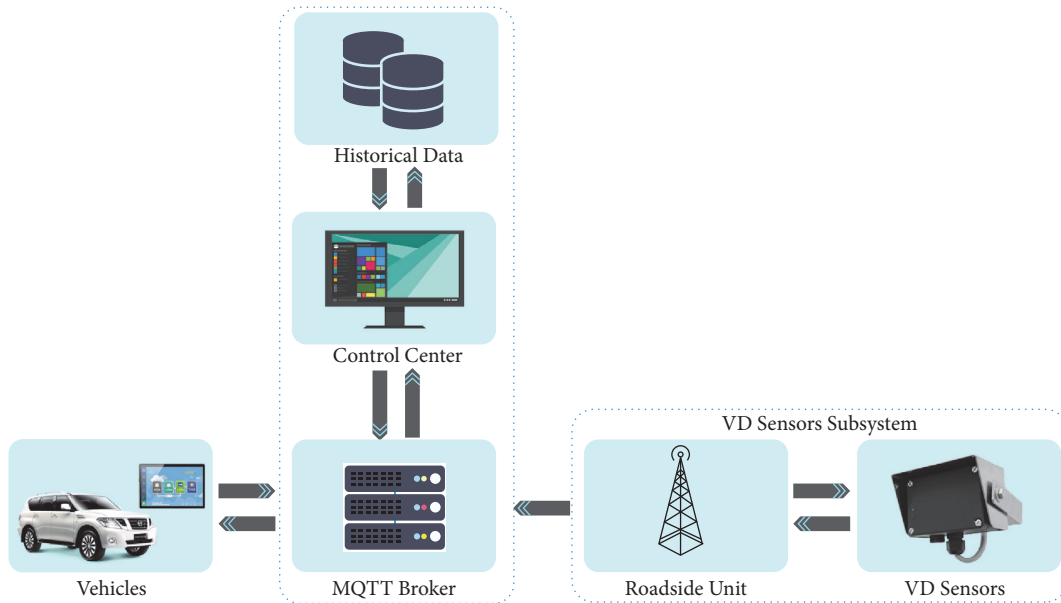


FIGURE 4: System architecture.

The RSU is an embedded platform equipped with two types of communication interface. The first interface is used to directly connect to the VD device. The second interface is used for wireless communication to connect to the control center subsystem using the web API. The collected data are then analyzed to characterize traffic-flow conditions. Then, the analyzed data are uploaded to the system database and

act as a source of historical data for determining locations at risk of future traffic congestion in order to provide a more effective traffic congestion monitoring service. The control center subsystem includes an MQTT broker, a control center unit, and a database. The MQTT broker is established to provide an MQTT connection as the core connection for both vehicles and the VD sensors subsystem. This allows

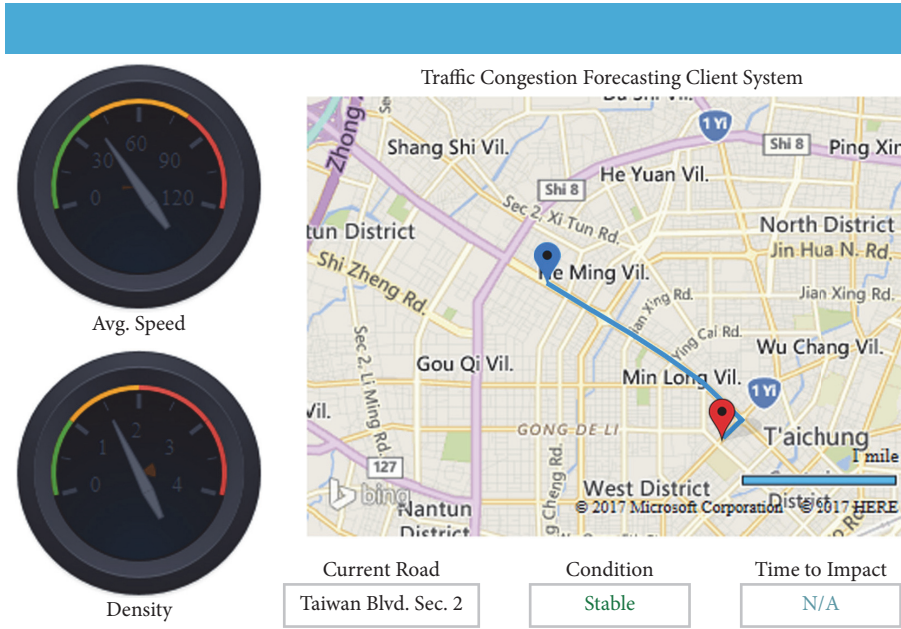


FIGURE 5: Client interface of traffic congestion monitoring system.

vehicles and the VD sensor subsystem to communicate with the control center unit. This unit is in turn responsible for data collection, data analysis, observation table maintenance, and publish/subscribe management to provide appropriate notifications to drivers.

For the first part of implementation, a simple application was designed to provide traffic-flow information regarding the current road segment where the vehicle and the origin-destination traffic congestion services are located. Drivers can use the onboard device with an integrated 3G or LTE interface to connect to the control center through the MQTT broker. For the second part implementation, an MQTT broker was established on a Windows-based server. The authors used Mosquitto, an open-source message broker, as the MQTT broker deployment package, which implements the MQTT protocol versions 3.1 and 3.1.1. The established MQTT broker allows drivers, the control center, and VD sensors to implement the publish/subscribe mechanism by using the public MQTT broker IP address and available topic name. For the final part implementation, the control center was implemented on a Microsoft Windows server-based host; the interface was designed using Microsoft Visual Studio 2015 as the integrated development environment and C# as the programming language. The ADO.NET entity data model was used to manipulate data exchange between the control center and database.

Figure 5 shows the application interface, which is designed for the driver. The interface displays the vehicle's speed and traffic-flow information regarding the current road segment. The driver can easily observe the traffic congestion state of the road segment and the entire predefined travel route. If traffic congestion occurs in any upcoming road segment on the predefined route, the application alerts the driver in advance and estimates the time remaining before

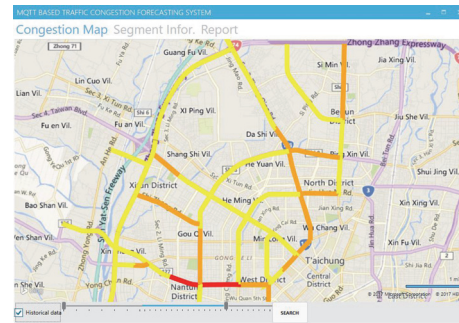


FIGURE 6: Control center interface of traffic congestion monitoring system.

reaching the area of congestion. This actively assists the driver in efficiently traveling to the destination. Figure 6 presents various types of traffic congestion information obtained from the road network that are used to assist the government's transportation division think tank, including congestion maps and detailed information of all segments and reports.

5. Experimental Results

The authors present the results in two subsections. The first subsection presents the TCC analysis results. The second subsection presents the evaluation results of the proposed traffic congestion monitoring scheme. Eclipse Neon, a Java EE IDE, was used as the environmental development tool to evaluate the average system response time of the proposed system in comparison with traditional HTTP protocol base systems. Furthermore, MATLAB version R2016a was used

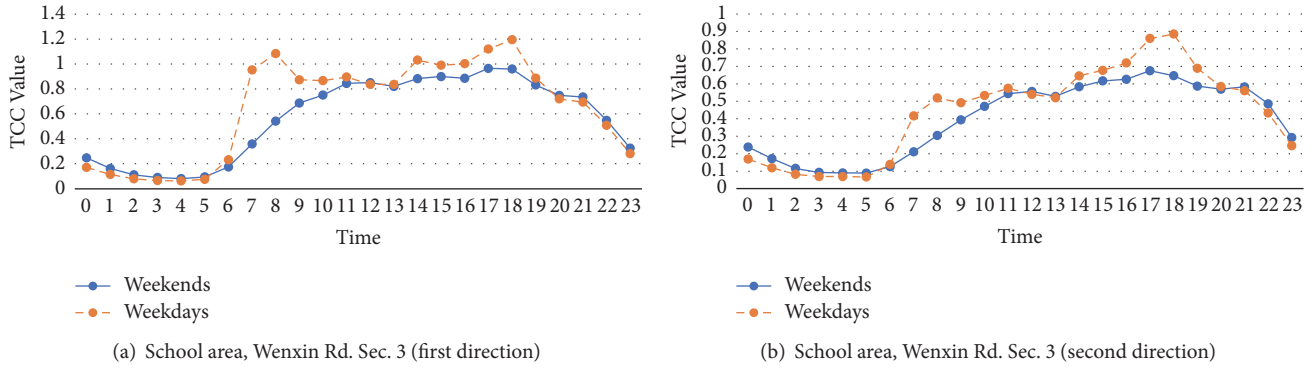


FIGURE 7: Traffic congestion coefficient analysis result of school area.

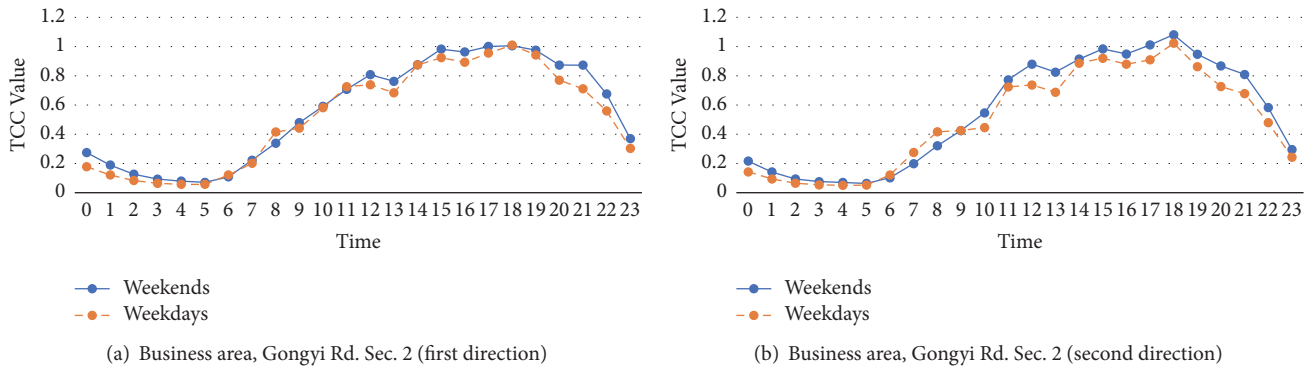


FIGURE 8: Traffic congestion coefficient analysis result of business area.

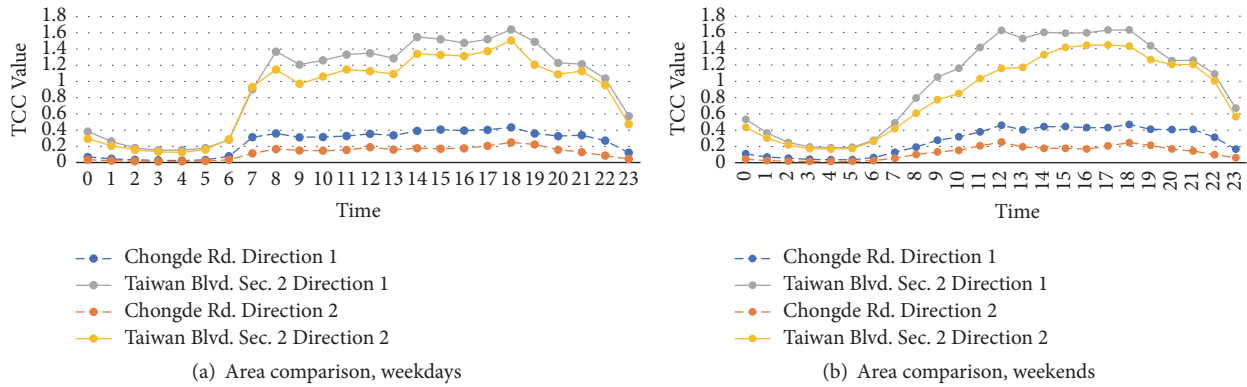


FIGURE 9: Area-based traffic congestion coefficient comparison.

to evaluate the performance of the proposed monitoring method in comparison with K -Nearest Neighbor method.

5.1. Analysis Results of Traffic Congestion Coefficient. The TCC was calculated for each road segment on the basis of its velocity performance index and density performance index, which were categorized according to hours of the day and days of the week. Figure 7 indicates that the analysis results of TCC distribution on Wenxin Road Section 3, a school area, where there are several elementary and high schools. Due to this characteristic, the Wenxin Road Section 3 has significantly decreased the number of vehicles on weekends

and increased the number of vehicles on weekdays, which directly affect the corresponding TCC values.

By contrast, the distributions of high TCC values on Gongyi Road Section 2, a business area, retained a stable distribution on both weekdays and weekends as shown in Figure 8. The Gongyi Road Section 2 area is concentrated on daily life services such as shopping, dining, and banking. Figures 7 and 8 also reveal that the time distributions of high TCC values in both areas, school area and business area, are similar; peak times are approximately 8–10 a.m. and 5–7 p.m.

The usability of TCC in identifying high risk of traffic congestion areas is also demonstrated as shown in Figure 9,

where Taiwan Boulevard Section 2, a main road in the city center, which usually faces the traffic congestion situation is marked with a much higher TCC value than that of Chongde Road, a suburban road.

5.2. Average System Response Time. To evaluate the system response time of the proposed system, which uses the Mosquitto MQTT protocol in comparison with the conventional HTTP-based systems such as Jayapal and Roy [26] or Sukode and Gite [1], an experimental HTTP server and Mosquitto MQTT broker environment were established on a local Microsoft Windows server-based host, and Java was used as the implementation programming language to evaluate simultaneous data transmission from vehicles to the HTTP server or MQTT broker. Figure 10 shows system response time results for HTTP and Mosquitto MQTT. MQTT ran in three quality of service (QoS) modes, namely, 0 (*at most once*), 1 (*at least once*), and 2 (*exactly once*). MQTT QoS mode 0 is the fastest; in this mode, the sender delivers messages across the network without an acknowledgement being sent. By contrast, MQTT QoS mode 2 is the slowest but the safest mode; at least two pairs of transmissions must be exchanged between sender and receiver to guarantee that messages are properly received by the receiver before they are deleted on the sender's side. MQTT QoS mode 1, in which the sender must receive an acknowledgement before sending a new message, is the default transfer mode and was used in the system prototype. The results demonstrate that the proposed system with MQTT outperformed the conventional HTTP-based system in system response time.

5.3. Local Segment Traffic Congestion Prediction Result. This subsection describes an evaluation of the performance of the proposed fuzzy rules-based local segment traffic congestion prediction conducted using MATLAB version R2016a. To evaluate performance in real-world conditions, real data recorded in May 2014 on Taiwan Boulevard Section 2 were adopted as the experimental environment and parameter values for the evaluation.

Figure 11(a) depicts the prediction results obtained using the k -nearest neighbor method with $k = 5$. The results show that the k -nearest neighbor method predictions properly predict the congestion state at the lowest traffic congestion level but exhibit decreased accuracy at higher congestion levels. In particular, the k -nearest neighbor method failed to predict some states of the highest congestion levels, which occurred at approximately 2 p.m. and 5 p.m. Figure 11(b) shows the prediction results for the proposed fuzzy rules-based method without a verification process. The proposed method produces a prediction result identical to that of the k -nearest neighbor method at the lowest level of traffic congestion but has improved accuracy at higher congestion levels. Furthermore, the proposed method can determine highest-level traffic congestion states which have been incorrectly predicted using the k -nearest neighbor method. However, without the verification process, several failed predictions occurred between 1 p.m. and 2 p.m. Figure 11(c) shows the

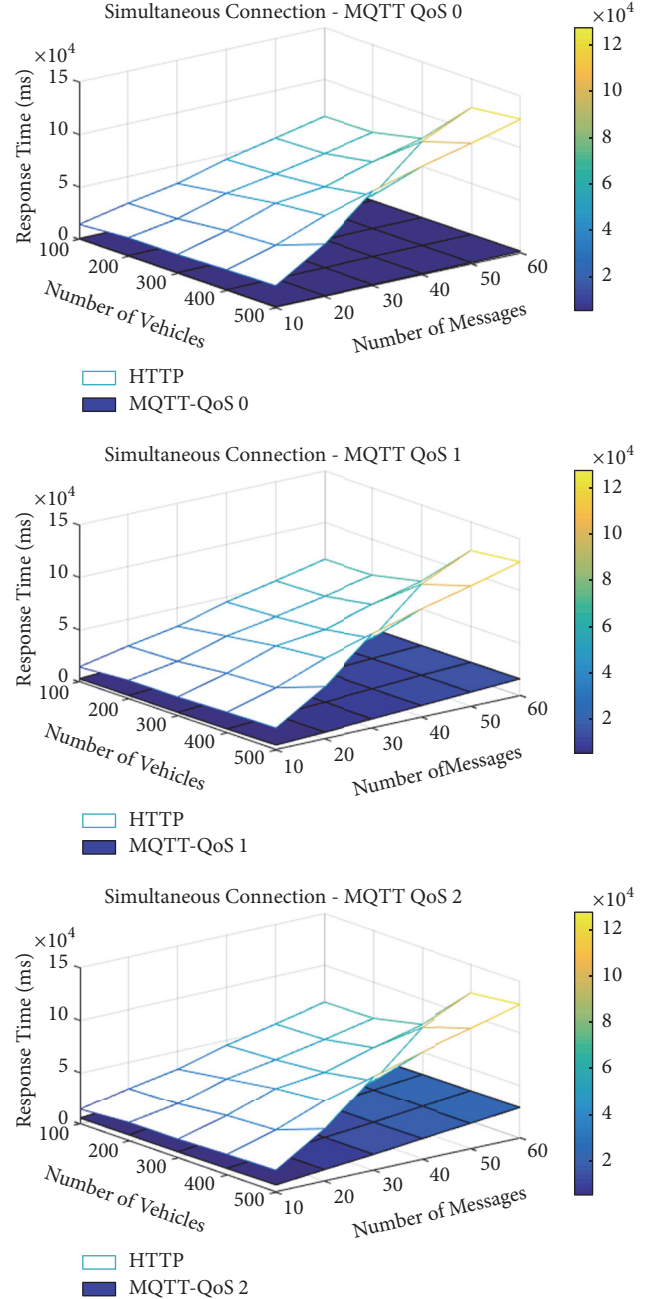


FIGURE 10: System response time.

prediction results for the proposed fuzzy rules-based method along with the verification process, which demonstrates that the verification process eliminated failed predictions during states of high-level traffic congestion, indicating the accuracy of the prediction.

Figure 12 provides a performance comparison of the aforementioned methods. Figure 12(a) depicts a performance comparison under the normal traffic condition. The normal traffic condition implies traffic congestion of levels 1 and 2, as indicated in Figure 11. The results revealed that the proposed method outperformed the traditional k -nearest neighbor method. Because the normal traffic condition does not imply

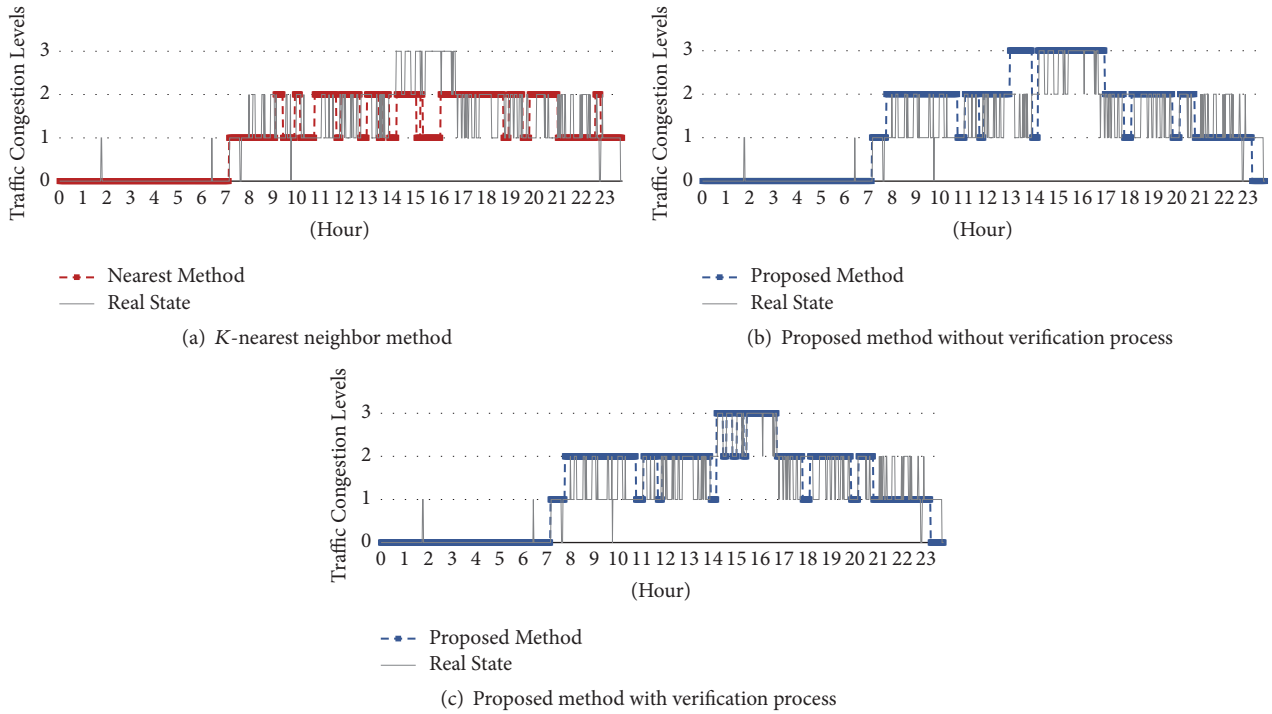


FIGURE 11: Traffic congestion evaluation results.

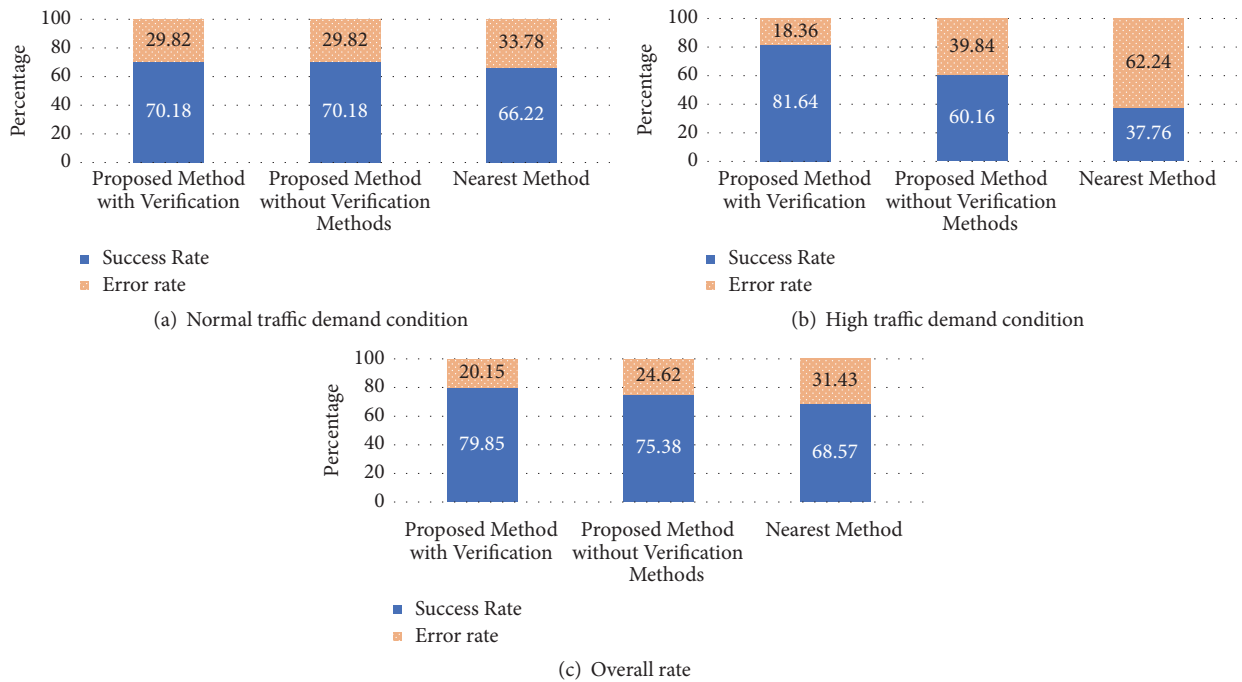


FIGURE 12: Performance comparison.

a congested situation (i.e., traffic congestion level 3), no verification is activated. Thus, the proposed method with verification was determined to retain identical performance to the original method for low levels of traffic congestion. Figure 12(b) provides a performance comparison under the high traffic condition in which traffic congestion level

3 is implied. Under this condition, the proposed method demonstrated its comparative effectiveness in predicting congested situations with verification, providing a high success rate of approximately 81%. Figure 12(c) depicts the overall performance comparison. The overall rate indicates the 24-hour performance of these methods. The results revealed

that the proposed method outperformed the k -nearest neighbor method with a greater than 10% lower error rate.

6. Conclusion

This paper proposes a distributed traffic congestion monitoring system on the IoV. The system responsively reacts to numerous requests concerning the traffic congestion situation by combining the advantages of MQTT, a lightweight protocol that has the ability to support low-bandwidth and high-latency vehicular environments, and VD sensors, which have high reliability and accuracy in traffic-flow monitoring. Furthermore, real-time data were used to formalize the traffic-flow factors and predict traffic congestion states through a fuzzy rule-based scheme. The proposed system not only effectively monitors traffic congestion but also reduces response time. The designed traffic congestion verification process can help in improving local traffic congestion prediction efficiency, and origin-destination traffic congestion service improves service quality, which will be provided for drivers. Experimental results showed that the proposed system was effective in predicting traffic congestion states in terms of accuracy and system response time. In future studies, the authors intend to improve the system's flexibility by enhancing the segmented structure to a hybrid structure in which traffic-flow estimation can be based on both VD sensors and vehicle-to-vehicle communications. The authors additionally intend to improve local segment traffic congestion prediction and origin-destination traffic congestion service for suitability with the hybrid segmented structure.

Conflicts of Interest

The authors declare that there are no conflicts of interest regarding the publication of this paper.

Acknowledgments

The authors would like to acknowledge the Ministry of Science and Technology of the Republic of China for supporting this research under Contract no. 105-2221-E-035-050-MY2 and Taiwan Government for assistance with the historical VD data.

References

- [1] S. Sukode and S. Gite, "Vehicle traffic congestion control & monitoring system in IoT," *International Journal of Applied Engineering Research*, vol. 10, no. 8, pp. 19513–19524, 2015.
- [2] M. Gramaglia, M. Calderon, and C. J. Bernardos, "ABEONA monitored traffic: VANET-assisted cooperative traffic congestion forecasting," *IEEE Vehicular Technology Magazine*, vol. 9, no. 2, pp. 50–57, 2014.
- [3] S. Gashaw and J. Harri, "V2X data dissemination delay for vehicular traffic density estimations," in *Proceedings of the 16th IEEE International Symposium on a World of Wireless, Mobile and Multimedia Networks, WoWMoM 2015*, USA, June 2015.
- [4] T. Ghosh and S. Mitra, "Congestion control by dynamic sharing of bandwidth among vehicles in VANET," in *Proceedings of the 2012 12th International Conference on Intelligent Systems Design and Applications, ISDA 2012*, pp. 291–296, India, November 2012.
- [5] P. Lai, X. Wang, N. Lu, and F. Liu, "A reliable broadcast routing scheme based on mobility prediction for VANET," in *Proceedings of the 2009 IEEE Intelligent Vehicles Symposium*, pp. 1083–1087, China, June 2009.
- [6] R. Riccardo, G. Massimiliano, G. Gregorio, and M. Claudio, "Comparative analysis of random utility models and fuzzy logic models for representing gap-acceptance behavior using data from driving simulator experiments," *Procedia: Social and Behavioral Sciences*, vol. 54, pp. 834–844, 2012.
- [7] P. Sathyamoorthy, E. C. Ngai, X. Hu, and V. C. Leung, "Profiling Energy Efficiency and Data Communications for Mobile Internet of Things," *Wireless Communications and Mobile Computing*, vol. 2017, pp. 1–15, 2017.
- [8] P. P. Ray, "A survey of IoT cloud platforms," *Future Computing and Informatics Journal*, vol. 1, no. 1-2, pp. 35–46, 2016.
- [9] B. Kim, H. Park, K. H. Kim, D. Godfrey, and K. Kim, "A Survey on Real-Time Communications in Wireless Sensor Networks," *Wireless Communications and Mobile Computing*, vol. 2017, pp. 1–14, 2017.
- [10] F. Yang, S. Wang, J. Li, Z. Liu, and Q. Sun, "An overview of internet of vehicles," *China Communications*, vol. 11, no. 10, pp. 1–15, 2014.
- [11] J. Fu, Z. Chen, R. Sun, and B. Yang, "Reservation based optimal parking lot recommendation model in Internet of Vehicle environment," *China Communications*, vol. 11, no. 10, pp. 38–48, 2014.
- [12] T. Yokotani and Y. Sasaki, "Comparison with HTTP and MQTT on required network resources for IoT," in *Proceedings of the 2nd International Conference on Control, Electronics, Renewable Energy, and Communications, ICCEREC 2016*, pp. 1–6, Indonesia, September 2016.
- [13] A. Del Campo, E. Gambi, L. Montanini, D. Perla, L. Raffaelli, and S. Spinsante, "MQTT in AAL systems for home monitoring of people with dementia," in *Proceedings of the 27th IEEE Annual International Symposium on Personal, Indoor, and Mobile Radio Communications, PIMRC 2016*, Spain, September 2016.
- [14] R. Szabó and K. Farkas, "Publish/Subscribe Communication for Crowd-Sourcing Based Smart City Application," in *Proceedings of the in Proceedings of the 2nd International Conference of Informatics and Management Sciences*, pp. 25–29, Slovakia, 2013.
- [15] K. Hoffman, F. Berardino, and G. Hunter, "Congestion pricing applications to manage high temporal demand for public services and their relevance to air space management," *Transport Policy*, vol. 28, pp. 28–41, 2013.
- [16] N. Isa, M. Yusoff, and A. Mohamed, "A Review on Recent Traffic Congestion Relief Approaches," in *Proceedings of the 4th International Conference on Artificial Intelligence with Applications in Engineering and Technology, ICAIET 2014*, pp. 121–126, Malaysia, December 2014.
- [17] K. Ishikawa, N. Hachiya, T. Aikoh, Y. Shoji, K. Nishinari, and A. Satake, "A decision support model for traffic congestion in protected areas: A case study of Shiretoko National Park," *Tourism Management Perspectives*, vol. 8, pp. 18–27, 2013.
- [18] A. Spiliopoulou, M. Kontorinaki, M. Papageorgiou, and P. Kopelias, "Macroscopic traffic flow model validation at congested freeway off-ramp areas," *Transportation Research Part C: Emerging Technologies*, vol. 41, pp. 18–29, 2014.
- [19] Y. Wang, M. Papageorgiou, J. Gaffney, I. Papamichail, and J. Guo, "Local ramp metering in the presence of random-location

- bottlenecks downstream of a metered on-ramp,” in *Proceedings of the 13th International IEEE Conference on Intelligent Transportation Systems (ITSC '10)*, vol. 2178, pp. 1462–1467, Madeira Island, Portugal, September 2010.
- [20] M. H. Gholve and S. Chougule, “Traffic Congestion Detection for Highways Using Wireless Sensors,” *International Journal of Electronics and Communication Engineering*, vol. 6, pp. 259–265, 2013.
- [21] R. Bhoraskar, N. Vankadhara, B. Raman, and P. Kulkarni, “Wolverine: traffic and road condition estimation using smart-phone sensors,” in *Proceedings of the Proceedings of the 4th International Conference on Communication Systems and Networks (COMSNETS '12)*, pp. 1–6, Bangalore, India, January 2012.
- [22] S. P. Hoogendoorn and P. H. Bovy, “State-of-the-art of vehicular traffic flow modelling,” *Proceedings of the Institution of Mechanical Engineers, Part I: Journal of Systems and Control Engineering*, vol. 215, no. 4, pp. 283–303, 2016.
- [23] X. Yan, P. Dong, T. Zheng, and H. Zhang, “Fuzzy and Utility Based Network Selection for Heterogeneous Networks in High-Speed Railway,” *Wireless Communications and Mobile Computing*, vol. 2017, pp. 1–14, 2017.
- [24] R. E. Franklin, “The Structure of a Traffic Shock Wave,” *Civil Engng Publ. Works Rev*, vol. 56, pp. 1186–1188, 1961.
- [25] C. Hirsch, *Numerical Computation of Internal and External Flows*, vol. 1 of *Fundamentals of Numerical Discretization*, John Wiley & Sons, 1991.
- [26] C. Jayapal and S. S. Roy, “Road traffic congestion management using VANET,” in *Proceedings of the International Conference on Advances in Human Machine Interaction, HMI 2016*, pp. 110–116, India, March 2016.

Research Article

A Progressive Extended Kalman Filter Method for Freeway Traffic State Estimation Integrating Multisource Data

Yingshun Liu,¹ Shanglu He ,¹ Bin Ran ,² and Yang Cheng ³

¹School of Automation, Nanjing University of Science & Technology, No. 200 Xiao Ling Wei Street, Nanjing, Jiangsu 210094, China

²School of Transportation, Southeast University, No. 2 Si Pai Lou, Nanjing, Jiangsu 210096, China

³Department of Civil & Environmental Engineering, University of Wisconsin-Madison, Madison, WI 53705, USA

Correspondence should be addressed to Shanglu He; slhemickey@126.com

Received 1 December 2017; Accepted 26 March 2018; Published 6 May 2018

Academic Editor: Li Zhu

Copyright © 2018 Yingshun Liu et al. This is an open access article distributed under the Creative Commons Attribution License, which permits unrestricted use, distribution, and reproduction in any medium, provided the original work is properly cited.

Variable techniques have been used to collect traffic data and estimate traffic conditions. In most cases, more than one technology is available. A legitimate need for research and application is how to use the heterogeneous data from multiple sources and provide reliable and consistent results. This paper aims to integrate the traffic features extracted from the wireless communication records and the measurements from the microwave sensors for the state estimation. A state-space model and a Progressive Extended Kalman Filter (PEKF) method are proposed. The results from the field test exhibit that the proposed method efficiently fuses the heterogeneous multisource data and adaptively tracks the variation of traffic conditions. The proposed method is satisfactory and promising for future development and implementation.

1. Introduction

Various traffic detection methods have been used for the freeway traffic surveillance and ITS application, such as loop detectors, microwave sensors, video cameras, Bluetooth sensors, cellphone probes, and GPS probes. In most cases, more than one technology is available on a freeway segment. Thus, it is a challenge to fully unitize the multisource data for the construction of traffic state. The critical issues include the following:

- (i) The heterogeneity in the multisource measurements
- (ii) The difference in the spatial or temporal resolution
- (iii) The inconsistency in the measurements when they should represent the same traffic state

Although the multisource data provide plentiful traffic information, they still have the limitation in the overall spatial or temporal coverage. A traditional method to construct the network-wide picture of traffic state with limited measurements is the model-based estimation [1–3]. One of the extensively used techniques for the estimation, known as

online Bayesian method, is Kalman filter and its extended version, such as Extended Kalman Filter (EKF). Kalman filter [4] has been implemented to solve the traffic problems with linear relation [5]. Extended Kalman Filter fits the estimation with nonlinear traffic flow models [3, 6–9]. A series of works based on the EKF algorithm conducted by Wang and Papageorgiou [3, 6–8, 10] have been applied in freeway network with data from the fixed detector. The EKF algorithm also has efficient performance on the estimation using data from probe vehicles, such as GPS-based probe technique [9], as well as cellphone activity data-based probe technique [1] which uses the wireless communication records. However, these works used a single-source data.

It has been proved that integrating multisource data can increase the accuracy, reduce the ambiguous, and improve the robust [11]. Bachmann et al. [12] provided a comparative assessment of the different data fusion techniques for traffic speed estimation, including distribution fusion techniques, Kalman filter techniques, ordered weighted averaging, fuzzy integral, and artificial neural network. The majority of recent works on traffic data fusion are data-driven approaches [11, 13–17], which required a set of training data for the calibration

of method. Hence, a data-driven method might fail when there is no sufficient data for training and testing. Mannini et al. made a further application of fused results by using EKF to estimate the traffic speed [18]. On the other hand, some model-based works using the macroscopic traffic flow models were developed to fuse multisource data. Heilmann et al. applied the linear Kalman filter to combine data from local detector and electronic toll collection (ETC) system [19]. Deng et al. [20] applied Clark's approximation method and Newell's method to fuse data from three detectors, and their estimator is also Kalman filter-based for the linear measurement equations. Recently, Nantes et al. [2] devoted to the development of an incremental EKF estimator for the fusion of three heterogeneous data sources collected from the arterials, with the assumption that all measurements are independent. Comparatively, the model-based method is superior to the data-driven method by considering the relationship among the traffic variables.

In the application of a model-based method, it is important to define the relation between the measurements and the traffic state variables. The newly developed data collection technique usually requires an update or adjustment to this relation model. The multisource data applied in this study are the traffic features that are extracted from wireless communication records and traffic measurements from microwave sensors. The traffic features from wireless communication records are not direct traffic state variables, which is a challenge for the application in the traffic state estimation. The wireless communication records are also known as the cellular communication records, including the records of handoff, normal location update, and data transition. The traffic features extracted from these wireless communication records are different from the traffic information from the handoff-based collection method [21]. Our recent work shows that the application of these traffic features in the traffic estimation is feasible [1]. This study aims to solve the integration of these traffic features with the data from the traditional fixed sensors for the traffic state estimation. Accordingly, the above three critical issues of traffic data fusion will be investigated in this study.

In this paper, we develop a Progressive Extended Kalman Filter- (PEKF-) based estimator. There are several obvious difference between the work of Nantes et al. [2] and our work. First, we use different data sources, which leads to different measurement equations in state-space model. And it also results in different semantic, spatial, and temporal synchronization of data. Moreover, the assumption of their method is the dependence of each data source, while our proposed method is based on the foreknowledge of the precision of multiple collection approaches. Besides, our study focuses on the application on the freeway while they focus on the urban arterial roads.

The organization of the rest of the paper is as follows. Section 2 presents a brief analysis on these two-source heterogeneous data. The following Section 3 describes the link-based freeway traffic model. We built up a PEKF estimator in Section 4. Section 5 applied the field data to assess the performance of the proposed approach. Finally, several key conclusions were drawn in Section 6.

2. Analysis on the Characteristics of the Multisource Data

2.1. The Multisource Data. As mentioned above, the multisource data stem from the wireless communication records and the microwave sensors. Similar to other fixed sensors (i.e., inductive loop detectors), the microwave sensors collect the value of traffic flow and speed at the spot. However, the sparse placement of sensors on the freeway in China makes this technique only achieve the traffic information from a small part of the road network. To some extent, the probe-based techniques have the larger spatial coverage. The wireless communication records of cellphones provide a source to extract traffic state information. In some studies, they used parts of these records; for instance, some used the handoff records to obtain the traffic speeds [22–24]. To achieve more samples and to better mine the potential value of these wireless communication records, this study applied all the records of wireless communication activities from the cellular network to extract traffic information. Mainly, two types of activities are included in the records: (1) system signal, such as location area updates, handoffs, and billing records, and (2) user activities, such as phone calls, text messaging, and data services, such as web browsing, sending, and checking emails [1].

The extraction procedure is named as the cellphone activity (CA) data-based method [1]. This method ambiguously locates the on-board cellphones on the freeway according to the geographic information of nearby cell towers. Two traffic features are extracted which are nominated as unique cellphone counts (UCC) and pseudo speed (PS). Compactly, the method includes the following steps. First, find out the cell towers whose signal covers the freeway. Second, project these cell towers on the freeway as the virtual sensor sites. Third, determine the moving direction of a on-board cellphone on the freeway by tracking the change of virtual sensor sites, that is, the cell towers that continuously record the activities of this cellphone. Fourth, the UCC of a freeway is calculated by counting the cellphones in the same direction and recorded by the cell towers on the same freeway link. Fifth, the PS of a cellphone ambiguously equals the distance of two adjacent virtual sensor sites divided by the time between two sequential records. Because of the ambiguous positioning of the on-board cellphones, UCC and PS could not directly equal the traffic state variables. It was found that these traffic features had a link-based characteristic, which meant that some freeway links could generate good data that closely related to the traffic state variables [1]. Besides, it was proven that the physical meaning of UCC changes depended on the traffic state. Accordingly, the relation models were set up as follows [1].

(1) The relation model of PS and traffic speed is as follows:

$$m_i^{vc}(k) = v_i(k) + \eta_i^{vc}(k), \quad (1)$$

where $v_i(k)$ (in km/h) denotes the traffic speed at Link i at the time interval k , $m_i^{vc}(k)$ (in km/h) denotes the measurements of PS at Link i at the time interval k , and $\eta_i^{vc}(k)$ denotes the corresponding PS noise.

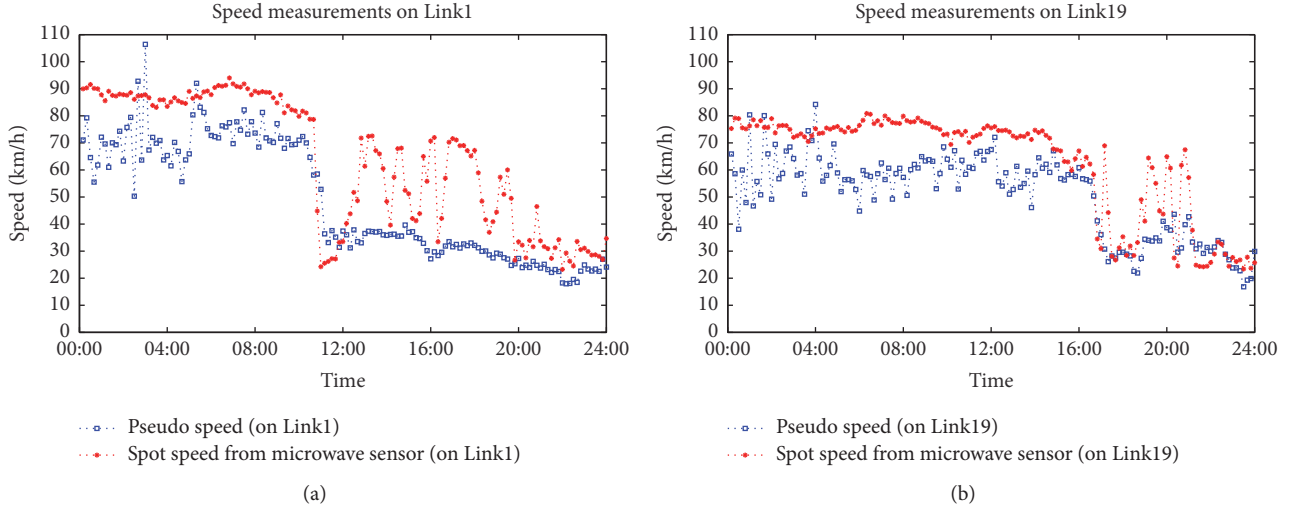


FIGURE 1: Speed measurements from multisensors: (a) on Link 1; (b) on Link 19.

(2) The relation model of UUC and the traffic state variable (density or flow) is as follows:

Since the relationship depended on the traffic state, a conditional function was developed [1]:

$$m_i^c(k) = \begin{cases} \theta(k) \cdot q_i(k) + \eta_i^{cq}(k) & \text{when } m_i^{vc}(k) \geq v_{cr} \\ \varphi \cdot \rho_i(k) + \eta_i^{cp}(k) & \text{when } m_i^{vc}(k) < v_{cr} \end{cases} \quad (2)$$

where $q_i(k)$ (in veh/h) denotes the traffic flow at Link i during the time interval k .

$\rho_i(k)$ (in veh/km/h) denotes the average traffic density of Link i during the time interval k , $m_i^c(k)$ denotes the measurements of UCC during the time interval k , $\eta_i^{cq}(k)$ and $\eta_i^{cp}(k)$ denote the corresponding UCC noise, $\theta(k)$ is a linear coefficient which is a time-dependent variate, φ is a linear coefficient which is a constant, and v_{cr} (in km/h) is the critical speed to identify the traffic state.

The later six parameters will be discussed in Section 5.

2.2. Characteristics of the Heterogeneous Data. In this study, it is essential to identify the differences between the heterogeneous multisource data to guide the fusion research. Obviously, the multisource data in this study differ in semantic, temporal, and spatial coverage. The microwave sensors provide the spot measurements while the traffic features of CA data-based method are the link-average values. Besides, they exhibit different accuracy. To explore their different in the precision, we use the field data collected from the Jiangsu freeway. The comparison between the speed measurements from these two collection methods is shown in Figure 1. It can be inferred from the figure that under free-flow condition (the speed is over 50 km/h), the PSs from the wireless communication records are not stable which fluctuate over a large range. Figure 1(a) shows that the PSs are all below

50 km/h from 11:00 to 24:00 on Link 1 and from 16:40 to 24:00 on Link 19, but the spot speeds from the microwave sensors show that the traffic switches between the free-flow state and the low-speed state. The incident/accident reports from the freeway operation center indicated that the traffic speeds were slow during that time period. It proves that the PSs are more accurate under the low-speed state compared with the speeds from microwave sensors. The possible cause for the instability of the microwave measurements is that the speed is collected on the spot which could not reflect the average speed of a link. There will be stop-and-go phenomenon especially under the low-speed or congested state.

Based on the comparison, we make the following inferences to promote the construction of the estimator. First, measurements from the microwave sensors are more stable and accurate than the traffic features from wireless communication records under the free-flow condition. Second, under the low-speed or congested condition, PS is regarded as the accurate speed measurements. Obviously, it is important to identify the traffic condition when both data sources are available but conflict. According to the inferences, PS is more reliable under the low-speed or congested condition. To avoid the impact of the biased PS under the free-flow condition, we set the following rules to identify the traffic condition when speeds from two-source conflict.

The condition is low-speed or congested if one of the following conditions is met:

- (i) $(m_i^{vc}(k) < v_{cr} \text{ and } m_i^{vc}(k-1) < v_{cr} \text{ but } m_i^{vm}(k) \geq v_{cr})$.
- (ii) $(m_i^{vc}(k) < v_{cr} \text{ and } m_i^{vc}(k+1) < v_{cr} \text{ but } m_i^{vm}(k) \geq v_{cr})$.
- (iii) $(m_i^{vm}(k) < v_{cr} \text{ but } m_i^{vc}(k) \geq v_{cr})$.

Otherwise, it is the free-flow condition, where $m_i^{vm}(k)$ (in km/h) denotes the speed measurement (the time mean speed) from the microwave sensors on Link i at the time interval k .

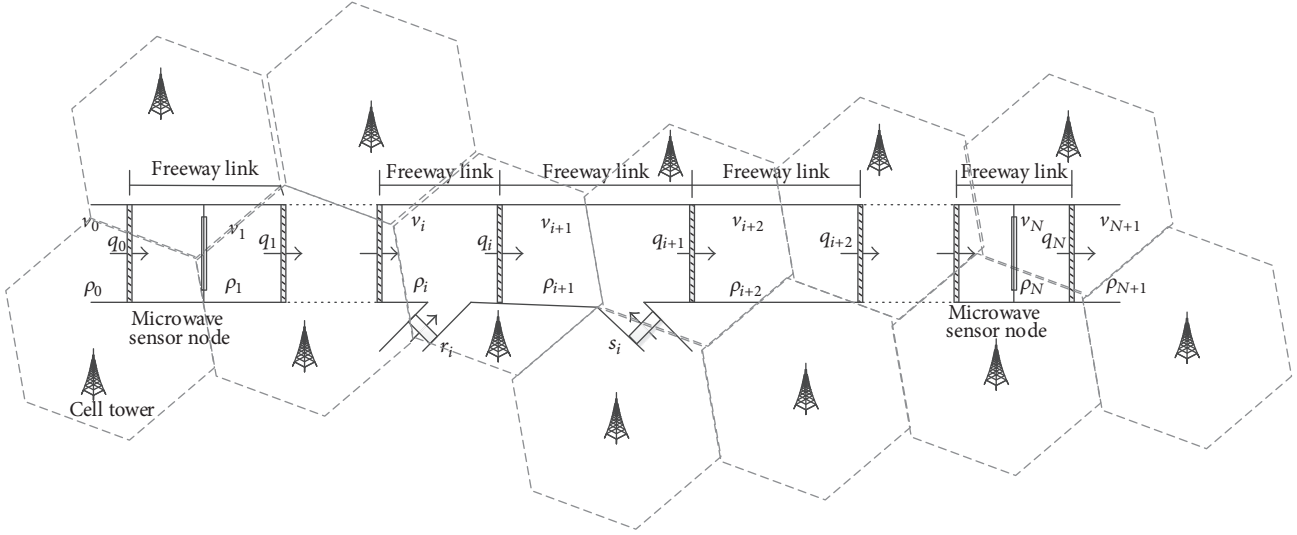


FIGURE 2: A freeway stretch, link division, sensor location, and cellular signal coverage [1].

3. Freeway Traffic Flow Modelling with Multisource Data

The models include a macroscopic traffic flow model and a measurement model. The macroscopic traffic flow model describes the relationship between traffic variables including speed, density, and flow. And the measurement model shows the relationship between the heterogeneous measurements and traffic variables.

3.1. Macroscopic Freeway Traffic Flow Model. This study utilized one of the validated macroscopic traffic flow models, that is, the METANET model [3]. The macroscopic model is discretized in space and time. As shown in Figure 2, a freeway stretch in a travel direction is divided into N links with length L_i , $i = 1, \dots, N$. Time is discretized in an equal time step T .

For the spatial synchronization of multisource measurements, the division of the freeway stretch follows some rules. First, if there is a microwave sensor on a link, it is better to locate in the middle of the link (or within the link), which is different from some works that put the fixed detector at the boundary of a link [3, 6]. Second, as an advantage of CA data-based method, any length can be used as long as one or more cell towers vertically projected to a link and the signal from this or these cell towers could cover this link. Other rules including the geometric difference (e.g., lane drops, on/off-ramps) could be applied, and it is optimal to have at most one on- or off- ramp within a link [3]. In this study, we applied a uniform length of 1 kilometer as a link length shown in the following test section.

Based on the divided freeway link and time step, the applied second-order macroscopic traffic flow model for Link i (i is the number of the link) includes the following four equations.

(1) Conservation equation is

$$\rho_i(k+1) = \rho_i(k) + \frac{T}{L_i} [q_{i-1}(k) - q_i(k) + i_i(k) - o_i(k)]. \quad (3)$$

(2) Dynamic speed equation is

$$v_i(k+1) = v_i(k) + \frac{T}{\tau} [v_e(\rho_i(k)) - v_i(k)] + \frac{T}{L_i} v_i(k) [v_{i-1}(k) - v_i(k)] - \frac{\gamma T}{\tau L_i} \frac{[\rho_{i+1}(k) - \rho_i(k)]}{\rho_i(k) + \kappa} + \xi_i^v(k). \quad (4)$$

(3) Stationary speed equation is

$$v_e(\rho_i(k)) = v_f \exp \left[\frac{1}{2} \left(\frac{\rho_i(k)}{\rho_{cr}} \right)^2 \right]. \quad (5)$$

(4) Flow equation is

$$q_i(k) = \rho_i(k) \cdot v_i(k) + \xi_i^q(k), \quad (6)$$

where T (in hour) is the discretized time step, L_i (in km) is the length of Link i , $\rho_i(k)$ (in veh/km/lane) is the traffic density of the Link i at the time interval k , $q_i(k)$ (in veh/h) is the traffic flow of the Link i at the time interval k , $i_i(k)$ (in veh/h) is the ramp inflow of the Link i at the time interval k , $o_i(k)$ (in veh/h) is the ramp outflow of the Link i at the time interval k , $v_i(k)$ (in km/h) is the space mean speed of the Link i at the time interval k , τ , ν , δ , and κ are model parameters, and all links share the same value of these parameters, $\xi_i^v(k)$ is zero-mean Gaussian white noise in the speed equation, $v_e(\rho_i(k))$ (in km/h) is the average corresponding speed according to

density, v_f (in km/h) is the free low speed, ρ_{cr} (in veh/km/h) is the critical density, and $\xi_i^q(k)$ denotes zero-mean Gaussian white noise in the flow equation.

3.2. Measurement Model and Date Synchronization. According to the characteristics of the multisource measurements, a set of measurement equations are established as follows.

3.2.1. Cellphone Density Measurement Equation. The conditional function (2) shows the relationship between UCC and the traffic state variables (flow and density) under different traffic conditions. Based on the relationship among flow, density, and speed, this relationship model could be transformed as follows:

$$m_i^{pc}(k) = \begin{cases} \frac{m_i^c(k)}{\theta(k) \cdot m_i^{vc}(k)} & m_i^{vc}(k) \geq v_{cr} \\ \frac{m_i^c(k)}{\varphi} & m_i^{vc}(k) < v_{cr}, \end{cases} \quad (7)$$

where $m_i^{pc}(k)$ (in veh/km/h) denotes the transferred density from UCC at Link i at the time interval k .

Afterwards, the cellphone density measurement model is set up as

$$m_i^{pc}(k) = \rho_i(k) + \eta_i^{pc}(k), \quad (8)$$

where $\eta_i^{pc}(k)$ is the measurement error of UCC.

3.2.2. Cellphone Speed Measurement Equation. The speed measurement equation could directly apply (1) in Section 2.

3.2.3. Speed Measurement Equation of Microwave Sensor. Speed measurements from the microwave sensors are average spot speeds, that is, the time mean speed. It is known that there is the difference between the time mean speed and space mean speed. In the model-based estimation, it is the space mean speed required. Rakha and Zhang [25] formulated the conversion between these two kinds of speeds. This formulation works when the variance of time mean speeds is known. However, it is difficult to achieve this variance some times. According to the analysis in Section 2, it is found that the speed measurements from the microwave sensors are more stable and reliable than the PS under the free-flow condition, because the PS are oscillating under the low-speed condition. Therefore, this study proposed the following conditional function using the two-source speeds as follows.

If $m_i^{vm}(k)$ conflicts with $m_i^{vc}(k)$ under the low-speed or congested condition, then

$$m_i^{vm}(k) = m_i^{vc}(k) = v_i(k) + \eta_i^{vc}(k). \quad (9)$$

Otherwise,

$$m_i^{vm}(k) = v_i(k) + \eta_i^{vm}(k), \quad (10)$$

where $\eta_i^{vm}(k)$ is the noise of speed measurements from the microwave sensor.

3.2.4. Flow Measurement Equation of Microwave Sensor. Consider a microwave sensor installed in the middle Link i , as illustrated in Figure 2. For the flow measurement, we have

$$m_i^{qm}(k) \times \left(\frac{60}{TI}\right) = q_i(k) + \eta_i^{qm}(k), \quad (11)$$

where TI (in min) is the time interval to collect the flow measurements.

$m_i^{qm}(k)$ (in veh/TI) is the flow measurement from the microwave sensor located at Link i during the time interval k .

$\eta_i^{qm}(k)$ denotes the corresponding flow measurement noise.

Considering the relation in flow equation (6), the traffic density can be calculated from the measurements of flow and speed. Accordingly, (11) can be transferred as follows, except for the measurement q_0 .

$$\frac{m_i^{qm}(k) \times (60/TI)}{m_i^{vm}(k)} = \rho_i(k) + \frac{\xi_i^q(k) + \zeta_i^{qm}(k)}{m_i^{vm}(k)}. \quad (12)$$

4. Design of PEKF-Based Estimator

4.1. State-Space Model. Based on the traffic flow model and measurement model mentioned above, a state-space model is set up with the state vectors \mathbf{x} , \mathbf{u} , ξ , and $\boldsymbol{\eta}^c, \boldsymbol{\eta}^m$ defined as follows:

$\mathbf{x} = [\rho_1 \ v_1 \ \rho_2 \ v_2 \ \cdots \ \rho_N \ v_N]^T$ denotes the density-speed state vector.

$\mathbf{u} = [q_0 \ v_0 \ \rho_{N+1} \ i_1 \ \cdots \ i_N \ o_1 \ \cdots \ o_N]^T$ denotes the boundary state vector.

$\xi = [\xi_1^q \ \xi_1^v \ \cdots \ \xi_N^q \ \xi_N^v]^T$ denotes the vector of the process noise.

$\boldsymbol{\eta}^c = [\eta_1^{pc} \ \eta_1^{vc} \ \cdots \ \eta_N^{pc} \ \eta_N^{vc}]^T$ denotes the vector of the measurement noise from CA data.

$\boldsymbol{\eta}^m = [\eta_1^{qm} \ \eta_1^{vm} \ \cdots \ \eta_N^{qm} \ \eta_N^{vm}]^T$ denotes the vector of the measurement noise from microwave sensors.

Then the macroscopic flow model and measurement model are rewritten to a compact state-space form including a process function (13) and two measurement functions (14) and (15) as follows:

$$\mathbf{x}(k) = \mathbf{f}[\mathbf{x}(k-1), \mathbf{u}(k), \xi(k-1)] \quad (13)$$

$$\mathbf{z}^c(k) = \mathbf{h}^c[\mathbf{x}(k), \boldsymbol{\eta}^c(k)] \quad (14)$$

$$\mathbf{z}^m(k) = \mathbf{h}^m[\mathbf{x}(k), \boldsymbol{\eta}^m(k)], \quad (15)$$

where the process function relates to (3), (4), (5), and (6). The measurement functions relate to (8), (1), (10), and (12). \mathbf{f} , \mathbf{h}^c , and \mathbf{h}^m are nonlinear differential vector functions. The vector \mathbf{z}^c consists of all available measurements from CA data and \mathbf{z}^m contains the measurements from the microwave sensors. In the application, the measurements will be transferred via function (7) and (10). The random variables $\xi(k)$, $\boldsymbol{\eta}^c(k)$, and $\boldsymbol{\eta}^m(k)$ represent the process and measurement noise, respectively. k is the number of time steps.

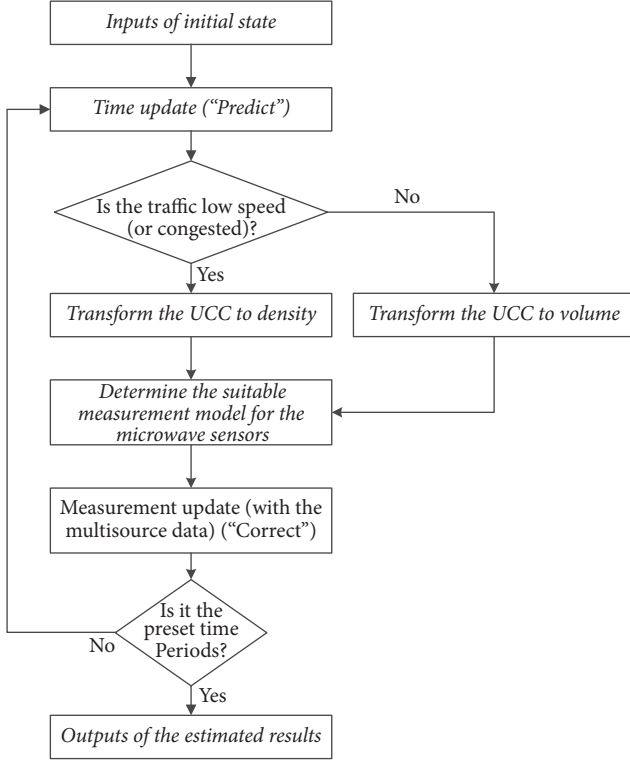


FIGURE 3: The operation of the Progressive Extended Kalman Filter estimator.

4.2. The PEKF Estimator for Multisource Data. The state-space model contains the nonlinear equations, and, thus, this study set up the estimator based on the Extended Kalman Filter (EKF) technique. As the exploration in the previous sections, the relationship between the multisource measurements and the traffic state variables highly relies on the judgment of the traffic condition. Therefore, we make some adjustments to the traditional EKF estimator, and the updated estimator is nominated as the progressive EKF (PEKF) estimator. The operation diagram of PEKF estimator is shown in Figure 3. The adjustments are mainly shown in the measurement update step. The purposes of these adjustments are to integrate the multisource data from the wireless communication records and microwave sensors in this study. As shown in Figure 3, the adjustments include the following contents. First, speeds from the microwave sensors (named as m -speed in the following description) and PSs are used to identify the traffic condition as shown in Section 2. Second, based on the identified traffic condition, the UCC are transformed to the corresponding traffic state variables via (7). Consequently, the speed measurement model can be decided via (10). Similar to the traditional EKF estimator, the partial derivatives of the process function and measurement function, transformed using the Jacobian matrix, are used to linearize the model [23, 26]. The proposed estimator includes the following steps.

Step 0 (initialization). Set time interval $k = 1$, and let $E[\mathbf{x}(0)] = \widehat{\mathbf{x}}(0)$, and $E[(\mathbf{x}(0) - \widehat{\mathbf{x}}(0))^2] = \mathbf{p}(0)$, where the

initial state $\mathbf{x}(0)$ and covariance $\mathbf{p}(0)$ are determined by the historical data.

Step 1 (time update). State estimate extrapolation is as follows: $\widehat{\mathbf{x}}(k)^- = \mathbf{f}[\widehat{\mathbf{x}}(k-1), \mathbf{u}(k), 0]$

Error covariance extrapolation is

$$\mathbf{P}(k)^- = \mathbf{A}(k) \cdot \mathbf{P}(k-1) \cdot \mathbf{A}(k)^T + \mathbf{W}(k) \cdot \mathbf{Q}(k-1) \cdot \mathbf{W}(k)^T, \quad (16)$$

where $\mathbf{P}(k)$ is the error covariance at the time step k .

Step 2 (measurement update)

Step 2.1. Identify the traffic state based on the rules in Section 2.2.

Step 2.2. Transform UCC to traffic density according to the traffic state using the conditional (7).

Step 2.3. Make a decision on the speed measurement model for the microwave sensor according to the traffic state by the conditional (10).

Step 2.4. Update the input measurement matrix \mathbf{h} .

Step 2.5. Measurement update using (14) and (15) is as follows. Kalman gain calculation is

$$\mathbf{K}(k) = \mathbf{P}(k)^- \cdot \mathbf{H}(k)^T \cdot \left(\mathbf{H}(k) \cdot \mathbf{P}(k)^- \cdot \mathbf{H}(k)^T + \mathbf{V}(k) \cdot \mathbf{R}(k) \cdot \mathbf{V}(k)^T \right)^{-1} \quad (17)$$

State estimate update is as follows: $\widehat{\mathbf{x}}(k) = \widehat{\mathbf{x}}(k)^- + \mathbf{K}(k) \cdot (\mathbf{z}(k) - \mathbf{h}(\widehat{\mathbf{x}}(k)^-), 0)$, where \mathbf{z} could be \mathbf{z}^c or \mathbf{z}^m and \mathbf{h} could be \mathbf{h}^c or \mathbf{h}^m depending on which source data is using.

Error covariance update is as follows: $\mathbf{P}(k) = (\mathbf{I} - \mathbf{K}(k) \cdot \mathbf{H}(k)) \cdot \mathbf{P}(k)^-$.

Step 3. Let $k = k + 1$ and go back to Step 1 until the preset time periods end, where \mathbf{I} is the identity matrix.

\mathbf{A} and \mathbf{W} are the Jacobian matrix of partial derivatives of \mathbf{f} with respect to \mathbf{x} and $\boldsymbol{\xi}$, respectively:

$$\begin{aligned} \mathbf{A}(k) &= \frac{\partial \mathbf{f}}{\partial \mathbf{x}} \left(\widehat{\mathbf{x}}(k-1), \mathbf{u}(k), 0 \right) \\ \mathbf{W}(k) &= \frac{\partial \mathbf{f}}{\partial \boldsymbol{\xi}} \left(\widehat{\mathbf{x}}(k-1), \mathbf{u}(k), 0 \right). \end{aligned} \quad (18)$$

\mathbf{H} and \mathbf{V} are the Jacobian matrix of partial derivatives of \mathbf{h} with respect to \mathbf{x} and $\boldsymbol{\eta}$. \mathbf{h} is the updated measurement matrix stemming from the multiple sources. $\boldsymbol{\eta}$ is the corresponding noise matrix compounding $\boldsymbol{\eta}^c$ and $\boldsymbol{\eta}^m$:

$$\begin{aligned} \mathbf{H}(k) &= \frac{\partial \mathbf{h}}{\partial \mathbf{x}} \left(\widehat{\mathbf{x}}(k), 0 \right) \\ \mathbf{V}(k) &= \frac{\partial \mathbf{h}}{\partial \boldsymbol{\eta}} \left(\widehat{\mathbf{x}}(k), 0 \right). \end{aligned} \quad (19)$$

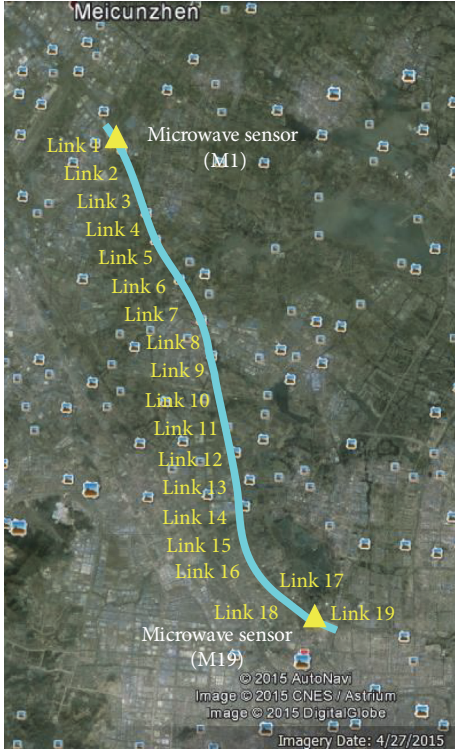


FIGURE 4: The test bed, part of Ning-Hu freeway, and a northbound segment. *Note.* The background photo is from Google Earth.

5. Test and Results

5.1. A Test Freeway Segment and Data Collection

5.1.1. Freeway Test Bed. The test bed is a 19 km, four-lane northbound segment of Ning-Hu freeway connecting Wuxi and Suzhou, China, which is part of the busiest freeway in China, as shown in Figure 4. Two microwave sensors (M1 and M19) are located near the ends of the segment. According to the freeway-division rules, the segment is divided into 19 links with uniform lengths of 1 km each. The links are labelled Link 1 to Link 19 from north to south opposite to the traveling direction. Microwave sensors are within Link 1 and Link 19, respectively. The segment is almost geometrically homogeneous without any lane drops.

5.1.2. Data Collection. The multisource data for the field test was provided by the Jiangsu Freeway Operation Center and was collected on September 30, 2014. Both collection methods (i.e., the microwave sensors and the CA data-based method) integrated their measurements by a time interval of ten minutes starting from 00:00, September 30, 2014. The spatial coverage of the microwave sensor is limited to Link 1 and Link 19, while the cellular signal covers all links.

In addition to these two data sources, there is a traffic incident/accident report which could be used in the following evaluation of the estimation results. The report indicates that an incident occurred on Link 4 at about 11:12 AM. The traffic was also quite heavy. These two traffic phenomena together

TABLE 1: Parameter settings.

Parameter	Value
τ	0.02 h
κ	40 veh/km
v_f	100 km/h
ν	24 km ² /h
ρ_{cr}	120 veh/km

lead to the traffic moving slowly from Link 1 to Link 10 as well as the nearby affected links. The report also shows that the traffic moved slowly from 10:00 to the late evening of that day due to the heavy traffic. The cause is the China National Day Holiday which begins from October 1 and the free tolling policy on freeway that works during this holiday, and, thus, it attracts tremendous traffic. Therefore, the traffic flow climbs high when it is closing to the midnight of the test day. Consequently, the high traffic flow triggered the speed drop and the large density.

5.2. Model Parameters

5.2.1. Parameters about Time. The time step T of the estimator is 10 seconds to meet the requirement that $T < L/v_f = 1 \text{ km}/100 \text{ (km/h)} = 36 \text{ seconds}$. The time interval for measurement update is 10 minutes. The estimator works when the measurements are available. It means that the time update and measurement update will work 60 steps (10 min/10 sec) using the same measurements.

5.2.2. Parameters about Links and Boundaries. Although there are 19 links, the measurements from the microwave sensors are only available on two links (Link 1 and Link 19). Our recent work found that the traffic features (UCC and PS) extracted from the wireless communication records on Link 6, Link 10, Link 14, and Link 18 had the closest relation with the traffic variables [1]. This study uses the UCC and PS from these links for the sake of high accuracy. Besides, the PSs on Link 1 and Link 19 are also used under the low-speed or congested condition, because these PSs are more reliable than the microwave speeds under this condition as discussed in Section 2. To avoid the impact of inaccurate boundary inputs, Link 1 and Link 19 are regarded as the boundary links, and, thus, the measurements on these links are used as the boundary variables.

5.2.3. Parameters in the Macroscopic Traffic Flow Model. The empirical parameters are set as Table 1. And the models of all links shared the same values. This study uses the value suggested in the work of Wang et al. [6] as the process noise.

5.2.4. Parameters in the Measurement Model. The coefficients in the measurement model for the UCC were calibrated using the historical data as follows [1]. The constant parameter φ approximately equals 8.5 for all links (Link 6, Link 10, Link 14, and Link 18). The time-varying parameter $\theta(k)$ is valued as follows: from the time 00:00 to 05:00, it approximately equals

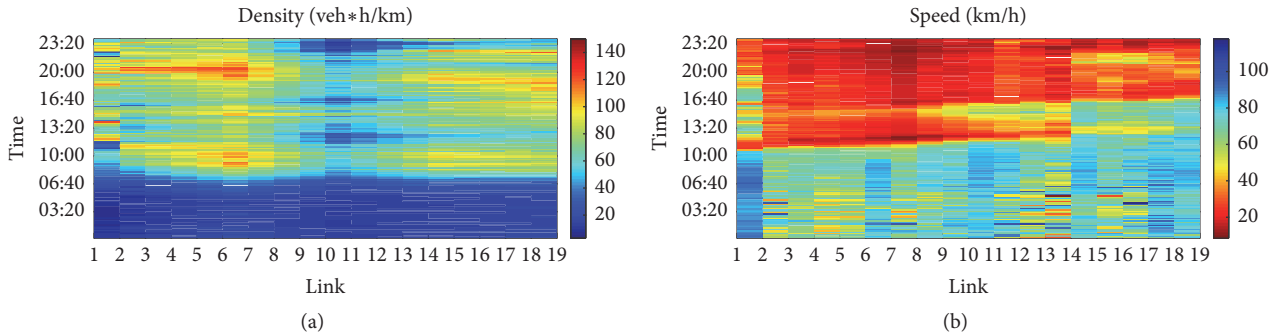


FIGURE 5: The estimation results. (a) The density estimates. (b) The speed estimates.

0.3; from 05:00 to 07:30, it gradually increases from 0.3 to 1.0; from 07:30 to the rest of a day, it approximately equals a constant 1.0 under the free-flow condition. Another critical parameter in the measurement update step is the critical speed for the identification of traffic condition. It is valued empirically as 50 km/h.

The measurement noise should be the standard deviation of measurements from cellphone activity data and microwave sensors. However, it is difficult to value the noise when there is no sufficient ground-truth data. Some existing studies indicate that the Extended Kalman Filter was found to have a slight sensitivity to the standard deviation-based measurement noise, which guaranteed the estimator's performance even with poor foreknowledge of model noise [3, 7]. Therefore, the deviation was set as a small value; that is, the density deviation was 1 veh/km and the speed deviation was 1 km/h for both sources.

5.3. Estimation Results. Figure 5 shows the estimation results via the proposed PEKF-based method. The gradual changes in the color represent the variations in the traffic state. The blue represents the low-density and high-speed condition, while the red indicates the high-density and low-speed condition. As shown in Figure 5, both the estimated speeds and densities are changing among the free-flow, dense, and congested conditions. For instance, the speeds of the entire freeway segment during 00:00 to 10:00 AM are rarely red as shown in Figure 5(b). With the color getting red, it means that the traffic slows down. When the color is dark red, the traffic speed is quite low which indicates a congestion. In Figure 5(a), the density is lower than 40 veh/km from 00:00 to 7:00 showing in the blue. It is reasonable that there is little traffic on the freeway at the midnight of a working day and the traffic increases in the day time.

On the other hand, the incident/accident report data are used to qualitatively evaluate the accuracy of results for lacking the "ground-truth" speeds and density. Figure 5(b) shows that the speed drops firstly on Link 1 and Link 2 at about 11:00 AM. Consequently, this phenomenon happens on Link 3 and Link 4 quickly. And speeds on Link 5 and Link 6 also decrease around that time. The variation of speed indicates that the estimation results exhibit the influence of traffic incidents. However, the reported incident happened

on Link 4 at about 11:00, but the estimation results on Link 4 have a small delay. Since the measurements are available only on Link 1 and Link 6 and the distance between two links is 6 km long, it is understandable for such a small delay. In Figure 5(a), the density on Link 1, Link 2, and Link 3 decreases when the incident happens. Since Link 1, Link 2, and Link 3 are downstream links of Link 4, this decline phenomenon reflects the propagation of a shock wave. Another incident record is about the heavy traffic later that day which induces the low speed. From Figure 5(b), we can see the large area of red later that day which validates the correctness of the estimation results. And the changing color in Figure 5(a) shows the variation of density which reflects the oscillation of traffic under the low-speed traffic condition. Roughly, the estimation results efficiently integrated the measurements from the multiple sources and exhibit the dynamic and real-time traffic state.

5.4. Evaluation. An evaluation of the proposed PEKF-based estimator is conducted by making a comparison between the results from multisource data and single-source data. We applied the estimation results from the previous work [1], which estimated the traffic state using the wireless communication data and EKF-based data assimilation method. Since the distance between the microwave sensors is extremely sparse, the data generated from these sensors is not qualified for the application of a model-based approach. Hence, the direct measurements from microwave sensors are used for the comparison. To make a precise comparison, the absolute difference (AD) is chosen as the performance measure. It can be calculated by the following equation:

$$AD(k) = |x_s(k) - x_f(k)|, \quad (20)$$

where $AD(k)$ is the absolute difference at the time interval k , $x_s(k)$ is the state estimates (density or speed) from single data source at the time interval k , $x_f(k)$ is the state estimates (density or speed) from multiple sources at the time interval k .

The iteration process of the progressive EKF-based estimator shows that the measurements from microwave sensors are usually taken as the more precise value compared with the traffic features from the wireless communication records.

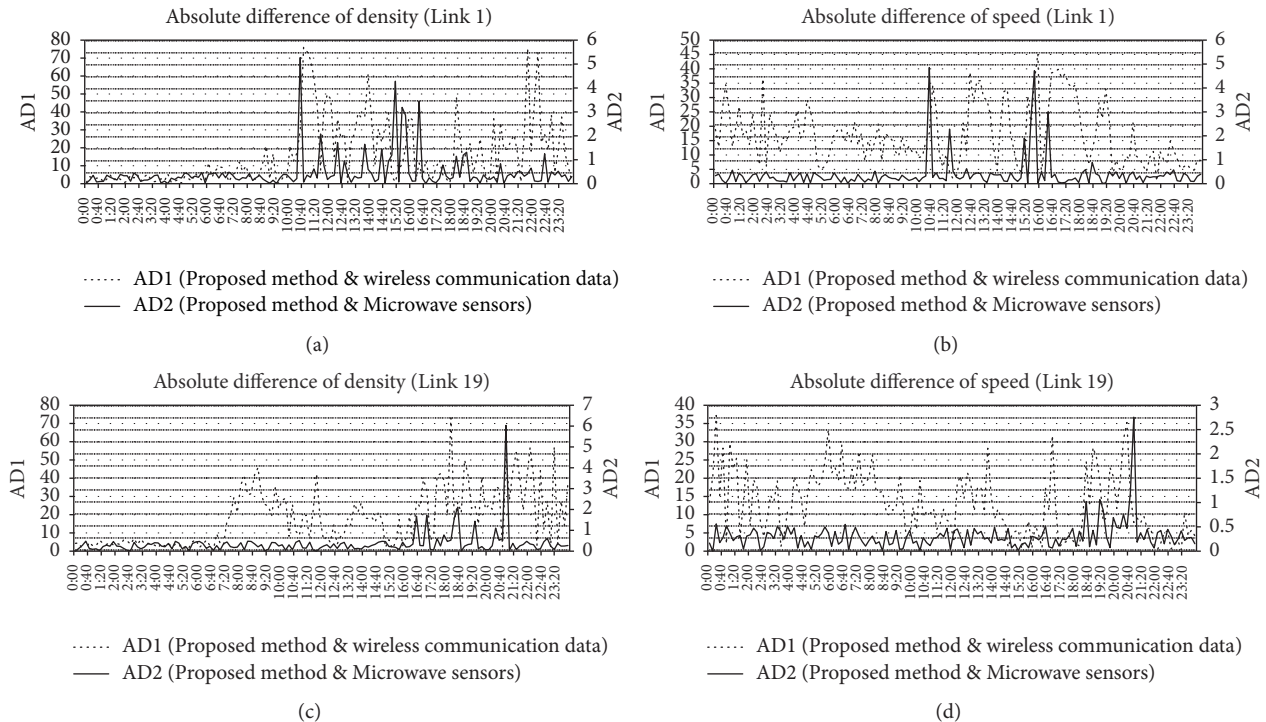


FIGURE 6: The AD results. (a) The ADs of density on Link 1. (b) The ADs of speed on Link 1. (c) The ADs of density on Link 19. (d) The ADs of speed on Link 19.

ADs between estimates from multisources and wireless communication data and ADs between estimates from multisources and measurements from microwave sensors in different links are present in Figure 6. Obviously, the progressive EKF-based method generated estimates which are more close to the more accurate measurements from microwave sensors. Generally, it will improve the total precision of estimation by fusing multisource data.

6. Conclusions

This paper proposed a Progressive Extended Kalman Filter (PEKF) method to estimate the freeway traffic state and integrate the heterogeneous data from the wireless communication data and the microwave sensors. The challenges in the application of these two data sources are the heterogeneities in the spatial coverage and the semantic of measurements. Via the characteristic analysis of the multisource data, we set up the relations between the measurements and traffic state variables and propose some rules to solve the conflicts between two data sources. The state-space model is constructed accordingly. The EKF technique is applied to establish the estimator, and it is improved to fit the multisource data and is nominated as the PEKF estimator. The test with the field data indicates that the proposed method successfully integrates the heterogeneous data, especially the new combination of measurements from the wireless communication records and microwave sensors. Moreover, the estimation results indicated that the PEKF is able to track the dynamic traffic conditions. The qualitative analysis between the estimates and

traffic incident reports validates the accuracy of the proposed method roughly. The final comparisons indicates the advantages of the proposed methods; that is, it has larger coverage compared with the microwave sensors, and it is more accurate than the estimates from wireless communication data.

This study makes an effort to use the limited, heterogeneous, and multisource data for the traffic state estimation, but there are still plenty of works before the field application. The most urgent task is to validate the method with the ground-truth data. Second, the test on other freeway links is required due to the spatial characteristic of the traffic features from the wireless communication data.

Conflicts of Interest

The authors declare that there are no conflicts of interest regarding the publication of this article.

Acknowledgments

The authors gratefully acknowledge the data support from the Jiangsu Freeway Operation Center and the Traffic Operations and Safety Laboratory (TOPS), University of Wisconsin-Madison.

References

- [1] S. He, Y. Cheng, F. Ding, J. Zhang, and B. Ran, "Extended Kalman Filter-based Freeway Traffic State Estimation Using Cellphone Activity Data," in *Transportation Research Board 95th Annual Meeting*, 2016.

- [2] A. Nantes, D. Ngoduy, A. Bhaskar, M. Miska, and E. Chung, "Real-time traffic state estimation in urban corridors from heterogeneous data," *Transportation Research Part C: Emerging Technologies*, vol. 66, pp. 99–118, 2016.
- [3] Y. Wang and M. Papageorgiou, "Real-time freeway traffic state estimation based on extended Kalman filter: a general approach," *Transportation Research Part B: Methodological*, vol. 39, no. 2, pp. 141–167, 2005.
- [4] R. E. Kalman, "A new approach to linear filtering and prediction problems," *Journal of Fluids Engineering*, vol. 82, no. 1, pp. 35–45, 1960.
- [5] Z. Lu, W. Rao, Y.-J. Wu, L. Guo, and J. Xia, "A Kalman filter approach to dynamic OD flow estimation for urban road networks using multi-sensor data," *Journal of Advanced Transportation*, vol. 49, no. 2, pp. 210–227, 2015.
- [6] Y. Wang, M. Papageorgiou, and A. Messmer, "a unified macroscopic model-based approach to real-time freeway network traffic surveillance," *Transportation Research Part C: Emerging Technologies*, vol. 14, no. 3, pp. 190–212, 2006.
- [7] Y. Wang, M. Papageorgiou, and A. Messmer, "Real-time freeway traffic state estimation based on extended Kalman filter: A case study," *Transportation Science*, vol. 41, no. 2, pp. 167–181, 2007.
- [8] Y. Wang, M. Papageorgiou, and A. Messmer, "Real-time freeway traffic state estimation based on extended Kalman filter: adaptive capabilities and real data testing," *Transportation Research Part A: Policy and Practice*, vol. 42, no. 10, pp. 1340–1358, 2008.
- [9] Y. Yuan, H. Van Lint, F. Van Wageningen-Kessels, and S. Hoogendoorn, "Network-wide traffic state estimation using loop detector and floating car data," *Journal of Intelligent Transportation Systems: Technology, Planning, and Operations*, vol. 18, no. 1, pp. 41–50, 2014.
- [10] Y. Wang, M. Papageorgiou, A. Messmer, P. Coppola, A. Tzimitsi, and A. Nuzzolo, "An adaptive freeway traffic state estimator," *Automatica*, vol. 45, no. 1, pp. 10–24, 2009.
- [11] S. He, J. Zhang, Y. Cheng, X. Wan, and B. Ran, "Neural network based freeway traffic state data fusion system using cellular handoff probe system and microwave sensors," in *Transportation Research Board 94th Annual Meeting*, 2015.
- [12] C. Bachmann, B. Abdulhai, M. J. Roorda, and B. Moshiri, "A comparative assessment of multi-sensor data fusion techniques for freeway traffic speed estimation using microsimulation modeling," *Transportation Research Part C: Emerging Technologies*, vol. 26, pp. 33–48, 2013.
- [13] C. Antoniou, H. N. Koutsopoulos, and G. Yannis, "Dynamic data-driven local traffic state estimation and prediction," *Transportation Research Part C: Emerging Technologies*, vol. 34, pp. 89–107, 2013.
- [14] N.-E. El Faouzi, "Data-driven aggregative schemes for multi-source estimation Fusion: A road travel time application," in *Proceedings of the Multisensor, Multisource Information Fusion: Architectures, Algorithms, and Applications 2004*, pp. 351–359, USA, April 2004.
- [15] M. Treiber, A. Kesting, and R. E. Wilson, "Reconstructing the traffic state by fusion of heterogeneous data," *Computer-Aided Civil and Infrastructure Engineering*, vol. 26, no. 6, pp. 408–419, 2011.
- [16] K. Choi and Y. Chung, "A data fusion algorithm for estimating link travel time," *Journal of Intelligent Transportation Systems: Technology, Planning, and Operations*, vol. 7, no. 3-4, pp. 235–260, 2002.
- [17] J. W. C. V. Lint and S. P. Hoogendoorn, "A robust and efficient method for fusing heterogeneous data from traffic sensors on freeways," *Computer-Aided Civil and Infrastructure Engineering*, vol. 25, no. 8, pp. 596–612, 2010.
- [18] L. Mannini, S. Carrese, E. Cipriani, and U. Crisalli, "On the short-term prediction of traffic state: An application on urban freeways in ROME," pp. 176–185.
- [19] B. Heilmann, N.-E. El Faouzi, O. de Mouzon et al., "Predicting Motorway Traffic Performance by Data Fusion of Local Sensor Data and Electronic Toll Collection Data," *Computer-Aided Civil and Infrastructure Engineering*, vol. 26, no. 6, pp. 451–463, 2011.
- [20] W. Deng, H. Lei, and X. Zhou, "Traffic state estimation and uncertainty quantification based on heterogeneous data sources: A three detector approach," *Transportation Research Part B: Methodological*, vol. 57, pp. 132–157, 2013.
- [21] S. He, Y. Cheng, G. Zhong, and B. Ran, "A data-driven study on the sample size of cellular handoff probe system," *Advances in Mechanical Engineering*, vol. 9, no. 4, pp. 1–9, 2017.
- [22] S. L. He, J. Zhang, Y. Cheng, X. Wan, and B. Ran, "Freeway Multisensor Data Fusion Approach Integrating Data from Cellphone Probes and Fixed Sensors," *Journal of Sensors*, vol. 2016, Article ID 7269382, 2016.
- [23] Z. T. Qiu, *Macroscopic traffic state estimation for large scale freeway network using wireless network data*, Doctor of Philosophy, University of Wisconsin-Madison, Madison, 2007.
- [24] J. Zhang, S. He, W. Wang, and F. Zhan, "Accuracy analysis of freeway traffic speed estimation based on the integration of cellular probe system and loop detectors," *Journal of Intelligent Transportation Systems: Technology, Planning, and Operations*, vol. 19, no. 4, pp. 411–426, 2015.
- [25] H. Rakha and W. Zhang, "Estimating traffic stream space-mean speed and reliability from dual and single loop detectors," *Transportation Research Record: Journal of the Transportation Research Board*, vol. 1925, pp. 38–47, 2005.
- [26] G. Welch and G. Bishop, *An Introduction to the Kalman filter*, University of North Carolina at Chapel Hill, 1995.

Research Article

QoS-Aware Resource Allocation for Network Virtualization in an Integrated Train Ground Communication System

Li Zhu ¹, Fei Wang,² and Hongli Zhao³

¹State Key Laboratory of Rail Traffic Control and Safety, Beijing Jiaotong University, Beijing, China

²Signal and Communication Research Institute, China Academy of Railway Sciences, Beijing, China

³National Engineering Research Center of Rail Transportation Operation and Control System, Beijing Jiaotong University, Beijing, China

Correspondence should be addressed to Li Zhu; zhulibjtu@gmail.com

Received 28 October 2017; Revised 26 January 2018; Accepted 11 February 2018; Published 3 May 2018

Academic Editor: Daniele Pinchera

Copyright © 2018 Li Zhu et al. This is an open access article distributed under the Creative Commons Attribution License, which permits unrestricted use, distribution, and reproduction in any medium, provided the original work is properly cited.

Urban rail transit plays an increasingly important role in urbanization processes. Communications-Based Train Control (CBTC) Systems, Passenger Information Systems (PIS), and Closed Circuit Television (CCTV) are key applications of urban rail transit to ensure its normal operation. In existing urban rail transit systems, different applications are deployed with independent train ground communication systems. When the train ground communication systems are built repeatedly, limited wireless spectrum will be wasted, and the maintenance work will also become complicated. In this paper, we design a network virtualization based integrated train ground communication system, in which all the applications in urban rail transit can share the same physical infrastructure. In order to better satisfy the Quality of Service (QoS) requirement of each application, this paper proposes a virtual resource allocation algorithm based on QoS guarantee, base station load balance, and application station fairness. Moreover, with the latest achievement of distributed convex optimization, we exploit a novel distributed optimization method based on alternating direction method of multipliers (ADMM) to solve the virtual resource allocation problem. Extensive simulation results indicate that the QoS of the designed integrated train ground communication system can be improved significantly using the proposed algorithm.

1. Introduction

With the city expansion and urban population explosion, the traditional road traffic facilities cannot satisfy the demand of modern society. Energetically developing urban rail transit system and improving the speed and capacity of rail transit have become desirable all over the world. Studies of urban rail transit have become a research focus among engineers and researchers all over the world.

The train ground communication is a key technology to ensure the normal operation of urban rail transit [1]. Most of the urban rail transit applications, such as Communications-Based Train Control (CBTC) Systems [2], Passenger Information Systems (PIS), and the Closed Circuit Television (CCTV), need train ground communication systems. In existing urban rail transit systems, CBTC, PIS, and CCTV adopt WLAN that use unlicensed spectrum as their train

ground communication technology [3]. The construction and management work of train ground communication systems for each application are independent in existing urban rail transit systems. It is a huge waste of limited wireless spectrum and other social resources to invest and build new communication infrastructures for each application. Maintaining these infrastructures will also become a great burden. In order to ensure the safety of urban rail transit operation, integrating all these communication system into a whole is quite desirable for urban rail transit systems.

The major opportunities and challenges in train ground communication systems are summarized in [4]. Lots of researchers have studied issues related to urban rail transit train ground communication recently. Literature [5] aims to present a comprehensive tutorial, as well as a survey of the state-of-the-art of CBTC and the role of radio communication in it. A summary of the evolution of the communication

technologies used for modern railway signalling, best practices in the design of a CBTC radio network, and the measures to optimize its availability are discussed as well. In [6], a MIMO-assisted handoff (MAHO) scheme for CBTC systems is proposed to reduce transmission and handoff delay. In [7], the Markov model of redundant and nonredundant CBTC train ground communication system structure is established to analyze the system reliability and availability. The effect of different system redundancy and the relationship between the availability of CBTC train ground communication system and the speed of train are also discussed. Channel modeling in CBTC train ground systems is intensively studied in [8, 9]. Combining Artificial Intelligence- (AI-) based decision-making and learning algorithms, Amanna et al. [10] present a railroad-specific cognitive radio (rail-CR) with software-defined radio (SDR). Based on periodical signal quality changes, the authors of [11] propose a scheduling and resource allocation mechanism to maximize the transmission rate for LTE based train ground communication system. For the handoff problem in train ground communication system, a seamless handoff scheme based on a dual-layer and dual-link system architecture is proposed in [12] to reduce communication interruption time. In our previous work, cross-layer handoff designs have been studied extensively in [13] for WLANs based CBTC train ground communication systems.

These above works study urban rail transit train ground communication system performance and analyze the influence of rail transit environment on system performance. However, most of the works only focus on independent applications. Few studies take all the train ground applications into consideration. Our previous works test an LTE based integrated train ground communication system performance [14–16]. We also study the handoff design in existing integrated train ground communication systems [3]. However, the problem of improper system wireless spectrum allocation is largely ignored in these works.

In the paper, we design a network virtualization based integrated train ground communication system for urban rail transit systems. With a variety of applications, the designed system can be updated from the existing system. This kind of design not only reduces construction and operational costs but also improves the spectrum utilization efficiency. In order to better meet the QoS requirement of applications in the designed system using wireless network virtualization technology [17], this paper proposes a virtual resource allocation algorithm based on QoS guarantee, base station (BS) load balance, and application station fairness. Meanwhile, we define a QoS satisfaction level (QoSL) parameter to reflect the application satisfaction. The final optimization goal is to ensure CBTC application reliability and maximize QoS satisfaction of all the application stations.

In addition, with the further development of distributed convex optimization, we develop a distributed wireless virtual resource allocation algorithm based on alternating direction method of multipliers (ADMM) [18] to solve the virtual resource allocation problem. Simulation results indicate that the QoS of the designed integrated train ground communication system can be remarkably improved with the proposed method.

The rest of the paper is organized as follows. In Section 2, the integrated train ground communication system architecture is introduced. Section 3 describes the system model and problem formulation. The virtual resource allocation problem transformation and solution using ADMM are discussed in Sections 4 and 5, respectively. Simulation results are given in Section 6. Finally, the conclusion is given in Section 7.

2. The Designed Integrated Train Ground Communication System Architecture

In this section, we first introduce the QoS requirement of different applications in train ground communication and then present the basic structure of the designed integrated train ground communication system. Next, we study how each of the virtualization characteristics are conducted in a physical BS. Finally, we depict the use of network virtualization in the designed system.

2.1. Applications in Urban Rail Transit Systems. Nowadays, there are mainly three applications in urban rail transit systems. They are Communication Based Train Control (CBTC) systems, Closed Circuit Television (CCTV), and Passenger Information Systems (PIS).

As shown in Figure 1, in CBTC systems, continuous bidirectional wireless communications between the ground base station (BS) and each onboard application station are used instead of the traditional track circuit based train control system. Trains will get the state of the front train and other obstacles from the Zone Controller (ZC). It will compute a braking curve, so as to stop at a proper position. Theoretically, the distance between two trains can be just a few meters, if both trains can get the real time position of the front train and both trains have the same speed and braking capability.

However, as explained in [19], when the train behind does not get the real time position of the front train due to train ground communication delay, it will trigger the brake to stop before entering a danger zone. This process will have a significant negative impact on CBTC system performance. Therefore, the most important QoS measure of train ground communication system is transmission delay. Typical values of required transmission delay and other suggested QoS measures in CBTC system are illustrated in Table 1.

In urban rail transit system, the other two crucial applications are PIS and CCTV. Taking advantages of advanced communication and multimedia techniques, diverse multimedia information such as weather forecast, train arriving time, and advertisement will be provided to passengers on trains and in stations through PIS. CCTV is a crucial additive means to guarantee train secure operation. By using CCTV, the urban rail control center can monitor the train carriage, station, and other essential zones through continuous train ground video transmission. For the PIS and CCTV application, throughput and jitter delay are the direct performance measure, since the high quality video needs higher throughput and less jitter delay.

The suggested values of transmission data rate and other suggested QoS measures in PIS and CCTV are illustrated in

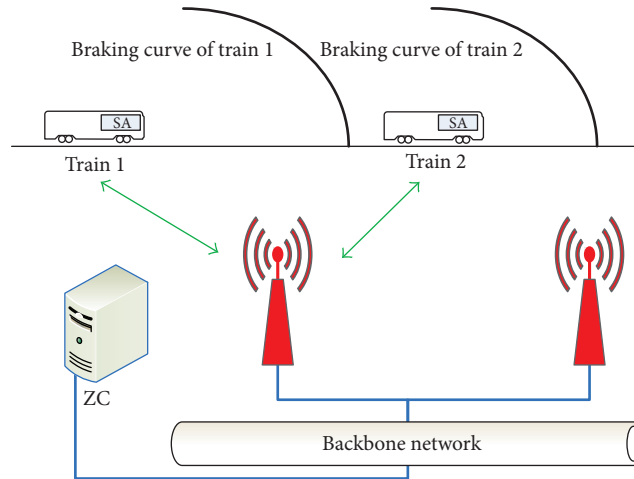


FIGURE 1: A typical CBTC system.

TABLE 1: The QoS requirement of different applications in urban rail transit systems.

Number	Application	Throughput	Packet loss rate	Transmission delay	Jitter delay	Reliability
1	CBTC	100 kbps	Less than 0.005	150 ms	None	High
2	CCTV	1 Mbps	None	500 ms	30 ms	Intermediate
3	PIS	4 Mbps	None	500 ms	30 ms	Intermediate

Table 1. We get this table by consulting several urban rail operation corporations in China. The data in Table 1 is not absolute performance requirement standard. As a matter of fact, urban rail operation corporations (especially corporations in different cities) have different communication QoS requirement for train ground applications. The performance requirement in this table is obtained by synthesizing various data from different corporations. We need to point out that the proposed optimization algorithm in our designed integrated train ground communication system is not dependent on the data in Table 1. Once we get more authoritative performance requirement parameters, they can be used in our optimization model and more accurate simulation results can be obtained.

The construction and management works of train ground communication system for each application are independent in existing urban rail transit system. It is a huge waste of limited wireless spectrum and other social resources to invest and build new communication infrastructures for each application. Recently, engineers try to design a system that combines all the applications together. The system architecture is shown in Figure 2. In order to improve CBTC system reliability, two independent ground infrastructures are used. There are two CBTC application stations on the train, which are installed on its nose and tail, and they are connected to different ground infrastructures. Two independent train ground infrastructures are allocated with constant spectrum. The PIS and CCTV application stations only connect to one of the ground infrastructures and share wireless spectrum with CBTC systems.

One disadvantage of the above system is the improper spectrum resource allocation scheme. The designed system

using two independent ground infrastructures guarantees the CBTC system reliability. However, the spectrum allocated to urban rail transit systems is limited, and all the channels used by different applications share the same spectrum. Channels needed by different applications are dynamically changing, and allocating constant channels to different applications will waste limited spectrum resource.

In order to better satisfy the QoS requirement of different applications, we design an integrated train ground communication system for urban rail transit system using wireless network virtualization techniques, which will be introduced in the next subsections.

2.2. Architecture of the Designed Integrated Train Ground Communication System. The designed system architecture is shown in Figure 3. Different from the existing system, in our designed system, the two infrastructures can be connected by PIS and CCTV application stations as well as both the two CBTC application stations.

The proposed integrated train ground communication system architecture is shown in Figure 4. For a certain railway line, it is assumed that there is only one physical infrastructure provider (PiP), which provides three different network services to the train with three different application stations. According to the general wireless network virtualization definition, the proposed architecture can be divided into two separate layers: the control and management layer (CML) and the virtualization layer (VL).

The main responsibility of CML is resource management. The main functions of CML are realized by several virtual network controllers and a hypervisor. Every virtual network has

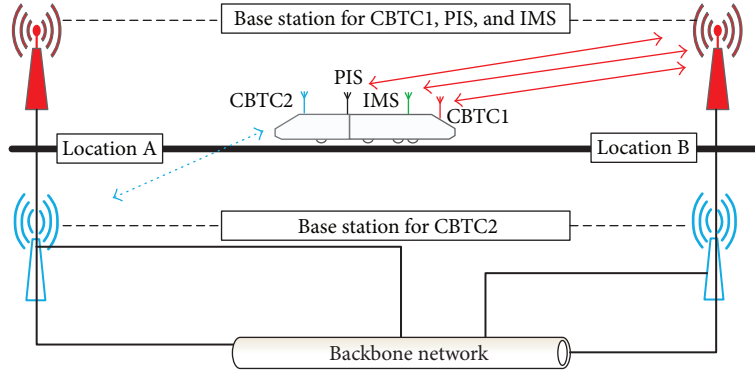


FIGURE 2: Existing integrated train ground communication systems.

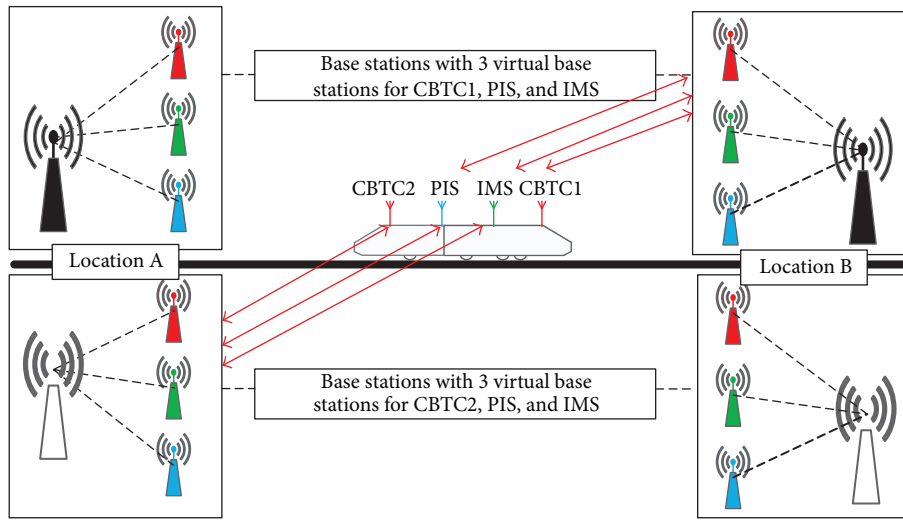


FIGURE 3: The proposed integrated train ground communication system.

its own network controller, which is responsible for scheduling application stations, determining their QoS requirement, and informing the hypervisor of them. The hypervisor can flexibly allocate the virtual resources to virtual networks under different circumstances according to the feedback information (transmit power, e.g., and available spectrum) and different QoS requirements. The whole network has one hypervisor. By using wireless network virtualization, each application station could be served via the same PiPs and different spectrum resources.

The VL is accountable for the abstraction, programmability, and isolation of physical resources in a certain physical base station (BS). Using various VL functions, the PiP will be able to broadcast beacons for virtual BSs of various applications. In addition, each of the virtual networks should have independent control of settings in their virtual BSs. They can set different attributes for virtual BSs, such as various security policies, broadcast domains, and IP settings. Furthermore, the virtual BSs can be isolated by different wireless spectrum.

The VL also provides the CML with the interfaces needed to control virtualized resources (spectrums, transmission

power, etc.). With VL, both the PiP and the wireless resources are virtualized and shared by various virtual networks.

The virtual resource allocation is one key issue in the above system. Physical and wireless virtual resources should be dynamically allocated to the CBTC, PIS, and CCTV according to their requirement. If the virtual resource allocation scheme is not carefully designed, the normal CBTC system function will not be ensured. The video transmission quality of PIS and CCTV will degrade. This will have a significant negative impact on urban rail transit system. To this point, we will study virtual resource allocation schemes in the following sections.

3. System Model and Problem Formulation

In the designed system, we define \mathcal{N} as the base station (BS) sets, $\mathcal{N} = \{1, 2, \dots, N\}$. The integrated system is virtualized into multiple virtual BSs (VBSS) for different services. The system has a set \mathcal{K} of VBSS, $\mathcal{K} = \{1, 2, \dots, K\}$. For each VBS k , $k \in \mathcal{K}$, \mathcal{V}_k is the set of application stations of VBS k , and v_k is one of application stations served by VBS k , $v_k \in \mathcal{V}_k$. In the integrated system, a wireless channel is a

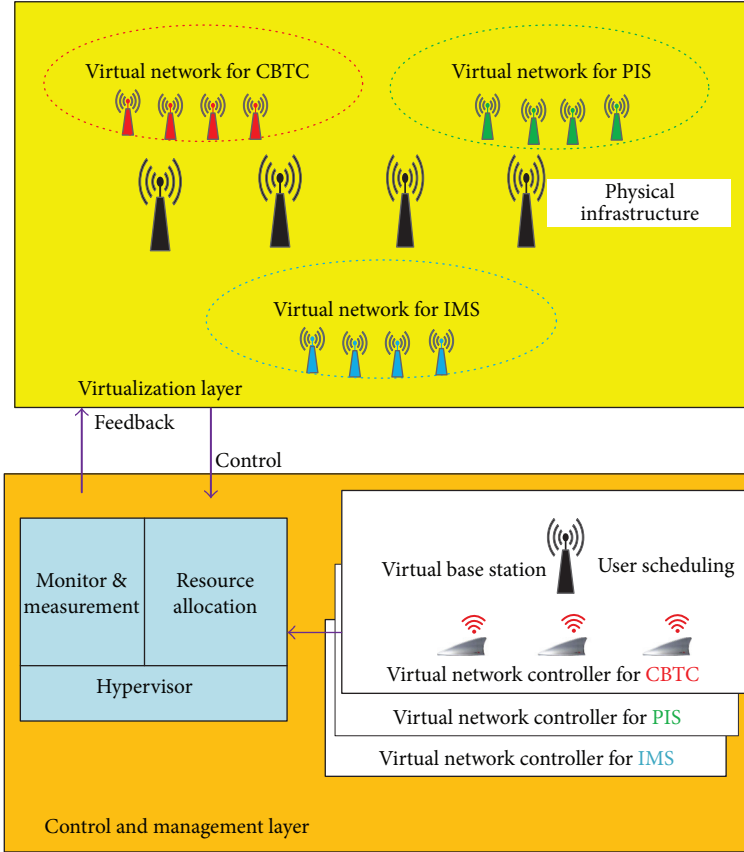


FIGURE 4: A framework of using wireless network virtualization in the proposed system.

granularity of physical wireless resources for the hypervisor. Each VBS needs a certain amount of subchannels to complete the QoS requirement for applications. We define m_n as a subchannel of BSn . \mathcal{M}_n is the set of all available channels of physical BSn , given the legal frequency spectrum. We assume power is evenly distributed in each channel. The hypervisor can accurately obtain the Channel state Information (CSI), available spectrum, and the QoS requirement of application stations. In order to improve the utilization of spectrum resource, each subchannel can adopt different

modulation mode according to the channel state information.

The virtual resource allocation optimization can be described as maximizing the total application satisfaction on the condition of system constraints. The strictly concave, monotonically increasing, and continuously differentiable logarithmic utility function [20] is used to ensure proportionally fair resource allocation. The Opt-U1 formulations are given as follows:

Opt-U1:

$$\begin{aligned}
 & \max_{\alpha, \beta} \sum_{k \in \mathcal{K}, v_k \in \mathcal{V}_k} \sum_{n \in \mathcal{N}, m_n \in \mathcal{M}_n} \log \left(\frac{\Gamma^P(\alpha_{v_k n}, \beta_{v_k m_n})}{\Psi^P} + \frac{\Gamma^I(\alpha_{v_k n}, \beta_{v_k m_n})}{\Psi^I} + \frac{\Gamma^C(\alpha_{v_k n}, \beta_{v_k m_n})}{\Psi^C} \right) \\
 & \text{s.t.} \quad \sum_{n \in \mathcal{N}} \alpha_{v_k n} = 1, \quad \alpha_{v_k n} \in \{0, 1\}, \quad \forall k \in \mathcal{K}, \quad \forall v_k \in \mathcal{V}_k \\
 & \quad \sum_{k \in \mathcal{K}, v_k \in \mathcal{V}_k} \beta_{v_k m_n} = 1, \quad \beta_{v_k m_n} \in \{0, 1\}, \quad \forall n \in \mathcal{N}, \quad \forall m_n \in \mathcal{M}_n \\
 & \quad \tau_{v_k}^{\text{CBTC}} \leq T_{\text{req}},
 \end{aligned} \tag{1}$$

where $\Gamma^P(x)$, $\Gamma^I(x)$, and $\Gamma^C(x)$ are the reward function for applications with virtual resource association strategies

$\alpha_{v_k n}$ and $\beta_{v_k m_n}$ and Ψ^P , Ψ^I , and Ψ^C denote the suggested performance value for different applications. $\alpha_{v_k n}$ and $\beta_{v_k m_n}$

are assignment indicators. If application station v_k is assigned to BS n and subchannel m is assigned to user v_k , $\alpha_{v_k n} = 1$, and $\beta_{v_k m_n} = 1$; otherwise $\alpha_{v_k n} = 0$, and $\beta_{v_k m_n} = 0$. An application station is only served by one BS, and one subchannel is not assigned to multiple application stations. The inequality reflects the fact that the transmission delay τ_{v_k} of CBTC application station cannot exceed its requirement threshold T_{req} .

When we define QoS satisfaction level (QoSL) of application station SL_{v_k} as

$$SL_{v_k} = \frac{\sum_{n \in N, m_n \in M_n} \Gamma^X(\alpha_{v_k n}, \beta_{v_k m_n})}{\Psi^X}, \quad X = P, I, C, \quad (2)$$

the optimization functions can be transformed as follows:

Opt-U2:

$$\max_{\alpha, \beta} \sum_{k \in \mathcal{K}, v_k \in \mathcal{V}_k} \log(SL_{v_k}). \quad (3)$$

For the PIS and CCTV application, our objective is to maximize their data transmission throughput and minimize their jitter delay. Therefore, the reward function for these two applications can be defined as

$$\Gamma_P(\alpha_{v_k n}, \beta_{v_k m_n}) = \Gamma_I(\alpha_{v_k n}, \beta_{v_k m_n}) = \alpha_{v_k n} \beta_{v_k m_n} \mathfrak{R}_{v_k m_n} \quad (4)$$

or

$$\Gamma_P(\alpha_{v_k n}, \beta_{v_k m_n}) = \Gamma_I(\alpha_{v_k n}, \beta_{v_k m_n}) = \alpha_{v_k n} \beta_{v_k m_n} \Xi_{v_k m_n}, \quad (5)$$

where $\mathfrak{R}_{v_k m_n}$ is the achievable data rate between the subchannel m_n and user v_k . It is a function of the subchannel available bandwidth B_{m_n} , the SNR ξ , and the bit error rate BER and can be computed as follows [21]:

$$\mathfrak{R}_{v_k m_n} = B_{m_n} * \log_2 \left(1 + \frac{-1.5 * \xi}{\ln(5 * P_{v_k}^{\text{BER}})} \right). \quad (6)$$

$\Xi_{v_k m_n}$ is the jitter delay when subchannel m_n is used for user v_k .

For the CBTC application, it is important to maintain the quick response time between the train and ground. Therefore, the reward function that reflects the transmission delay can be defined as

$$\Gamma_C(\alpha_{v_k n}, \beta_{v_k m_n}) = \alpha_{v_k n} \beta_{v_k m_n} \Upsilon_{v_k m_n}, \quad (7)$$

where $\Upsilon_{v_k m_n}$ is the achievable data transmission delay.

Combined with small-scale fading and large-scale fading, we get the received SNR ξ as

$$\xi = P_t - P_{\text{loss}} + \chi + 10 \log_{10}(\vartheta) + G_t + G_r - P_{\text{noise}}, \quad (8)$$

where P_t is the transmitted power, P_{loss} is the large-scale path loss, ϑ is a Rayleigh random variable with a mean of 1 when we use Rayleigh distribution to describe the fading envelope, χ is a Gaussian random variable with a variance of ζ and a mean of 0, G_t and G_r are the antenna gains for the transmitter and

receiver, respectively, and P_{noise} is the noise power. The path loss value P_{loss} is dependent on the working frequency and transmission environment. In this paper, we use the path loss model described in [21].

The BER is determined by the suggested packet loss rate PLR given in Table 1. This is because, given the link BER, the Frame Error Rate FER and PLR are computed as

$$\begin{aligned} \text{FER} &= 1 - (1 - \text{BER})^L, \\ \text{PLR} &= \text{FER}^{\text{MR}}, \end{aligned} \quad (9)$$

where L is the packet length and MR is the maximum transmission time.

In this paper, we take LTE link layer as an example to compute the end to end transmission delay. LTE is a new generation of wireless communication technology, and it has become the dominant train ground communication technology for next-generation CBTC systems [15]. In LTE systems, Hybrid Automatic Repeat Quest (HARQ) is used as an error control code. Given a retransmission time R , the transmission delay can be computed as

$$Y_{v_k m_n}(R) = T_{\text{data}} + R \times T_{\text{RTT}}, \quad (10)$$

where T_{data} is the packet transmission time dependent on transmission rate.

T_{RTT} is the Round Trip Time (RTT), which is approximately computed as

$$T_{\text{RTT}} = T_{\text{data}}^u + T_{\text{data}}^d + T_{\text{process}}, \quad (11)$$

where T_{data}^u and T_{data}^d are the uplink and downlink data transmission delay, and T_{process} is the process time at BS and application stations.

Given the retransmission time with R times retransmission, the average transmission time with maximum retransmission time MR can be computed as

$$\begin{aligned} T_{\text{MR}}^{\text{ave}} &= (1 - \text{FER}) * Y_{v_k m_n}(0) + \text{FER} (1 - \text{FER}) \\ &\quad * Y_{v_k m_n}(1) + \dots + \text{FER}^{\text{MR}-1} (1 - \text{FER}) \\ &\quad * Y_{v_k m_n}(\text{MR} - 1). \end{aligned} \quad (12)$$

The jitter delay is considered as the standard deviation of transmission delay at any slot. Therefore, with the maximum retransmission time MR, the jitter delay can be computed as

$$\begin{aligned} \text{JD}_{\text{MR}} &= \sqrt{(Y_{v_k m_n}(0) - T_{\text{MR}}^{\text{ave}})^2 + \dots + (Y_{v_k m_n}(\text{MR}) - T_{\text{MR}}^{\text{ave}})^2}. \end{aligned} \quad (13)$$

4. Problem Transformation

It is hard to solve problem Opt-U1 based on the following reasons. First, too many constraints make the problem becomes complex. And next, due to the Boolean value of $\{\alpha_{v_k n}\}$ and $\{\beta_{v_k m_n}\}$, both the objective function and the feasible set of Opt-U1 are not convex.

According to the method in [22], the binary variables of $\{\alpha_{v_k n}\}$ and $\{\beta_{v_k m_n}\}$ can be relaxed (i.e., we assume that $0 \leq \alpha_{v_k n} \leq 1$ and $0 \leq \beta_{v_k m_n} \leq 1$, for all k, n). We define $\omega_{v_k n} = \alpha_{v_k n} \beta_{v_k n}$, and

$$\beta_{v_k n} = \sum_{m_n \in \mathcal{M}_n} \beta_{v_k m_n}, \quad (14)$$

where $\beta_{v_k n} \in [0, 1]$ is used to denote the proportion of wireless resource allocated by BS n to user v_k . Then the problem Opt-U2 obtains an equivalent transformation as follows:

Opt-U3:

$$\max_{\alpha, \beta} \sum_{k \in \mathcal{K}, v_k \in \mathcal{V}_k} \sum_{n \in \mathcal{N}} \alpha_{v_k n} \log \left(\frac{\mathfrak{R}_{v_k n} \omega_{v_k n}}{\Psi^P \alpha_{v_k n}} \right) \quad (15a)$$

$$\frac{\mathfrak{R}_{v_k n} \omega_{v_k n}}{\Psi^I \alpha_{v_k n}} + \frac{\Xi_{v_k n} \omega_{v_k n}}{\Psi^P \alpha_{v_k n}} + \frac{\Xi_{v_k n} \omega_{v_k n}}{\Psi^I \alpha_{v_k n}} + \frac{\Upsilon_{v_k n} \omega_{v_k n}}{\Psi^C \alpha_{v_k n}} \quad (15b)$$

$$\text{s.t.} \quad \sum_{n \in \mathcal{N}} \alpha_{v_k n} = 1, \quad \alpha_{v_k n} \in \{0, 1\}, \quad \forall k \in \mathcal{K}, \quad \forall v_k \in \mathcal{V}_k \quad (15c)$$

$$\sum_{k \in \mathcal{K}, v_k \in \mathcal{V}_k} \omega_{v_k n} \leq 1, \quad \forall n \in \mathcal{N}. \quad (15d)$$

Obviously, when $\alpha_{v_k n} = 0$, we have $\beta_{v_k n} = 0$, which means that the application station is not associated with any BS. Literature [23] gives the proof of the convexity for problem (14).

5. Virtual Resource Allocation Using ADMM

As a general solution, the CVX tool can be used to solve the convex program in (14). Given the optimal association indicator matrix $X^* = \{\alpha_{v_k n}\}$ and the optimal resource allocation indicators matrix $Y^* = \{\beta_{v_k n}\}$ at time t , the corresponding allocation scheme can be described as

$$\begin{aligned} X^* &= \arg \max_{\alpha} \sum_{k \in \mathcal{K}, v_k \in \mathcal{V}_k} \sum_{n \in \mathcal{N}} \frac{\partial U_{v_k}(\text{SL}_{v_k})}{\text{SL}_{v_k}} \\ &\cdot \left(\frac{\mathfrak{R}_{v_k n} \beta_{v_k n}}{\Psi^P} + \frac{\mathfrak{R}_{v_k n} \beta_{v_k n}}{\Psi^I} \right. \\ &\quad \left. + \frac{\Xi_{v_k n} \beta_{v_k n}}{\Psi^P} + \frac{\Xi_{v_k n} \beta_{v_k n}}{\Psi^I} + \frac{\Upsilon_{v_k n} \beta_{v_k n}}{\Psi^C} \right) \\ Y^* &= \arg \max_{\beta} \sum_{k \in \mathcal{K}, v_k \in \mathcal{V}_k} \sum_{n \in \mathcal{N}} \frac{\partial U_{v_k}(\text{SL}_{v_k})}{\text{SL}_{v_k}} \\ &\cdot \left(\frac{\mathfrak{R}_{v_k n} \alpha_{v_k n}}{\Psi^P} + \frac{\mathfrak{R}_{v_k n} \alpha_{v_k n}}{\Psi^I} + \frac{\Xi_{v_k n} \beta_{v_k n}}{\Psi^P} + \frac{\Xi_{v_k n} \beta_{v_k n}}{\Psi^I} \right. \\ &\quad \left. + \frac{\Upsilon_{v_k n} \beta_{v_k n}}{\Psi^C} \right). \end{aligned} \quad (16)$$

Observed from the above two formulas, to get the optimal allocation scheme, the centralized algorithm must obtain the achievable rate $\mathfrak{R}_{v_k n}$ of all users at time t and the average satisfaction level $\partial U_{v_k}(\text{SL}_{v_k})/\text{SL}_{v_k}$ of all users at time $t - 1$. This results in a relatively large amount of calculation for the high speed urban rail transit system. In order to overcome it, we use ADMM to solve the convex problem. ADMM is a computing framework for optimization. It is suitable for solving distributed convex optimization problem, especially the statistical learning problems [18].

In order to use ADMM to solve the convex optimization, local copies of the global assignment indicators are introduced. Roughly speaking, each local variable can be interpreted as the information owned by each BS about the corresponding global assignment indicators variable.

To drive the local copies into consensus, we use distributed consensus ADMM method [18]. Let $\Delta = \{\alpha_{v_k n}, \forall v, k, n\}$ denote the vector of assignment indicators and ε_n denote the local copy of Δ at BS n . To the consensus constraints, we introduce an auxiliary variable $\varepsilon_{v_k n}$ which represents the local copies of our assignment indicators as equality constraints:

$$\varepsilon_{v_k n} = \alpha_{v_k n}, \quad \forall v, k, n. \quad (17)$$

Given the local vectors $\Omega_n = \{\varepsilon_n, \forall n\}$ and $\ell_n = \{\omega_n, \forall n\}$, we define a feasible local variable set for each BS $n \in \mathcal{N}$. The constraints in (15b) can be decomposed into N independent convex sets as

$$\Lambda_n = \left\{ \Omega_n, \ell_n \mid \sum_{k \in \mathcal{K}, v_k \in \mathcal{V}_k} \omega_{v_k n} \leq 1, \quad \forall n \in \mathcal{N} \right\} \quad (18)$$

and an associated local utility function as

$$\begin{aligned} u_n &= \begin{cases} - \sum_{k \in \mathcal{K}, v_k \in \mathcal{V}_k} \varepsilon_{v_k n} \log \left(\frac{\mathfrak{R}_{v_k n} \omega_{v_k n}}{\Upsilon_{v_k n} \varepsilon_{v_k n}} \right) \Omega_n, & \ell_n \in \Lambda_n \\ \infty & \text{otherwise.} \end{cases} \quad (19) \end{aligned}$$

Using (17) and (18) and the auxiliary variable $\varepsilon_{v_k n}$, we can compactly write the global consensus problem (14) as

$$\begin{aligned} \min \quad & \sum_{n \in \mathcal{N}} u_n(\Omega_n, \ell_n) \\ \text{s.t.} \quad & \varepsilon_{v_k n} = \alpha_{v_k n}, \quad \forall v, k, n. \end{aligned} \quad (20)$$

Then the augmented Lagrangian function for (19) can be rewritten as

$$\begin{aligned} \mathcal{L}_{\rho}(\{\Omega_n, \ell_n\}, \{\Delta\}, \{\sigma_n\}) &= \sum_{n \in \mathcal{N}} u_n(\Omega_n, \ell_n) + \sum_{n \in \mathcal{N}} \sum_{k \in \mathcal{K}, v_k \in \mathcal{V}_k} \sigma_{v_k n} (\varepsilon_{v_k n} - \alpha_{v_k n}) \\ &\quad + \left(\frac{\rho}{2} \right) \sum_{n \in \mathcal{N}} \sum_{k \in \mathcal{K}, v_k \in \mathcal{V}_k} (\varepsilon_{v_k n} - \alpha_{v_k n})^2, \end{aligned} \quad (21)$$

where $\sigma_{v_k n}$ is the Lagrange multipliers related to the constraints of consensus in problem (19) and $\rho > 0$ is a penalty parameter for adjusting the convergence speed of the ADMM [18].

The basic idea of ADMM is that convex optimization is broken into smaller partitions, each of which are then easier

to handle. The ADMM method is composed of successive optimization steps by updating the primal and dual variables alternately. For optimization, at iteration q we need to take the following steps:

$$\begin{aligned} \{\Omega_n, \ell_n\}_{n \in \mathcal{N}}^{q+1} &= \arg \min \left\{ u_n(\Omega_n, \ell_n) + \sum_{k \in \mathcal{K}, v_k \in \mathcal{V}_k} \sigma_{v_k n}^q (\varepsilon_{v_k n} - \alpha_{v_k n}^q) + \left(\frac{\rho}{2}\right) \sum_{k \in \mathcal{K}, v_k \in \mathcal{V}_k} (\varepsilon_{v_k n} - \alpha_{v_k n}^q)^2 \right\} \\ \{\Delta\}^{q+1} &= \arg \min \left\{ \sum_{n \in \mathcal{N}} \sum_{k \in \mathcal{K}, v_k \in \mathcal{V}_k} \sigma_{v_k n}^q (\varepsilon_{v_k n}^{q+1} - \alpha_{v_k n}) + \left(\frac{\rho}{2}\right) \sum_{n \in \mathcal{N}} \sum_{k \in \mathcal{K}, v_k \in \mathcal{V}_k} (\varepsilon_{v_k n}^{q+1} - \alpha_{v_k n})^2 \right\} \\ \{\sigma_n\}_{n \in \mathcal{N}}^{q+1} &= \sigma_n^q + \rho (\Omega_n^{q+1} - \Delta^{q+1}) \end{aligned} \quad (22)$$

6. Simulation Results and Discussions

In this section, we use MATLAB 2015b to carry out simulation. Simulation results are presented to illustrate the optimal performance of the proposed algorithm.

In order to simplify the simulation model, we consider that there are four physical base stations in the integrated train ground communication system and each physical BS can be virtualized into three virtual base stations, providing three services, CBTC, PIS, and CCTV, respectively, as shown in Figure 5. Among them, the red network base stations BS1 and BS2 belong to the infrastructure InP1, and the blue network base stations BS3 and BS4 belong to the infrastructure InP2. BS1 and BS3 or BS2 and BS4 cover the same geographic area, which forms the redundant coverage and ensures the reliability of CBTC systems. We assume wireless virtualization can be used between different InPs. Wireless spectrum resources can be shared by multiple virtual base stations virtualized from BS1 and BS3 or BS2 and BS4. For application stations, there is no obvious difference between different infrastructures as if all resources are within the same resource pool (e.g., f_{CBTC} , f_{PIS} , and f_{CCTV} are within the same resource pool).

In order to illustrate the performance improvement of our proposed algorithm, we compare it with the existing algorithm. In the existing algorithm, the application stations connect base stations providing the maximum received signal strength (RSS), and each BS carries out wireless spectrum resource allocation with proportional fairness. We name the existing scheme as Max-RSS.

As we can observe from Figure 6(a), under the Max-RSS scheme, some of the application station satisfaction level is less than zero, which makes the QoS of these application stations not guaranteed. However, the QoS requirement of all application stations can be satisfied with the proposed WVRA scheme as shown in Figure 6(b). This is because there are more than one application station associated with the same base station at the same time, but the application stations connect base stations providing the maximum received signal strength (RSS) when Max-RSS scheme is adopted, and the QoS guarantee is not considered. On the contrary, the WVRA

scheme fully considers the QoS guarantee, base station (BS) load balance, and application station fairness. By taking this scheme, the QoS requirement of each application station is guaranteed.

Next, we assess the fairness performance of different algorithms using fairness index described in literature [24]. If the fairness index is close to 1, it means the algorithm has a higher degree of fairness, and vice versa. The fairness index is defined as follows:

$$\text{FI}(\text{SL}_{v_k}) = \frac{(\sum_{k=1}^{K} \text{SL}_{v_k})^2}{K \sum_{k=1}^{K} \text{SL}_{v_k}^2}. \quad (23)$$

As we can observe from Figure 7, with the gradual increase of the application stations in the cell, the Max-RSS algorithm cannot guarantee the fair distribution of virtual resources. It is mainly because the wireless resources are limited, and strong competition between applications leads to the decrease of fairness. However, our proposed algorithm WVRA effectively ensures the fairness of the virtual resource allocation. Although application stations continue to increase, the fairness index keeps unchanged, which means the virtual resources can still be fairly allocated.

In order to verify the jitter delay performance improvement of PIS and CCTV applications, we illustrate the transmission delay of CCTV application in Figure 8. The transmission delays of our proposed WVRA scheme are more volatile compared with the existing scheme, which means the proposed WVRA scheme performs better in terms of jitter delay. This is due to the fact that the WVRA scheme fully considers the QoS requirement of all applications, and one of the direct optimization objectives is to minimize the jitter delay of PIS and CCTV. We also notice that WVRA scheme sacrifices part of transmission delay performance to realize its optimization objective.

We study the spectrum allocation between virtual base station of physical base stations and compare each BS load fluctuation in Figures 9 and 10, respectively. As illustrated in Figure 9, the spectrum allocated to VBS1 with the CBTC application is approximately unchanged in each time slot.

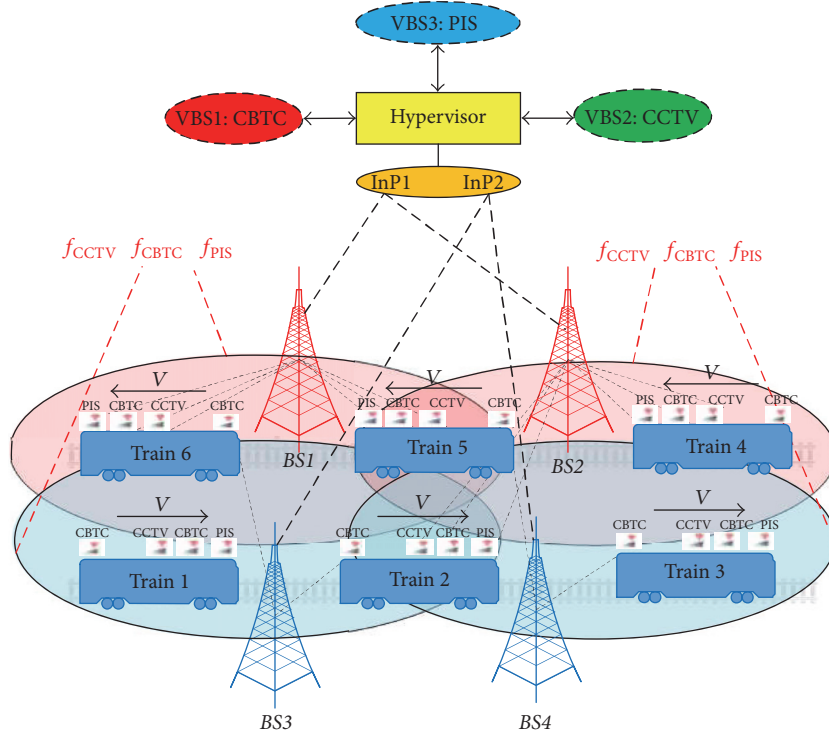


FIGURE 5: System model with four base stations and three virtual base stations for CBTC, PIS, and CCTV, respectively.

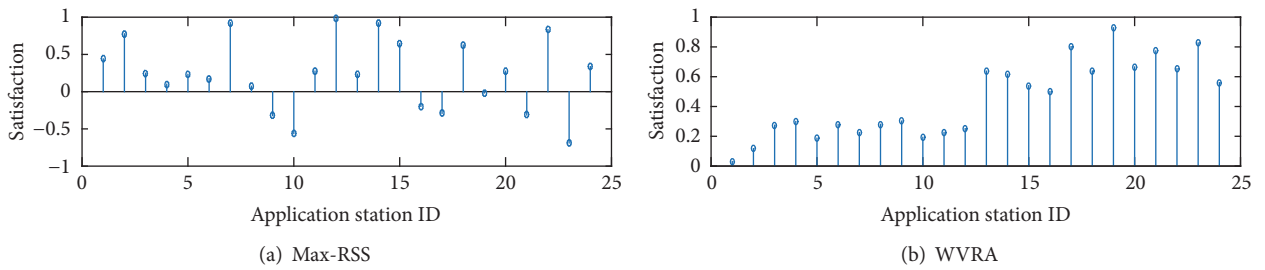


FIGURE 6: QoS satisfaction level improvement under different algorithms.

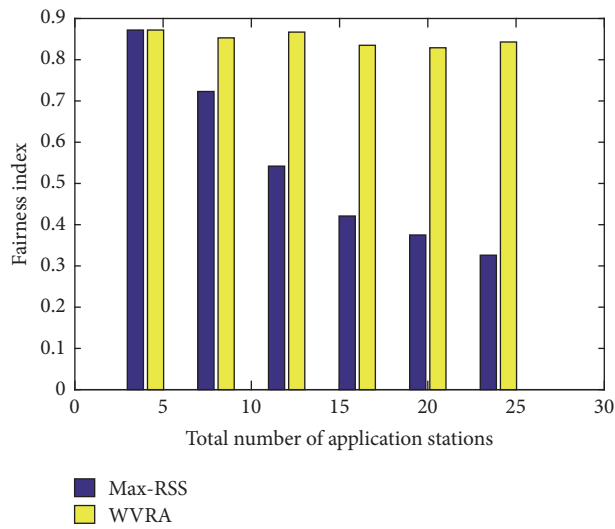


FIGURE 7: Comparison of fairness index for different resource allocation algorithms.

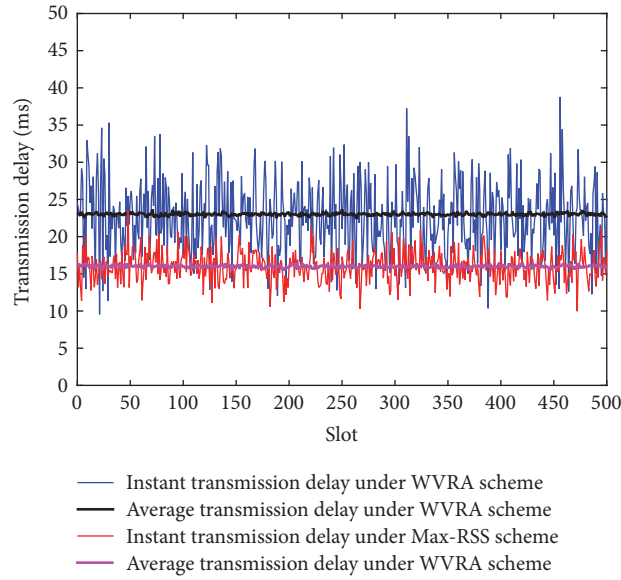


FIGURE 8: Transmission delay of the CCTV application under different scheme.

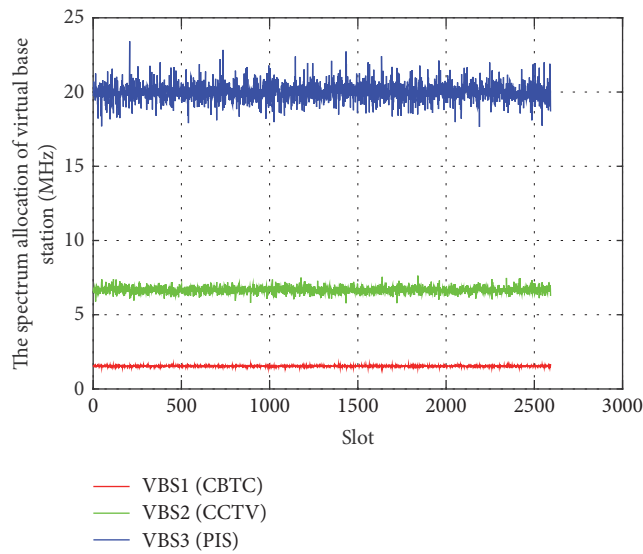


FIGURE 9: Wireless spectrum allocation for each VBS using WVRA.

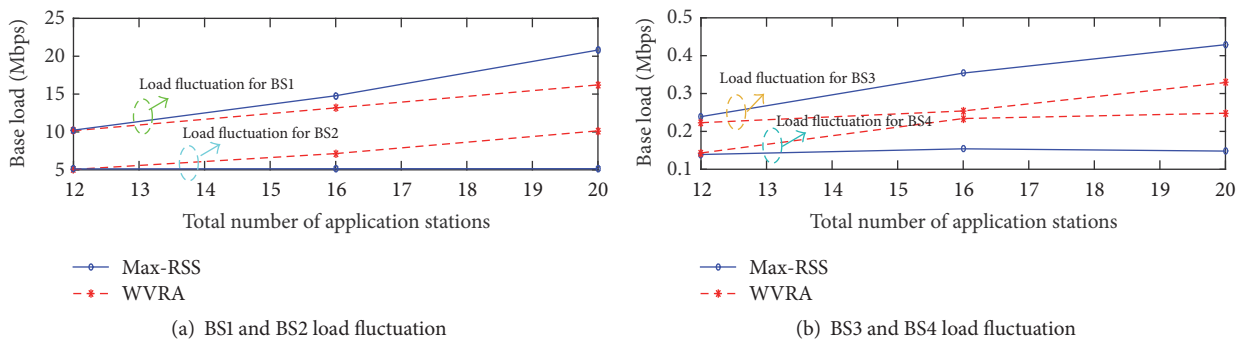


FIGURE 10: BS load using different resource allocation algorithms.

This is because the optimization objective of CBTC application is not the transmission data rate, and the required spectrum is relatively stable. As for the other two VBSs that carry the PIS and CCTV application traffic, we can notice that the spectrum allocated to them changes at each time slot with the traffic load. This is due to the fact that maximizing the transmission throughput needs large amount of spectrums.

In order to verify the load balance performance, we set up the simulation environment where the BS1 and BS3 give a higher received signal strength in the overlap zone. Figure 10 shows the change of base station load when the number of application stations increases in its coverage area. The red line in the figure represents the effect of the Max-RSS scheme on the base station load. The blue line represents the effect of the WVRA scheme on the base station load. The green oval represents BS1 load fluctuations. The aquamarine blue oval represents BS2 load fluctuations. The yellow oval represents BS3 load fluctuation. The final oval represents the BS4 load fluctuations. As shown in Figure 10, we can observe that, by using the Max-RSS scheme, the loads of BS1 and BS3 increase constantly, while the loads of BS2 and BS4 do not change with the increase of the number of the application stations. This is due to the fact that application station fairness is not considered under this scheme. On the contrary, the WVRA scheme successfully separates part of the load of BS1 and BS3 to the more lightly loaded BS2 and BS4, although BS2 and BS4 offer a lower instantaneous received signal strength than BS1 and BS3.

7. Conclusions

In this paper, we have proposed a framework of using network virtualization in an integrated train ground communication system. We have formulated and transformed the QoS-aware virtual resource allocation problem in the integrated system to a convex optimization problem. We define the QoS salification level parameter to reflect the application satisfaction. The final objective is fairness driven optimization function based on QoS guarantee, base station load balance, and application station fairness. We use the distributed method based on ADMM to solve the convex problem. Simulation results indicate that our algorithm can guarantee the QoS requirement of all application stations. Meanwhile, the traffic load of different base stations can be balanced to achieve better performance of the whole system.

Simulation Parameters

τ :	Slot time, 50 ms
P_t :	Transmission power, 43 dBm
G_t, G_r :	Antenna gain, 8 dB
L :	Average packet size, 200 bytes
MR:	Maximum transmission time, 6
T_{process} :	Process time at BS or station, 10 ms
D :	Average base station space, 1000 m
v :	Train speed, 80 km/h
ζ :	Shadowing fading standard deviation, 8
P_{noise} :	Noise power, -100 dbm.

Conflicts of Interest

The authors declare that there are no conflicts of interest regarding the publication of this paper.

Acknowledgments

This paper was supported by grants from Beijing Natural Science Foundation (L171004, I18E300010), by the National Natural Science Foundation of China (no. 61603026), by Technological Research and Development Program of China Railway Corporation (Grant 2016X008-B), by Fundamental Research Funds for the Central Universities (2015JBM005), by Projects RCS2017ZT003, RCS2017ZT006, and KIE017001531, and by the Beijing Key Laboratory of Urban Rail Transit Automation and Control.

References

- [1] T. Xu, T. Tang, C. Gao, and B. Cai, "Dependability analysis of the data communication system in train control system," *Science China Technological Sciences*, vol. 52, no. 9, pp. 2605–2618, 2009.
- [2] R. Pascoe and T. Eichorn, "What is communication-based train control?" *IEEE Vehicular Technology Magazine*, vol. 4, no. 4, pp. 16–21, 2009.
- [3] L. Zhu, F. R. Yu, T. Tang, and B. Ning, "Handoff Performance Improvements in an Integrated Train-Ground Communication System Based on Wireless Network Virtualization," *IEEE Transactions on Intelligent Transportation Systems*, vol. 18, no. 5, pp. 1165–1178, 2017.
- [4] J. Moreno, J. Riera, L. De Haro, and C. Rodriguez, "A survey on future railway radio communications services: challenges and opportunities," *IEEE Communications Magazine*, vol. 53, no. 10, pp. 62–68, 2015.
- [5] J. Farooq and J. Soler, "Radio Communication for Communications-Based Train Control (CBTC): A Tutorial and Survey," *IEEE Communications Surveys & Tutorials*, vol. 19, no. 3, pp. 1377–1402, 2017.
- [6] H. Jiang, V. C. M. Leung, C. Gao, and T. Tang, "MIMO-assisted handoff scheme for communication-based train control systems," *IEEE Transactions on Vehicular Technology*, vol. 64, no. 4, pp. 1578–1590, 2015.
- [7] X. U. Tian-Hua, L. I. Shu, and T. Tao, "Dependability analysis of data communication subsystem in train control system," *Journal of Beijing Jiaotong University*, vol. 31, no. 5, pp. 23–21, 2007.
- [8] K. Guan, Z. Zhong, B. Ai, and C. Briso-Rodríguez, "Measurement and modeling of subway near shadowing phenomenon," in *Proceedings of the 5th International ICST Conference on Communications and Networking in China, ChinaCom 2010*, August 2010.
- [9] K. Guan, Z. D. Zhong, J. I. Alonso, and C. Briso-Rodríguez, "Measurement of distributed antenna systems at 2.4 GHz in a realistic subway tunnel environment," *IEEE Transactions on Vehicular Technology*, vol. 61, no. 2, pp. 834–837, 2012.
- [10] A. Amanna, M. Gadniok, M. Price, J. Reed, W. Siriwongpairat, and T. Himsoon, "Railway cognitive radio: Future wireless communication systems for railways," *IEEE Vehicular Technology Magazine*, vol. 5, no. 3, pp. 82–89, 2010.
- [11] O. B. Karimi, J. Liu, and C. Wang, "Seamless wireless connectivity for multimedia services in high speed trains," *IEEE Journal*

- on *Selected Areas in Communications*, vol. 30, no. 4, pp. 729–739, 2012.
- [12] L. Tian, J. Li, Y. Huang, J. Shi, and J. Zhou, “Seamless dual-link handover scheme in broadband wireless communication systems for high-speed rail,” *IEEE Journal on Selected Areas in Communications*, vol. 30, no. 4, pp. 708–717, 2012.
- [13] L. Zhu, F. Richard Yu, T. Tang, and B. Ning, “An Integrated Train-Ground Communication System Using Wireless Network Virtualization: Security and Quality of Service Provisioning,” *IEEE Transactions on Vehicular Technology*, vol. 65, no. 12, pp. 9607–9616, 2016.
- [14] H. Zhao, L. Zhu, H. Jiang, and T. Tang, “Design and performance tests in an integrated TD-LTE based train ground communication system,” in *Proceedings of the 2014 17th IEEE International Conference on Intelligent Transportation Systems, ITSC 2014*, pp. 747–750, China, October 2014.
- [15] T. Tang, K. Dai, Y. Zhang, H. Zhao, and H. Jiang, “Field test results analysis in urban rail transit train ground communication systems of integrated service using LTE-M,” in *Proceedings of the 19th IEEE International Conference on Intelligent Transportation Systems, ITSC 2016*, pp. 2017–2021, Brazil, November 2016.
- [16] F. Wang, L. Zhu, and H. Zhao, “Virtual resource allocation in a network virtualization based integrated train ground communication system,” in *Proceedings of the 19th IEEE International Conference on Intelligent Transportation Systems, ITSC 2016*, pp. 2012–2016, Brazil, November 2016.
- [17] C. Liang and F. R. Yu, “Wireless network virtualization: a survey, some research issues and challenges,” *IEEE Communications Surveys & Tutorials*, vol. 17, no. 1, pp. 358–380, 2015.
- [18] S. Boyd, N. Parikh, E. Chu, B. Peleato, and J. Eckstein, “Distributed optimization and statistical learning via the alternating direction method of multipliers,” *Foundations and Trends in Machine Learning*, vol. 3, no. 1, pp. 1–122, 2010.
- [19] L. Zhu, F. R. Yu, B. Ning, and T. Tang, “Cross-layer handoff design in MIMO-enabled WLANs for Communication-Based Train Control (CBTC) systems,” *IEEE Journal on Selected Areas in Communications*, vol. 30, no. 4, pp. 719–728, 2012.
- [20] H. Yaïche, R. R. Mazumdar, and C. Rosenberg, “A game theoretic framework for bandwidth allocation and pricing in broadband networks,” *IEEE/ACM Transactions on Networking*, vol. 8, no. 5, pp. 667–678, 2000.
- [21] X. Qiu and K. Chawla, “On the performance of adaptive modulation in cellular systems,” *IEEE Transactions on Communications*, vol. 47, no. 6, pp. 884–895, 1999.
- [22] Q. Ye, B. Rong, Y. Chen, M. Al-Shalash, C. Caramanis, and J. G. Andrews, “User association for load balancing in heterogeneous cellular networks,” *IEEE Transactions on Wireless Communications*, vol. 12, no. 6, pp. 2706–2716, 2013.
- [23] S. Gortzen and A. Schmeink, “Optimality of dual methods for discrete multiuser multicarrier resource allocation problems,” *IEEE Transactions on Wireless Communications*, vol. 11, no. 10, pp. 3810–3817, 2012.
- [24] R. Jain, D.-M. Chiu, and W. R. Hawe, *A quantitative measure of fairness and discrimination for resource allocation in shared computer system*, vol. 38, Eastern Research Laboratory, Digital Equipment Corporation, Hudson, 1984.

Research Article

Wideband Channel Modeling for mm-Wave inside Trains for 5G-Related Applications

Juan Moreno García-Loygorri ¹, **César Briso-Rodríguez** ¹,
Israel Arnedo ², **César Calvo** ¹, **Miguel A. G. Laso** ², **Danping He**,³
Florentino Jiménez,¹ and **Vicente González Posadas**¹

¹*TSC Department, ETSIST, Universidad Politécnica de Madrid, Madrid, Spain*

²*Universidad Pública de Navarra, Pamplona, Spain*

³*Beijing Jiaotong University, Beijing, China*

Correspondence should be addressed to Juan Moreno García-Loygorri; juanmorenogl@diac.upm.es

Received 2 November 2017; Accepted 14 February 2018; Published 15 April 2018

Academic Editor: Dajana Cassioli

Copyright © 2018 Juan Moreno García-Loygorri et al. This is an open access article distributed under the Creative Commons Attribution License, which permits unrestricted use, distribution, and reproduction in any medium, provided the original work is properly cited.

Passenger trains and especially metro trains have been identified as one of the key scenarios for 5G deployments. The wireless channel inside a train car is reported in the frequency range between 26.5 GHz and 40 GHz. These bands have received a lot of interest for high-density scenarios with a high-traffic demand, two of the most relevant aspects of a 5G network. In this paper we provide a full description of the wideband channel estimating Power-Delay Profiles (PDP), Saleh-Valenzuela model parameters, time-of-arrival (TOA) ranging, and path-loss results. Moreover, the performance of an automatic clustering algorithm is evaluated. The results show a remarkable degree of coherence and general conclusions are obtained.

1. Introduction

Metro lines are one of the most acknowledged high-density scenarios, as well as stadiums and other large venues. These places are a clear target for 5G mobile [1] deployments, which is intended to provide very large throughputs and ultra-low latencies in dense environments and sustain a high number of simultaneous connections, among others. It is noteworthy that it is possible to have more than 1200 people inside a 120-meter long train, which means around 5 persons/m². There are many railway-related applications like Train-to-Ground, Train-to-Train, Train-to-Car, Train-to-Satellite, intratrain communications, and so on, which are usually grouped under the T2X notation, or perhaps in the more generic V2X notation, where “V” stands for vehicular. In this paper we focus on the intratrain channel, which has an enormous importance to provide connectivity to passengers. Also, this wireless channel could be used for the internal communications of the train, which is one of the objectives of the EU-H2020 Roll2Rail Project [2].

There is still some vagueness in the frequency bands to be assigned, but some things are clear: there will be 5G deployments both above and below 6 GHz [3]. This fact has attracted much attention on millimeter waves (mm-wave) in order to have larger bandwidths than in lower frequencies, where the entire spectrum has been allocated. For example, in USA both the 28 GHz (27.5–28.35 GHz) and the 37 GHz band (37–40 GHz) have been licensed for mobile applications; in both China and the European Union, the 26 GHz band (24.25–27.5 GHz) is the chosen one. On the other side, there is no clear direction on which bands will be allocated for unlicensed use, but the 37 GHz band (37–37.6 GHz) is perhaps the most promising one. All these spectrum policies lead to the need of a proper channel model for 5G-related scenarios in the aforementioned bands.

There are many papers related to channel measurements and modeling in railway scenarios but, as far as we know, only very few of them are focused on mm-wave for intratrain environments (i.e., the work carried out by ETRI in Korea [4]). Regarding the Train-to-Ground link for high-speed

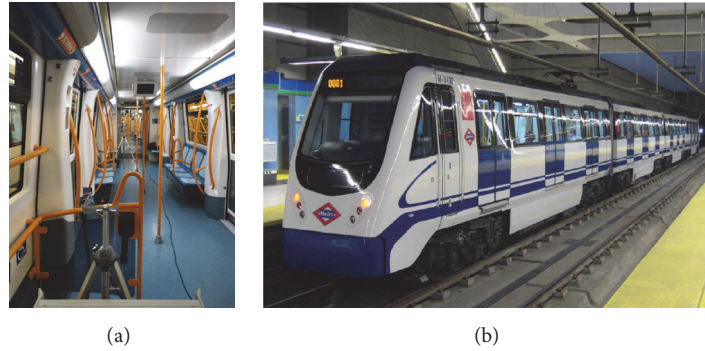


FIGURE 1: Rolling stock used in the measurements campaign. (a) The train interior and (b) the exterior are shown.

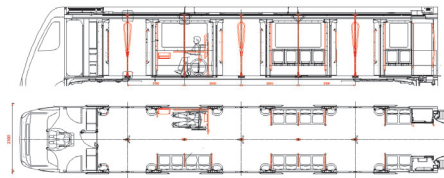


FIGURE 2: Top and lateral view of one car of the s3000 rolling stock.

trains, a very complete reference is [5] but it is focused on frequencies below 6 GHz; for tunnels which are a very common scenario in railways, there are many papers, like [6, 7]; inside metro stations there are many research papers like [8]; and for mm-wave research in railways there are some ray-tracing simulations in mm-wave and THz [9]. For intratrain link, there are some recent papers but below 6 GHz [10, 11].

The structure of the paper is the following: in Section 2 we will describe the experiment setup, covering the environment details, the measurement setup, and the processing of the data; in Section 3 we will explain all the results obtained from the measurements, and, finally, in Section 4 a conclusion and some discussion are provided.

2. Experimental Setup

2.1. Environment. The environment for the measurement campaign is the train interior of a metro train. It is depicted in Figures 1 and 2. This vehicle under test is a Madrid Metro train of the s3000 series. It has the capacity to carry 442 persons in the four-car consist, which amounts to 132 persons on each car.

The maximum dimensions of the train are $2.3 \times 3.6 \times 59.7$ meters, but the interior of the train has a maximum section of $2.2 \text{ m} \times 2.2 \text{ m}$. As usual in this type of trains, there are many handholds, seats, and other furniture. The seats are resin-coated reinforced with glass fiber and both the handholds and the roof are made of stainless steel covered with a 500 micrometers thick yellow painting. The floor is made of stratified rubber, the windows are made of laminated glass and the doors are of aluminum and glass like the windows' one. This layout and materials are very common in

modern subway trains, with very small differences between them.

2.2. Measurement Setup. The measurements were carried out using an Agilent 8722ES Vector Network Analyzer (VNA). The approach for this VNA-based measurement is the usual one: connecting the transmitter to port 1 and the receiver to port 2, measure the s_{21} parameter, which is a good approximation for the channel transfer function $H(f)$ [12]. The connection of both antennas to the VNA ports was done using phase stable RTK040 wires. The length of this wire was 18 m and we used 2.4 mm connectors.

All the measurements but one were carried out using horn antennas (see Figure 3), model 22240 by FLANN, which is an antenna designed to be used in the 26.5–40 GHz, which is the band where our experiment was focused on. The gain of this antenna is 20 dB, and the variations of this parameter are bounded to 2 dB in the band of interest, which gives us a great stability. In the last measurement an omnidirectional antenna (Vivaldi, see Figure 3) was used in the receiver as a replacement of the horn antennas mentioned before.

The measured positions for the receiver (the transmitter was fixed) are depicted in Figure 2. We measured at five different transmitter-receiver distances $d = \{2, 4, 6, 9.5, 17\}$ m, moving only the receiver (in the last one the receiver is in the next train car). The height of both the transmitting and the receiving antennas was 1 m over the train floor. Both the transmitter and the receiver were placed inside the train at all time, as well as the VNA. In the measurement setup the number of dots in the 13.5 GHz wideband (26.5–40 GHz) was 1601. The processing of the data was done offline with MATLAB. As we explain in a more detailed form later in this paper, we decided to employ an automatic

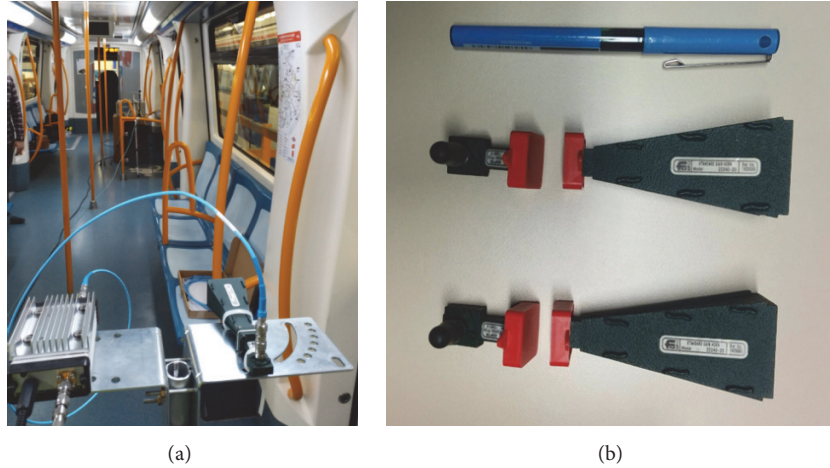


FIGURE 3: (a) Measurement setup (from the receiver's point of view). (b) Both horn antennas are shown.

TABLE 1: Path loss [dB].

Distance [m]	θ						\overline{PL}
	0°	45°	90°	135°	180°		
2.0	29.37	61.71	63.19	60.70	57.72	54.54	
4.0	36.77	61.24	61.69	60.78	62.75	56.65	
6.0	40.62	60.86	61.23	62.58	62.26	57.51	
9.5	45.52	53.98	65.84	64.67	65.23	59.05	
17.0	54.94	54.97	66.48	66.71	66.93	62.01	

clustering algorithm instead of identifying them by visual inspection.

3. Channel Model

3.1. Path-Loss. The path-loss is obtained from the measured data in the VNA. This result is the average in the entire frequency range (26.5–40 GHz) [13]. N equals 1601 which is the number of dots

$$PL = 10 \log_{10} \left(\frac{1}{N} \sum_{i=1}^N |H(f_i)|^{-2} \right). \quad (1)$$

The obtained values are detailed in Table 1.

The path-loss increases together with the distance, both the average path-loss and the LOS ($\theta = 0^\circ$) scenario, as it was expected. Regarding the influence of the angle (θ), for $\theta = 0^\circ$ the received power is the maximum one for every measured distance, and we can see a great increase in the path-loss when we misalign the antennas $\{\theta = 45^\circ, 90^\circ, 135^\circ, 180^\circ\}$. This increase is more significant at lower distances. For example, the average path-loss increases 31.46 dB at $d = 2$ m and only 8.84 dB at $d = 17$ m. This is because at higher distances the multipath is less severe and the impact of reflections on handlers and other diffuse scatters is significantly lower (the so-called Waveguide Effect).

The variation of the path-loss for the different angles (given a fixed distance) is more or less random. However, at the highest distances $\{d = 9.5, 17$ m $\}$ the angle that experiences

a lower path-loss is clearly $\theta = 45^\circ$. The reason for this is the same as before: the Waveguide Effect. To properly assess the Waveguide Effect, we have calculated the path-loss exponent (n) for 0° . The obtained value is 1.6, which is below the free-space one ($n = 2$) so, under this premises, we can conclude that we are experiencing this effect inside the train at this frequency band. The whole one-slope model is shown in

$$L_x = L_0 + 10n \log_{10} \left(\frac{d}{d_0} \right) = 29 + 16.0 \log_{10}(d), \quad (2)$$

where L_x is the total losses in dB, d_0 is the reference distance, L_0 is the losses at the reference distance, n is the path-loss exponent, and d is the distance.

We also measured the path-loss at a given distance ($d = 9.5$ m) with six people moving around between the transmitter and the receiver. This impact is an average path-loss 2.28 dB higher and some fading 30 dB deep.

3.2. Ranging. If we measure the time of arrival (TOA) we can easily estimate the distance between the transmitter and the receiver

$$\tilde{d} = c \cdot \tau, \quad (3)$$

where τ is the time for the first peak in the PDP (i.e., the first path that arrives to the receiver) and c is the speed of light. In Table 2 we can see the estimated distances using this TOA-based technique to estimate the distance between transmitter and receiver. The estimation based on the LOS path is the

TABLE 2: Estimated distances for TOA-based method (m).

Distance [m]	θ					% error
	0°	45°	90°	135°	180°	
2.0	2.11	2.02	2.51	2.51	14.09	
4.0	4.18	6.42	6.38	13.16	5.02	<10%
6.0	6.13	7.02	6.40	8.69	11.20	10–50%
9.5	9.47	10.00	10.49	10.91	9.8	>50%
17.0	16.89	16.89	17.47		19.24	

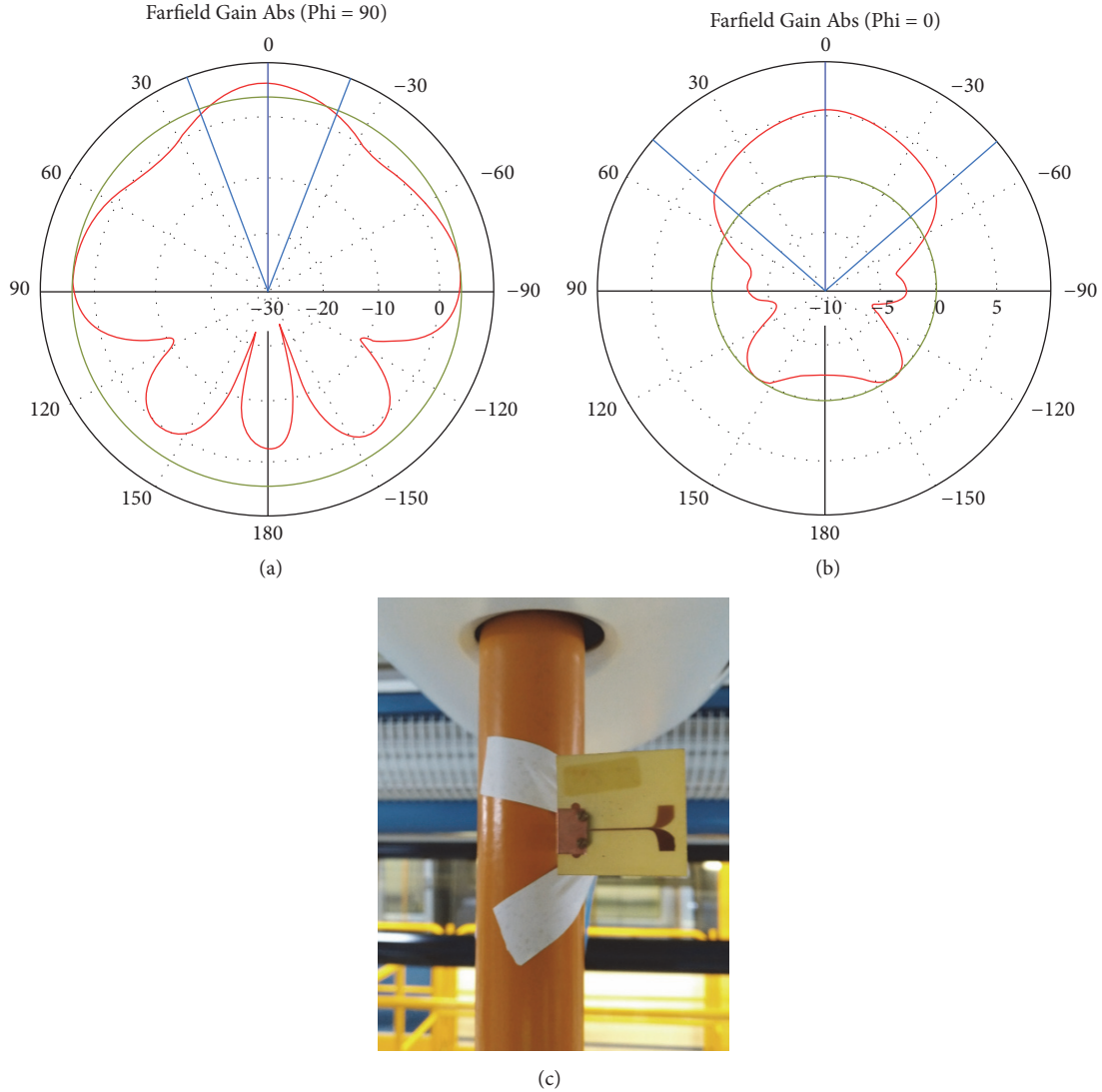


FIGURE 4: Radiation patterns at 25 GHz for E-plane (a) and H-plane (b) for the Vivaldi antenna. (c) The antenna is shown being installed near the top of one of the handholds of the train.

most accurate (5.56% error in the worst case and 0.35% in the best one); for $\theta = 45^\circ$ it is slightly worse and for the other angles we have large errors. This method seems to be more accurate when the distance increases (for $d = 17$ m, the error is lower than 3% for $\theta = 0^\circ, 45^\circ,$ and 90° and 13.20% for $\theta = 180^\circ$). The reason behind this good performance at higher

distances is because the impact of reflections from handlers and other furniture is less significant than at lower distances.

3.3. *Power-Delay-Profiles and Clustering.* Regarding the Power-Delay Profiles (PDP) we have computed them for all the scenarios described in Section 2. In Figures 5–9 we can

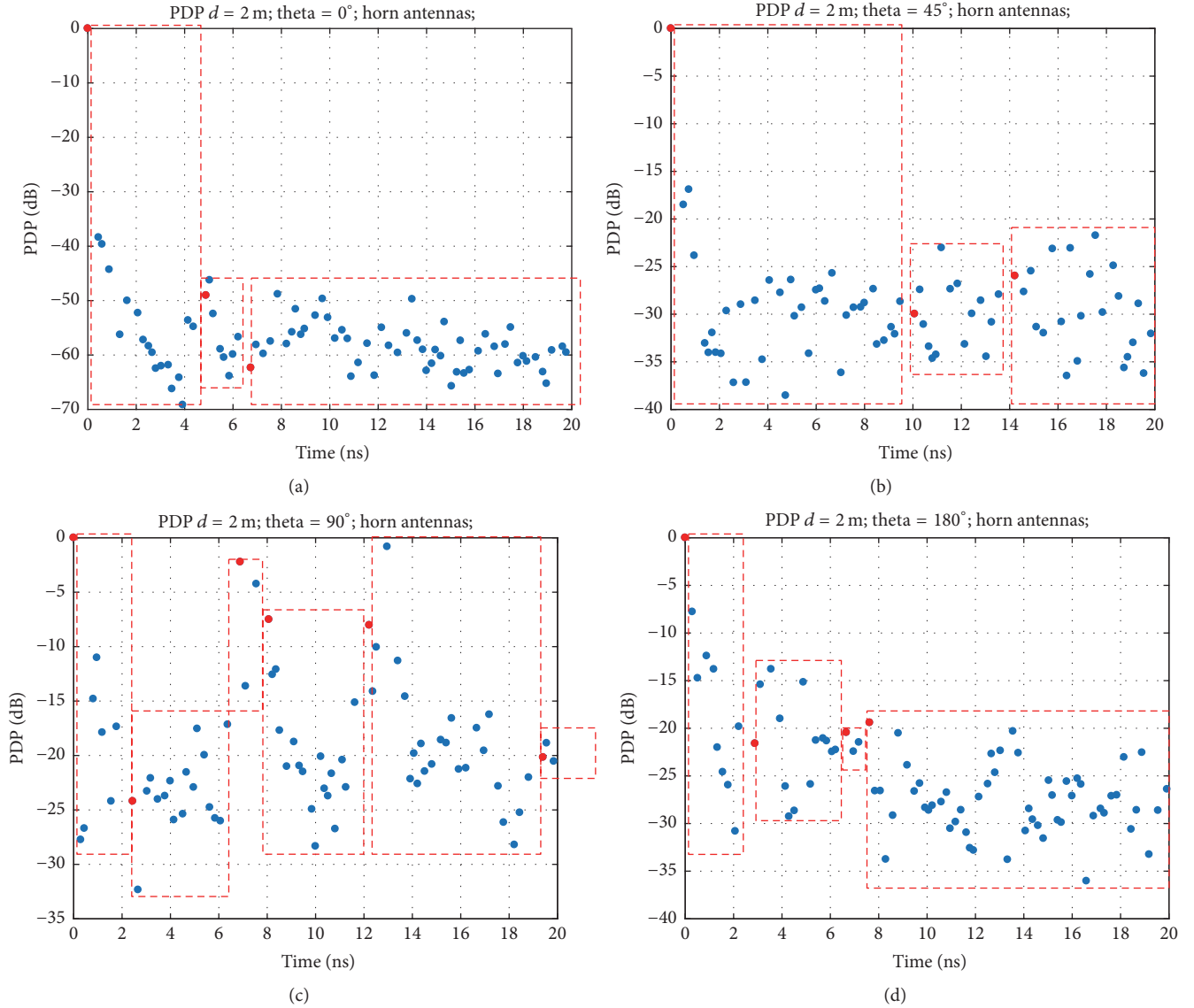


FIGURE 5: Power-Delay Profile and cluster identification for $d = 2$ m. (a) $\theta = 0^\circ$. (b) $\theta = 45^\circ$. (c) $\theta = 90^\circ$. (d) $\theta = 180^\circ$.

see the PDPs for $d = \{2, 4, 6, 9.5, 17\}$ m and an extra one for the omnidirectional antenna at a distance of $d = 4$ m.

Multipath components are clustered according to Saleh-Valenzuela [14] model and the estimation of the clusters that these multipath components form has been done using the automatic algorithm proposed in [15]. This algorithm takes into account both the amplitude and time delay to form the clusters. The usual approach to identify multipath component clusters is the visual inspection [15] but we found preferable to use an automatic algorithm. The main advantage of this algorithm is that it allows us to do a fast estimation of the clusters, and that it takes into account both time and amplitude values. Therefore, the clustering process is very dependent on the thresholds we propose (as it is acknowledged in [15]), but after some iterations, it seems to have a good performance if we look to Figures 5–11. In these figures we have highlighted in red the clusters that this

algorithm has identified (dots in red are the first ray from a cluster).

For $d = 2$ m (Figure 5) we can see that the number of clusters increases with θ . For $\theta = 90^\circ$ the number of clusters increases significantly, and for $\theta = 180^\circ$ it decreases. This is an expectable result, because as we go towards a pure NLOS scenario, with many scatters between transmitter and receiver, this leads to different times of arrival (i.e., clusters).

Regarding the $d = 4$ m scenario (Figure 6) the number of clusters does not increase significantly from the previous scenario, but we have more or less the same dependence to θ . The difference between $\theta = 0^\circ$ and $\theta = 45^\circ$ is small if we visually inspect both PDPs, but for $\theta = 180^\circ$ we have more clusters in the receiver. In our opinion, this is attributable to the layout of the train that makes this PDP possible for this angle. If we employ an omnidirectional antenna in the receiver (Figure 11) we can see that we are able to see a significantly

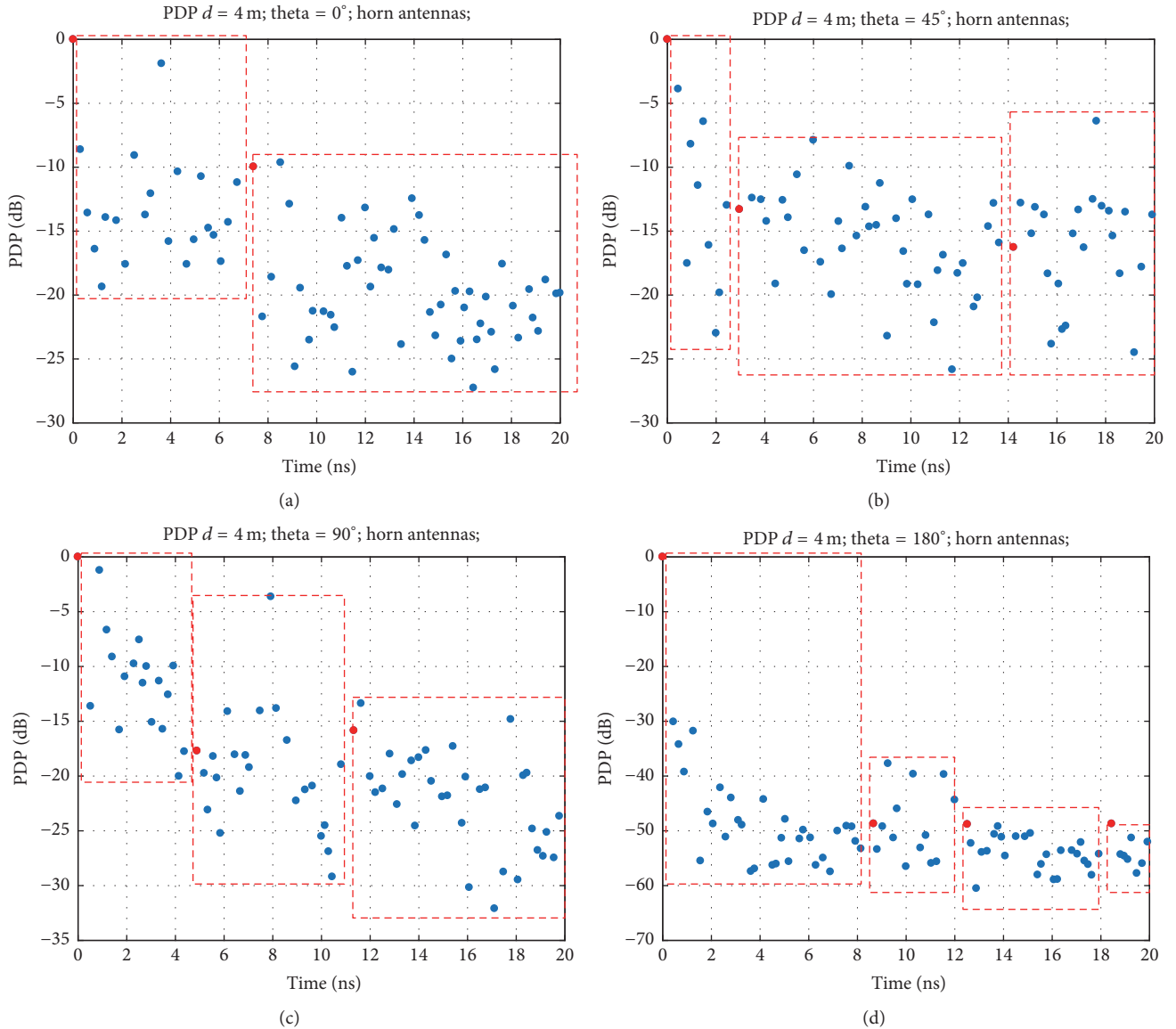


FIGURE 6: Power-Delay Profile and cluster identification for $d = 4$ m. (a) $\theta = 0^\circ$. (b) $\theta = 45^\circ$. (c) $\theta = 90^\circ$. (d) $\theta = 180^\circ$. For the $\theta = 0^\circ$ setup there is almost no room for reflections to arrive to the receiver. As we increase θ , many more clusters surge.

higher number of clusters. This is an expected result because the wider radiation pattern allows more different directions of arrival to the receiver. We still have a strong first cluster, associated with the LOS direct link plus four more clusters for the reflection through the train car.

In Figure 7 we can see the PDPs for $d = 6$ m. The number of clusters remain stable and similar to $d = \{2, 4\}$ m for $\theta = 0^\circ$. For $\theta = 45^\circ$ we see more clusters for the same reason as before: losing the LOS link leads to more reflections due to the presence of obstacles inside the train. This is coherent with the fact that for $\theta = \{90^\circ, 180^\circ\}$ the number of clusters does not increase.

For $d = 9.5$ m (Figure 8), the estimated number of clusters is stable (and lower than before) for both $\theta = \{0^\circ, 45^\circ\}$ because we are experiencing a significant Waveguide Effect and there are many rays that are suppressed. For $\theta = \{90^\circ, 180^\circ\}$ we

have the same increase in the number of clusters experienced before. So the pattern does not change from the $d = 6$ m scenario. Nevertheless, for this distance we also measured the channel with people moving randomly inside the train (between transmitter and receiver). The result can be seen in Figure 10, and the number of clusters increases significantly from any other angle at the same distance. The reason is the expected one: people act as supplementary scatters, so the PDP changes (we have more clusters, obviously). This result is very important because intratrain-based applications will work on trains with people onboard.

Finally, for $d = 17$ m (Figure 9), if we inspect visually the PDPs for the four angles considered, we can see that it does not change significantly, but the algorithm estimates 2, 6, 3, and 4, clusters for $\theta = \{0^\circ, 45^\circ, 90^\circ, 180^\circ\}$. This is perhaps the most debatable outcome of the algorithm. In this

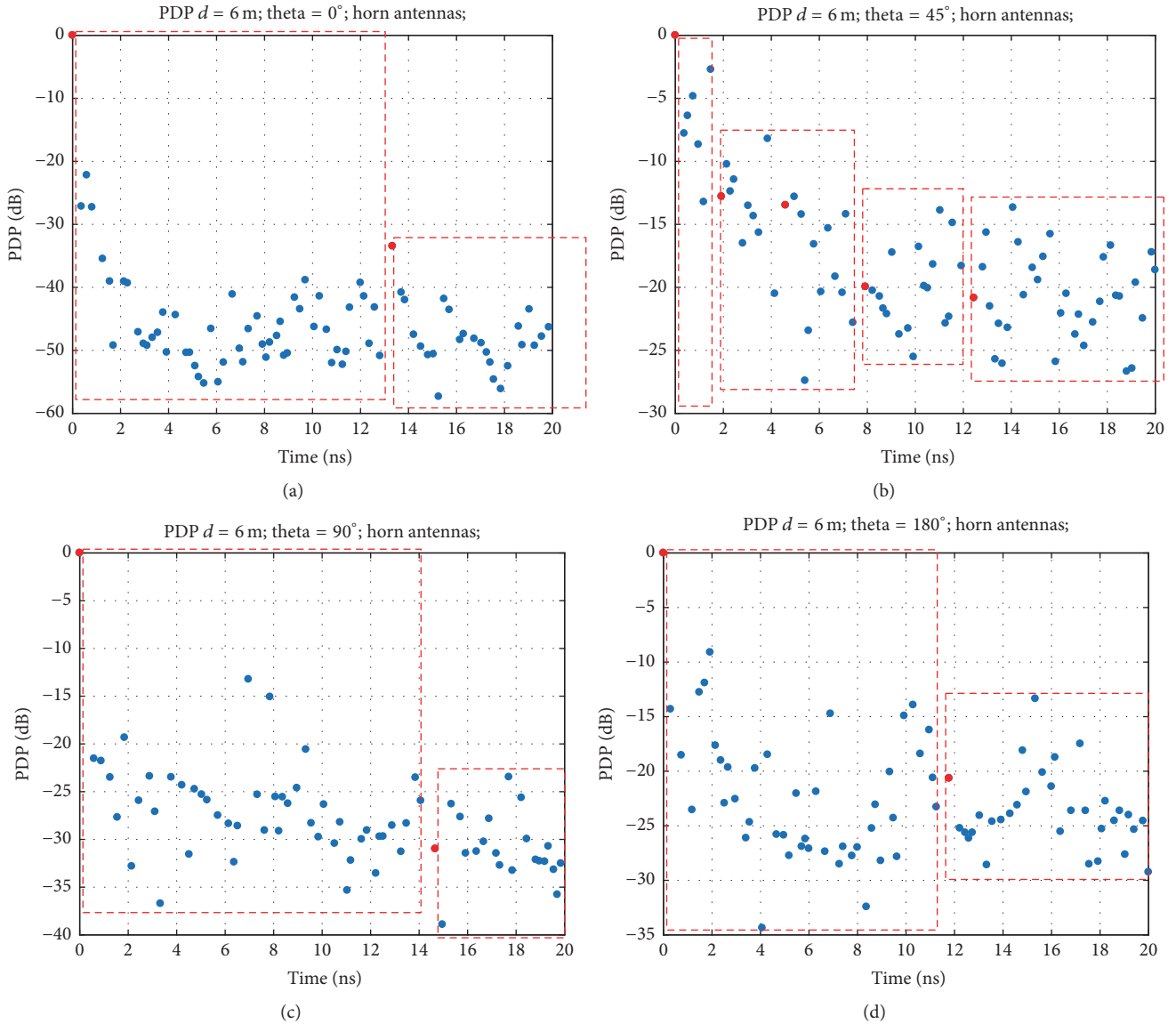


FIGURE 7: Power-Delay Profile and cluster identification for $d = 6$ m. (a) $\theta = 0^\circ$. (b) $\theta = 45^\circ$. (c) $\theta = 90^\circ$. (d) $\theta = 180^\circ$. At this distance, the clustering algorithm behaves in a very similar manner as for $d = 2$ m, but for $\theta = \{90^\circ, 180^\circ\}$ there are fewer clusters than in $d = 2$ m.

case, the distance is significantly higher than in the other scenarios, where the Waveguide Effect is dominant and the PDP is smoother (which means fewer clusters). It is also the scenario where we have less differences between angles (together with $d = 2$ m, where there were almost no scatters between transmitter and receiver). An expected result is that, at a distance like this, the power is mostly concentrated on the first cluster of rays that arrives to the receiver (this is easy to see in the $\theta = 0^\circ$, obviously). This is another consequence of the “Waveguide Effect.”

3.4. Saleh-Valenzuela Parameters. The classical Saleh-Valenzuela (SV) model is intended for indoor scenarios and we have chosen it for its statistical nature and simplicity: it describes the channel with only four parameters (λ , Λ , γ , and Γ). Λ is the cluster arrival rate, which is assumed to follow

a Poisson distribution [14], the same distribution as the ray arrival rate “ λ ”; “ γ ” is the exponential decay within a cluster; and “ Γ ” is the exponential decay for the whole PDP. In Table 3 we have included our estimation of these four SV parameters for all the scenarios that we have measured.

If we look at the average SV parameters in the column on the right of Table 3, we can see that we have a “slow” decay. This is because the distance between the objects that reflect the signal is very low, and all of them are very similar (metallic surfaces). That is for the “overall decay” (parameter Γ). If we look inside the clusters, we can see that they decay rapidly (parameter γ), which means a higher attenuation (due to the high frequencies) and very few reflections (apart from the first one). Anyway, this is coherent because the clustering algorithm that we chose is adequate, because the calculation of SV model parameters is very dependent on the clustering algorithm.

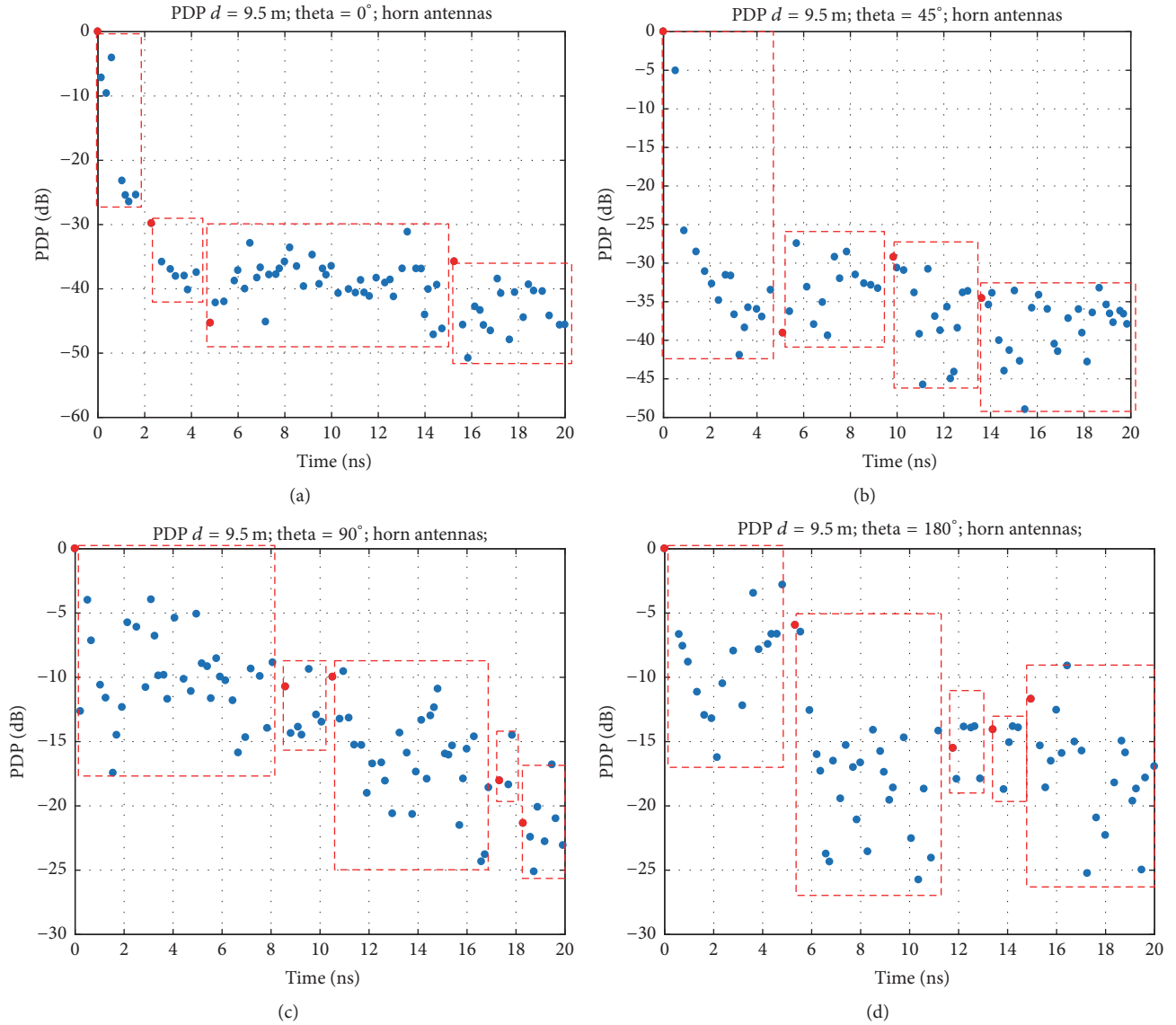


FIGURE 8: Power-Delay Profile and cluster identification for $d = 9.5$ m. (a) $\theta = 0^\circ$. (b) $\theta = 45^\circ$. (c) $\theta = 90^\circ$. (d) $\theta = 180^\circ$. We still have many clusters, especially in the angles different to 0° .

Explaining properly all the estimated SV parameters would take a lot of time, so here we will discuss some of the most significant parameters. First of all, it is noteworthy that λ (ray arrival rate) has small variations no matter in which scenario we are. This parameter is very dependent on the limitations of the measurement devices, so perhaps with a different device able to increase the number of resolvable rays this parameter could experience higher variations. The main difficulty to improve this is that the VNA employed is a state-of-the-art device, so it will take some time to achieve a better resolution in this parameter.

The cluster arrival rate (Λ) has a direct relation with the number of clusters and we have gone through this parameter in Section 3.3. Regarding the overall decay rate (Γ), it is generally higher than the cluster decay rate (γ), which is an expected result. Moreover, the clustering algorithm does

not allow negative slopes (if it resolves a cluster with a negative slope; that cluster is joined to the next one) which increases—in general terms—the values of γ . If we look at some particular results, we can see that the Γ for the shortest distance ($d = 2$ m) and LOS scenario has the smallest value calculated. For higher distances and angles, the Γ increases, but the general trend is to decrease (but for $d = 2$ m), which is an expected result. It is hard to find a clear pattern in the angle variation, but a possible reason behind this behavior is that the first ray of the cluster is not always the one with more power [15]. This could lead to an underestimation of the Γ parameter.

We also took two more measurements: with people moving around inside the train ($d = 9.5$ m) and also using an omnidirectional antenna ($d = 4$ m). The Saleh-Valenzuela model parameters for the omnidirectional antenna are $\gamma =$

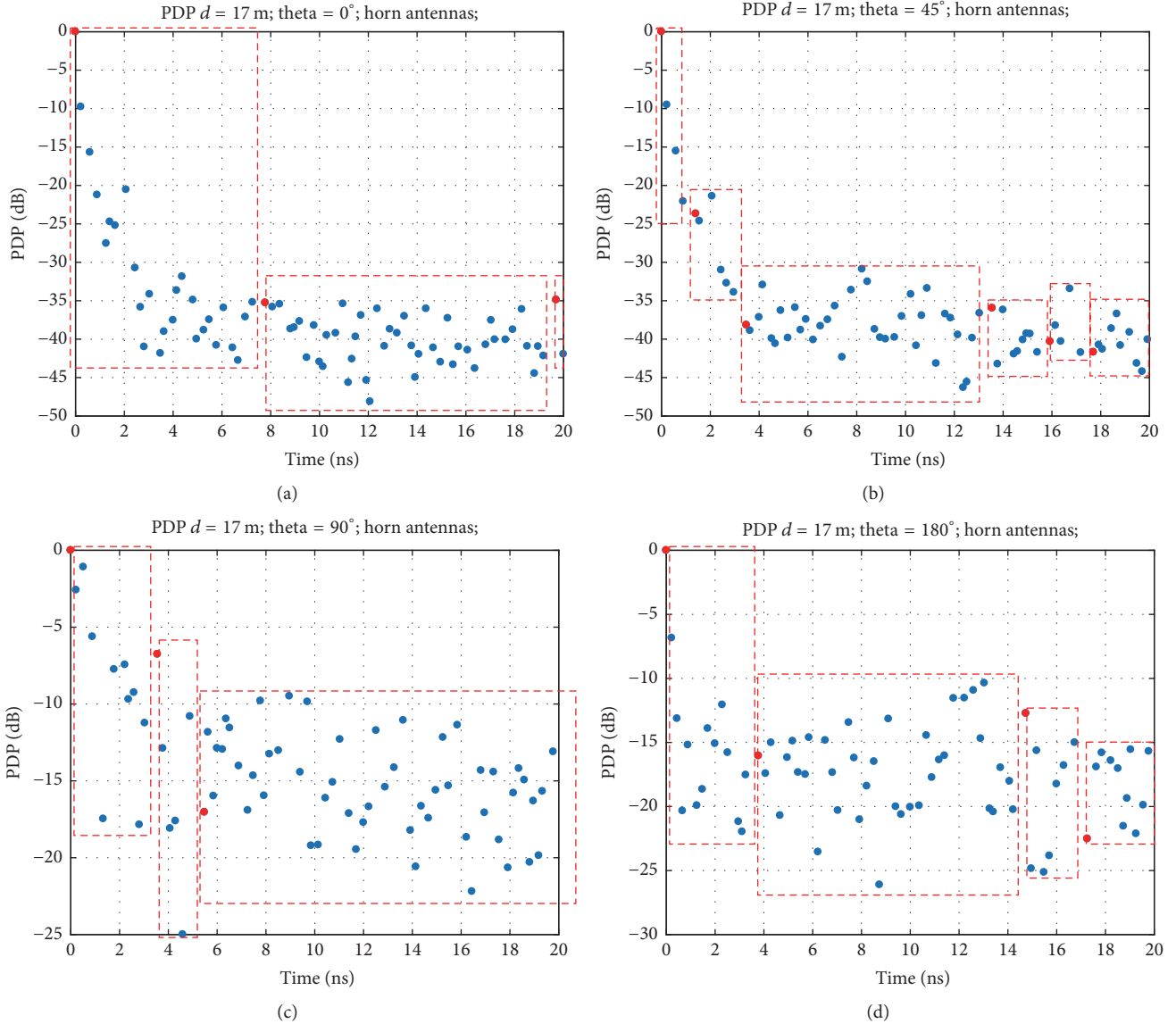


FIGURE 9: Power-Delay Profile and cluster identification for $d = 17$ m. (a) $\theta = 0^\circ$. (b) $\theta = 45^\circ$. (c) $\theta = 90^\circ$. (d) $\theta = 180^\circ$. The automatic algorithm identifies very few clusters for the $\theta = 0^\circ$, but many more rise if we misalign the antennas.

0.187; $\Gamma = 0.208$; $\lambda = 3.800$; $\Lambda = 0.277$. This is similar “ γ ” and “ λ ” for horn antenna in the receiver at the same distance. The apparent invariability of “ λ ” was discussed before and for “ γ ” it could be an impact of the clustering algorithm, which prevents higher variations inside a cluster, which leads to an approximately constant “ γ .” The number of clusters is significantly different, as the parameter “ Γ ” highlights, so this is coherent with the “conservative” nature (regarding “ γ ”) of the clustering algorithm.

If we consider the difference between having people in motion between transmitter and receiver (the SV parameters are $\gamma = 0.134$; $\Gamma = 0.188$; $\lambda = 3.745$; $\Lambda = 0.277$) and not, using horn antennas and the same distance, equal to 9.5 m, we can see that we have a lower “ Λ ” when we have people in motion, and also a lower “ Γ .” It is also noteworthy that the average parameters using horn antennas (this is $\theta = \{0,$

$45^\circ, 90^\circ, 180^\circ\}$) are a good approximation of the scenario with an omnidirectional antenna. This is a coherent result because using an antenna like this is the same as we average the contributions from all directions. However, as we can see in Figure 4, the radiation pattern of the Vivaldi antenna is not perfectly omnidirectional, so this “averaging” process is not as precise as it could be otherwise.

4. Conclusion

The SV model can be applicable directly to an intratrain scenario, as it is an indoor scenario (the scope of the SV model). It is only necessary to estimate the parameters of the model to each environment. In particular, intratrain communications at high frequency are a high multipath environment, where SV model is intended to work.

TABLE 3: Saleh-Valenzuela parameters.

Distance [m]	Parameter	Angle [°]				Average
		0°	45°	90°	180°	
2.0	γ	0.058	0.172	0.264	0.124	0.155
	Γ	0.046	0.196	0.448	0.139	0.207
	λ	3.944	3.728	3.728	4.065	3.866
	Λ	0.152	0.151	0.302	0.201	0.202
4.0	γ	0.236	0.256	0.198	0.104	0.199
	Γ	0.323	0.338	0.249	0.129	0.260
	λ	3.600	3.563	3.742	3.965	3.718
	Λ	0.100	0.151	0.152	0.201	0.151
6.0	γ	0.116	0.173	0.199	0.221	0.177
	Γ	0.173	0.209	0.206	0.248	0.209
	λ	3.929	4.000	3.476	3.800	3.801
	Λ	0.101	0.250	0.101	0.100	0.138
9.5	γ	0.090	0.118	0.351	0.315	0.219
	Γ	0.136	0.140	0.395	0.429	0.275
	λ	3.700	3.576	4.115	3.650	3.760
	Λ	0.200	0.201	0.251	0.250	0.226
17.0	γ	0.145	0.117	0.200	0.187	0.162
	Γ	0.203	0.163	0.158	0.208	0.183
	λ	3.700	3.513	3.539	3.800	3.638
	Λ	0.150	0.301	0.152	0.100	0.176

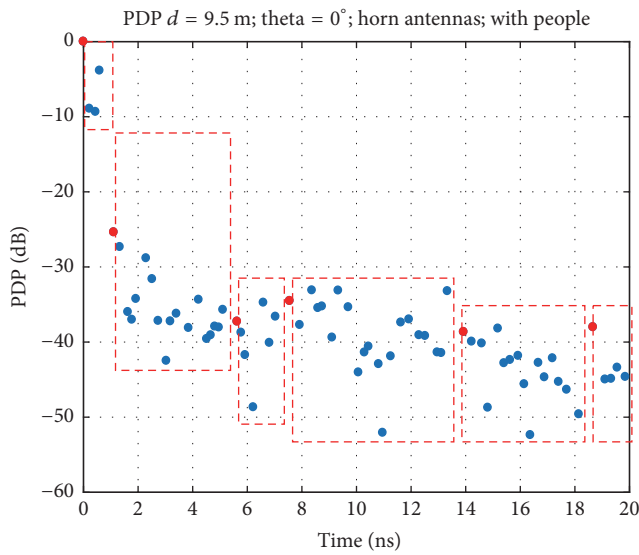


FIGURE 10: Power-Delay Profile for $d = 9.5$ m, $\theta = 0^\circ$; using horn antennas and people moving around between transmitter and receiver. The effect of people increases the number of clusters and impacts the overall PDP.

The intratrain link is one of the most likely scenarios to require high throughputs, ultra-dense networks, and very low latencies. These three requirements are the core of 5G technologies. In this paper we have assessed this link in a region of the spectrum related to future 5G developments (26.5–40 GHz), providing estimations for the

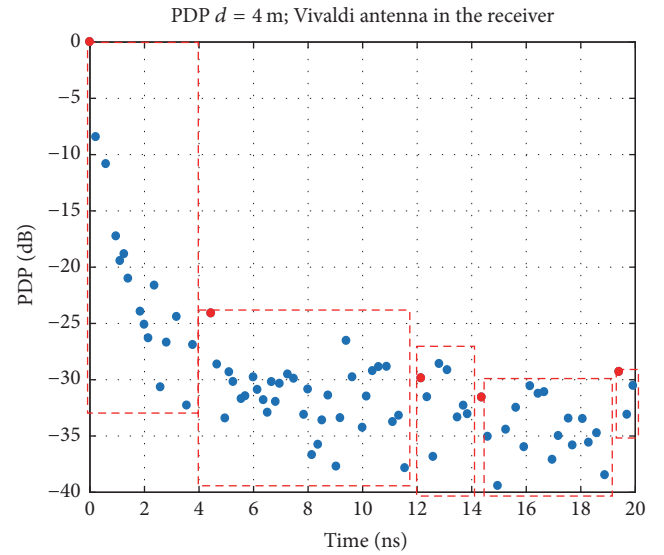


FIGURE 11: Power-Delay Profile for $d = 4$ m, with the Vivaldi antenna in the receiver. The automatic algorithm identifies 5 clusters.

path-loss, Power-Delay Profile and Saleh-Valenzuela model parameters. We have seen the dependence of all these results on distance and angle; moreover, we have seen the impact of people moving around and also the differences coming from the radiation pattern of the receiving antenna (using an omnidirectional antenna instead of the horn antennas used in all measurements but one). The performance of the clustering

algorithm is remarkable (with some limitations, as we have discussed) and the obtained SV parameters are coherent as well.

Conflicts of Interest

The authors declare that there are no conflicts of interest regarding the publication of this paper.

Acknowledgments

Enabling 5G TEC2014-55735-C3-2-R is funded by the Spanish Ministry of Economy and Competitiveness and also is funded by the Chinese Strategic International Cooperative Project of National key R&D Plan, 2016YFE0200200.

References

- [1] 5G for Europe: An Action Plan, European Commission, Brussels, 2016, <https://ec.europa.eu/transparency/regdoc/rep/1/2016/EN/1-2016-588-EN-F1-1.PDF>.
- [2] Roll2Rail Project, <http://roll2rail.eu>.
- [3] S.-Y. Lien, S.-L. Shieh, Y. Huang, B. Su, Y.-L. Hsu, and H.-Y. Wei, "5G New Radio: Waveform, Frame Structure, Multiple Access, and Initial Access," *IEEE Communications Magazine*, vol. 55, no. 6, pp. 64–71, 2017.
- [4] G. Noh, J. Kim, H. S. Chung, B. Hui, Y. Choi, and I. Kim, "mmWave-based mobile backhaul transceiver for high speed train communication systems," in *Proceedings of the IEEE Globecom Workshops (GC Wkshps)*, pp. 1–5, Singapore, Singapore, December 2017.
- [5] T. Zhou, C. Tao, S. Salous, L. Liu, and Z. Tan, "Implementation of an LTE-based channel measurement method for high-speed railway scenarios," *IEEE Transactions on Instrumentation and Measurement*, vol. 65, no. 1, pp. 25–36, 2016.
- [6] J.-M. Molina-García-Pardo, M. Lienard, P. Degauque, C. García-Pardo, and L. Juan-Llácer, "MIMO Channel capacity with polarization diversity in arched tunnels," *IEEE Antennas and Wireless Propagation Letters*, vol. 8, pp. 1186–1189, 2009.
- [7] S. Hairoud, P. Combeau, Y. Pousset, Y. Cocheril, and M. Berbineau, "WINNER model for subway tunnel at 5.8 GHz," in *Proceedings of the 12th International Conference on ITS Telecommunications (ITST '12)*, pp. 743–747, Taiwan, November 2012.
- [8] et. Al. Ke Guan, "Broadband Channel Measurements inside Metro Station," in *Proceedings of the Progress In Electromagnetics Research Symposium Proceedings*, Guangzhou, China, 2014.
- [9] K. Guan, X. Lin, D. He et al., "Scenario modules and ray-tracing simulations of millimeter wave and terahertz channels for smart rail mobility," in *Proceedings of the 11th European Conference on Antennas and Propagation (EUCAP)*, pp. 113–117, Paris, France, March 2017.
- [10] I. Val, A. Arriola, P. M. Rodríguez et al., "Wireless channel measurements and modeling for TCMS communications in metro environments," in *Proceedings of the 11th European Conference on Antennas and Propagation (EUCAP '17)*, pp. 108–112, Paris, France, March 2017.
- [11] A. Gonzalez-Plaza, J. Moreno, I. Val et al., "5G communications in high speed and metropolitan railways," in *Proceedings of the 11th European Conference on Antennas and Propagation (EUCAP '17)*, pp. 658–660, Paris, France, March 2017.
- [12] A. Chandra, P. Kukolev, A. Prokes, T. Mikulasek, and C. F. Mecklenbrauker, "UWB measurements for spatial variability and ranging: parked car in underground garage," *IEEE Antennas and Wireless Propagation Letters*, vol. 16, pp. 1859–1862, 2017.
- [13] A. Chandra, A. Prokeš, T. Mikulášek et al., "Frequency-Domain In-Vehicle UWB Channel Modeling," *IEEE Transactions on Vehicular Technology*, vol. 65, no. 6, pp. 3929–3940, 2016.
- [14] A. A. Saleh and R. A. Valenzuela, "A statistical model for indoor multipath propagation," *IEEE Journal on Selected Areas in Communications*, vol. 5, no. 2, pp. 128–137, 1987.
- [15] M. Corrigan, A. Walton, W. Niu, J. Li, and T. Talty, "Automatic UWB clusters identification," in *Proceedings of the IEEE Radio and Wireless Symposium (RWS '09)*, pp. 376–379, USA, January 2008.

Research Article

An Operation Control Strategy for the Connected Maglev Trains Based on Vehicle-Borne Battery Condition Monitoring

Wenjing Zhang , Wenjun Wei, Yifan Yang, and Nan Nan

School of Electronic and Information Engineering, Beijing Jiaotong University, Beijing 100044, China

Correspondence should be addressed to Wenjing Zhang; zhangwj@bjtu.edu.cn

Received 8 December 2017; Accepted 7 March 2018; Published 12 April 2018

Academic Editor: Cesar Briso-Rodriguez

Copyright © 2018 Wenjing Zhang et al. This is an open access article distributed under the Creative Commons Attribution License, which permits unrestricted use, distribution, and reproduction in any medium, provided the original work is properly cited.

Vehicle-borne battery condition is an important factor affecting the efficiency of the maglev train operation and other connected ones. To effectively eliminate the influence of the battery condition and improve the operation efficiency of the connected maglev trains, an operation control strategy is proposed to guarantee train operation safety. First, based on Internet of Things, a sensor network is designed to monitor vehicle-borne battery condition in each vehicle of the train. Second, the train Operation Control System collects battery data of all vehicles in a maglev train by Train Communication Network. Third, all connected maglev trains share the battery data via a 38 GHz directional Radio Communication System and adjust operation control strategy accordingly. Simulation results indicate that the proposed strategy can guarantee the operation safety of the connected maglev trains.

1. Introduction

After the introduction of high-speed maglev train Transrapid-08 into Shanghai in 2002 and with the operations of both Airport Line of Changsha in 2016 and S1 Line of Beijing in 2017, maglev transportation system has received more and more attention in China [1, 2]. Compared with the conventional wheel-rail transportation systems, the maglev transportation system has many excellent features such as low environmental noise, small turning radius, high climbing slope ability, strong weather resistance, low maintenance cost, and long life-span [3].

Normally, based on five speed curve limits including the minimum speed-up limit, the minimum levitation limit, the maximum safety braking limit, the maximum speed running limit, and the maximum speed limit, the train Operation Control System (OCS), which has four subsystems including Central Control System (CCS), Decentralization Control System (DCS), Vehicle Control System (VCS), and 38 GHz directional Radio Communication System (RCS), formulates an operation control strategy real-timely to guarantee train operation safety [4].

However, for construction cost consideration, only station decentralizations and Auxiliary Stopping Area (ASA) of section decentralizations are equipped with Power Rail (PR),

making it discontinuous. In case of emergency, VCS requests DCS to shut off the Propulsion Power-Supply System (PPS) and then the train-borne batteries are the only energy source for all train-borne electrical equipment to keep the train running to the next ASA. Unfortunately, the train cannot run again after it stops in the track without PR [5].

In the routine operation, the running speed is around 200 km/h for the medium-speed train and about 400 km/h for the high-speed train; the Vehicle Electrical Grid (VEG) is supplied by the vehicle-borne linear generator because of high power-generating efficiency at high speed. However, when the train speed decreases to 100 km/h or lower, the power-generating capacity of the linear generator drops too much to supply enough power to VEG. In this case, the train-borne batteries provide supplementary energy to VEG. For safety, during pull-in and departure station, the train speed is relatively low (lower than 100 km/h); VEG has to depend on the train-borne batteries. Hence, the battery conditions, especially the remaining capacity, are crucial to the train operation safety.

When the maglev train stops in the station or ASA in the section decentralization, vehicle-borne collectors will charge batteries through PR and the vehicle-borne batteries are in the high current mode, resulting in performance degradation easily. Therefore, it is of great significance to monitor the

battery condition to prolong the battery life [6, 7] and adjust the operation strategy dynamically. Moreover, during the following operation for the connected trains, the following train has to adjust the operation control strategy in real-time according to both its self-condition and that of the leading one to prevent it from crashing.

In these years, with the rapid development of wireless communication and network technique, a wide range of Internet of Things (IoT) applications has been found in many areas such as smart cities [8], spatial crowdsourcing [9], and crowd dynamics management [10]. IoT is expected to achieve intelligent information processing, pervasive sensing, and efficient resource management in sensor network [11–14].

The Train Communication Network (TCN) standard was approved by the International Electrotechnical Commission (IEC) and the IEEE in 1999 to warrant interoperability of train and equipment. TCN encompasses two serial master-slave buses: the Wire Train Bus (WTB) and the Multifunction Vehicle Bus (MVB). Nowadays, TCN is widely used in high-speed rail trains and metro trains [15–19].

Recently, several fault detection methods have been presented to enhance the safety of the maglev train. A Bayesian network based detection method has been conducted [20, 21] to investigate acceleration sensor failures and analyse the multistate of the braking system. For maglev train, a risk modelling method of the failure event tree is given to detect the failure of levitation control system in [22].

In this paper, using IoT, a sensor network architecture is designed to monitor the vehicle-borne battery condition data in each vehicle; all these data in the train are collected by OCS through TCN and connected trains share them via RCS. Further, a new operation control strategy is proposed to guarantee the safety of the following operation for the connected maglev trains.

The main contributions of this paper are as follows.

(1) For existing operation control strategies, it is assumed that the train-borne batteries have full capacity all the time. The proposed operation control strategy regards the battery conditions as variable states and formulates strategy in real-time according to the conditions of the batteries.

(2) Comparing with existing operation control strategies, the proposed strategy takes other connected trains into consideration and adjusts the operation control strategy dynamically.

The rest of this paper is organized as follows. In Section 2, we analyse main resistance and energy consumption of the maglev train briefly. Section 3 is dedicated to designing a sensor network for the connected maglev trains to monitor battery conditions and exchange related information. In Section 4, based on battery condition data, an operation control strategy is proposed to guarantee the train safety in both station and section decentralizations. Section 5 is devoted to the simulation evaluation of the proposed scheme. Finally, conclusions are presented in Section 6.

2. Dynamic Analysis of the Maglev Train

Generally, the maglev train can be regarded as a rigid body when we study the operation control strategy. The total resistance f_{sum} mainly comes from the air, rail line, magnetic force, eddy current braking force, and other additional forces. The total resistance f_{sum} (unit is KN, the same below) can be described as

$$f_{\text{sum}} = f_{\text{air}} + f_{\text{mag}} + f_{\text{eddy}} + f_{\text{motor}} + f_{\text{skid}} + f_i + f_r, \quad (1)$$

where f_{air} is the air resistance, f_{mag} is the magnetic resistance, f_{eddy} is the eddy current braking resistance, f_{motor} is the linear motor braking resistance, f_{skid} is the gliding skid braking resistance, f_i is the curve resistance, and f_r is the gradient resistance.

The intrinsic resistance includes air resistance and intrinsic magnetic resistance [11]. Without considering the wind condition, the air resistance and magnetic resistance are given by

$$\begin{aligned} f_{\text{air}} &= 2.8 \times 10^{-3} \times (0.265N + 0.3) v^2, \\ f_{\text{mag}} &= 1.86N \left(1 - e^{-v/108}\right), \end{aligned} \quad (2)$$

where N is the number of train vehicles and v is the train speed.

For the maglev train, the braking force is mainly from the reverse braking, the resistance braking, the eddy current braking, the wearing plate braking, and the gliding skid braking.

Normally, the linear motor makes maglev train slow down by reverse braking and energy consume braking. The braking force f_{motor} is given as

$$f_{\text{motor}} = \begin{cases} 0, & (v < 10 \text{ km/h}) \\ 2.03N, & (10 \text{ km/h} < v < 70 \text{ km/h}) \\ N \left(\frac{146}{v} - 0.2 \right), & (v > 70 \text{ km/h}). \end{cases} \quad (3)$$

In case of emergency, VSC sends blocking propulsion power request to DCS to shut off PPS and the eddy current braking is initiated. The force of the eddy current braking is as follows:

$$f_{\text{eddy}} = f_{\text{eddy-x}} + f_{\text{plate}}, \quad (4)$$

where $f_{\text{eddy-x}}$ is the eddy current braking resistance in running direction and can be described as follows:

$$f_{\text{eddy-x}} = \begin{cases} 2.28qN (0.014I^2 + 0.004I) \cdot (1 - 0.6e^{-v/30}) & (10 \text{ km/h} < v < 150 \text{ km/h}) \\ 0.032qNI^2 & (v > 150 \text{ km/h}). \end{cases} \quad (5)$$

When the speed decreases to 130 km/h or lower, the wearing plate braking is initiated to make attractive force between the eddy current electromagnet and the side rail of the line increase gradually; f_{plate} is described as

$$f_{plate} = N (0.0027v^2 - 0.92v + 74). \quad (6)$$

Once the speed of the maglev train decreases to 10 km/h or lower, the gliding skid braking is initiated to make the train stop.

$$f_{skid} = \mu_{skid} N m g \left(1 - \frac{i}{1000}\right), \quad (7)$$

where i is the gradient per millage, m is train weight, g is gravitational acceleration, and μ_{skid} is friction coefficient of the gliding skid braking and is given by

$$\mu_{skid} = (0.123 \times 10^{-5}v^2 - 0.0025v + 0.2642). \quad (8)$$

Moreover, the gradient line forms an additional resistance to the train. The additional gradient resistance f_i is

$$f_i = \frac{i N m g}{1000}. \quad (9)$$

In addition to the above-mentioned resistances, the curve line adds another additional curve resistance that can be described as follows:

$$f_r = \frac{600 N m g}{R}. \quad (10)$$

The train-borne equipment energy E is

$$E = E_{lev} + E_{brake} + E_{equip}, \quad (11)$$

where E_{lev} is levitation energy, E_{brake} is emergency braking energy, and E_{equip} is vehicle-borne equipment consumption energy.

The train levitation power is

$$P_{lev} = 0.1049v + 1.006m. \quad (12)$$

Although the whole deceleration process of the train is variable, the deceleration in a short differential time within $\Delta t = [t_i, t_{i+1}]$ can be assumed to remain constant. During $[t_i, t_{i+1}]$, the deceleration is $a(v_i)$. Therefore, the running distance S can be obtained by

$$v_{i+1} = v_i + a(v_i) \Delta t, \quad (13)$$

$$S_{i+1} = S_i + a(v_i) \Delta t + 0.5a(v_i) (\Delta t)^2.$$

3. Vehicle-Borne Battery Condition Sensor Network for Connected Maglev Trains

In this section, the impact of battery conditions on the operation and the monitored battery parameters are analyzed briefly. To share battery conditions for the connected maglev trains, a sensor network and a data exchange method are designed in detail.

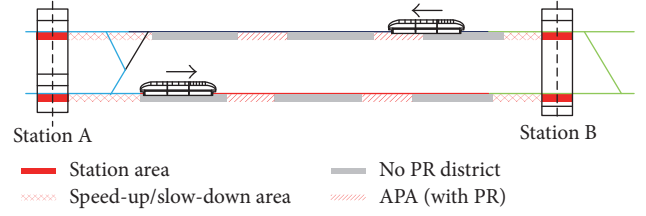


FIGURE 1: The sketch of a typical maglev transportation line.

3.1. The Impact of Battery Conditions on Maglev Train Operation. The line for the maglev train is divided into four types including station, speed-up area, track with ASA and PR, and track without PR, as shown in Figure 1.

As is shown in Figure 2(a), the train speed is usually lower than 100 km/h in the station and vehicle-borne collectors provide the energy from PR for levitation and vehicle equipment including batteries and other electrical loads. When departing the station, with the power from PR, the train accelerates quickly to exceed the minimum levitation limit. In case of emergency, the train has to be braked to stop within either station or speed-up area. In this case, two possibilities should be evaluated by OCS: (1) if the train can still stop within the speed-up area, an emergency braking should be initiated; (2) if the train can only stop beyond the speed-up area, current operation strategy is kept for certain time and then train is braked to run to the next ASA in the section decentralization.

During section decentralization operation, when train speed is higher than 100 km/h, the vehicle-borne linear generators supply the levitation energy, as shown in Figure 2(b). However, when its speed is lower than 100 km/h, the vehicle-borne batteries provide the levitation energy because vehicle-borne linear generators cannot supply enough energy, as shown in Figure 2(c). Moreover, a stop-point-stepping method is employed to make the train run through ASA until forwarding to next station according to the arranged speed curves. In case of emergency, similar to the situation in the station, two possibilities should be considered: (1) if the train has to stop immediately because of some unexpected emergencies like a maintenance vehicle ahead, the train has to brake with the maximum deceleration; (2) otherwise, the running state and the deceleration process should be adjusted accordingly to make train stop in the next ASA.

3.2. Vehicle-Borne Battery Condition Monitoring. The normal working ranges of lithium batteries in the maglev train are shown in Table 1.

(1) *Battery Temperature Monitoring.* When discharging rate is too high, battery temperature increases quickly and forms hot air to rise in the tank. Therefore, the temperature sensors should be placed on the upper part of the box to obtain the actual temperature information easily. Using MicaZ modules of MEMSIC Inc., the temperature values and their corresponding conditions are described in Table 2.

(2) *Battery Remaining Capacity Monitoring.* The voltage and current of the battery are obtained from Vehicle Diagnosis

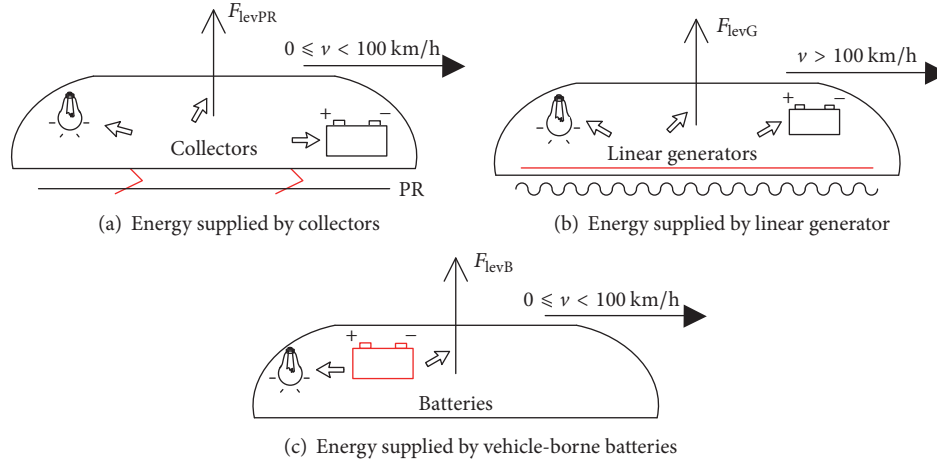


FIGURE 2: Power supply modes for the maglev train.

TABLE 1: Lithium battery operating characteristics.

Parameters	Normal working range
Temperature	-20°C to $+55^{\circ}\text{C}$ (The maximum relative humidity below 95% RH)
Voltage	DC 440 V (± 20 V)
Current	DC 0 A–40 A

TABLE 2: Temperature values and corresponding conditions.

Temperature values	Condition
Lower than -20°C	Too low
-20°C to 55°C	Normal
Higher than 55°C	Too high

Computer (VDC), and the remaining capacity of the battery can be evaluated to realize the real-time monitoring of remaining capacity. The relationships between remaining capacity and corresponding conditions are shown in Table 3.

(3) *Battery Visible Flame Monitoring.* In the practical operation, the battery temperature often exceeds the normal limits. Unfortunately, VDC cannot tell whether there is fire or not. The flame sensors can be used to detect the visible battery flame. The relationships between the visible flame and corresponding conditions are shown in Table 4.

3.3. *Vehicle-Borne Battery Sensor Network.* The parameters indicating the conditions of the vehicle-borne battery include temperature, voltage, and current [23–26]. During the train operation, in order to prevent the batteries from overheating, their temperature ought to maintain a safe range. Meantime, voltage and current of each battery should keep at an appropriate level to guarantee the remaining energy for vehicle-borne equipment and train levitation. When a maglev train stops in the station or ASA, its batteries must be checked to remain enough energy to provide its levitation to the

next ASA and can perform an emergency braking before its departure.

Each vehicle of the maglev train has eight batteries including four 440 V and four 24 V. Except for emergency-lighting depending on 24 V batteries, almost all train-borne systems including levitation and direction, braking, air-conditioning, and other ones are supplied by four 440 V batteries. Here, we only take four 440 V batteries into consideration. For a typical maglev train with six vehicles, a sensor network based on IoT to monitor vehicle-borne battery condition is shown in Figure 3. The network includes two Vehicle Safety Computers (VSCs) and two Mobile Radio Control Units (MRCUs) for two terminal vehicles and one Data Acquisition Unit (DAU) for each vehicle. In a vehicle, DAU gathers batteries condition data and sends them to VSCs; the master VSC formulates the operation control strategy accordingly (the master VSC is active and the slave one is in hot standby state).

Both head and tail vehicles have 2 directional antennas on top of them to form redundancy communication channels. Connected maglev trains exchange condition data via existing RCS, whose base stations are located along the rail line, as shown in Figure 4.

4. Operation Control Strategy for the Connected Maglev Trains

Considering the train-borne battery conditions, an operation control strategy for the independent maglev train is given in this section. Further, for the connected trains, based on five speed limits as shown in Figure 5, an operation control strategy for the following operation of the connected trains is discussed in detail.

Curve (1) is a minimum speed-up limit used to reach minimum speed, curve (2) is a minimum levitation limit considering running resistance and slope influence, curve (3) is a maximum safety-brake limit considering safe braking characteristics and slope influence, curve (4) is a maximum speed running limit, curve (5) is a maximum speed limit considering the train structure and all line conditions, and curve (6) is actual running speed limit.

TABLE 3: Remaining capacity and corresponding condition.

Remaining capacity	Condition
Not enough to provide energy for levitation and emergency braking	Battery exhausted
Enough to provide energy for levitation and emergency braking, but cannot provide extra energy for vehicle-borne equipment	No enough energy
Meets all the vehicle energy requirements	Sufficient electricity

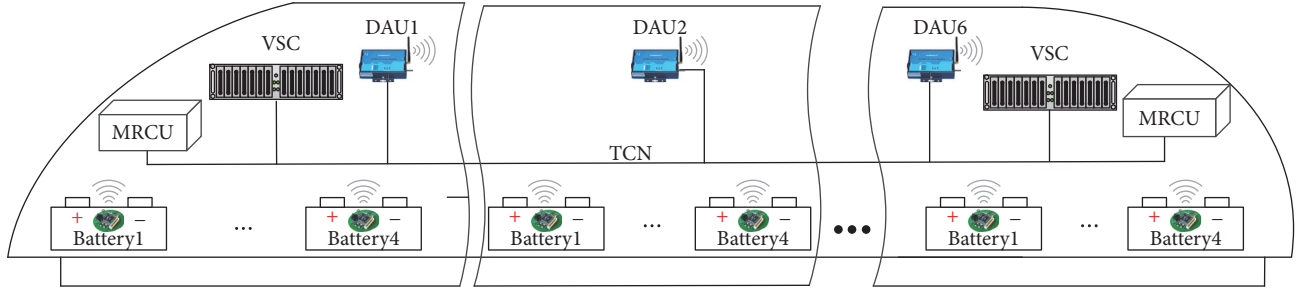


FIGURE 3: An IoT based sensor network scheme for the maglev train.

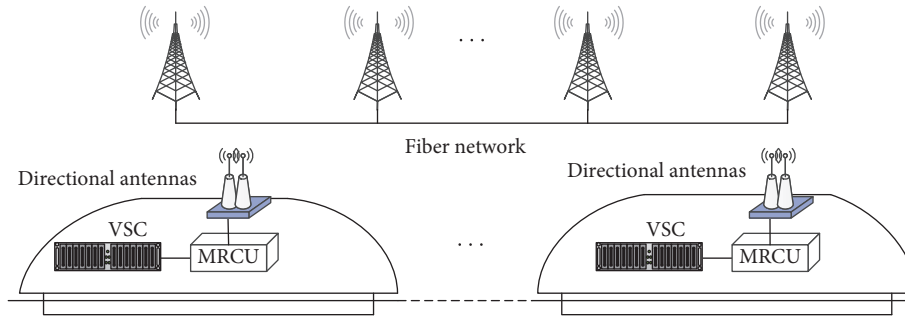


FIGURE 4: Data exchange scheme for connected maglev trains.

TABLE 4: Visible flame and corresponding condition.

Visible flame	Condition
Yes	On fire
No	No fire

4.1. *Battery Conditions Based Operation Strategy.* Based on the battery parameters including temperature, voltage, current, and visible flame, different operation control strategies are employed to ensure the train operation safety. The battery remaining capacity can be calculated with battery voltage and current [23]. The battery parameters and corresponding operation control strategies are shown in Tables 5–7.

4.2. *Operation Control Strategy for Departure and Pull-In.* When the train departs from the station, the energy for levitation and vehicle-borne equipment is supplied by the collectors that are connected to PR. In order to run to the next ASA, all the vehicle-borne batteries have to be evaluated. The operation control strategy is to satisfy the minimum capacity requirement for levitation and emergency braking (at least once). Once the train speed is lower than the minimum

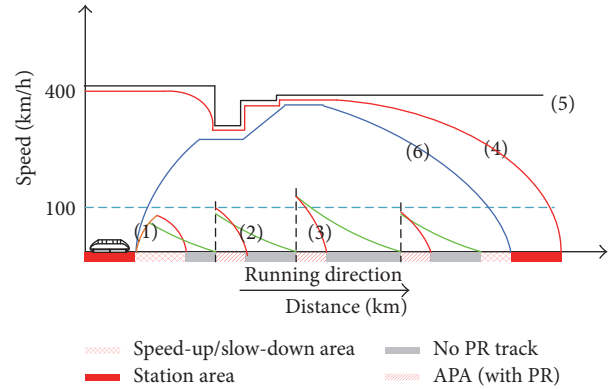


FIGURE 5: Speed limits for the maglev train.

levitation limit, PPS will be shut off, making the train float to the nearest ASA in levitation state.

In the pull-in deceleration area, the operation control strategy is to use kinetic and potential energy to run into the station, as shown in Figure 6. During approaching the station, if the initial speed $v_1 > 100$ km/h, the gliding distance S_{v1} and the operation mode switching point (see point A: from

TABLE 5: The temperature related strategies.

Temperature	Operation control strategies
Lower than -20°C	Pump hot air into the battery box
-20°C to 55°C	Run normally
Higher than 55°C	(1) VDC sends the high-temperature alarm to OCS to increase the cooling fan. (2) VDC sends battery failure to OCS when the alarm keeps for over 3 minutes. (3) If the temperature continues to rise but does not reach the limit of combustion, all passengers get off after the train stops. (4) If the temperature reaches the limit of combustion, VDC releases fire alarm, the train stops in the nearest ASA.

TABLE 6: The remaining capacity related strategies.

Remaining capacity	Operation control strategies
Not enough to provide energy for levitation and emergency braking	Turn off air conditioners and other vehicle-borne equipment. The train is not allowed to run unless the required capacity is charged.
Enough to provide energy for levitation and emergency braking, but cannot provide enough energy for vehicle-borne equipment	Turn off the vehicle-borne equipment to keep safe levitation to the next ASA for recharging.
Meets all the vehicle energy requirements	Run normally

TABLE 7: The visible flame related strategies.

Visible flame	Operation control strategies
Yes	Perform an emergency braking
No	Run normally

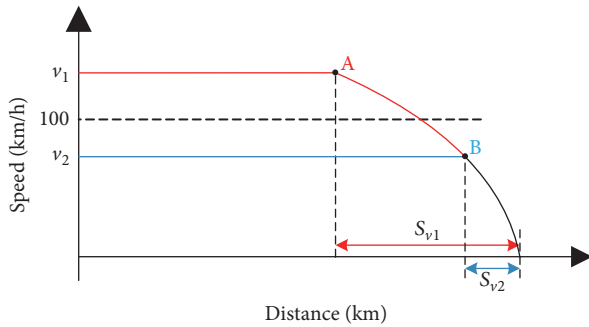


FIGURE 6: The lowest power consumption in the pull-in.

constant speed coasting mode to braking deceleration mode) are determined firstly according to (1)–(8) and (13), making the batteries supplied energy minimum in the distance S_{v1} . On the other hand, when the initial speed $v_2 < 100$ km/h, the energy for levitation and other equipment is supplied by the train-borne batteries; the gliding distance with kinetic and potential energy is only S_{v2} from the switching point B obtained in the same way of switching point A. In such case, the operation control strategy is to cut off the power for other train-borne equipment to guarantee the energy supply for levitation and emergency braking.

4.3. Section Operation Control Strategy for the Connected Trains. When connected trains run with the same direction

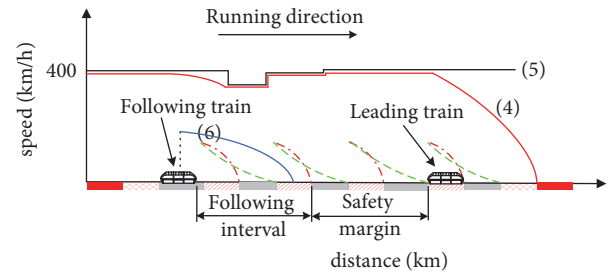


FIGURE 7: The following operation of connected maglev trains.

in the same line, the location and speed of the leading train can affect the following train according to the mobile blocking principle. In this case, the leading train is treated as a mobile obstacle for the following train. As shown in Figure 7, to guarantee the safety of the following operation, together with the mobile blocking method and the leading train state, the operation control strategy for the following train is to formulate a speed limit (i.e., speed limit 6) that can satisfy the following interval and also leave a safety margin.

Normally, the following train runs behind the leading one for more than the safety distance. If the leading train decelerates or performs an emergency braking, the following one performs corresponding strategy to prevent it from crashing into the leading one. In the extreme case, when the leading train stops on the line for some reasons, the operation control strategy for the following train is to stop in the ASA that is behind the leading train for at least one safe ASA.

As is shown in Figure 8, during the following operation, if the train-borne batteries of the leading train break down to bring an emergency braking, the following train can obtain the related data through RCS. In this case, two operation control strategies can be formulated to save battery energy

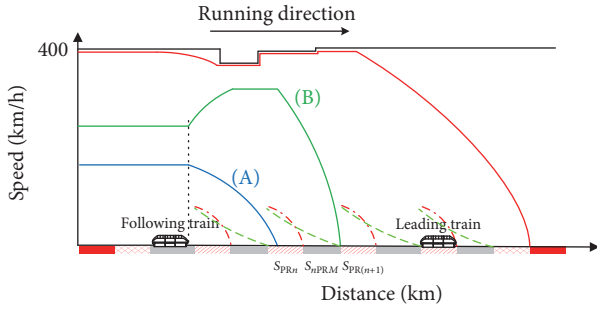


FIGURE 8: The operation control strategy for following train.



FIGURE 9: Map of the scenario for the experiment.

of the following train: (1) if the following interval is long enough and the following train cannot stop in the next ASA because of high speed, the following train can accelerate to the maximum speed, coast for a specific distance, and then brake to stop in the ASA that is behind the leading train (see curve (B)); (2) if the current speed is relatively low, the following train is braked to stop in the next ASA (see curve (A)).

5. Simulation and Experimental Results

In this section, a simulation is carried out and an experiment is performed to verify the effectiveness of the proposed operation control strategy and illustrate the applicability of the obtained results. The map of the scenario and the line sketch are shown in Figures 9 and 10; the parameters of the maglev train and the line are described Table 8.

The resistance and corresponding deceleration of the train at different speeds are shown in Figure 11. It can be seen that total deceleration is higher than 1 m/s^2 . When the train speed is lower than 10 km/h , the deceleration is mainly from the gliding skid. When $10 \text{ km/h} < v < 140 \text{ km/h}$, the eddy current braking provides the main resistance for the train. However, the air resistance and the eddy current braking supply the resistance for the train when $v > 140 \text{ km/h}$.

The remaining capacity of the vehicle-borne battery is a key factor that affects the operation control strategy formulating. The speed-distance and energy-distance curves under the emergency braking and intrinsic resistance braking are shown in Figures 12 and 13. From Figure 12, the minimum running point and the related energy for levitation and other vehicle-borne equipment can be obtained. When the initial speed is 400 km/h , the braking distance is 2.65 km and the minimum battery capacity for levitation and other train equipment is 4.38 kWh . Meanwhile, the maximum running

TABLE 8: Parameters of the experimental line.

Parameters	Numerical value
Total weight of single full load vehicle, m (t)	62 (terminal) 64.5 (middle)
Length of single vehicle, L_{veh} (m)	27 (terminal) 24.5 (middle)
Number of vehicles, N	6
Total train weight, m_T (t)	382
Total train length, L_{trn} (m)	153
Maximum speed, v_{max} (km/h)	400
Total capacity of four sets of batteries per vehicle, E_{btry} (kwh)	70.4
Braking power P_b (kW)	109
Vehicle equipment power, P_e (kW)	105
Average propulsion acceleration, a_{ac} (m/s^2)	0.9
Average propulsion deceleration, a_{dc} (m/s^2)	0.8
Platform length, L_{stn} (m)	210
Shortest length of departure PR, S_{dprt} (m)	2648
Shortest length of pull-in PR, S_{pi} (m)	1718
The length of the first departure track without PR, S_{nPR1} (m)	551
The length of first approaching track without PR, S_{nPRz} (m)	420
The length of the longest track without PR in the section decentralization, S_{nPRM} (m)	6025
The length of PR in section decentralization, S_{PR} (m)	455

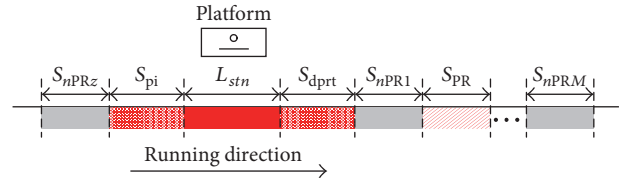


FIGURE 10: The sketch of the experimental line.

speed and the corresponding energy can be obtained from Figure 13. During the operation control strategy formulating, any ASA within these two points can be chosen to stop the train.

During the running, if a vehicle-borne battery related emergency happens, based on our proposed operation control strategy, the train can run for a given distance at the constant speed and then the emergency braking is performed to stop the train quickly to consume the battery energy as little as possible. From Figure 14, it can be seen that the train consumes less vehicle-borne battery energy and total running time is shorter at a higher initial speed. In our simulation, the initial speed is supposed to be 400 km/h and the distance from the train location to the stop-point is 2774.5 m according to Table 8. From (1)–(8) and (13), the distance for emergency braking with initial speed 400 km/h is 2651.3 m , leaving 123.2 m for the train running with constant

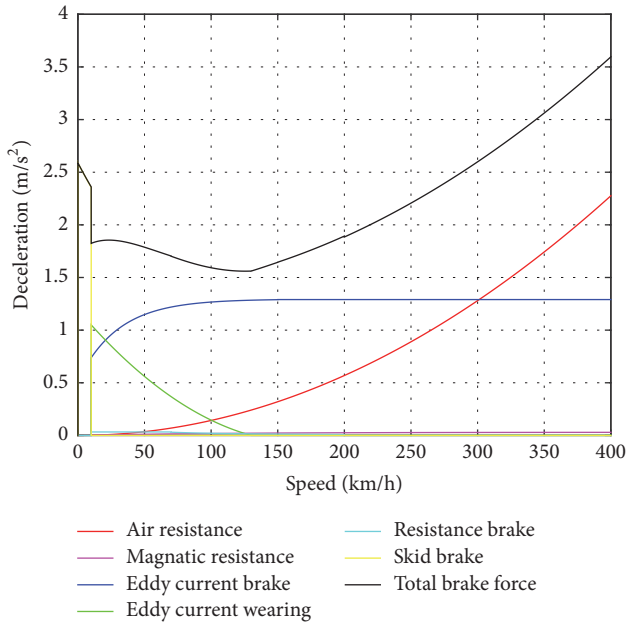


FIGURE 11: Deceleration of train at different speeds.

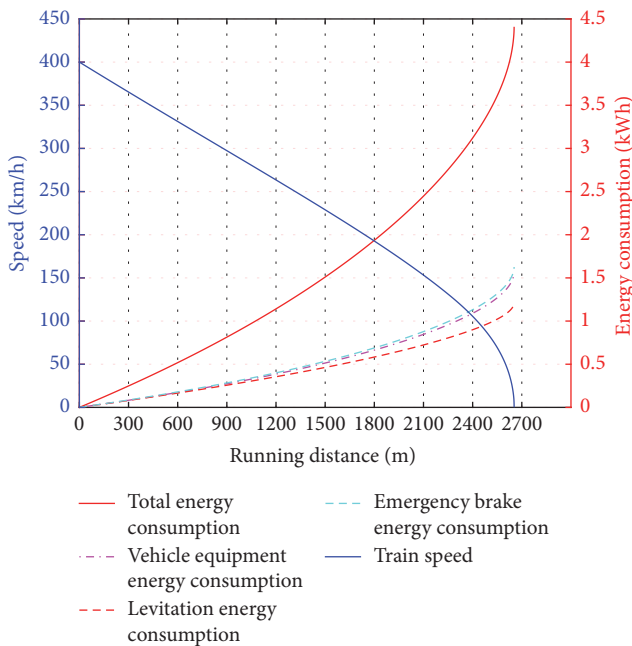


FIGURE 12: Speed-distance and energy-distance curves of the train under emergency braking.

speed at 400 km/h and the total running time is 54.8 s. From (11) and (12), the total energy consumption is 4.47 kWh.

As is shown in Figure 15, during the following operation for the connected trains, if the leading train performs an emergency or decelerates for some reasons, the following train should adjust the operation strategy to prevent it from crashing. Suppose the distance between the two trains is 15 km. Because the minimum braking distance for the initial speed 400 km/h is 2.65 km and the minimum capacity of

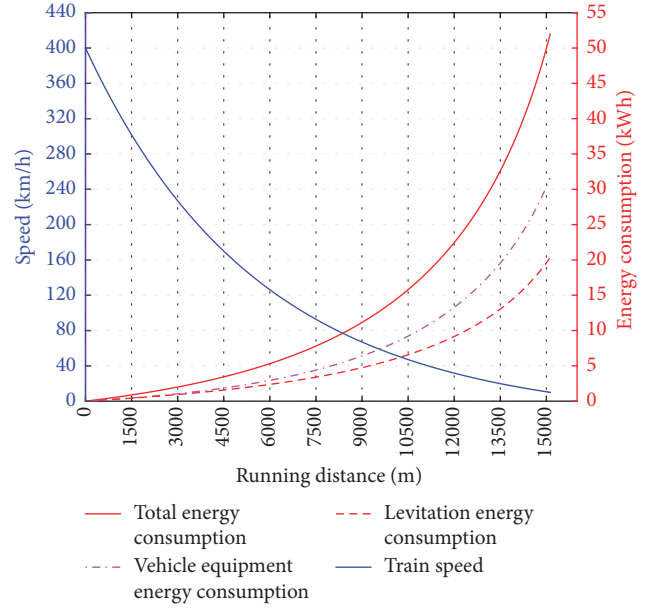


FIGURE 13: Speed-distance and energy-distance of a train under intrinsic resistance.

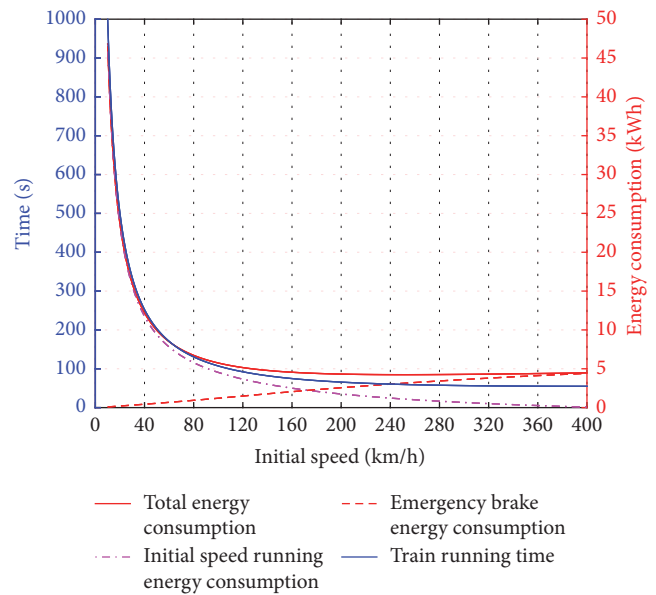


FIGURE 14: The running time and the energy consumption versus the initial speed.

the train-borne battery is 4.38 kWh, the operation control strategy for the following train is to speed up to 400 km/h, run for about 9.45 km, and then perform a maximum braking to run to an ASA that is behind the leading train for about 3 km (here considering the safety margin of about 3 km). Thus, the safety of the following operation for the connected trains can be guaranteed.

For the connected trains, in case of shutting-off PPS for the following train, the operation control strategy for the following train is to evaluate whether the following interval

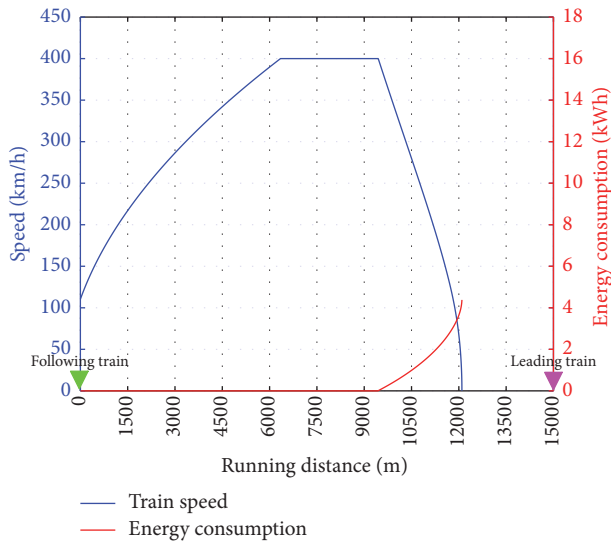


FIGURE 15: The following operation of the connected trains.

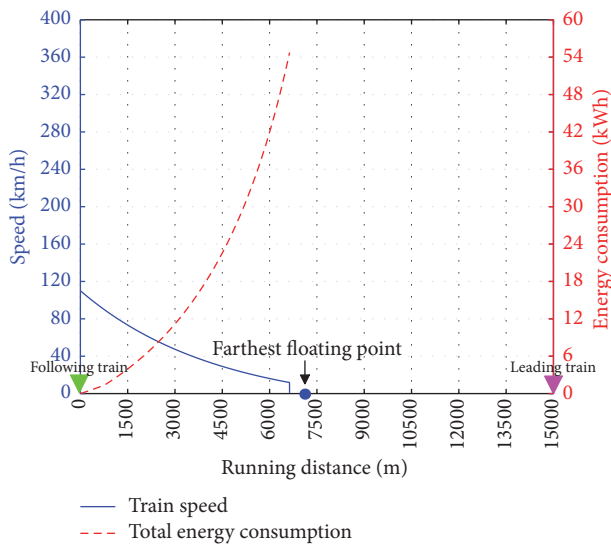


FIGURE 16: The floating running for the following train without PPS.

between the two trains is larger than the floating distance and the train-borne battery capacity is enough to supply the levitation for the floating. If true, the following train can float to the next ASA. As is shown in Figure 16, the energy for floating running of the following train is about 54 kWh, and the floating distance is about 6.6 km. Because the following interval is larger than the floating distance, the following train can float to the ASA between the train location and the farthest floating point.

6. Conclusions

In this paper, considering the vehicle-borne battery condition monitoring, an operation control strategy is proposed to guarantee the operation safety of the connected maglev

trains. The condition information of the vehicle-borne battery temperature and remaining capacity is gathered by IoT and collected by OCS via TCN; the connected trains share the condition data through RCS. The following train formulates the operation control strategy in real-time according to train-borne battery conditions and the operation state of the leading train. The simulation and experiment are given to demonstrate the effectiveness of the proposed strategy.

Further investigations could be concerned with operation control strategy formulation for the connected trains considering the state of other vehicle-borne equipment and combining these constraints together.

Conflicts of Interest

The authors declare that there are no conflicts of interest regarding the publication of this paper.

Acknowledgments

This work was supported in part by the Fundamental Research Funds for the Central Universities under Grant 2017JBM017, in part by National Key R&D Program of China under Grant 2016YFB1200601, in part by National Natural Science Foundation of China under Grant 61573504, and in part by National Aerospace Science Foundation of China under Grant 201501M5001.

References

- [1] L. Yan, "The linear motor powered transportation development and application in China," in *Proceedings of the IEEE*, vol. 97, pp. 1872–1880, 2009.
- [2] L. G. Yan, "Development and application of the Maglev transportation system," *IEEE Transactions on Applied Superconductivity*, vol. 18, no. 2, pp. 92–99, 2008.
- [3] H.-W. Lee, K.-C. Kim, and J. Lee, "Review of Maglev train technologies," *IEEE Transactions on Magnetics*, vol. 42, no. 7, pp. 1917–1925, 2006.
- [4] J. Liu and W. Wu, "Research on 2-D speed protection curve and its algorithm of high-speed maglev transportation," *China Railway Science*, vol. 23, no. 4, pp. 106–110, 2002.
- [5] D. Chen, J. Yin, L. Chen, and H. Xu, "Parallel control and management for high-speed maglev systems," *IEEE Transactions on Intelligent Transportation Systems*, vol. 18, no. 2, pp. 431–440, 2017.
- [6] L. Liao and F. Köttig, "Review of hybrid prognostics approaches for remaining useful life prediction of engineered systems, and an application to battery life prediction," *IEEE Transactions on Reliability*, vol. 63, no. 1, pp. 191–207, 2014.
- [7] M. Pilar, G. Miguel, S. Carlos et al., "On condition maintenance based on the impedance measurement for traction batteries: development and industrial implementation," *IEEE Transactions on Industrial Electronics*, vol. 60, no. 7, pp. 2750–2759, 2013.
- [8] S. Dey, S. Mohon, P. Pisu, and B. Ayalew, "Sensor fault detection, isolation, and estimation in lithium-ion batteries," *IEEE Transactions on Control Systems Technology*, vol. 24, no. 6, pp. 2141–2149, 2016.
- [9] P. Yang, N. Zhang, S. Zhang, K. Yang, L. Yu, and X. Shen, "Identifying the most valuable workers in fog-assisted spatial

- crowdsourcing,” *IEEE Internet of Things Journal*, vol. 4, no. 5, pp. 1193–1203, 2017.
- [10] Y. Kawamoto, N. Yamada, H. Nishiyama, N. Kato, Y. Shimizu, and Y. Zheng, “A Feedback Control Based Crowd Dynamics Management in IoT System,” *IEEE Internet of Things Journal*, vol. 4, no. 5, p. 1476, 2017.
- [11] Z. Long, X. Wang, and C. Fan, “Braking system multi-state analysis of maglev train based on Bayesian networks,” in *Proceedings of the 2017 Prognostics and System Health Management Conference (PHM-Harbin)*, pp. 1–8, Harbin, China, July 2017.
- [12] X. Jiang, W. Nai, A. Yilixiati, Y. Yu, S. Wang, and D. Dong, “A train positioning mechanism for medium-low speed maglev train based on parity check cross coding inductive loop wire,” in *Proceedings of the 2017 3rd IEEE International Conference on Control Science and Systems Engineering (ICCSSE)*, pp. 269–272, Beijing, China, August 2017.
- [13] A. J. Stankovic, “Research directions for the internet of things,” *IEEE Internet of Things Journal*, vol. 1, no. 1, pp. 3–9, 2014.
- [14] K. Zhang, J. Ni, K. Yang, X. Liang, J. Ren, and X. S. Shen, “Security and privacy in smart city applications: challenges and solutions,” *IEEE Communications Magazine*, vol. 55, no. 1, pp. 122–129, 2017.
- [15] J. Jiménez, J. L. Martín, A. Zuloaga, U. Bidarte, and J. Arias, “Comparison of two designs for the multifunction vehicle bus,” *IEEE Transactions on Computer-Aided Design of Integrated Circuits and Systems*, vol. 25, no. 5, pp. 797–805, 2006.
- [16] A. Chavarría, J. L. De Arroyabe, A. Zuloaga, J. Jimenez, J. L. Martin, and G. Aranguren, “Slave node architecture for train communications networks,” pp. 2431–2436.
- [17] G. A. zur Bensen, “Multifunction vehicle bus (MVB),” in *Proceedings of the 1995 IEEE International Workshop on Factory Communication Systems, WFCS’95*, pp. 27–34, October 1995.
- [18] Z. Liu, Y. Hou, and W. Fu, “Communication simulation of on-board diagnosis network in high-speed Maglev trains,” *Journal of Modern Transportation*, vol. 19, no. 4, pp. 240–246, 2011.
- [19] H. Kirrmann and P. A. Zuber, “The IEC/IEEE train communication network,” *IEEE Micro*, vol. 21, no. 2, pp. 81–92, 2001.
- [20] H. Zhang, Y. Xie, and Z. Long, “Fault detection based on tracking differentiator applied on the suspension system of maglev train,” *Mathematical Problems in Engineering*, vol. 2015, Article ID 242431, 2015.
- [21] B. Kim, H. Park, K. H. Kim, D. Godfrey, and K. Kim, “A Survey on Real-Time Communications in Wireless Sensor Networks,” *Wireless Communications and Mobile Computing*, vol. 2017, pp. 1–14, 2017.
- [22] Z. Long, X. Chen, and C. Fan, “Middle — Low speed maglev train suspension control system common cause failure risk analysis,” in *Proceedings of the 2017 36th Chinese Control Conference (CCC)*, pp. 7218–7224, Dalian, China, July 2017.
- [23] H. He, R. Xiong, and H. Guo, “Online estimation of model parameters and state-of-charge of LiFePO4 batteries in electric vehicles,” *Applied Energy*, vol. 89, no. 1, pp. 413–420, 2012.
- [24] A. A. A. Elgammal and A. M. Sharaf, “Self-regulating particle swarm optimised controller for (photovoltaic-fuel cell) battery charging of hybrid electric vehicles,” *IET Electrical Systems in Transportation*, vol. 2, no. 2, pp. 77–89, 2012.
- [25] Z. Liu, Q. Ahmed, G. Rizzoni, and H. He, “Fault detection and isolation for lithium-ion battery system using structural analysis and sequential residual generation,” in *Proceedings of ASME 2014 Dynamic Systems and Control Conference*, vol. 21, pp. 1–14, 2014.
- [26] C. Hu, G. Jain, P. Tamirisa, and T. Gorka, “Method for estimating capacity and predicting remaining useful life of lithium-ion battery,” *Applied Energy*, vol. 126, pp. 182–189, 2014.

Research Article

Adaptive Equalizer Design for Unmanned Aircraft Vehicle Image Transmission over Relay Channels

Huang Wenqian  and Ding Wenrui

School of Electronic and Information Engineering, Beihang University, Beijing, China

Correspondence should be addressed to Huang Wenqian; huangwenqian@buaa.edu.cn

Received 8 December 2017; Revised 23 February 2018; Accepted 5 March 2018; Published 11 April 2018

Academic Editor: Hongwei Wang

Copyright © 2018 Huang Wenqian and Ding Wenrui. This is an open access article distributed under the Creative Commons Attribution License, which permits unrestricted use, distribution, and reproduction in any medium, provided the original work is properly cited.

A novel length adaptive method is proposed for time domain equalizer by taking the channel attenuation ratio between different multipath components into account in UAV-UAV and UAV-ground channels. Then, considering received image quality, the minimum bit error ratio (MBER) criterion is exploited to design adaptive equalizers for both amplify-and-forward (AF) and decode-and-forward (DF) relaying systems by the proposed length adaptive method. Results show that proposed MBER adaptive equalizers outperform the traditional ones in both AF relaying and DF relaying as channel attenuation ratio in UAV-ground channel increases. Moreover, DF outperforms AF as channel attenuation ratio in UAV-UAV channel increases. Furthermore, bit error ratio (BER) and peak signal-to-noise ratio (PSNR) performances in both AF and DF are evaluated to show the enhancement by the proposed MBER adaptive equalizers.

1. Introduction

With the explosive growth of using unmanned aircraft vehicle (UAV) for various applications, there is a tremendous demand for image wireless transmission in UAV remote sensing system [1, 2]. The performance of traditional direct UAV-to-ground communication is severely degraded by the fading of the wireless channel and can be easily shadowed by buildings in urban areas or by mountains in rural areas, leading to drop in the quality of the received images. Thus it is imperative to develop the future communication schemes to mitigate the impact caused by the fading and shadowing.

Relaying as an approach to increase the reliability and extend the coverage area of the UAV remote sensing system, as depicted in Figure 1, has attracted a huge interest [3–5]. In [3], UAVs are deployed as flying relays between aerial and ground mesh networks in an emergency scenario. Reference [5] investigated how to deploy UAVs as flying relays to increase coverage in the wireless network. Generally, there are mainly two widely used relaying schemes: amplify-and-forward (AF) and decode-and-forward (DF). In AF, the relay amplifies and retransmits the received signal from the source

to the destination. In DF, the relay decodes the signal and then forwards it to the destination.

According to recent measurement campaign and literatures [6–8], UAV-to-ground and UAV-to-UAV channels, two kinds of channels widely used in UAV-based relaying systems, can be typically modeled as frequency-selective multipath channels whose dispersive nature can easily cause the inter-symbol interference (ISI), leading to inevitable performance degradation. Additionally, channel taps of UAV-ground channel are larger than those of UAV-UAV channel [9–11]. Reference [7] found that the UAV-ground channel in over-sea scenarios can be well modeled by the two-ray model plus an intermittent multipath component. UAV-ground channels in hilly/mountainous and suburban/near-urban scenarios can be modeled by nine-tap multipath channels [8, 11]: line-of-sight (LoS) component as the first tap, Ground Reflection (GR) component as the second tap, and seven intermittent components.

High-speed single-carrier wideband transmission systems are widely used in aeronautical communication due to severe size, weight, and power (SWAP) of drones [12], and ISI caused by multipath propagation tends to be the main

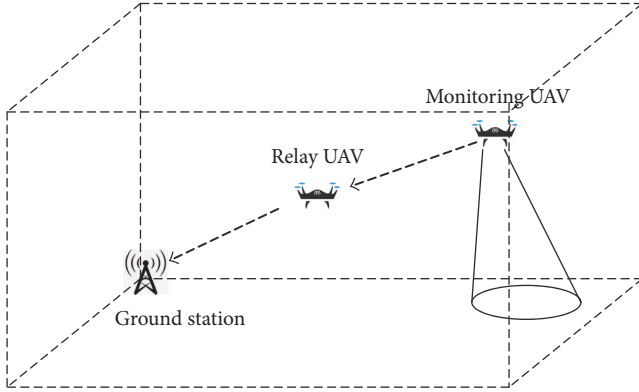


FIGURE 1: UAV remote sensing system.

factor limiting the reliability of these systems. Thus, time domain equalizer plays an important role mitigating ISI in aeronautical communication [12]. Zero-forcing (ZF) and minimum mean-squared error (MMSE) equalizers are proposed for single-hop aeronautical communication in [13].

In traditional terrestrial relaying systems, [14] designed the minimum bit error ratio (MBER) equalizer for AF relaying. A new detector for AF relaying is proposed in [15] using a minimum symbol error ratio (MSER) equalizer. MMSE and MBER equalizers are proposed and investigated in [16] for nonorthogonal AF relaying.

Different from terrestrial relaying systems, LoS communication links can always be established in UAV-based relaying systems. In particular, UAV-ground channel has some unique features due to the GR multipath component which can more easily cause severe ISI [9]. To the best of our knowledge, there is lack of works dealing with equalizer design for UAV-based relaying systems that take the characteristics of UAV-UAV and UAV-ground channels into account in previous literatures.

The main contributions of this work are the following:

- (i) A length adaptive method for equalizer design is proposed according to channel attenuation ratio between different multipath components.
- (ii) For image wireless transmission in UAV-based relaying systems, MBER criterion is exploited to design equalizers in both AF and DF relaying systems, since MBER, rather than the widely used MMSE, is more suitable to reflect image quality with high fidelity [17, 18].
- (iii) Bit error ratio (BER) and peak signal-to-noise ratio (PSNR) performances of AF and DF relaying with MBER adaptive equalizers are evaluated in relation to critical system parameters like the number of training symbols, defined complexity penalty parameter of DF, and average signal-to-noise ratio (SNR), which are important for practical application in UAV remote sensing system.

Notation. Bold uppercase and lowercase letters denote matrices and vectors, respectively. The superscript $(\cdot)^H$ denotes the

conjugate transpose of a matrix. $\text{Re}(\cdot)$ represents the real part of a complex number. $\text{sgn}(\cdot)$ denotes the sign function.

2. System Model

As depicted in Figure 2, we consider a three-node relaying system consisting of a monitoring UAV (M-UAV) as the source node, a ground station (GS) as the destination node, and a relay UAV (R-UAV) as the relay node without direct path between M-UAV and GS (e.g., due to shadowing or large separation). Each node is equipped with only one antenna and operates in the half-duplex mode. Two UAVs are assumed to have the same height h_U . Thus, the three-dimensional (3D) coordinates of M-UAV, R-UAV, and GS can be denoted as $\mathbf{s} = (x_s, y_s, h_U)$, $\mathbf{r} = (x_r, y_r, h_U)$, and $\mathbf{d} = (x_d, y_d, h_G)$, respectively.

The image bit stream is sent to GS from M-UAV via R-UAV using AF or DF relaying. In AF relaying, M-UAV transmits image bit stream to R-UAV in the first time slot and then R-UAV amplifies and retransmits the received bit stream to the GS in the second time slot. In DF relaying, M-UAV transmits the image bit stream to R-UAV in the first time slot and R-UAV decodes and retransmits the image bit stream in the second time slot. In AF relaying, the equalizer is considered only at GS; in DF relaying, two equalizers are considered at both R-UAV and GS.

2.1. UAV-UAV Channel Model. Considering UAV-UAV channel as a discrete-time Rician multipath channel, the channel outputs at R-UAV for both AF and DF can be expressed as

$$r_k^A = r_k^D = h_0^{UU} x_k + h_1^{UU} x_{k-1} + n. \quad (1)$$

$x_k \in \{\pm 1\}$ is k th BPSK data symbol, which is coded and modulated from image bit stream. n denotes additive white Gaussian noise (AWGN). h_0^{UU} and h_1^{UU} denote the channel attenuation of LoS and scattered components, respectively. The channel attenuation of LoS component in dB can be expressed as [6]

$$h_0^{UU} = 10\alpha \log\left(\frac{4\pi f_c R_{\text{LoS}}}{c}\right) + \psi_{\text{LoS}}, \quad (2)$$

where α is path loss exponent, f_c is the carrier frequency, c is the speed of light, and R_{LoS} denotes the range of LoS component. $\psi_{\text{LoS}} \sim N(\mu_{\text{LoS}}, \delta_{\text{LoS}})$ is the shadow fading with normal distribution in dB for LoS link. The channel attenuation of scattered components in dB can be expressed as

$$h_1^{UU} = h_0^{UU} - K, \quad (3)$$

where K in dB is the Rician K -factor for UAV-UAV channel.

2.2. UAV-Ground Channel Model. Considering the discrete-time UAV-ground multipath channel based on the recent

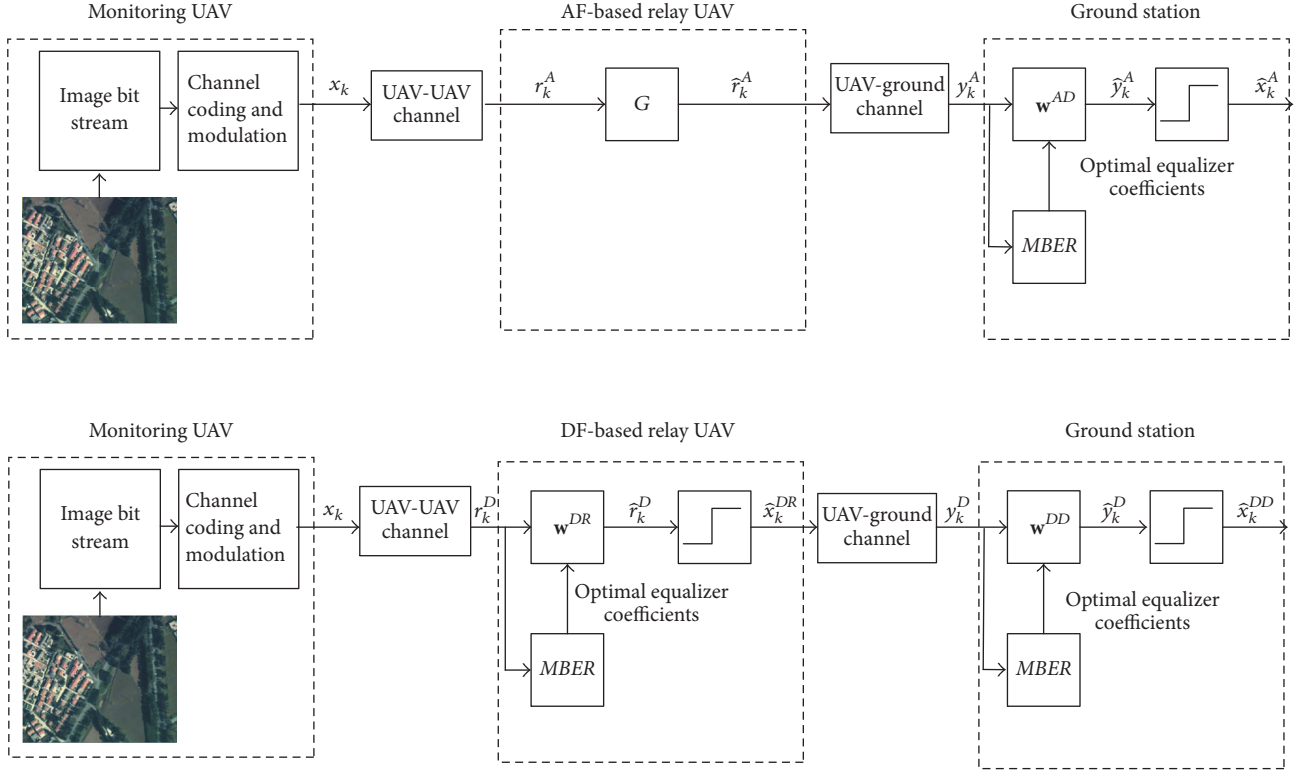


FIGURE 2: System model.

works [7, 8, 11], the channel outputs at GSs for AF and DF can be expressed as

$$y_k^A = \sum_{i=0}^{C_{UG}} h_i^{UG} \tilde{r}_{k-i}^A + n, \quad (4)$$

$$y_k^D = \sum_{i=0}^{C_{UG}} h_i^{UG} \tilde{x}_{k-i}^{DR} + n, \quad (5)$$

respectively. $C_{UG} \geq 3$ denotes the channel taps for UAV-ground channel. The value of these channel taps depends on environment; for instance, $C_{UG} = 3$ in the over-water scenarios, while $C_{UG} = 9$ in the mountainous and hilly scenarios [7, 11]. h_0^{UG} denotes the channel attenuation of LoS component and can be expressed the same as (2):

$$h_0^{UG} = 10\alpha \log \left(\frac{4\pi f_c R_{LoS}}{c} \right) + \psi_{LoS}. \quad (6)$$

Similarly, h_1^{UG} denotes the channel attenuation of the GR component and can be expressed as

$$h_1^{UG} = 10\alpha \log \left(\frac{4\pi f_c R_{GR}}{c} \right) + \psi_{GR}, \quad (7)$$

where $\psi_{GR} \sim N(\mu_{GR}, \delta_{GR})$ is the shadow fading with normal distribution in dB for GR link and R_{GR} denotes the range of GR component.

Assuming a UAV-ground channel geometry as depicted in Figure 3 [10, 19], the ranges of LoS and GR components in UAV-ground channel can be calculated as

$$R_{LoS} = \sqrt{(h_U - h_G)^2 + d^2}, \quad (8)$$

$$R_{GR} = \sqrt{(h_U + h_G)^2 + d^2},$$

where d denotes the distance between R-UAV and GS in the horizontal plane.

For simplicity, the channels between all nodes are assumed to be constant during the transmission time of one image (moving distances of nodes can be negligible within this period, since UAV datalink speed, whose carrier frequency usually uses L-band (960-997 MHz) or C-band (5030-5091 MHz) [9], can reach 10 Mbps [20]).

3. MBER Adaptive Equalizer Design for Relaying System

3.1. Length Adaptive Mechanism. For example, in (1), the desired received signal component for k th symbol is $h_0^{UU} x_k$, but the component $h_1^{UU} x_{k-1}$, also called ISI, could have an influence on the received signal decision performance due to the delay transmission of $(k-1)$ th symbol x_k over the channel h_1^{UU} . This decision performance depends on some system parameters. One of them is the channel attenuation ratio between LoS and GR components in UAV-ground channel or scattered components in UAV-UAV channel. For

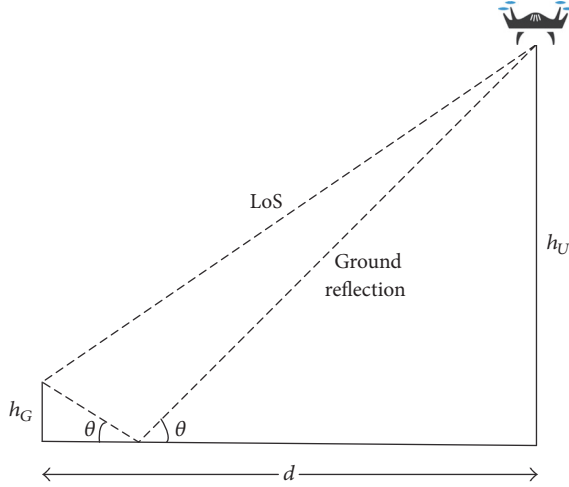


FIGURE 3: UAV-ground channel geometry.

example, in (1), if the magnitude of component $h_0^{UU} x_k$ is much larger than that of component $h_1^{UU} x_{k-1}$, the ISI influence on decision performance is very limited; otherwise, the decision performance could be severely degraded.

Generally, the reliability performance of equalizers aiming at mitigating ISI increases with the equalizer length but at the cost of more training time. Considering equalizer performance as well as training time, traditional fixed length equalizers have limited adaptive performance: equalizers with large length could generate severe signal processing delay due to more training time, while the one with small length could not mitigate ISI as much as possible.

Thus, the proposed length adaptive mechanism is that equalizer can adjust its length to optimal ISI mitigation performance according to the channel attenuation ratio between different multipath components:

$$\frac{L - L_{\min}}{L_{\max} - L_{\min}} = \frac{\gamma - \gamma_{\min}}{\gamma_{\max} - \gamma_{\min}}, \quad (9)$$

where L denotes the equalizer length using proposed method. $L_{\min} = 2$ is the minimal equalizer length. L_{\max} is the maximal equalizer length depending on the calculating resources of receivers.

In UAV-ground channel, the channel attenuation ratio in dB between LoS and GR components can be expressed as

$$\gamma^{UG} = h_1^{UG} - h_0^{UG}. \quad (10)$$

We assume that the position of R-UAV is known by GS by control signals at first; then γ^{UG} can be calculated using (6) and (7) at GS. Thus the length of equalizer at GS can be adjusted using (9).

In UAV-UAV channel, this ratio is also related to Rician K-factor:

$$\gamma^{UU} = \frac{1}{K}. \quad (11)$$

γ_{\min} and γ_{\max} denote the maximal and minimal channel attenuation ratio, respectively. The values of γ_{\min} and γ_{\max} depend on the environment [7, 8, 11].

The proposed optimal equalizer length can be rewritten as

$$L = f(\gamma) = \frac{\gamma - \gamma_{\min}}{\gamma_{\max} - \gamma_{\min}} (L_{\max} - L_{\min}) + L_{\min}. \quad (12)$$

3.2. Equalizer Design for AF. The equalizer at GS in AF relaying can be described by the vector $\mathbf{w}^{AD} = \{w_1^{AD} \dots w_{L^A}^{AD}\}^T$ and equalizer outputs can be expressed as

$$\hat{y}_k^A = \sum_{i=1}^{L^A} w_i^{AD} \hat{r}_{k-i}^A + n, \quad (13)$$

where L^A denotes the optimal length of equalizer at GS in AF relaying and can be calculated by

$$L^A = f(\gamma^{UG}). \quad (14)$$

The equalizer outputs are then passed to the decision device and the decision can be expressed as

$$\hat{x}_k^A = \text{sgn}(\text{Re}(\hat{y}_k^A)) = \begin{cases} +1 & \text{Re}(\hat{y}_k^A) \geq 0, \\ -1 & \text{Re}(\hat{y}_k^A) \leq 0. \end{cases} \quad (15)$$

Then, based on (1), (4), (13), and (15), the end-to-end signal transmission over the whole link can be expressed as

$$\begin{aligned} \hat{x}_k^A &= \text{sgn}(\text{Re}(\hat{y}_k^A)) \\ &= \text{sgn}(\text{Re}((\mathbf{w}^{AD})^H \mathbf{H}^{A2} \mathbf{G} \mathbf{H}^{A1} \mathbf{x}_k^A + n)) \end{aligned} \quad (16)$$

where $\mathbf{x}_k^A = \{x_k, x_{k-1}, \dots, x_{k-(L^A+2+C_{UG}-1)}\}^T$ is a vector of channel inputs from M-UAV. $\mathbf{G} = \sqrt{1/((h_0^{UU})^2 + (h_1^{UU})^2)}$ is ideal amplifying gain at R-UAV for each received symbol. \mathbf{H}^{A2} is the $L^A \times (L^A + C_{UG})$ Toeplitz convolution matrix; \mathbf{H}^{A1} is the $(L^A + C_{UG}) \times (L^A + C_{UG} + 2)$ Toeplitz convolution matrix. \mathbf{H}^{A2} and \mathbf{H}^{A1} can be expressed as

$$\begin{aligned} \mathbf{H}^{A2} &= \begin{bmatrix} h_0^{UG} & h_1^{UG} & \dots & h_{C_{UG}}^{UG} & 0 & \dots & 0 \\ 0 & h_0^{UG} & h_1^{UG} & \dots & h_{C_{UG}}^{UG} & 0 & \vdots \\ & & & & & \ddots & \\ 0 & \dots & 0 & h_0^{UG} & h_1^{UG} & \dots & h_{C_{UG}}^{UG} \end{bmatrix}, \\ \mathbf{H}^{A1} &= \begin{bmatrix} h_0^{UU} & h_1^{UU} & 0 & \dots & 0 \\ 0 & h_0^{UU} & h_1^{UU} & 0 & \vdots \\ & & & \ddots & \\ 0 & \dots & 0 & h_0^{UU} & h_1^{UU} \end{bmatrix}. \end{aligned} \quad (17)$$

The BER for AF relaying after equalizer \mathbf{w}^{AD} can be defined as

$$\begin{aligned} P_E^A &= \Pr(\hat{x}_k^A x_k < 0) \\ &= \int_{-\infty}^0 P(\mathbf{w}^{AD}, \text{Re}(\hat{y}_k^A)) x_k d(\text{Re}(\hat{y}_k^A)), \end{aligned} \quad (18)$$

where $p(\mathbf{w}^{AD}, \text{Re}(\hat{y}_k^A))$ denotes the probability density function (PDF) of $\text{Re}(\hat{y}_k^A)$ and is also the function of \mathbf{w}^{AD} . Then, the tap coefficient vector for MBER adaptive equalizer at GS for AF relaying can be expressed as

$$\mathbf{w}^{AD} = \arg \min_{\mathbf{w}} P_E^A(\mathbf{w}^{AD}). \quad (19)$$

3.3. Equalizer Design for DF. Equalizers at R-UAV and GS can be described by the vectors $\mathbf{w}^{DR} = \{w_1^{DR} \dots w_{L^{DR}}^{DR}\}^T$ and $\mathbf{w}^{DD} = \{w_1^{DD} \dots w_{L^{DD}}^{DD}\}^T$, respectively. Then, the equalizer outputs at R-UAV and GS can be expressed as

$$\hat{r}_k^D = \sum_{i=1}^{L^{DR}} w_i^{DR} r_{k-i}^D + n, \quad (20)$$

$$\hat{y}_k^D = \sum_{i=1}^{L^{DD}} w_i^{DD} y_{k-i}^D + n, \quad (21)$$

respectively. L^{DR} and L^{DD} denote the optimal equalizer lengths. Similar to (14), these two lengths can be calculated by

$$\begin{aligned} L^{DR} &= f(\gamma^{UU}), \\ L^{DD} &= f(\gamma^{UG}). \end{aligned} \quad (22)$$

The two equalizer outputs are then passed to the decision devices and the decisions can be expressed as

$$\hat{x}_k^{DR} = \text{sgn}(\text{Re}(\hat{r}_k^D)) = \begin{cases} +1 & \text{Re}(\hat{r}_k^D) \geq 0, \\ -1 & \text{Re}(\hat{r}_k^D) \leq 0, \end{cases} \quad (23)$$

$$\hat{x}_k^{DD} = \text{sgn}(\text{Re}(\hat{y}_k^D)) = \begin{cases} +1 & \text{Re}(\hat{y}_k^D) \geq 0, \\ -1 & \text{Re}(\hat{y}_k^D) \leq 0. \end{cases} \quad (24)$$

Similar to the equalizer design in AF, the end-to-end signal transmission at R-UAV and GS in DF can be rewritten as

$$\hat{\mathbf{x}}_k^{DR} = \text{sgn}(\text{Re}((\mathbf{w}^{DR})^H \mathbf{H}^{D1} \mathbf{x}_k + n)), \quad (25)$$

$$\hat{\mathbf{x}}_k^{DD} = \text{sgn}(\text{Re}((\mathbf{w}^{DD})^H \mathbf{H}^{D2} \hat{\mathbf{x}}_k^{DR} + n)), \quad (26)$$

respectively. $\mathbf{x}_k = \{x_k, x_{k-1}, \dots, x_{k-(L^{DR}+2-1)}\}^T$ and $\hat{\mathbf{x}}_k^{DR} = \{\hat{x}_k^{DR}, \hat{x}_{k-1}^{DR}, \dots, \hat{x}_{k-(L^{DD}+C_{UG}-1)}^{DR}\}^T$ are two vectors of channel inputs from M-UAV and R-UAV. \mathbf{H}^{D2} and \mathbf{H}^{D1} are $L^{DR} \times (L^{DR} + C_{UG})$ and $L^{DD} \times (L^{DD} + 2)$ Toeplitz convolution matrices, respectively. These two matrices can be expressed as

$$\mathbf{H}^{D2} = \begin{bmatrix} h_0^{UG} & h_1^{UG} & \dots & h_{C_{UG}}^{RD} & 0 & \dots & 0 \\ 0 & h_0^{UG} & h_1^{UG} & \dots & h_{C_{UG}}^{UG} & 0 & \vdots \\ & & & & & \ddots & \\ 0 & \dots & 0 & h_0^{UG} & h_1^{UG} & \dots & h_{C_{UG}}^{UG} \end{bmatrix}, \quad (27)$$

$$\mathbf{H}^{D1} = \begin{bmatrix} h_0^{UU} & h_1^{UU} & 0 & \dots & 0 \\ 0 & h_0^{UU} & h_1^{UU} & 0 & \vdots \\ & & & \ddots & \\ 0 & \dots & 0 & h_0^{UU} & h_1^{UU} \end{bmatrix}. \quad (28)$$

Following the same approach as carried out to obtain (19), the optimal tap coefficient vectors for MBER adaptive equalizers at R-UAV and GS for DF relaying can be expressed as

$$\begin{aligned} \mathbf{w}^{DR} &= \arg \min_{\mathbf{w}} P_E^{DR}(\mathbf{w}^{DR}), \\ \mathbf{w}^{DD} &= \arg \min_{\mathbf{w}} P_E^{DD}(\mathbf{w}^{DD}), \end{aligned} \quad (29)$$

where $P_E^{DR}(\mathbf{w}^{DR})$ and $P_E^{DD}(\mathbf{w}^{DD})$ can be expressed as

$$\begin{aligned} P_E^{DR} &= \Pr(\text{sgn}(\text{Re}(\hat{r}_k^D)) x_k < 0) \\ &= \int_{-\infty}^0 p(\mathbf{w}^{DR}, \text{Re}(\hat{r}_k^D)) x_k d(\text{Re}(\hat{r}_k^D)), \\ P_E^{DD} &= \Pr(\text{sgn}(\text{Re}(\hat{y}_k^D)) x_k < 0) \\ &= \int_{-\infty}^0 p(\mathbf{w}^{DR}, \text{Re}(\hat{y}_k^D)) x_k d(\text{Re}(\hat{y}_k^D)). \end{aligned} \quad (30)$$

3.4. Adaptive Equalizer Algorithm. We first consider the optimal equalizer coefficients for AF. To obtain optimal equalizer coefficients \mathbf{w}^{AD} , the PDF of $\text{Re}(\hat{y}_k^A)$ is necessary. It is seen that PDF of $\text{Re}(\hat{y}_k^A)$ is Gaussian mixture and can be estimated using nonparametric estimation [21]. Parzen window method is good at estimating PDF with relatively short data, which is efficient for equalizer training [21].

Given the training symbols $\{x_k, \mathbf{y}_k^A\}_{k=1}^N$ and using Parzen window function method, the PDF of $\text{Re}(\hat{y}_k^A)$ can be expressed as

$$p(t) = \frac{1}{N\sqrt{2\pi}\rho_n} \sum_{k=1}^N e^{-|t - \text{Re}(\hat{y}_k^A)|^2 / 2\rho_n^2}, \quad (31)$$

where N is the length of training symbols and ρ_n is the window width. Substituting (31) in (18), the BER for AF relaying can be rewritten as

$$P_E^A = \frac{1}{N} \sum_{k=1}^N Q\left(\frac{\text{sgn}(x_k) \text{Re}((\mathbf{w}^{AD})^H \mathbf{y}_k^A + n)}{\rho_n}\right), \quad (32)$$

where Q is the Gaussian error function. Then the gradient of P_E^A can be given as

$$\nabla P_E^A = -\frac{1}{2N\sqrt{2\pi}\rho_n} \times \sum_{k=1}^N e^{-|\text{Re}(\mathbf{w}^{AD})^H \mathbf{y}_k^A|^2 / 2\rho_n^2} \text{sgn}(x_k) \mathbf{y}_k^A. \quad (33)$$

Then, the solution to optimize equalizer coefficients \mathbf{w}^{AD} is described as

$$\begin{aligned} \hat{\mathbf{y}}_k^A &= (\mathbf{w}_{k-1}^{AD})^H \mathbf{y}_k^A, \\ \mathbf{w}_k^{AD} &= \mathbf{w}_{k-1}^{AD} + \mu \frac{\text{sgn}(x_k)}{2\sqrt{2\pi}\rho_n} e^{-|\text{Re}(\mathbf{w}_{k-1}^{AD})^H \mathbf{y}_k^A|^2 / 2\rho_n^2} \mathbf{y}_k^A, \end{aligned} \quad (34)$$

where μ is the step size that has to be set to balance the convergence rate and the steady-state BER.

Following the same approach as carried out to solve (19), given the training symbols $\{x_k, \mathbf{r}_k^D, \mathbf{y}_k^D\}_{k=1}^N$ for relay and destination, respectively, and using Parzen window function method, the BER for DF relaying at relay and destination can be given as

$$P_E^{DR} = \frac{1}{N} \sum_{k=1}^N Q\left(\frac{\text{sgn}(x_k) \text{Re}\left((\mathbf{w}^{DR})^H \mathbf{r}_k^D + n\right)}{\rho_n}\right), \quad (35)$$

$$P_E^{DD} = \frac{1}{N} \sum_{k=1}^N Q\left(\frac{\text{sgn}(x_k) \text{Re}\left((\mathbf{w}^{DD})^H \mathbf{y}_k^D + n\right)}{\rho_n}\right), \quad (36)$$

respectively. Then, the solution to optimize equalizer coefficients \mathbf{w}^{DR} and \mathbf{w}^{DD} for DF relaying at relay and destination can be described as

$$\begin{aligned} \hat{\mathbf{r}}_k^D &= (\mathbf{w}_{k-1}^{DR})^H \mathbf{r}_k^D, \\ \mathbf{w}_k^{DR} &= \mathbf{w}_{k-1}^{DR} + \mu \frac{\text{sgn}(x_k)}{2\sqrt{2\pi}\rho_n} e^{-|\text{Re}(\mathbf{w}_{k-1}^{DR})^H \mathbf{r}_k^D|^2 / 2\rho_n^2} \mathbf{r}_k^D, \\ \hat{\mathbf{y}}_k^D &= (\mathbf{w}_{k-1}^{DD})^H \mathbf{y}_k^D, \\ \mathbf{w}_k^{DD} &= \mathbf{w}_{k-1}^{DD} + \mu \frac{\text{sgn}(x_k)}{2\sqrt{2\pi}\rho_n} e^{-|\text{Re}(\mathbf{w}_{k-1}^{DD})^H \mathbf{y}_k^D|^2 / 2\rho_n^2} \mathbf{y}_k^D. \end{aligned} \quad (37)$$

3.5. Performance Comparison. The end-to-end BER ratio of AF and DF with MBER adaptive equalizers can be defined as

$$\eta = \frac{P_E^A}{\alpha P_E^D}, \quad (38)$$

where α denotes the complexity penalty parameter of DF, which represents the complexity of DF relaying technology. On one hand, DF relaying has more complexity in signal processing, leading to more delay and resource consumption

TABLE I: Simulation parameters.

Parameter	Value
ρ_n	$4\sigma_n^2$ [21]
μ	0.05 [23]
f_c	2 GHz
L_{\max}	12
γ^{UU}	2
SNR	15 dB
α	1
σ_n^2	-120 dBm
c	3×10^8 m/s
C_{UG}	3
L_{\min}	2
γ^{UG}	6
N	20000

than AF relaying. In this case, $\alpha \geq 1$ can be considered as the penalty to DF relaying. On the other hand, DF can be implemented directly using the traditional transceiver, while AF requires the additional transceiver design, since the relay needs to amplify the received signals. In this case, $0 \leq \alpha \leq 1$ can be considered as the reward to DF relaying. The value of α depends on the energy assumption, network setup, and QoS requirement.

Note that, following (34) and (37), the equalizer coefficients can be calculated using the training symbols. Then, substituting (32) and (24) into (38), the ratio can be rewritten as a function of complexity parameter and training symbols:

$$\begin{aligned} \eta &\left(\alpha, \{x_k, \mathbf{y}_k^A\}_{k=1}^N, \{x_k, \mathbf{r}_k^D, \mathbf{y}_k^D\}_{k=1}^N\right) \\ &= \alpha \frac{\sum_{k=1}^N Q\left(\text{sgn}(x_k) \text{Re}\left((\mathbf{w}^{AD})^H \mathbf{y}_k^A + n\right) / \rho_n\right)}{\sum_{k=1}^N Q\left(\text{sgn}(x_k) \text{Re}\left((\mathbf{w}^{DD})^H \mathbf{y}_k^D + n\right) / \rho_n\right)}. \end{aligned} \quad (39)$$

Given a complexity parameter α and training symbols, the BER ratio between AF and DF with MBER adaptive equalizers can be calculated.

4. Numerical Results

4.1. Simulation Setup. The experimental UAV images, with the size of 1392×1040 pixels [22], are captured by a medium-altitude UAV that can cruise at an altitude of 1000 m. The M-UAV plans to transmit the image to GS via R-UAV. The distance between M-UAV and R-UAV and that between R-UAV and GS are both assumed to be 5 km. Antenna heights of UAVs and GS are assumed to be 1000 m and 10 m, respectively. Thus, the coordinates of the three nodes are $\mathbf{d} = (x_d, y_d, h_G) = (0, 0, 10)$, $\mathbf{r} = (x_r, y_r, h_U) = (5000, 0, 1000)$, and $\mathbf{s} = (x_s, y_s, h_U) = (10000, 0, 1000)$. Simulation parameters, unless explicitly mentioned, are listed in Table 1.

4.2. Results and Discussion. First, we characterize the BER performance of proposed adaptive MBER equalizer against

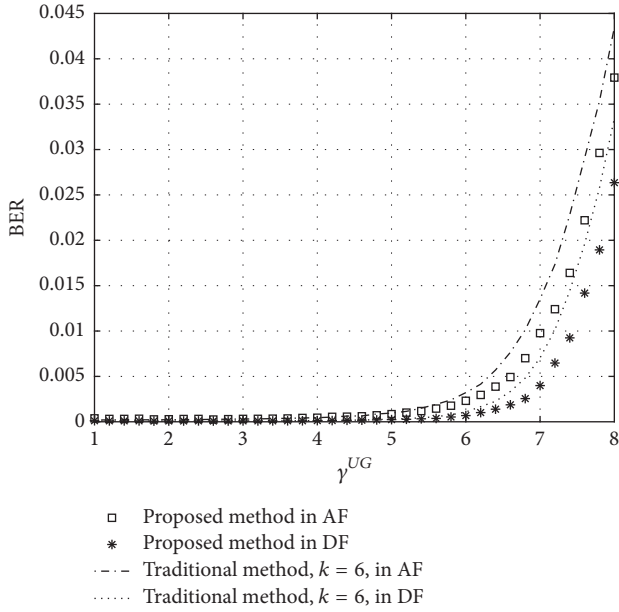


FIGURE 4: BER performance against channel attenuation ratio in UAV-ground channel.

channel attenuation ratio between different multipath components in both UAV-ground and UAV-UAV channels. Considering fixed channel attenuation ratio $\gamma^{UU} = 5$ in UAV-UAV channel, Figure 4 shows the BER performance of traditional fixed length and proposed length adaptive equalizers in both AF relaying and DF relaying. It can be seen from this figure that the proposed method has similar BER performance to traditional one in low γ^{UG} region but achieves better performance in high γ^{UG} . The reason is that proposed length adaptive method can adjust the GS' equalizer length according to the channel attenuation ratio of UAV-ground channel. Additionally, BER performance in DF relaying is better than that in AF relaying. Performance comparison with attenuation ratio in UAV-UAV channel is illustrated in Figure 5 with fixed attenuation ratio $\gamma^{UG} = 5$ in UAV-ground channel. It can be seen that BER performance of proposed method in DF relaying stays constant, while the performance of that in AF relaying decreases when γ^{UU} increases. This is because length adaptive method can adjust the R-UAV's equalizer length according to γ^{UU} in DF relaying, avoiding the drop of BER performance.

Next, we compare the BER performance of AF relaying and DF relaying with the proposed adaptive MBER equalizers against number of training symbols and complexity penalty parameter of DF. BER performance against number of training symbols is shown in Figure 6. Note that these two scenarios should be compared with each other under the same total number of training symbols, resulting in the same end-to-end delay due to training process. Thus, number of training symbols in AF only denotes the symbol number of GS's equalizer. In DF, however, this number denotes the sum of training symbol numbers of R-UAV and GS. Simply assuming that R-UAV and GS in DF relaying use the same

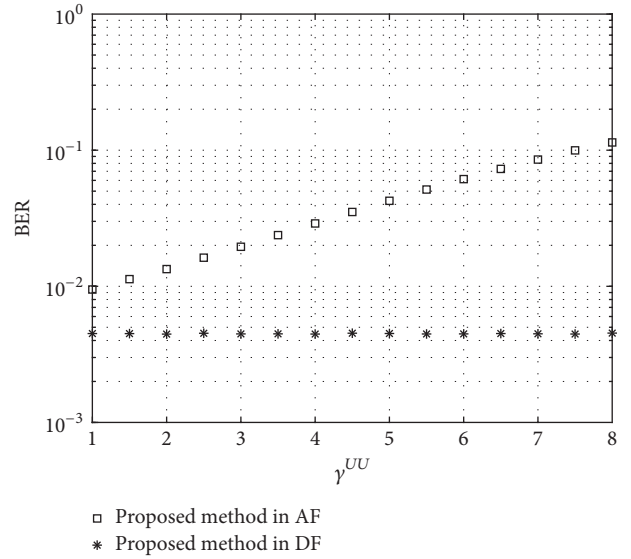


FIGURE 5: BER performance against channel attenuation ratio in UAV-UAV channel.

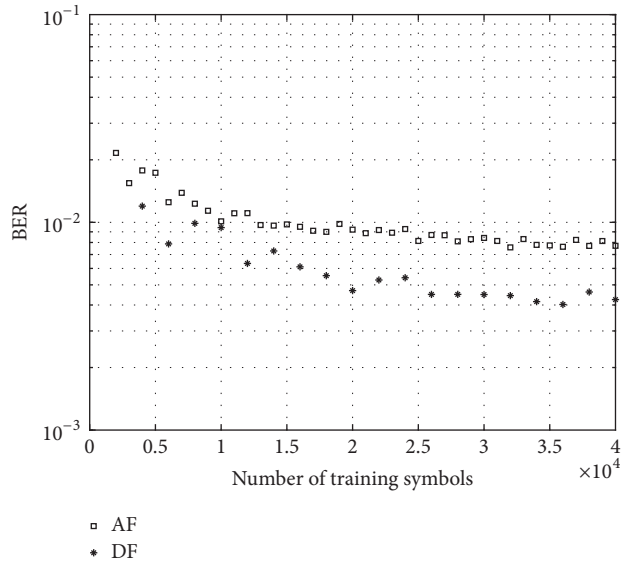


FIGURE 6: BER performance of equalizers against number of training symbols.

amount of training symbols, that is, half of training symbols of GS in AF relaying, DF relaying can still achieve better BER performance than AF relaying but with the slower convergence speed. Figure 7 shows the BER ratio against complexity penalty parameter. It can be seen that DF relaying achieves much better BER performance compared to AF relaying when α is between 0 and 1 and worse BER performance than AF relaying when α is larger than 1. This phenomenon indicates that AF relaying and DF relaying can be selected based on resource consumption, network setup, and QoS requirement of practical application.

Finally, we examine the quality of received images in both AF relaying and DF relaying with adaptive MBER equalizers

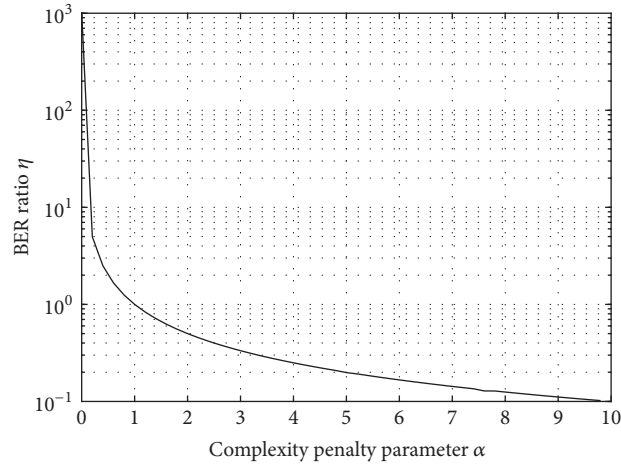


FIGURE 7: BER ratio of AF and DF relaying with adaptive MBER equalizers against complexity penalty parameter.

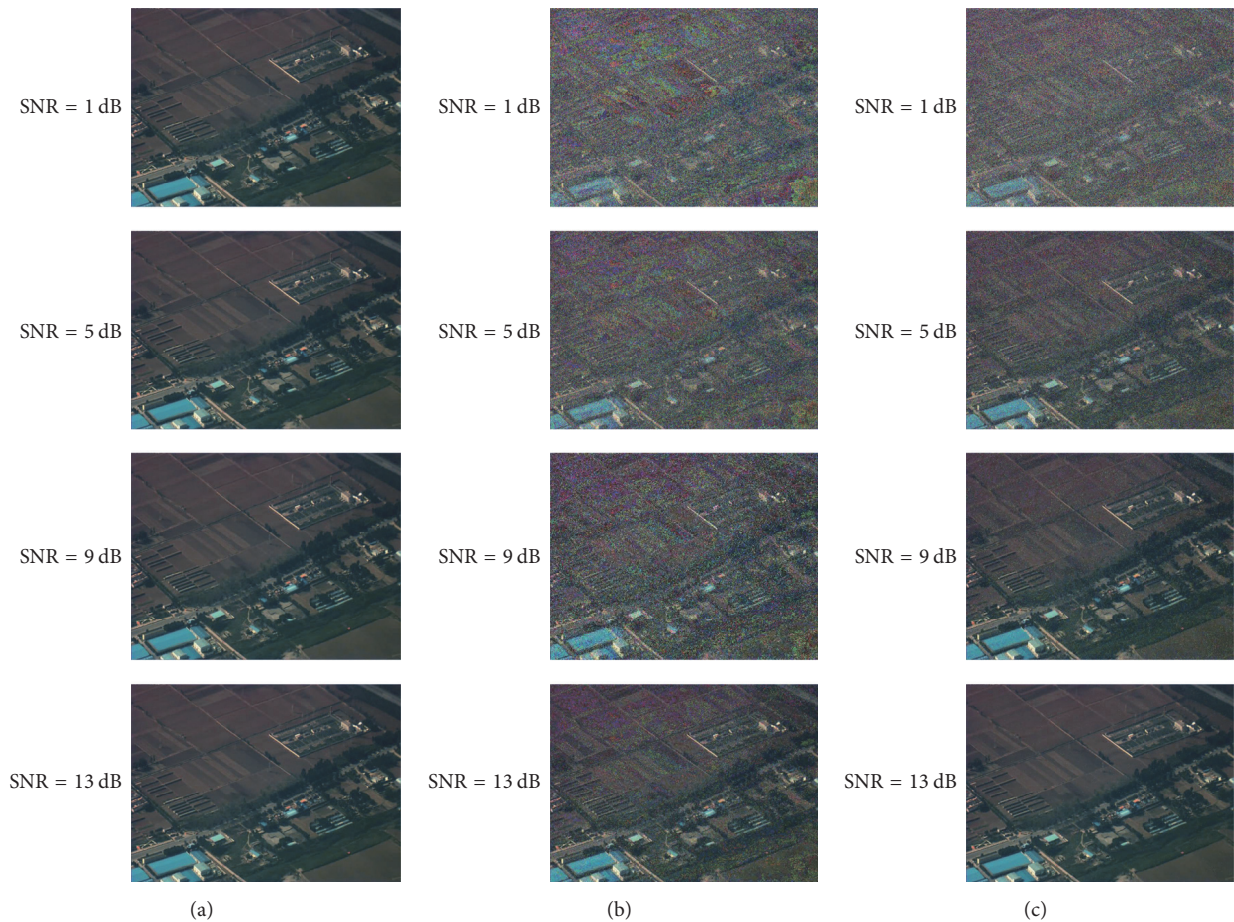


FIGURE 8: Images in different relaying schemes with adaptive MBER equalizers against SNR: (a) original images at M-UAV, (b) after equalizer in AF relaying at GS, and (c) after equalizer in DF relaying at GS.

against SNR. From Figure 8, we can see that images have very poor quality even after equalizers in the low SNR region. This is because relaying schemes perform poorly in the low SNR region as noted in [21]. Images after equalizers in DF relaying perform better than those in AF relaying at the same SNR.

The average PSNRs of received images at GSs for AF relaying and DF relaying with MBER adaptive equalizers are presented in Figure 9. It is shown that the average PSNR performances in AF relaying and DF relaying schemes increase with SNR. Furthermore, the average PSNR performance in DF relaying

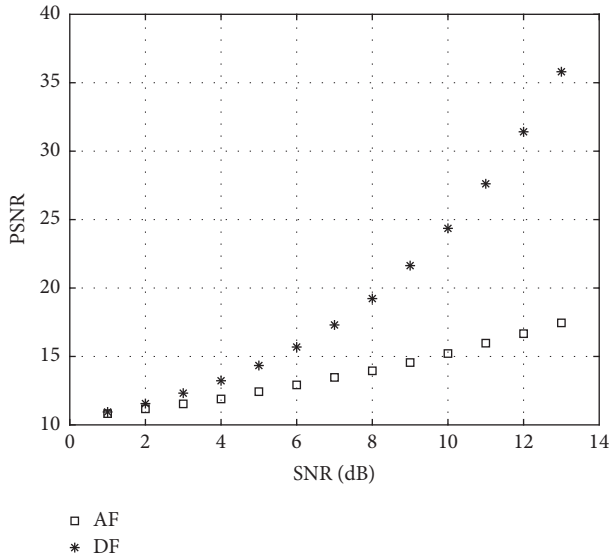


FIGURE 9: Average PSNR performance comparison of received image between AF and DF relaying with adaptive MBER equalizers against SNR.

is better than that in AF relaying across the whole SNR regions and the performance gap significantly increases with SNR.

5. Conclusion

In this paper, MBER equalizers with length adaptive method are designed for both AF and DF in UAV-based relaying system. The results show that proposed length adaptive method can achieve better BER performance as channel attenuation ratio between different multipath components increases. Moreover, DF relaying performs better than AF relaying as the channel attenuation ratio in UAV-UAV channel increases. Additionally, results show that the quality of received images is largely improved by proposed adaptive MBER equalizers in both AF relaying and DF relaying.

Conflicts of Interest

The authors declare that there are no conflicts of interest regarding the publication of this paper.

Acknowledgments

This work was supported by the National Key Research and Development Program of China (Grant no. 2016YFB0502602) and the National Natural Science Foundation of China (Grant no. 91538204).

References

[1] J. Kelcey and A. Lucieer, "Sensor correction of a 6-band multispectral imaging sensor for UAV remote sensing," *Remote Sensing*, vol. 4, no. 5, pp. 1462–1493, 2012.

[2] S. Hayat, E. Yanmaz, and R. Muzaffar, "Survey on Unmanned Aerial Vehicle Networks for Civil Applications: A Communications Viewpoint," *IEEE Communications Surveys & Tutorials*, vol. 18, no. 4, pp. 2624–2661, 2016.

[3] G. Tuna, B. Nefzi, and G. Conte, "Unmanned aerial vehicle-aided communications system for disaster recovery," *Journal of Network and Computer Applications*, vol. 41, no. 1, pp. 27–36, 2014.

[4] Y. Zhou, N. Cheng, N. Lu, and X. S. Shen, "Multi-UAV-Aided Networks: Aerial-Ground Cooperative Vehicular Networking Architecture," *IEEE Vehicular Technology Magazine*, vol. 10, no. 4, pp. 36–44, 2015.

[5] J. Chen and D. Gesbert, "Optimal positioning of flying relays for wireless networks: A LOS map approach," in *Proceedings of the 2017 IEEE International Conference on Communications, ICC 2017, France, May 2017*.

[6] A. Al-Hourani, S. Kandeepan, and A. Jamalipour, "Modeling air-to-ground path loss for low altitude platforms in urban environments," in *Proceedings of the 2014 IEEE Global Communications Conference, GLOBECOM 2014*, pp. 2898–2904, December 2014.

[7] D. W. Matolak and R. Sun, "Air-Ground Channel Characterization for Unmanned Aircraft Systems-Part I: Methods, Measurements, and Models for Over-Water Settings," *IEEE Transactions on Vehicular Technology*, vol. 66, no. 1, pp. 26–44, 2017.

[8] R. Sun and D. W. Matolak, "Air-Ground Channel Characterization for Unmanned Aircraft Systems Part II: Hilly and Mountainous Settings," *IEEE Transactions on Vehicular Technology*, vol. 66, no. 3, pp. 1913–1925, 2017.

[9] Y. Zeng, R. Zhang, and T. J. Lim, "Wireless communications with unmanned aerial vehicles: Opportunities and challenges," *IEEE Communications Magazine*, vol. 54, no. 5, pp. 36–42, 2016.

[10] D. W. Matolak and R. Sun, "Unmanned aircraft systems: Air-ground channel characterization for future applications," *IEEE Vehicular Technology Magazine*, vol. 10, no. 2, pp. 79–85, 2015.

[11] D. W. Matolak and R. Sun, "Air-Ground Channel Characterization for Unmanned Aircraft Systems—Part III: The Suburban and Near-Urban Environments," *IEEE Transactions on Vehicular Technology*, vol. 66, no. 8, pp. 6607–6618, 2017.

[12] M. Rice, M. S. Afran, and M. Saquib, "Equalization in aeronautical telemetry using multiple transmit antennas," *IEEE Transactions on Aerospace and Electronic Systems*, vol. 51, no. 3, pp. 2148–2165, 2015.

[13] M. Rice, M. Saquib, M. S. Afran, A. Cole-Rhodes, and F. Moazzami, "On the performance of equalization techniques for aeronautical telemetry," in *Proceedings of the 33rd Annual IEEE Military Communications Conference, MILCOM 2014*, pp. 456–461, USA, October 2014.

[14] Q. Z. Ahmed, M. Alouini, and S. Aissa, "Bit error-rate minimizing detector for amplify-and-forward relaying systems using generalized gaussian kernel," *IEEE Signal Processing Letters*, vol. 20, no. 1, pp. 55–58, 2013.

[15] Q. Z. Ahmed, S. Ahmed, M.-S. Alouini, and S. Aïssa, "Minimizing the symbol-error-rate for amplify-and-forward relaying systems using evolutionary algorithms," *IEEE Transactions on Communications*, vol. 63, no. 2, pp. 390–400, 2015.

[16] Q. Z. Ahmed, K.-H. Park, M.-S. Alouini, and S. Aïssa, "Optimal linear detectors for nonorthogonal amplify-and-forward protocol," in *Proceedings of the 2013 IEEE International Conference on Communications, ICC 2013*, pp. 4829–4833, Hungary, June 2013.

- [17] P. G. Sherwood, X. Tian, and K. Zeger, "Channel code block-length and rate optimization for progressive image transmission," in *Proceedings of the 1st IEEE Annual Wireless Communications and Networking Conference, WCNC 1999*, pp. 978–982, USA, September 1999.
- [18] A. K. Dutta, K. V. S. Hari, and L. Hanzo, "Linear transceiver design for an amplify-and-forward relay based on the MBER criterion," *IEEE Transactions on Communications*, vol. 62, no. 11, pp. 3765–3777, 2014.
- [19] D. Jordane, "Electromagnetic waves and radiating systems. 1em plus 0.5em minus 0.4em Prentice-Hall Of Lndia Private Limited," *Electromagnetic waves and radiating systems. 1em plus 0.5em minus 0.4em Prentice-Hall Of Lndia Private Limited*, 1967.
- [20] M. Rice, T. Nelson, J. Palmer, C. Lavin, and K. Temple, "Space-Time Coding for Aeronautical Telemetry: Part II - Decoder and System Performance," *IEEE Transactions on Aerospace and Electronic Systems*, vol. 53, no. 4, pp. 1732–1754, 2017.
- [21] S. Chen, S. Tan, L. Xu, and L. Hanzo, "Adaptive minimum error-rate filtering design: A review," *Signal Processing*, vol. 88, no. 7, pp. 1671–1697, 2008.
- [22] H. Li, X. Li, W. Ding, and Y. Huang, "Metadata-assisted global motion estimation for medium-altitude unmanned aerial vehicle video applications," *Remote Sensing*, vol. 7, no. 10, pp. 12606–12634, 2015.
- [23] S. Chen, "Adaptive minimum bit-error-rate filtering," *IEE Proceedings Vision, Image and Signal Processing*, vol. 151, no. 1, pp. 76–85, 2004.

Research Article

A New Movement Authority Based on Vehicle-Centric Communication

Tuo Shen ¹ and Haifeng Song ²

¹*School of Optical-Electrical and Computer Engineering, University of Shanghai for Science and Technology, Shanghai 200093, China*

²*Institute for Traffic Safety and Automation Engineering, Technische Universität Braunschweig, 38108 Braunschweig, Germany*

Correspondence should be addressed to Haifeng Song; h.song@tu-braunschweig.de

Received 7 December 2017; Revised 16 February 2018; Accepted 4 March 2018; Published 4 April 2018

Academic Editor: Li Zhu

Copyright © 2018 Tuo Shen and Haifeng Song. This is an open access article distributed under the Creative Commons Attribution License, which permits unrestricted use, distribution, and reproduction in any medium, provided the original work is properly cited.

The communication system that is presently applied in the European Train Control System can only support data exchange between vehicles and ground, but the direct vehicle-to-vehicle communication is not available. The details of interlocking information and other vehicles' movements are invisible to drivers who are the last defense to prevent unsafe scenarios. As connected vehicles have been envisioned to enhance transportation efficiency and improve safety, the direct vehicle-to-vehicle communication network is involved in this paper to increase the safety of railway transport. In this paper, a new train movement authority (MA+) is proposed. Apart from a wireless communication unit, this system does not require any other infrastructure. With the assistance of vehicle-centric communication technology, MA+ can detect the condition of switches and trains within a certain scope. In this paper, the system structure of MA+ is proposed. Additionally, different implementation scenarios are also discussed. The detection range is estimated and validated based on mathematical calculation and experimental equations. An application demo of MA+ is presented on the Driver Machine Interface of the onboard equipment. The results indicate that MA+ can be a flexible and scalable system for furthering the improvement of railway safety.

1. Introduction

To guarantee railway transport safety, various technologies have been applied. The latest European Train Control System (ETCS), which is based on the moving block principle, safely optimizes the maximum capacity of the rail network. Different kinds of data are submitted to the Centralized Traffic Control (CTC) system, such as the interlocking information, train position, and train diagram. Hence, CTC has a “God’s view” of all trains and interlocking details [1]. The Radio Block Center (RBC) transfers the movement authority (MA) to the trains in its scope of jurisdiction. The train vehicles can only passively move based on the MA. Once the MA is a fault, it may lead to a risk scenario, which results in catastrophic consequences.

For instance, in the 2016 Berlin Tram-Crash, two commuter trains collided on a single-track stretch of railway in Germany; additionally, there was a head-on collision involving two passenger trains in southern Italy; two cargo trains

collided in Finland; the 7.23 Yongwen line train collision and the Shanghai Metro Line 10 collision in China are further examples [2]. As shown in Figure 1, even though the latest technologies have been implemented, accidents happened all the same. Hence, we should not be lulled by the guarantee of the train control system safety.

Based on the technology trends, the train control system should weaken the proportion of ground faculties and provide trains with more information than in the past [3]. Some projects based on the vehicle-centric communications have been carried out in these years [4]. For instance, Alstom offered a train-centric communications-based train control (CBTC) system. This system can carry out direct train-to-train communication and control the switch by the train. With implementing this system, the maintenance costs have been decreased by 20% and energy has been saved up to 30% [5]. Publication [6] introduces a train collision avoidance system, which is based on the Global Navigation Satellite System (GNSS) to obtain the location data; potential

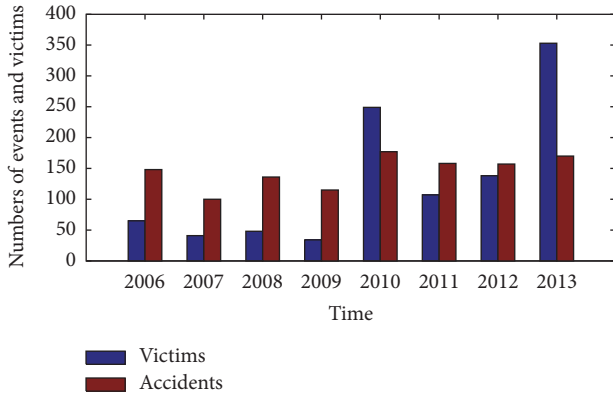


FIGURE 1: Numbers of events and victims of train collisions and derailments in Europe from 2006 to 2013.

collisions are avoided in the future. Publication [7] proposed a direct vehicle-to-vehicle distance measurement system in railways, and the system availability is validated by using colored Petri nets.

Varying from the systems mentioned in publications [5–7], in this paper, we propose a system that requires no additional position and speed measurement system. The essential information is collected using the internal wireless packets generated by ETCS’s onboard equipment. The vehicle-to-vehicle data exchange is implemented via a vehicle-centric communication link.

Improving transport safety requires numerous suitable methods. Reducing transitions to hazardous operations and increasing transitions to safer operations are the most effective implementation methods [8]. Limiting movement violation is one of the most efficient and innovative methods to reduce accidents, such as train-to-train and train-object collisions. This paper intends to provide researchers with a new movement authority (MA+), which combines advantages of the vehicle-centric communication with current movement authority (MA) mechanisms.

MA+ works as a supplementary part of the ETCS. When the ETCS is working normally and there is no potential risk, MA+ will remain silent. Otherwise, MA+ outputs a warning or alarm. It is important to know that MA+ cannot replace the statue of the current MA. This is mostly due to the fact that the safety of MA+ cannot achieve an equivalent security level as compared with the ETCS in its infancy. Furthermore, any modifications of this current system require a substantial amount of discussion and verification. This paper focuses on such a proposal and the system description.

The remainder of the paper is organized as follows: Section 2 is dedicated to discussing the system’s structure and different application scenarios. The feasibility of proposing a new movement authority, which is based on the vehicle-centric communication, is also further discussed in Section 3. In Section 4, an MA+ interface demo is introduced on the Driver Machine Interface (DMI), which can be utilized for the further simulation or practical application in the actual system. Finally, Section 5 presents the conclusion and further works.

2. Structure and Application Scenarios of MA+

As defined in ETCS-2, the MA contains the distance information, by which the train is authorized to move forward [9]. However, no surrounding details are available for the train. The MA+ proposed in this paper can obtain extra information by applying the vehicle-centric communication method. The extra information includes but is not limited to other trains’ speed and position and switch’s position and situation. In this section, the system structure, logical model, and data exchange process are presented; different implementation scenarios are then further discussed.

2.1. MA+ Structure and Logical Model Description. Except for the existing infrastructures in ETCS-2, there are two main components in the structure of MA+. As shown in Figure 2, the vehicle-centric communication architecture is installed in each train, and this architecture permits internal and external data exchange. The switch announcement architecture repeatedly broadcasts the switch’s location and situation.

The communication link between vehicles and switches is shown in Figure 3. In the vehicle-centric communication architecture, the MA+ algorithm collects the train messages from the onboard equipment and transmits the information via the *Transceiver Unit*. These messages provide the train’s MA, speed, position, direction, and vehicle ID number. The *Transceiver Unit* is also in charge of receiving the train messages sent by other vehicles and switch messages from the switch announcement. After obtaining the MA and localization data, the MA+ algorithm matches the *digital map* and displays which particular track the train is on through the DMI. When there are potential hazardous scenarios, the MA+ algorithm will output alarms.

Before the communication link between vehicles and switches is established, MA+ works in a surveillance mode (*Smod*). As shown in Figure 4, there are no switches and trains in its detection range; the blue line and the yellow line represent the original MA data and the MA route, respectively. The system continuously detects the situation of potential nearby switches and trains.

The overall logical model of the MA+ algorithm is shown in Figure 5. MA+ starts from *IDLE* and turns into *Smod* after obtaining the train message data. Combining with the digital map, the MA+ shows which track the train is on (*MA+_T*). Once the information is sufficient to be updated, the MA+ turns into corresponding modes (T, V, and S represent track, vehicle, and switch, resp.). For instance, *MA+_T_S* displays the track and switch details once the MA+ obtains the information broadcasted by the switch announcement architecture. Some specific situations trigger *shortening MA* (SMA), and the MA will be updated based on a new end of authority (EOA). In the following section, the logical details are discussed based on different scenarios, which are used to describe how MA+ is implemented.

2.2. MA+ Implementation Scenarios. A switch can lead a train onto a different path. Hence, obtaining the position and situation of the approaching switch is essential in the MA+ implementation. Vehicle-to-switch communication provides

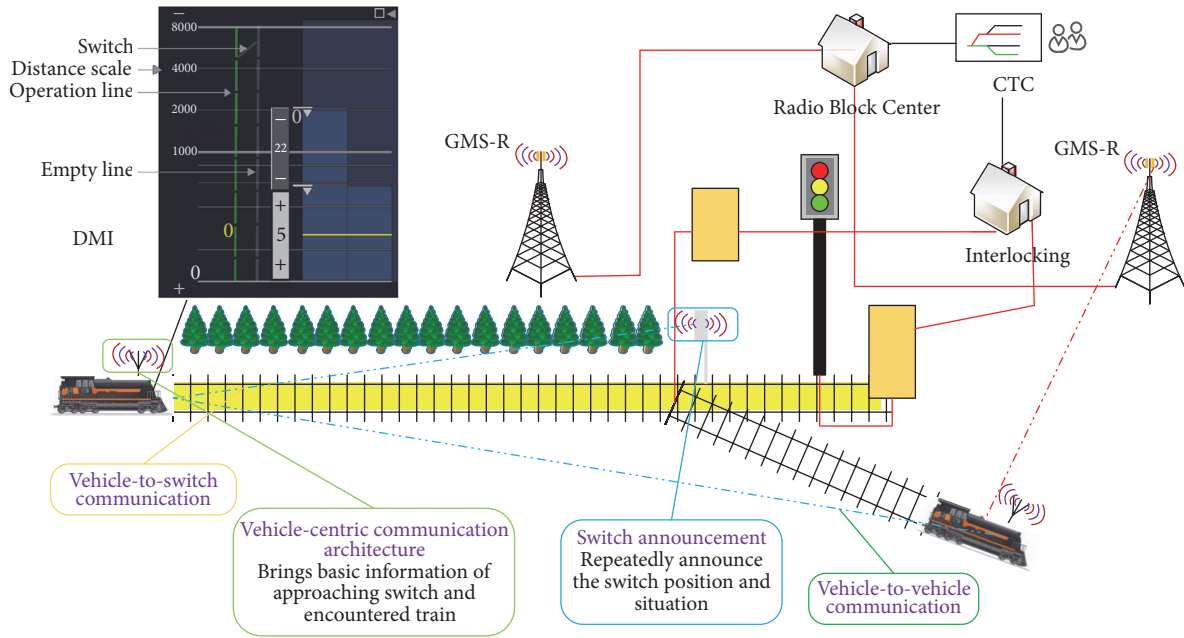


FIGURE 2: Structure of MA+.

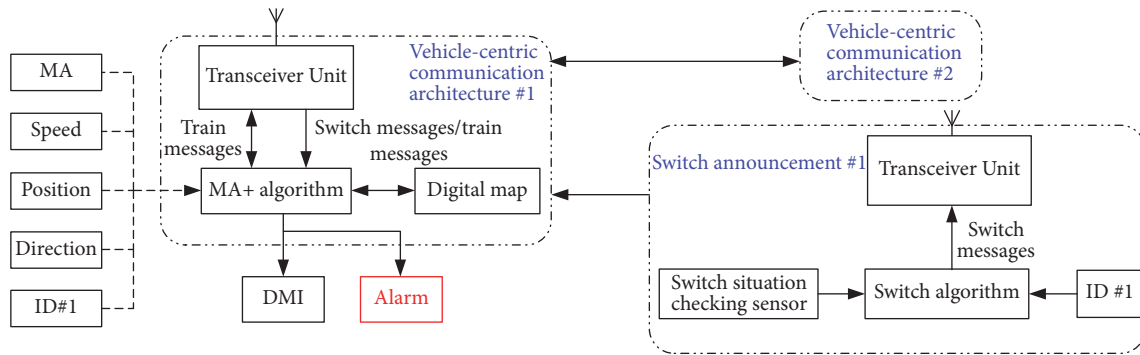


FIGURE 3: Communication link between vehicles and switches.

fundamental vector information. The following procedures are involved: surveillance, detection and appropriate avoidance, and output results:

- (i) *Surveillance*: the local MA+ works in a monitoring mode. The switch announcement continuously broadcasts its location and position
- (ii) *Detection and appropriate avoidance*: once the connection between the switch announcement and the local vehicle-centric communication architecture is established, the local system turns to the appropriate avoidance mode
- (iii) *Output results*: after obtaining the position and situation of the approaching switch, the system's output results vary depending on different scenarios

In the appropriate avoidance procedure, the switch conditions are described as shown in Figure 6. In this section, four different combinations of the switch conditions are discussed to do the illustration. The red line represents the SMA. The

blue and yellow rectangles indicate the normal and reverse switch positions, respectively. The switch's name turns into green or yellow depending on the switch position.

In the normal operation the switch position can be shown as Figures 6(a) and 6(b), which represent the situation that the switch is in normal and reverse positions, respectively. When the switch is in an uncertain position, it will be marked with red-dotted lines as shown in Figures 6(c) and 6(d).

It is important to note that situations 3 and 4 do not exist when the interlocking system is working correctly. The ETCS is a critical safety system, and the MA generation obeys specific fault-safety strategies. Under the scenario illustrated in Figure 6(c), switch split is likely to occur along with derailments and side collisions. Hence, among these four different scenarios, only this one can trigger the SMA. Additionally, to reduce the frequency of false alarms, the following condition is considered. When the original MA is available and the database shows that there is an approaching switch but the vehicle-to-switch connection is not established, the system ignores this scenario and no SMA is required.

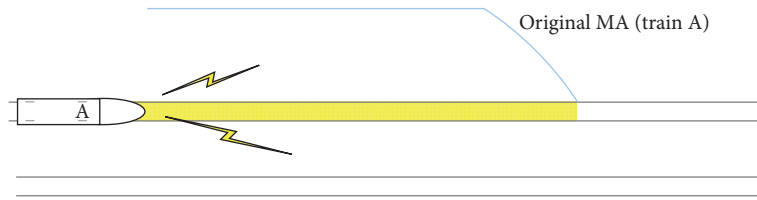


FIGURE 4: MA+ surveillance mode.

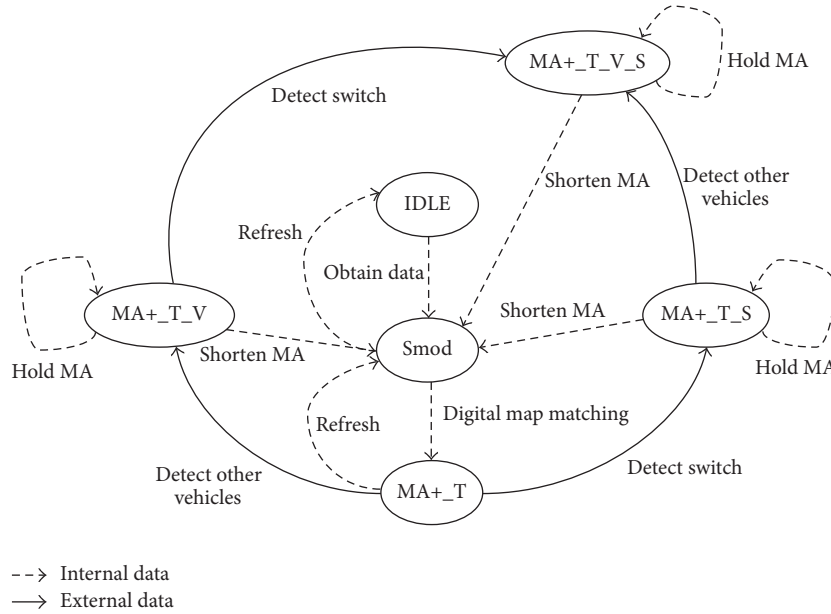


FIGURE 5: Logical model of the MA+ algorithm.

Different like the vehicle-to-switch communication, more information has to be taken into consideration when the vehicle-to-vehicle communication is established. If *train A* detects another *train B* in its detection range, *train A* communicates with *train B* and obtains the MA+ details of *train B*. In general, the scenarios can be divided into two main parts:

- (i) There is no overlap of the two MA, as shown in Figure 7(a). The green part is the available extension area for the detected trains' MA. Under this scenario, *train A*'s EOA can be reached without a risk for a hazardous situation (the train position is calculated based on the train's head position; the absolute real length of the train should be considered when SMA is triggered).
- (ii) If the routes of *train A* and *train B* have an overlap as shown in Figure 7(b), both of them have to activate the SMA based on their speed and position to prevent collisions as shown in Figure 7(c).

The practical situations are the combinations of aforementioned scenarios of switches and trains. When drivers are required to take responsibility, they can have an extended version of the surrounding switches and trains in a certain distance with the assistance of MA+. For drivers, the benefit of MA+ implementation is that it helps them understand

better the surrounding environment of tasks they have to perform, especially in special scenarios where the drivers have to make sure the situation of the train ahead is safe. For instance, the onboard equipment works in modes as ON SIGHT (OS), ISOLATION (IS), and so on. Hence, MA+ is an efficient way to extend drivers' ability and improve the operational safety.

The contemporary control system has a high safety level. However, if the signal system fails, the "driver see and avoid" will be activated. MA+ can output alarm and shorten the MA automatically; furthermore, it should be kept in radio silence if there is no potential accident. Otherwise, MA+ can also be turned on manually. Hence, it is clear that MA+ will not increase drivers' responsibility and workload. Additionally, it can also provide additional communication other than just the communication between trains and ground.

3. MA+ Detection Range Estimation

Any theoretical proposal should be put forward in engineering implementation, and then the proposal makes sense. Before the practice using, a suitable simulation based on an existing technology is essential. For the vehicle-centric communication, different kinds of communication technologies are available, such as Global System for Mobile Communications (GSM), Code Division Multiple

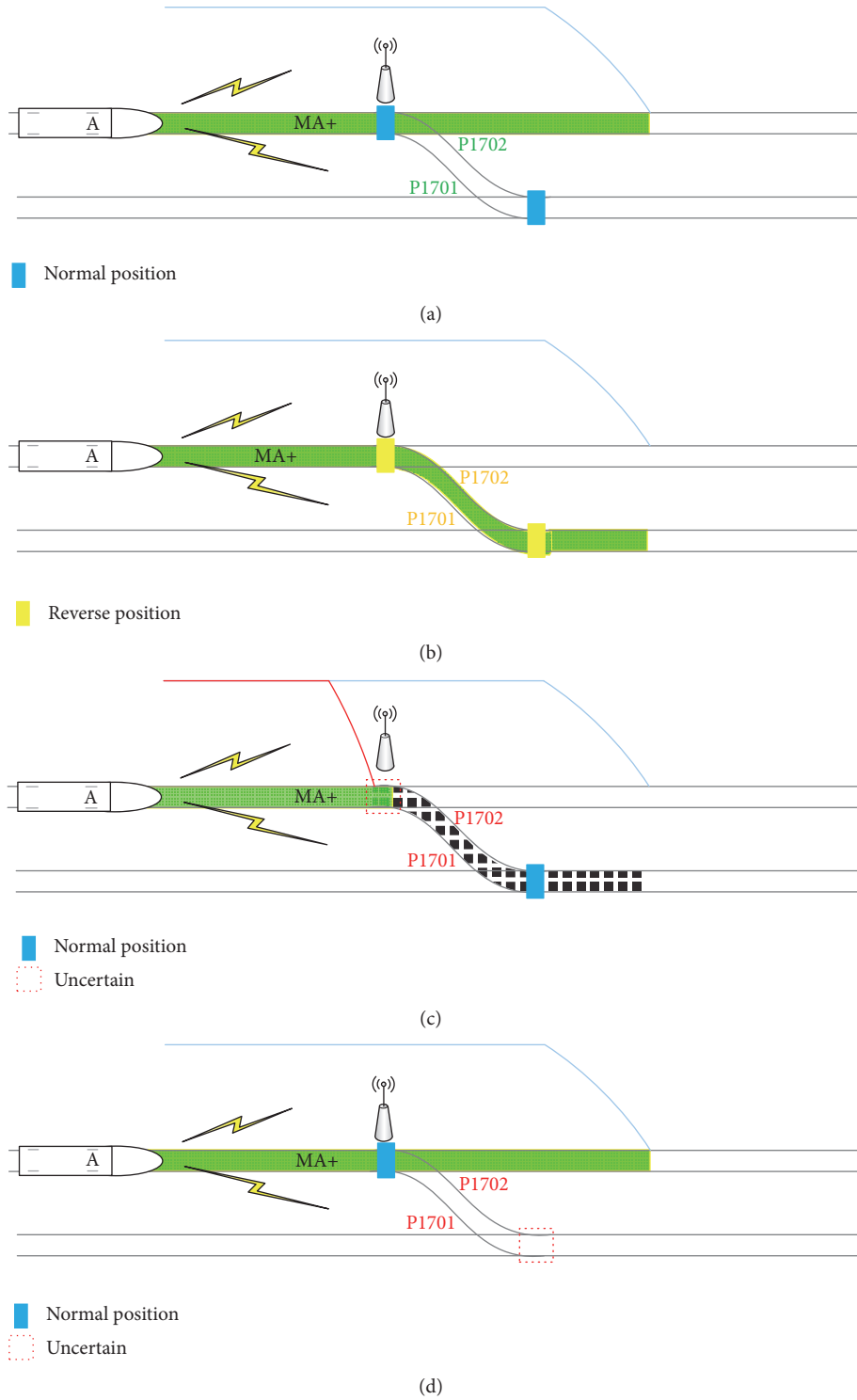


FIGURE 6: MA+ operates with approaching switch scenarios.

Access (CDMA), Wideband Code Division Multiple Access (WCDMA). In recent years, the evolution of the data communication technology promotes the application of wireless communication in rail transportations, for the Long-Term Evolution (LTE) as an example [10]. Based on the high capacity and speed of LTE and less time delay (as shown

in Table 1), direct communications between waysides and vehicles are possible. This will enhance the safety level of the previous control method that relied principally on the information delivered from RBC.

For the vehicle-centric communication, the detection range is an important assessment target. In this section, the

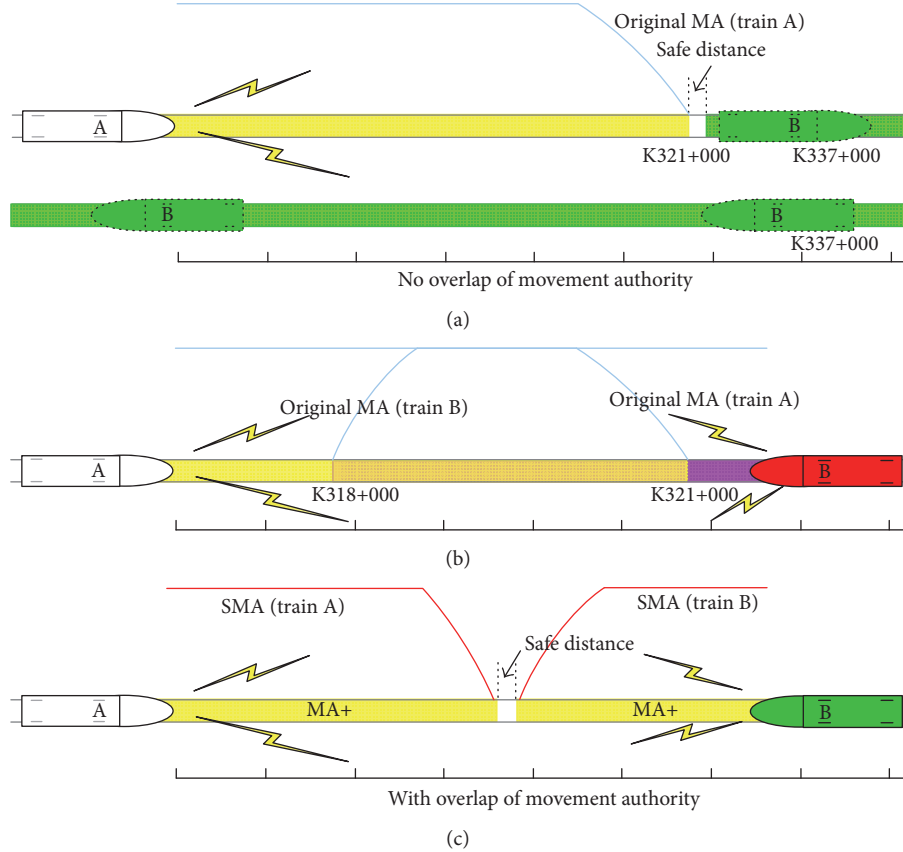


FIGURE 7: MA+ operates with encountering trains.

TABLE 1: The maximum time delays comparison of mobile communication system.

Communication system	Maximum time delay (10^{-6} s)
GSM	1.805
CDMA2000	0.813
WCDMA	0.130
LTE	0.030

distance detection range of MA+ is discussed based on the path loss calculation.

Different factors have various influences on the signal quality. One harsh transition environment is that in non-line-of-sight (NLOS) propagation with mountain barrier, for example, in railway curve lines, as shown in Figure 8. Under this scenario, the path loss in curve line is treated as a single round obstacle for mathematical calculations. Here,

h is height of the curve line above the straight line of the local train and detected train,

R is the radius of the curve line,

d_1, d_2 are the tangent lines through the local train and detected train position.

The diffraction loss is influenced by the frequency, curve radius, and distance. The mathematical calculation is based

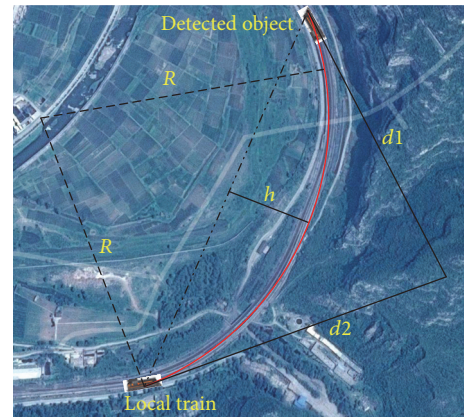


FIGURE 8: The power attenuation simulation in the curve line application scenario.

on the International Telecommunication Union (ITU) recommendation [11]. The attenuation loss A can be calculated as follows:

$$A = J(v) + T(m, n), \quad (1)$$

where $J(v)$ is the Fresnel-Kirchhoff loss caused by equivalent blade shape barrier and it can be given by

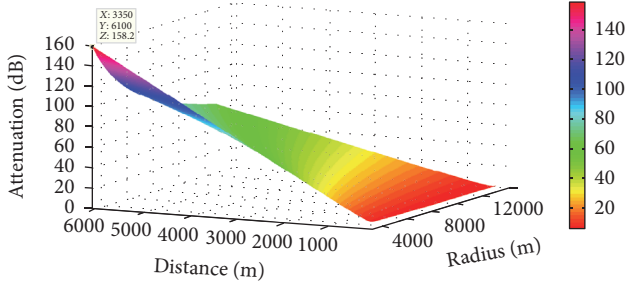


FIGURE 9: Wireless power attenuation with distance and radius.

$$J(\nu) = -20 \log \left(\frac{\sqrt{[1 - C(\nu) - S(\nu)]^2 + [C(\nu) - S(\nu)]^2}}{2} \right), \quad (2)$$

where $C(\nu)$ and $S(\nu)$ are the real and imaginary parts of Fresnel integral, respectively. For the transition with a barrier blocking the line-of-sight transmission, $J(\nu)$ can be approximately described as follows:

$$J(\nu) = 6.9 + 20 \log \left(\sqrt{(\nu - 0.1)^2 + 1} + \nu - 0.1 \right), \quad (3)$$

$$\nu = 0.0316h \left[\frac{2(d_1 + d_2)}{\lambda d_1 d_2} \right]^{1/2}, \quad (4)$$

where h and λ are in meters, λ is the wavelength, and d_1, d_2 are in kilometers.

$T(m, n)$ is the additional loss caused by barrier curvature, which is the curve line radius R . m and n are given by (5) and (6), respectively:

$$m = \frac{R[(d_1 + d_2)/d_1 d_2]}{[\pi R/\lambda]^{1/3}}, \quad (5)$$

$$n = \frac{h[\pi R/\lambda]^{2/3}}{R}. \quad (6)$$

When $mn \leq 4$, $T(m, n)$ equals (7); when $mn > 4$, $T(m, n)$ equals (8).

$$T(m, n) = 7.2m^{1/2} - (2 - 12.5n)m + 3.6m^{3/2} - 0.8m^2, \quad (7)$$

$$T(m, n) = -6 - 20 \log(mn) + 7.2m^{1/2} - (2 - 17n)m + 3.6m^{3/2} - 0.8m^2. \quad (8)$$

In Europe, LTE frequencies are bands 1/3/7/8/20. Band 8 is currently used mostly by GSM. Band 8 is attractive from a coverage point of view due to the lower propagation losses. The band can be reused for LTE or HSPA. Bands 8 and 20 hold the uplink frequencies 880–915 MHz and 832–862 MHz. The downlink frequencies are 925–960 MHz and 791–821 MHz [12]. Here we choose the frequency 930 MHz to do the simulation. The result is shown in Figure 9, which indicates

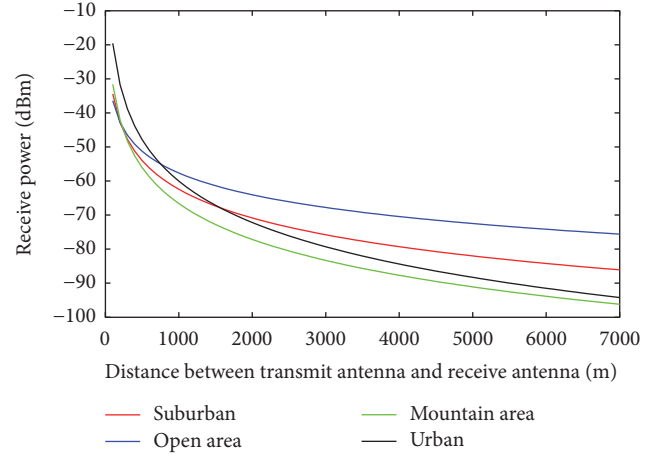


FIGURE 10: Receive signal power in different scenarios.

the interrelationship among the diffraction loss, detection distance, frequency, and radius. The received signal power should be greater than the sensitivity of a receiver, as shown in (9).

$$P_r(d) \text{ [dBm]} = P_t \text{ [dBm]} + G - A - PL_{\Delta}, \quad (9)$$

$$G = 10 \log(G_t G_r), \quad (10)$$

where $P_r(d)$ [dBm] is the received power; P_t [dBm] is the transfer power; G is the gain; G_t and G_r are the gains of the transfer and receiver antennas, respectively; PL_{Δ} is the attenuation caused by device and feeder cable.

For the received power, some experimental data is available to be referenced. In publication [13], the path loss measurements at the 930 MHz in the different scenario were done. The empirical power of received signal models for suburban area, open area, mountain area, and urban area was proposed, as shown in (11), (12), (13), and (14), respectively. The simulation result is shown in Figure 10. As shown in the result, the received signal power is greater than -90 dBm within 4000 m. Hence, the detection range is not a limitation of this system's practical application. Taking ICE-3 as an example, the train emergency braking distance is between 2300 and 2800 m depending on the actual speed.

$$P_r(d) = 21.577 - 28.001 \log(d), \quad (11)$$

$$P_r(d) = 6.0246 - 21.2261 \log(d), \quad (12)$$

$$P_r(d) = 38.432 - 35.015 \log(d), \quad (13)$$

$$P_r(d) = 61.337 - 40.452 \log(d). \quad (14)$$

Here we take an actual line as a case study. The minimum railway curve radius is different in various railway lines, and several cases are shown in Table 2 [14]. The simulation results indicate that, under the minimum curve radius of 3350 m in Köln-Rhein/Mann line, the signal attenuation is 158.2 dB when the detected distance is 6100 m. In current practice application, the typical maximum path loss of LTE can be 163.5 dB [15]. In order to make the detection range as further

TABLE 2: Symbol form/shape and descriptions.

Symbol No.	Form/shape	Description
SW1		Switch in normal position
SW2		Switch in reverse position
SW3		Switch in reverse and normal position
SW4		Switch in normal and reverse position
TR1		Train without collision risk
TR2		Train with collision risk
TC1		Operation line
TC2		Empty line

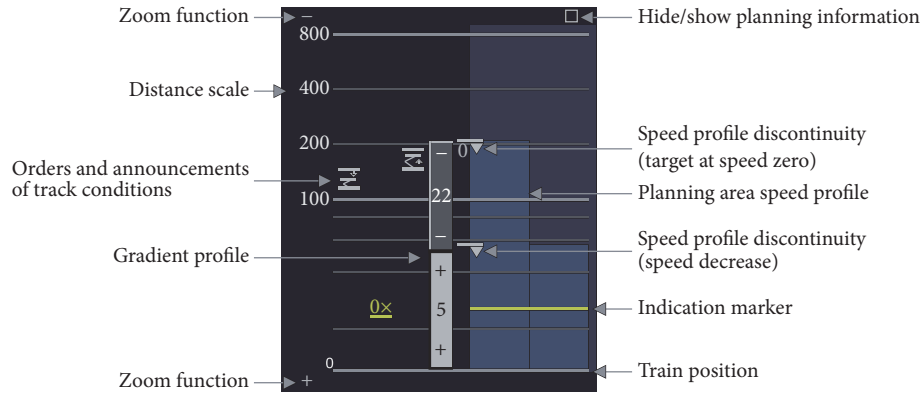


FIGURE 11: Main objects of the planning information.

as possible, many different methods can be used, for instance, choosing a suitable wireless frequency spectrum according to the simulation result in Figure 9, increasing transmitter power, enhancing receiver sensitivity, and building repeater stations. Both the simulation result and practical results indicate that the vehicle-centric communication is available at the technical level. Hence, the detection range is not a limitation of the MA+ practical application.

4. An Application Demo on the DMI

The MA+ can be merged into the current train control system. In this section, a demo is proposed on the DMI of ETCS. The onboard equipment displays the essential information on the DMI for drivers. MA+ is combined with the planning information on DMI. On DMI, the orders and announcements overview displays within the MA and up to the first target at zero speed. The following aspects are involved, if any, as shown in Figure 11.

Here we add MA+ information in orders and announcements of track conditions area, and the basic symbols are shown in Table 3. Symbols or shapes having a certain meaning in general railway control systems are avoided, and the display permits no interaction with the driver during the normal operation.

Operation line and empty line are defined in the local train's view. Based on the switch conditions, there are different MA operation routes. The driver will know which route is being implemented. As shown in Figure 12, the length of MA

is assumed to be 800 m. The train was transferred from the current operation line to the empty line through SW2, which locates at 280 m in front, as shown in Figure 12(b). SW3 and SW4 are in hazardous conditions; trailed switch accidents may happen. SW3 will lead the local train to another track and switch split will occur. Hence, SMA is required and an alert is triggered. There is no risk of collisions to the local train under SW4, and no SMA action can be triggered automatically.

Once other trains are detected and if there is no overlap between operation lines, the system will show the positions of other trains as green symbols. The angle shows the train operation direction. If there are overlaps between two operation lines, SMA is immediately executed. Then, because of different train directions, two different scenarios should be discussed: scenario one: after the new EOA was refreshed, there is still an overlap of the MA of two trains; both two trains have to shorten their MA again based on their speed, distance, and location, as shown in Figure 13(a); scenario two: if the detected trains and local train have the same route direction, the new EOA will be updated based on the end of the detected train, as shown in Figure 13(b).

5. Conclusion and Further Work

In this paper, a new movement authority based on vehicle-centric communication was proposed to increase the safety level of the railway operation. The structure of the system was given, and implementation scenarios were also discussed.

TABLE 3: Comparison among different curve radiuses.

Organization	JR	JR	DB	DB	SNC	SNCF	CRH
Item	Tokaido Shinkansen	Tokyo-Joetsu	Hannover-Wrzburg	Köln-Rhein/Mann	Paris-Sud-Est	Atlantique	Beijing-Shanghai
Maximum design speed km/h	<i>null</i>	280	300	300	350	380	380
Maximum service speed km/h	300	275	250	<i>null</i>	270	300	300
Minimum curve radius m	4000	4000	7000	3350	4000	6250	7000

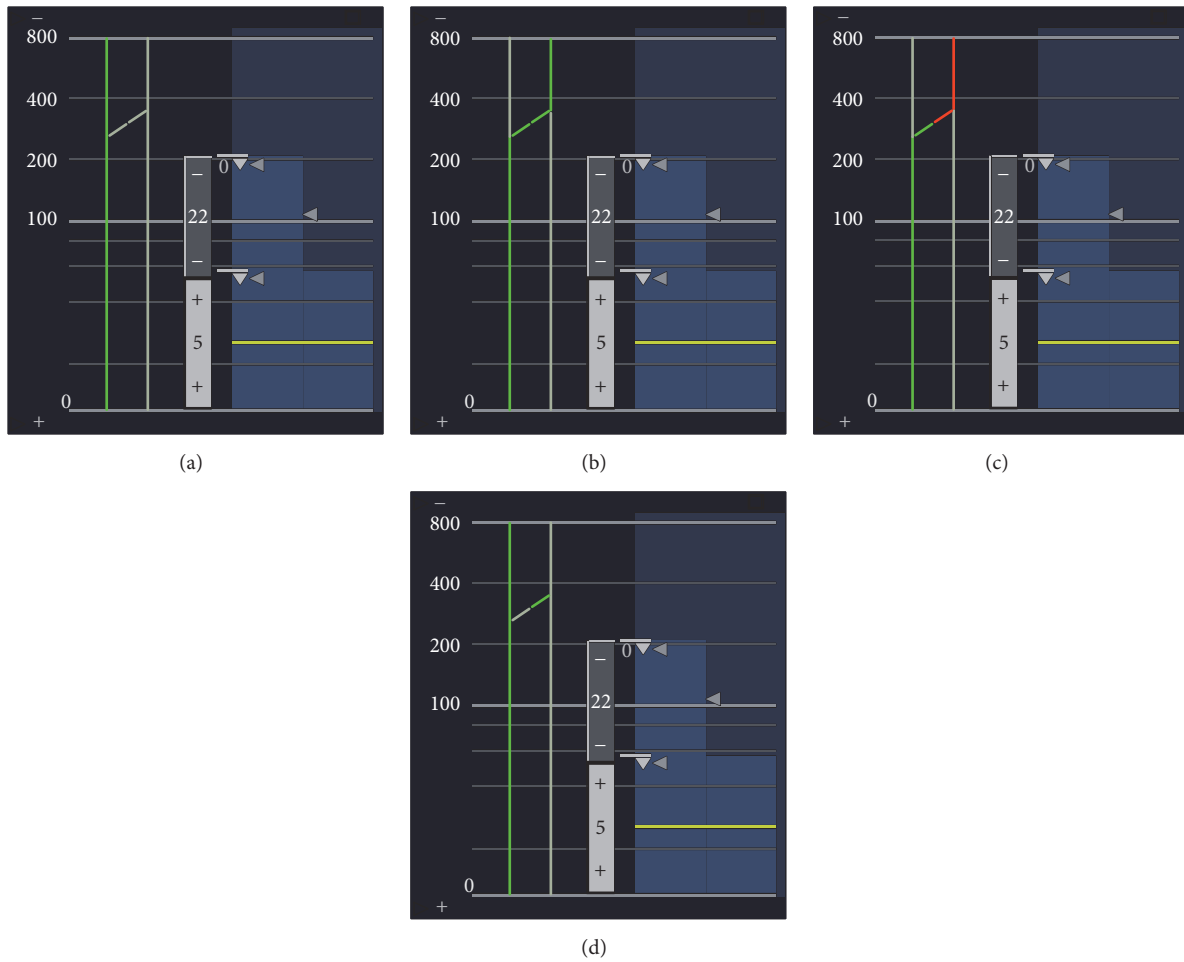


FIGURE 12: DMI operates with approaching switch scenarios.

With the assistance of vehicle-centric wireless communication, local trains can have an overview of surrounding scenarios. By estimating the detection range based on attenuation calculation, the results indicated that this vehicle-centric communication proposal was engineering-feasible. Finally, a demo for the MA+ application on DMI was presented. It is clear that similar vehicle-centric technologies can be widely used in the future to increase the safety level of railway transport.

In further works, an MA+ prototype machine will be designed, which can carry out the fundamental functions proposed in this paper. Given that the current DMI has been developed with a view to optimizing information provision and providing drivers with the information they need, any change to the DMI and information provided should be validated under careful consideration. Hence, in the following research, we will try to get railway companies support to revise the system's industry requirements and provide a more

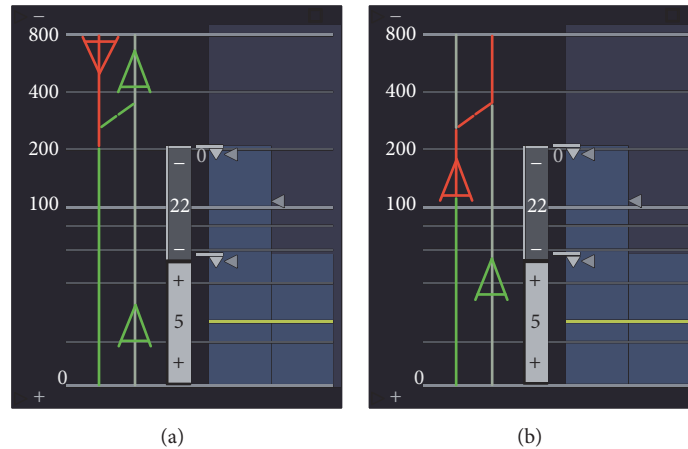


FIGURE 13: DMI with detected trains.

actual analysis. A full function device will be available to be applied on the actual DMI.

Conflicts of Interest

The authors declare that there are no conflicts of interest regarding the publication of this paper.

Acknowledgments

This work is supported by the National Natural Science Foundation of China (U1734211 and 61603026), Shanghai Committee of Science and Technology research program (17DZ1100106), and Beijing Municipal Natural Science Foundation (I18E300010 and L171004).

References

- [1] H. Song and E. Schnieder, "Modeling of railway system maintenance and availability by means of colored petri nets," *Maintenance and Reliability*, vol. 20, no. 2, pp. 232–239, 2018.
- [2] H. Dong, B. Ning, Y. Chen et al., "Emergency management of urban rail transportation based on parallel systems," *IEEE Transactions on Intelligent Transportation Systems*, vol. 14, no. 2, pp. 627–636, 2013.
- [3] J. Wang, J. Wang, C. Roberts, and L. Chen, "Parallel monitoring for the next generation of train control systems," *IEEE Transactions on Intelligent Transportation Systems*, vol. 16, no. 1, pp. 330–338, 2015.
- [4] B. Ai, X. Cheng, T. Kurner et al., "Challenges toward wireless communications for high-speed railway," *IEEE Transactions on Intelligent Transportation Systems*, vol. 15, no. 5, pp. 2143–2158, 2014.
- [5] J. Moreno, J. Riera, L. De Haro, and C. Rodriguez, "A survey on future railway radio communications services: challenges and opportunities," *IEEE Communications Magazine*, vol. 53, no. 10, pp. 62–68, 2015.
- [6] A. Lehner, T. Strang, and C. R. Garca, "A reliable surveillance strategy for an autonomous rail collision avoidance system," in *Proceedings of the 15th ITS World Congress*, New York, NY, USA, 2008.
- [7] H. Song and E. Schnieder, "Validation, verification and evaluation of a train to train distance measurement system by means of colored petri nets," *Reliability Engineering and System Safety*, vol. 164, pp. 10–23, 2017.
- [8] E. Schnieder, "Traffic safety and availability - contradiction or attraction," in *Proceedings of 2nd International Symposium of Networks for Mobility*, 2004.
- [9] "Ertms/etcs - baseline 3, system requirements specification. chapter 3, principles, subset-026-3, issue 3.0.0. 23, 2008".
- [10] L. Lei, J. Lu, Y. Jiang et al., "Stochastic delay analysis for train control services in next-generation high-speed railway communications system," *IEEE Transactions on Intelligent Transportation Systems*, vol. 17, no. 1, pp. 48–64, 2016.
- [11] ITU-R Recommendation P.526-11, "Propagation by diffraction, 2009".
- [12] H. Holma and A. Toskala, *LTE for UMTS: Evolution to LTE-advanced*, John Wiley and Sons, 2011.
- [13] R. He, B. Ai, Z. Zhong, A. F. Molisch, R. Chen, and Y. Yang, "A measurement-based stochastic model for high-speed railway channels," *IEEE Transactions on Intelligent Transportation Systems*, vol. 16, no. 3, pp. 1120–1135, 2015.
- [14] M. Lindahl, "Track geometry for high-speed railways," TRITA-FKT Report, Tech. Rep., 54.
- [15] H. Abid, T. C. Chung, S. Lee, and S. Qaisar, "Performance analysis of lte smartphones-based vehicle-to-infrastructure communication," in *Ubiquitous Intelligence and Computing and 9th International Conference on Autonomic and Trusted Computing (UIC/ATC)*, pp. 72–78, 2012.

Research Article

The QoS Indicators Analysis of Integrated EUHT Wireless Communication System Based on Urban Rail Transit in High-Speed Scenario

Xiaoxuan Wang ¹, Hailin Jiang,² Tao Tang,¹ and Hongli Zhao¹

¹State Key Laboratory of Rail Traffic Control and Safety, Beijing Jiaotong University, Beijing 100044, China

²National Engineering Research Center of Rail Transportation Operation and Control System, Beijing Jiaotong University, Beijing 100044, China

Correspondence should be addressed to Xiaoxuan Wang; wangxiaoxuan@bjtu.edu.cn

Received 2 November 2017; Accepted 15 February 2018; Published 3 April 2018

Academic Editor: Yan Zhang

Copyright © 2018 Xiaoxuan Wang et al. This is an open access article distributed under the Creative Commons Attribution License, which permits unrestricted use, distribution, and reproduction in any medium, provided the original work is properly cited.

Nowadays, in urban rail transit systems, train wayside communication system uses Wireless Local Area Network (WLAN) as wireless technologies to achieve safety-related information exchange between trains and wayside equipment. However, according to the high speed mobility of trains and the limitations of frequency band, WLAN is unable to meet the demands of future intracity and intercity rail transit. And although the Time Division-Long Term Evolution (TD-LTE) technology has high performance compared with WLAN, only 20 MHz bandwidth can be used at most. Moreover, in high-speed scenario over 300 km/h, TD-LTE can hardly meet the future requirement as well. The equipment based on Enhanced Ultra High Throughput (EUHT) technology can achieve a better performance in high-speed scenario compared with WLAN and TD-LTE. Furthermore, it allows using the frequency resource flexibly based on 5.8 GHz, such as 20 MHz, 40 MHz, and 80 MHz. In this paper, we set up an EUHT wireless communication system for urban rail transit in high-speed scenario integrated all the traffics of it. An outdoor testing environment in Beijing-Tianjin High-speed Railway is set up to measure the performance of integrated EUHT wireless communication system based on urban rail transit. The communication delay, handoff latency, and throughput of this system are analyzed. Extensive testing results show that the Quality of Service (QoS) of the designed integrated EUHT wireless communication system satisfies the requirements of urban rail transit system in high-speed scenario. Moreover, compared with testing results of TD-LTE which we got before, the maximum handoff latency of safety-critical traffics can be decreased from 225 ms to 150 ms. The performance of throughput-critical traffics can achieve 2-way 2 Mbps CCTV and 1-way 8 Mbps PIS which are much better than 2-way 1 Mbps CCTV and 1-way 2 Mbps PIS in TD-LTE.

1. Introduction

With the rapid development of the city size, the urban rail transit becomes the main trip mode of human beings which could provide safe, punctual passenger services within urban areas and intercity. In order to release the traffic pressure in urban area, the transit speed and capacity need to be improved along with more and more urban population. So, an automated train control system called communication-based train control (CBTC), which uses high capacity and bidirectional train-wayside communication, becomes one of the key subsystems in urban rail transit systems to guarantee the safe operation of rail vehicles [1]. According

to the open standards and available commercial-off-the-shelf equipment [2], the WLANs are often used as the train-wayside communication in urban rail transit, such as Singapore North-East Line from Alstom [3] and Beijing Metro Line 10 from Siemens. However, with the development of urban rail transit, such as high-speed operation and integrated services including CBTC information, train state monitor information, passenger information systems (PIS) video, closed-circuit television (CCTV) video, and emergency text, WLAN cannot meet the developed safety-critical and throughput-critical requirements of urban rail transit and QoS of wireless communication system due to increasing operation density.

Although TD-LTE obtains some improvement in communication performance comparing with WLAN, the performance of TD-LTE is degraded greatly in high-speed scenario around 300 km/h, such as reduced throughput and large communication delay [4]. Therefore, the existing technology can hardly guarantee the strict QoS requirements of urban rail transit systems in high-speed scenario over 300 km/h.

Hence, a new technology which can solve the problems in high-speed scenario needs to be sought. Fortunately, these problems can be addressed by a new technology named EUHT. EUHT is a novel wireless communication technology based on 802.11ac which can achieve the requirements of 5G [5]. The highest throughput of this system can reach 3.48 Gbps which is much larger than the TD-LTE. The analysis of throughput is described in Section 3. And the communication delay can be lower than 10 ms normally. Furthermore, other advantages of EUHT are set as follows:

- (i) Frame length of EUHT can be configured according to different scenarios from 0.5 ms to 10 ms and EUHT designed configurable pilot for effective channel estimation for high speed scenario.
- (ii) EUHT physical frame is the first to use the self-contained structure, that is, uplink and downlink resource allocation. downlink data transmission and the uplink acknowledgment transmission are completed in the same frame, which is considered to be one of the key technologies of 5G by Qualcomm. The self-contained frame structure can greatly reduce the system latency.
- (iii) EUHT has designed a special sequence at the header of frame to enable the receiver to achieve a more efficient and reliable synchronization process. The receiver can perform frame detection, automatic gain control (AGC), and other operations based on the EUHT header without any other auxiliary synchronization sources (such as base station, GPS). Through the optimization design of the synchronization sequence, the receiver can achieve a reliable estimate of the large frequency deviation at low cost, thus greatly reducing the requirement of crystal performance to ± 20 ppm.

Due to these advantages, EUHT has a better performance than existing WLAN and TD-LTE technology in high-speed scenario up to 500 km/h.

At present, there are some researches about the communication system based on 802.11ac. Authors propose delayed dynamic bandwidth channel access scheme with virtual primary channel reservation in [6]. This scheme mitigates the performance bottleneck problem as well as a scalability problem. In [7], an antenna allocation scheme for a full-duplex communication is proposed in IEEE 802.11ac WLAN. A set of results from a performance evaluation study of wireless communication based on the IEEE 802.11ac standard are proposed to study the performances of IEEE 802.11ac communication system in [8]. These related works make some contributions on using the 802.11ac technology in public wireless communication networks, but they do not

consider the integrated urban rail transit traffics in high-speed scenario.

Recently, substantial works have been done on the wireless communication issues in the railway environment. Authors of [9] use the cross layer Reliable Mobility Pattern Aware (RMPA) handover strategy to improve handover performance for broadband wireless communication in high-speed railway. Not only do He et al. in [10] test the broadband delay cluster performance at 2.4 GHz in subway tunnel, but also the analysis of the results are given. In [11], a field test has been done in Madrid subway to build the radio channel in tunnels at 2.4 GHz. The authors in [12] give us a cross-layer admission control scheme for high-speed railway communication system. Zhu et al. design a cross-layer handoff method for CBTC wireless communication system in [13].

Although these aforementioned works consider the CBTC performance under different railway wireless communication environment, few of them study the integrated urban rail transit traffics in the same environment. Moreover, the working frequency of related works is all based on 2.4 GHz or lower. There are few studies that consider the high working frequency communication system in high-speed scenario. In this paper, an integrated EUHT wireless communication system based on urban rail transit in high-speed scenario is designed, which works in the 5.8 GHz and includes all the traffics in CBTC systems.

In this paper, we firstly study the integrated EUHT wireless communication system based on urban rail transit in high-speed scenario, which works in the 5.8 GHz. Then, the theoretical calculation of communication delay without handoff, handoff latency, and throughput in EUHT wireless communication system based on urban rail transit are given. In order to get the real integrated EUHT wireless communication system performance, we set up an outdoor test scenario in Beijing-Tianjin High-Speed Railway. The test results show that the QoS performance of integrated EUHT wireless communication system based on urban rail transit not only satisfies the requirements of safety-critical traffics and throughput-critical traffics in high-speed scenario well, but also has greatly performance improvement comparing with TD-LTE system.

The remainder of this paper is organized as follows. Section 2 describes the integrated EUHT wireless communication system based on urban rail transit. In Section 3, the theoretical calculation of communication delay without handoff, handoff latency, and throughput are given. The test scenario in Beijing-Tianjin High-Speed Railway is introduced in Section 4. The requirements of all the traffics in CBTC systems and test results are presented in Section 5. Finally, the conclusion is given.

2. The Integrated EUHT Wireless Communication System Based on Urban Rail Transit

As we can see in Figure 1, the integrated EUHT wireless communication system based on urban rail transit includes the

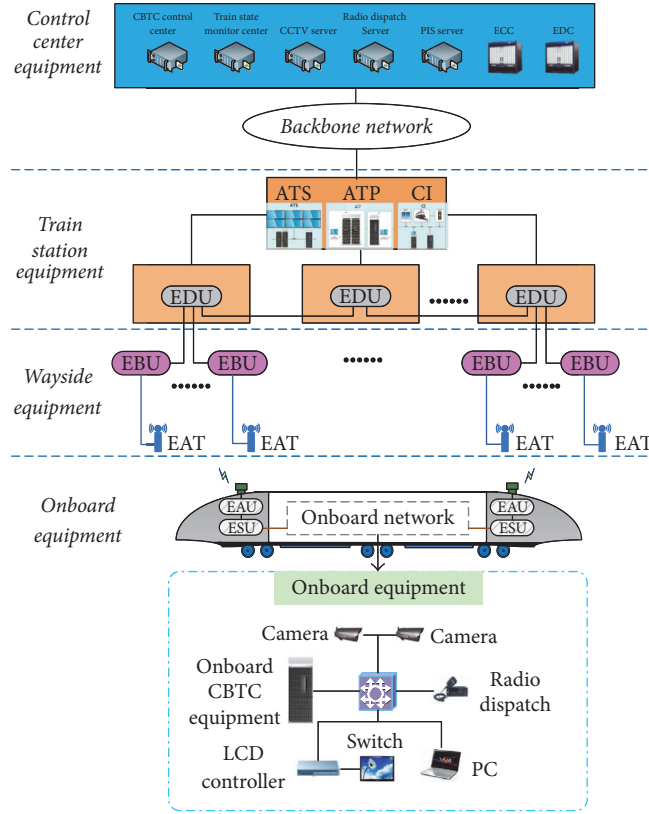


FIGURE 1: System architecture of EUHT wireless communication system based on urban rail transit.

control center subsystem, train station subsystem, trackside subsystem, and on-board subsystem.

The main task of control center subsystem is to use plenty of equipment such as EUHT Control Center (ECC), EUHT Data Center (EDC), CBTC control center, train state monitor center, CCTV server, radio dispatch server, and PIS server to control and manage the integrated CBTC system. Moreover, the backbone network is used to provide the wired communication link between control center subsystem and train station subsystem. As there are trains operating in the management area of any train station, the train station subsystem will charge the communication with all trains. The track-side subsystem consists of the EUHT Base-Station Unit (EBU) and EUHT Antenna (EAT). The EBU is the base station of the EUHT system and connected to EAT using optical fiber. The EAT exchanges the information with on-board subsystem through air interface. The on-board subsystem can be divided into EUHT Access Unit (EAU), EUHT Service Unit (ESU), PIS screens, CCTV cameras, onboard CBTC equipment, train radio dispatch equipment, and train state sensors. All these types of equipment are connected by switches.

Moreover, in order to verify whether the integrated EUHT wireless communication system can satisfy the QoS requirements of different traffics in urban rail transit, the theoretical analysis is shown in Section 3 and the details about test scenario and procedure are presented in Section 4.

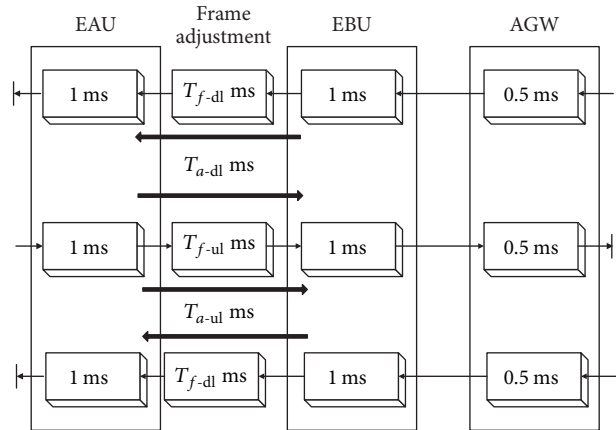


FIGURE 2: Transmission delay without handoff.

3. The Theoretical Analysis of Integrated EUHT Wireless Communication System

In this section, the theoretical analysis of communication delay, handoff latency, and throughput are analyzed.

3.1. *Communication Delay without Handoff.* The communication delay without handoff is shown in Figure 2, where T_{a-dl} and T_{a-ul} are the downlink and uplink average Automatic

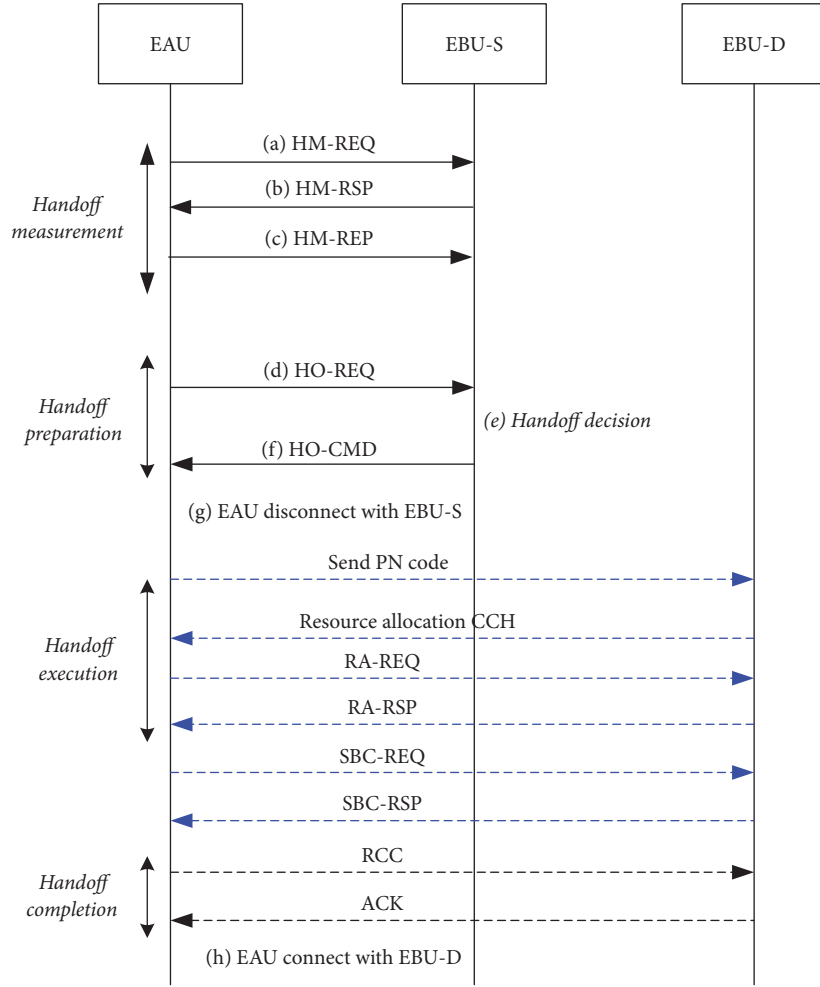


FIGURE 3: The handoff procedure of EUHT system.

Repeat Request-Round Trip Time (ARQ-RTT), respectively, and T_{f-dl} and T_{f-ul} are the average downlink and uplink frame adjustment time, respectively. With the analysis, the EUHT communication delay $Comm_{delay}$ is shown as follows:

$$Comm_{delay} = 1 + T_f + 1 + p * T_a, \quad (1)$$

where T_a and T_f are the average ARQ-RTT and frame adjustment time.

For our test, the theoretical calculation result with typical parameters of communication delay without handoff and retransmission is 4–8 ms. However, there is no ideal wireless environment of the high speed scenario around 300 km/h. Therefore, the real communication delay is greater than this result.

3.2. Handoff Latency. In order to make the best of the frequency resources and eliminate the intercell interference, the Interfrequency Handoff (IFHO) is selected by EUHT. The theoretical analysis of it is set below.

As is shown in Figure 3, the handoff procedure includes handoff measurement, handoff preparation, handoff execution, and handoff completion. The handoff measurement and

preparation phases are performed without EBU-Destination (EBU-D), so that the messages in these two phases are directly exchanged among the EAU and the EBU-Service (EBU-S). At the beginning, when the Radio Signal Strength Indicator (RSSI) of EBU-S has been lower than the measurement threshold for a certain period set before, the EAU will send the Handoff Measurement Request (HM-REQ) to EBU-S to apply to starting the handoff measurement. Then, when the EAU receives the Handoff Measurement Response (HM-RSP), it will measure the RSSI of EBU-S and EBU-D and report the information to EBU-S using a Handoff Measurement Report (HM-REP). When RSSI of the EBU-D has been stronger than that of the EBU-S for a certain period, the EAU will decide to execute handoff and initiate the handoff preparation phase by sending a Handoff Request (HO-REQ) to the EBU-S. A HO-REQ includes EAU context information, QoS parameters, and the information of EBU-D candidates. EBU-S selects an EBU-D from the candidates and replies to the EAU with a Handoff Command (HO-CMD). Therefore, the latency for the handoff preparation phase is represented as follows:

$$T_{HO-Prep} = 2 * T_{EAU-EBU-S} + T_{con1} + T_{dec1}, \quad (2)$$

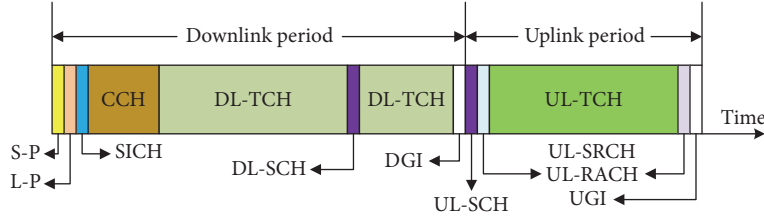


FIGURE 4: The frame structure of EUHT system.

where $T_{\text{EAU-EBU-S}}$ indicates the transmission delay between the EAU and EBU-S, T_{con1} is the latency of the measurement frequency conversion of EAU, and T_{dec1} represents the processing delay of the EBU-S, where T_{dec1} includes the processing of EBU-D selection and handoff decision.

The handoff execution phase is most critical on the handoff performance due to the handoff interruption/disconnection that occurs. The handoff execution phase is triggered by the EBU-S sending a HO-CMD to the EAU. Upon reception of the HO-CMD, the EAU disconnects from the EBU-S and changes the working frequency to be the same as EBU-D. Then, EAU sends Pseudo-Noise (PN) code to the assigned EBU-D through the Random Access Channel (RACH) and attempts to initiate the Random Access (RA) process. Next, As the EBU-D receives the PN code, it will allocate the Control Channel (CCH) resources for EAU and EAU will send RA-REQ message through the CCH. After receiving RA-REQ message and RAU MAC, the EBU-D will reply the RA-RSP to EAU. Then, in order to inform EAU capability parameters to EBU-D, EAU sends the Station Basic Capability (SBC-REQ) to EBU-D. As EBU-D receives the request, it will compare the capability parameters of EAU and EBU-D and reply the SBC-RSP which includes the capability parameters supported by EBU-D, the allocated EAU ID, and scheduling information to EAU. The latency for the handoff execution phase $T_{\text{HO-Exe}}$ is represented as

$$T_{\text{HO-Exe}} = 6 * T_{\text{EAU-EBU-D}} + T_{\text{con2}} + T_{\text{dec2}}, \quad (3)$$

where $T_{\text{EAU-EBU-S}}$ indicates the transmission delay between the EAU and EBU-D, T_{con1} is the latency of the measurement frequency conversion of EAU, and T_{dec1} represents the processing delay of the EBU-S, where T_{dec1} includes the processing of EBU-D selection and handoff decision.

During the handoff completion phase, when the EAU completes the RA process, the EAU informs the EBU-D by sending a RA Connection Complete (RCC) and the EBU-D replies to the EAU with an ACK. Finally, the EAU connects with EBU-D and transmits traffics through the Uplink/Downlink-Transmission Channel (UL/DL-TCH). The handoff completion latency is expressed as

$$T_{\text{HO-Comp}} = 2 * T_{\text{EAU-EBU-D}} + T_{\text{ACK}}, \quad (4)$$

where T_{ACK} is the processing delay of the EBU-D, which includes the processing of RRC and sending ACK.

So, the total handoff latency is presented below:

$$T_{\text{HO}} = 2 * T_{\text{EAU-EBU-S}} + 8 * T_{\text{EAU-EBU-D}} + T_{\text{con1}} + T_{\text{con2}} + T_{\text{dec1}} + T_{\text{dec2}} + T_{\text{ACK}}. \quad (5)$$

In our test, given the typical parameters, the handoff latency without failure is about 20 ms, and with high speed scenario reaching up to 300 km/h and complex environment in the field test, the real handoff latency is greater than this.

3.3. Throughput. In this subsection, the throughput with overhead needs to be calculated at first. According to the characteristic of 802.11ac [14], the single cell throughput of EUHT system mainly depends on system bandwidth, length of OFDM symbol, and Modulation and Coding Scheme (MCS). Thus, the peak data rate is

$$\text{Throughput} = \frac{N_{\text{DBPS}}}{L}, \quad (6)$$

where N_{DBPS} is the number of data bits per symbol and L is the length of OFDM symbol, which is 14.4 μs . Moreover, N_{DBPS} is represented as

$$N_{\text{DBPS}} = N_{\text{BPSCS}} * R * N_{\text{SS}} * N_{\text{subcarrier}}, \quad (7)$$

where N_{BPSCS} indicates the modulation order, R is the code rate, N_{SS} represents the number of spatial streams, and $N_{\text{subcarrier}}$ is the number of subcarrier.

However, as is shown in Figure 4, the transmission frame of EUHT system consists of Short-Preamble (S-P), Long-Preamble (L-P), System Information Channel (SICH), CCH, UL/DL-TCH, Uplink/Downlink-Search Channel (UL/DL-SCH), Uplink/Downlink-Guard Interval (U/D-GI), Uplink-Scheduling Request Channel (UL-SRCH), and Uplink-RACH (UL-RACH). Because UL/DL-TCH can only be used to transmit train-ground communication traffics in one transmission frame, the uplink and downlink peak throughput need to be calculated with data bits of carrying without overhead which contains S/L-P overhead, SICH overhead, CCH overhead, UL/DL-SCH overhead, U/D-GI overhead, UL-SRCH overhead, UL-RACH overhead, and pilot frequency (PF) overhead, over a single wireless frame time.

In this paper, the length of one frame is 2 ms, which totally have 139 OFDM symbols and the UL/DL configuration is 1:1.2. Moreover, in our test, S/L-P, SICH, CCH, UL/DL-SCH, U/D-GI, UL-SRCH, UL-RACH, and PF occupy 2, 1, 4, 2, 8,

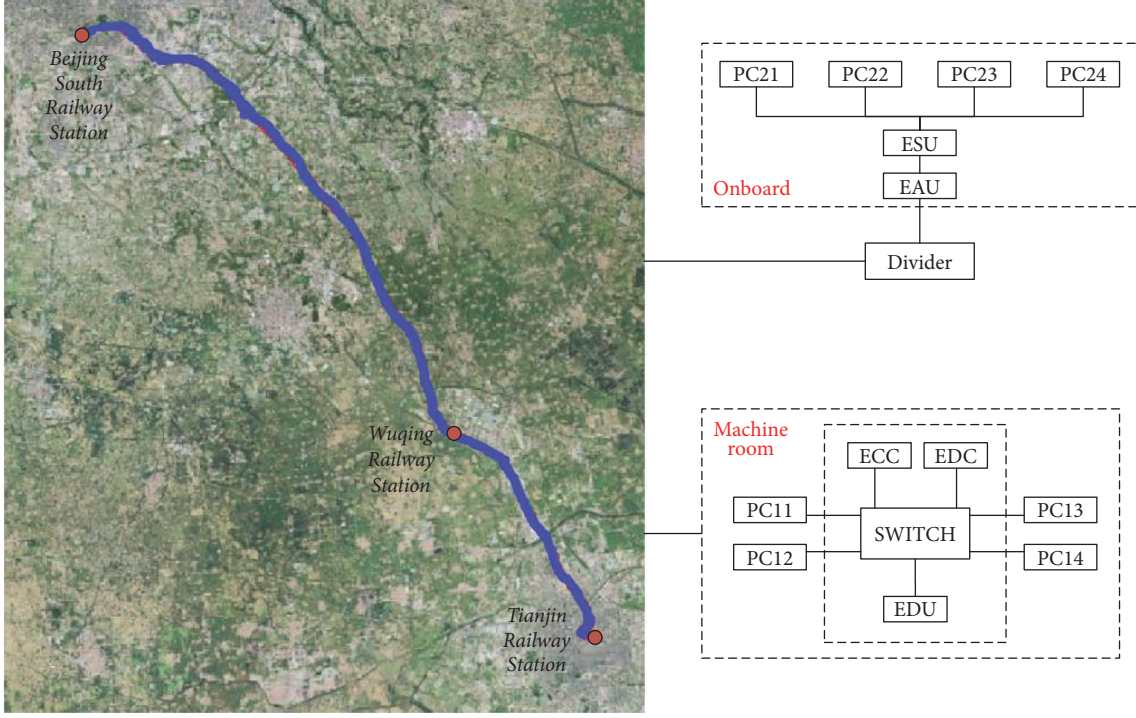


FIGURE 5: Test scenario of Beijing-Tianjin High-Speed Railway.

1, 2, and 9 OFDM symbols in one frame, respectively. So, the total overhead is 29 OFDM symbols in one frame. The total overhead of EUHT system in one frame is represented as

$$\begin{aligned} OH_{\text{total}} = & OH_{S/L-P} + OH_{SICH} + OH_{CCH} \\ & + OH_{UL/DL-SCH} + OH_{U/D-GI} + OH_{UL-SRCH} \quad (8) \\ & + OH_{UL-RACH} + OH_{PF}. \end{aligned}$$

According to the analysis in this subsection, the downlink throughput of EUHT which does not include the overhead can be shown as

$$\text{Throughput}_{DL} = \text{Throughput} * (1 - OH_{\text{total}}) * \frac{1.2}{2.2}. \quad (9)$$

The uplink throughput of EUHT without overhead can be written as

$$\text{Throughput}_{UL} = \text{Throughput} * (1 - OH_{\text{total}}) * \frac{1}{2.2}. \quad (10)$$

For our field test, the bandwidth and maximum MCS are 80 MHz and 21. So, the maximum uplink and downlink throughput are 179.06 Mbps and 214.87 Mbps, respectively. But with high speed scenario reaching up to 300 km/h and complex environment in the field test, the real throughput is lower than this.

4. Test Scenario and Parameters

In this section, a field test scenario has been done in the Beijing-Tianjin High-Speed Railway to make the testing

results more accurate than that in the laboratory. The test scenario is made up of three parts, obviously, the high-speed railway, machine room plant, and on-board space. As is shown in Figure 5, the Beijing-Tianjin High-Speed railway is located between Beijing and Tianjin and has a length of 115.2 km. It starts from Beijing South Railway Station and ends at Tianjin Railway Station by way of Wuqing Railway Station. The high-speed railway is made up of elevated railway except the area around railway station. So, in most area of the railway, there is no tall building which can affect the wireless transmission.

In this field test, in order to guarantee the Quality of Coverage (QoC), 109 EBU are deployed along the railway in total. The distance between every two EBU is about 1 km. So, the average RSSI received by onboard EAU is above -90 dBm which can meet the demand of urban rail transit wireless communication system. Moreover, every adjacent EBU works at different frequency point due to IFHO. Thus, to make the different traffics meet the QoS requirement described in Table 2, we allocate 160 MHz for the whole system. Half of the EBUs run in 5560 MHz–5640 MHz frequency band, and others run in 5725 MHz–5805 MHz frequency band. These two frequency bands are all possibly used for high-speed railway and urban rail transit system. Furthermore, because of less use of the frequency resources in 5.6 GHz–5.8 GHz, there is little wireless interference in this frequency band along the railway. So, the radio free wave is used in wireless communication system instead of leaky cable and leaky waveguide. What is more, Table 1 shows the other configurations of this test scenario.

TABLE 1: The configurations in Beijing-Tianjin High-Speed Railway.

Parameters	Value
EBU TX power	17 dBm
Track-side antenna gain	17 dB
Frequency point	120 (5600 MHz), 153 (5765 MHz)
Working bandwidth	80 MHz
Handoff model	IFHO (interfrequency handoff)
Wireless coverage	Free wave
Maximum train speed	300 km/h
Onboard antenna height	3 m
Track-side antenna height	5 m

As we can see in Figure 5, in the machine room, ECC is used for controlling the EUHT network. All the data are analyzed and processed by EDC. The EDU is connected to the wayside equipment with optical fiber. Four PCs are the analog servers for CBTC, train state monitor, PIS, CCTV, and emergency text, respectively. There are also EAU used for onboard network access and ESU used for analyzing and processing the data received by EAU, and four PCs connected with ESU are the analog on-board servers for CBTC, train state monitor, PIS, CCTV, and emergency text, respectively. Therefore, one-way CBTC traffic (200 Kbps), two-way CCTV traffic (2 Mbps), one-way PIS traffic (8 Mbps), one-way emergency text traffic (200 Kbps), and one-way train state monitor traffic (200 Kbps) are set to be transmitted between the PCs located at the machine room plant and on-board space.

The test tool used for test is Ixchariot software which can simulate different urban rail transit traffics. There are also different IP and traffics set for different pair of PCs. PC11 and PC21 are for CBTC traffic. PC12 and PC22 are for train state monitor traffic. PC13 and PC23 are for CCTV traffic. PC14 and PC24 are for PIS traffic and emergency text traffic.

5. Test Results and Discussions

As is shown in our previous works, the requirements of all the traffics in CBTC systems, such as communication delay, handoff latency, and throughput, are much stricter than that in public wireless networks. Thus, the communication delay and handoff latency must be stipulated less than the train-wayside communication period which is 200 ms in the traditional CBTC systems; otherwise the trains may experience some serious accidents [15]. Furthermore, the throughput is related to the performance of the high throughput demand traffics, such as PIS and CCTV.

Table 2 shows the different requirements for different traffics in integrated urban rail transit [16]. Therefore, in order to ensure the safe operation of the trains on the line, the transmission delay of safety-critical traffics, such as CBTC information, train state monitor, and emergency text, should be stipulated less than 150 ms through wireless and wired transmission whether the handoff happens or not. And the latency requirement of the other nonsafety critical traffics is less than 500 ms. In the requirement of throughput, at least 100 kbps should be allocated to CBTC traffic both in uplink

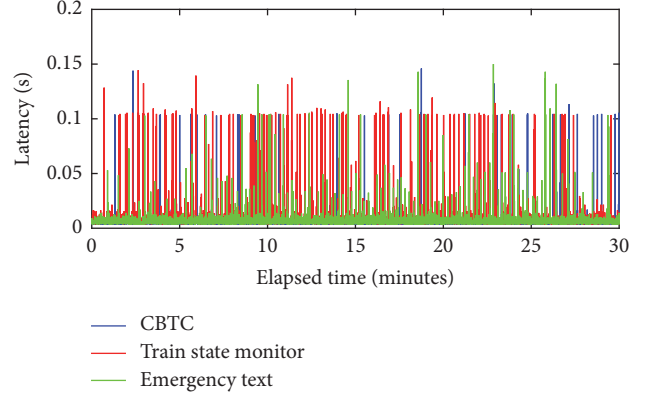


FIGURE 6: Test result of communication delay and handoff latency based on EUHT.

and in downlink due to the bidirectional transmission of it. And according to the unidirectional transmission of train state monitor and emergency text, there are total 200 kbps allocated to these two traffics. Furthermore, the throughput-critical traffics, such as PIS and CCTV, are required 8 Mbps in downlink and 4 Mbps in uplink at least, respectively.

Therefore, in this section, some testing results about communication delay, handoff latency, and throughput are shown to describe whether the integrated EUHT system can satisfy the requirements of CBTC system in high-speed scenario firstly. As we know, the most important QoS parameter for safety critical traffics is transmission delay which include communication delay without handoff and handoff latency. Figure 6 shows the communication delay without handoff and the handoff latency performance for these traffics. As we can see, when handoff does not happen, the average communication delay without handoff is 5 ms, 5 ms, and 6 ms for CBTC, train state monitoring traffic, and emergency text, respectively. The maximum values are 33 ms, 55 ms, and 103 ms for them, respectively. Therefore, the communication delay without handoff of safety-critical traffics can satisfy the requirements shown in Table 2 very well in high-speed scenario.

Moreover, as is shown in Figure 6, comparing with the communication delay without handoff, the maximum handoff latency of CBTC, train state monitoring, and emergency text can reach 146 ms, 144 ms, and 150 ms. Even so, all the handoff latency still satisfy the requirement of CBTC safety critical traffics in high-speed scenario.

Figure 7 describes the throughput testing results of throughput critical traffics. In our test, 2-way CCTV analogue videos, 2 Mbps for each, and 1-way 8 Mbps PIS analogue video are transmitted in this integrated system. Thus, as is shown in Figure 7, because of the handoff, there are some fluctuations in the throughput results of CCTV and PIS, but the average value of CCTV and PIS all stabilize around the throughput requirements presented in Table 2.

Something needs to be pointed out; when handoff happens, the EAU will be disconnected with EBU. During this period, the data cannot transmit between EAU and EBU. As is shown in Figure 7, the throughput will be decreased during

TABLE 2: The requirement of different traffics in integrated urban rail transit.

Application	Throughput uplink	Throughput downlink	Delay	Handoff latency	Reliability
CBTC	100 kbps	100 kbps	150 ms	150 ms	High
Train state monitor	100 kbps	None	150 ms	150 ms	High
Emergency text	None	100 kbps	150 ms	150 ms	High
CCTV	4 Mbps	None	500 ms	500 ms	Medium
PIS	None	8 Mbps	500 ms	500 ms	Low

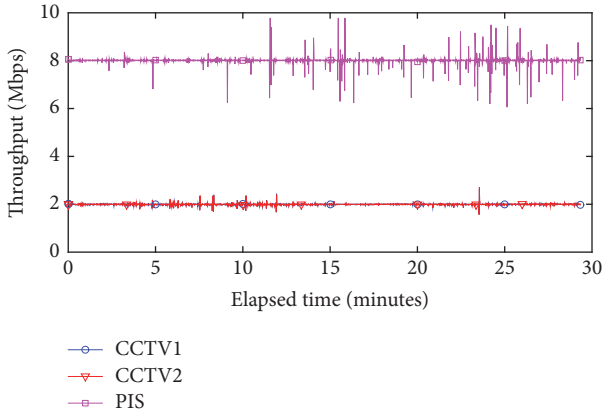


FIGURE 7: Test result of throughput of PIS and CCTV based on EUHT.

the handoff procedure. When the EAU completes the IFHO procedure, it connects with new EBU. The untransmission data will be transmitted in a short period. The throughput will be increased after the IFHO.

After the analysis of EUHT test results, we will show the comparison with the TD-LTE test results which we get in the Circular Railway Experiment Station of China Academy of Railway Sciences [16, 17]. Figures 8 and 9 are the test results of TD-LTE under the scenario with 200 km/h. As we can see, the maximum handoff latency of safety-critical traffics can reach 225 ms which is much larger than the requirement in Table 2. Moreover, the throughput results can only satisfy the requirements with 1-way 1 Mbps CCTV analogue videos and 1-way 2 Mbps PIS analogue video.

Therefore, compared with TD-LTE, the integrated EUHT wireless communication system can achieve better performance in safety-critical and throughput-critical traffics in high-speed scenario.

6. Conclusion

In this paper, we first detailed presented the structure of integrated EUHT wireless communication system based on urban rail transit and described all the traffics of traditional CBTC system. Then, the theoretical values including communication delay without handoff, handoff latency, and throughput were calculated in ideal condition. In order to get the real EUHT wireless communication system performance, an outdoor test scenario in Beijing-Tianjin High-Speed Railway was set up. Plenty of test results and the comparison

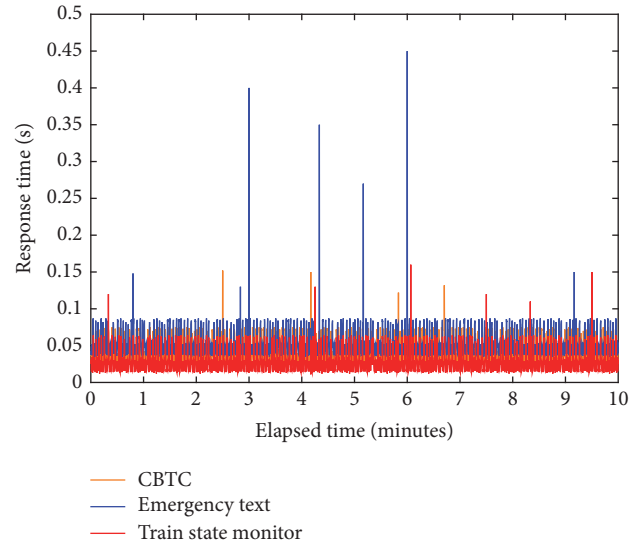


FIGURE 8: Test result of communication delay and handoff latency based on TD-LTE.

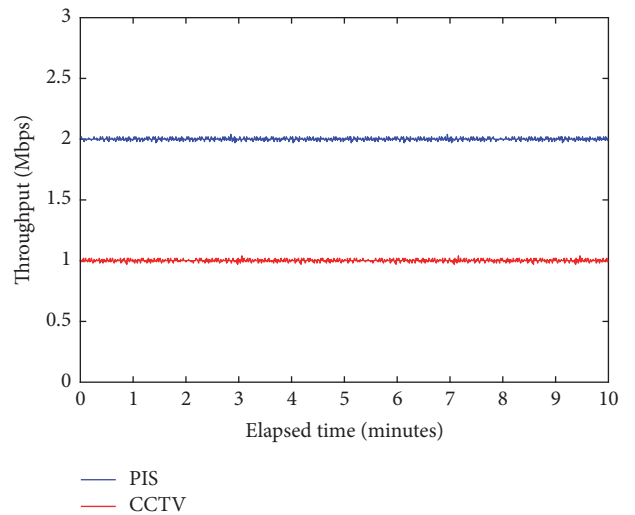


FIGURE 9: Test result of throughput of PIS and CCTV based on TD-LTE.

with TD-LTE were shown in this paper. As we can see, not only can the QoS performance of integrated EUHT wireless communication system based on urban rail transit satisfy the requirement of safety critical traffics and throughput critical

traffics in high-speed scenario well, but also it has better performance than TD-LTE in the high-speed scenario.

Conflicts of Interest

The authors declare that there are no conflicts of interest regarding the publication of this paper.

Acknowledgments

This paper was supported by grants from Beijing Natural Science Foundation (L171004, I18E300010, and K1E017001531), the National Natural Science Foundation of China (no. 61603026), China Railway (K1D16001531), projects (RCS2016ZT011, RCS2017ZT006, and K1K17006531), and the Beijing Key Laboratory of Urban Rail Transit Automation and Control.

References

- [1] R. Pascoe and T. Eichorn, "What is communication-based train control?" *IEEE Vehicular Technology Magazine*, vol. 4, no. 4, pp. 16–21, 2009.
- [2] M. Aguado, E. Jacob, P. Saiz, and J. J. Unzilla, "Railway signaling systems and new trends in wireless data communication," in *Proceedings of the Vehicular Technology Conference (VTC'05)*, pp. 1333–1336, IEEE, 2005.
- [3] S. G. Shirlaw, "Radio and communications-based train control: Migration, interoperation and system engineering issues," in *Proceedings of the international conference on railway engineering-challenges for railway transportation in information age*, pp. 1–5, 2008.
- [4] Y. Zhang, M. Wu, R. Zhang, P. Zhou, and S. Di, "Adaptive QoS-aware resource allocation for high-speed mobile LTE wireless systems," in *Proceedings of the IEEE Globecom Workshops (GC Wkshps'13)*, pp. 947–952, 2013.
- [5] E. Dahlman, G. Mildh, S. Parkvall et al., "5G wireless access: Requirements and realization," *IEEE Communications Magazine*, vol. 52, no. 12, pp. 42–47, 2014.
- [6] W. Kim, J.-P. Jeong, and Y.-J. Suh, "Delayed Dynamic Bandwidth Channel Access scheme for IEEE 802.11ac WLANs," in *Proceedings of the 31st International Conference on Information Networking (ICOIN'17)*, pp. 70–75, IEEE, 2017.
- [7] W. Choi, I.-S. Jang, and T. Kim, "Antenna allocation scheme for full-duplex communication in IEEE 802.11ac WLAN," in *Proceedings of the 2017 IEEE International Conference on Consumer Electronics (ICCE'17)*, pp. 120–121, 2017.
- [8] Tarabuta, D. Balan, A. Potorac, and A. Graur, "Performance investigation over 802.11ac communication environment," in *Proceedings of the 22nd International Conference on Applied Electromagnetics and Communications (ICECom'16)*, IEEE, 2016.
- [9] M. Aguado, E. Jacob, J. Astorga, N. Toledo, and M. Berbineau, "The cross layer RMPA handover: a reliable mobility pattern aware handover strategy for broadband wireless communication in a high-speed railway domain," *EURASIP Journal on Wireless Communications and Networking*, vol. 2012, no. 1, 2012.
- [10] R. He, Z. Zhong, and C. Briso, "Broadband channel long delay cluster measurements and analysis at 2.4GHz in subway tunnels," in *Proceedings of the IEEE 73rd Vehicular Technology Conference (VTC-Spring)*, 5, 1 pages, IEEE, 2011.
- [11] K. Guan, Z. D. Zhong, J. I. Alonso, and C. Briso-Rodríguez, "Measurement of distributed antenna systems at 2.4 GHz in a realistic subway tunnel environment," *IEEE Transactions on Vehicular Technology*, vol. 61, no. 2, pp. 834–837, 2012.
- [12] Q. Xu, X. Li, H. Ji, and L. Yao, "A cross-layer admission control scheme for high-speed railway communication system," in *Proceedings of the 2013 IEEE International Conference on Communications (ICC'13)*, pp. 6343–6347, 2013.
- [13] L. Zhu, F. R. Yu, B. Ning, and T. Tang, "Handoff performance improvements in MIMO-enabled communication-based train control systems," *IEEE Transactions on Intelligent Transportation Systems*, vol. 13, no. 2, pp. 582–593, 2012.
- [14] E. Perahia and R. Stacey, "Next generation wireless LANs: 802.11n and 802.11ac," *Next Generation Wireless LANs: 802.11n and 802.11ac*, pp. 1–452, 2005.
- [15] B. Bu, F. R. Yu, T. Tang, and C. Gao, "Performance improvements of communication-based train control (CBTC) systems with unreliable wireless networks," *Wireless Networks*, vol. 20, no. 1, pp. 53–71, 2014.
- [16] Z. Hongli, C. Yuan, Z. Li, and X. Wei, "Integrated train ground radio communication system based TD-LTE," *Journal of Electronics*, vol. 25, no. 4, pp. 740–745, 2016.
- [17] X. Wang, H. Jiang, T. Tang, and H. Zhao, "The QoS analysis of train-ground communication system based on TD-LTE in urban rail transit," in *Proceedings of the IEEE International Conference on Intelligent Rail Transportation (ICIRT'16)*, pp. 49–54, IEEE, 2016.

Research Article

Propagation at mmW Band in Metropolitan Railway Tunnels

Ana González-Plaza ¹, César Calvo-Ramírez,¹ César Briso-Rodríguez ¹,
Juan Moreno García-Loygorri,¹ David Oliva,² and José I. Alonso²

¹Departamento de Teoría de la Señal y Comunicaciones, ETSIS de Telecomunicación,
Universidad Politécnica de Madrid, Madrid, Spain

²Departamento de SSR, ETSI de Telecomunicación, Universidad Politécnica de Madrid, Madrid, Spain

Correspondence should be addressed to Ana González-Plaza; gonzalezplaza.ana@gmail.com

Received 3 November 2017; Revised 17 January 2018; Accepted 14 February 2018; Published 26 March 2018

Academic Editor: Eva Antonino-Daviu

Copyright © 2018 Ana González-Plaza et al. This is an open access article distributed under the Creative Commons Attribution License, which permits unrestricted use, distribution, and reproduction in any medium, provided the original work is properly cited.

The next generation of mobile communications, 5G, will provide a wideband network based on microwave and millimeter-wave (mmW) communication radio links with the goal of fulfilling the strict and severe requirements of the future test cases. In particular, this paper research is focused on mmW bands in metropolitan railway tunnels. For that purpose, a propagation measurement campaign was performed at 24 GHz band in a passenger train on a realist subway environment, and these results were combined with simulations ad hoc for tunnels and a theoretical modal propagation model. A narrowband and a wideband study have been conducted with the aim of obtaining the path loss, fading, power-delay profile, and angle of arrival, taking into consideration horizontal and vertical polarization in the receiving and transmitting antennas. This validation can be used to design and deploy wideband mobile communication networks at mmW bands in railway scenarios.

1. Introduction

The anticipated increase in demand for data traffic is one of the key requirements of the upcoming years in mobile communication technologies. The fifth generation (5G) aims to provide considerable broader bandwidths and a network capable of offering a flexible technology for very different cases studies [1].

In this context, 5G could be the most disruptive technology in railways since it can allow the addition of new services and applications that make railway a more efficient, safer, and profitable transportation option [2].

However, there are important challenges to overcome: The first one is to provide a wideband service for the plenty of passengers who will demand a large capacity. The second one is the critical signalling control applications which will require very high quality of service and moderate data rate to allow real-time applications such as high definition video for automatic driving and surveillance [3, 4].

In the case of signalling, current railway mobile communication systems such as GSM-R are not able to provide such ambitious features [5]. For this reason, LTE-R and

future 5G are being examined as new railway communication technologies. In the latter, 3GPP new radio (NR) system for 5G proposes a large spectrum solution from bands under 6 GHz to 100 GHz [6]. Among all, millimeter-wave (mmW) bands, particularly from 24 to 33 GHz, are considered as a suitable option to establish mobile communication services in high-speed scenarios. This band has been chosen because it is an industrial scientific and medical band (ISM), which can be used for railway communications. In fact, 28 and 37 GHz have been already licensed in the USA and 26 GHz band in China and Europe [7].

The study of electromagnetic field propagation in the different specific scenarios of the railway environment is a key prerequisite in order to succeed in the design and installation of these mobile communication systems. In this sense, mmW communications in tunnels offer some interesting features over lower frequency bands for communications in tunnels [8].

- (i) Electromagnetic discharges of catenary pulses, usual in tunnels, have little influence on millimeter-wave propagation.

- (ii) Losses produced by reflection and refraction of electromagnetic waves at mmWs are relatively small.
- (iii) Very wide bandwidth is available.
- (iv) Latency reduction is achieved.

Nevertheless, an assessment of the propagation channel is a mandatory requirement to ensure reliable communication links. For that reason, although there is already some literature on mmW measurements in tunnels at 30 GHz [9], 38 GHz [10], 60 GHz [11], and 240 GHz [12] bands, there are no measurements in a realistic railway environment.

This paper focused its research on the propagation at 24 GHz frequency band in realistic metropolitan railway tunnels. For that purpose, three methods have been applied. Firstly, a modal propagation model has been described and put into practice; then, a ray tracing (RT) simulator developed specially for propagation in tunnels has been employed; and, finally, measurements in a passenger train on a realist subway environment have been performed.

The goal of this study is to present an accurate path loss model at 24 GHz directly applicable to railway communication systems and to show meaningful results for wideband simulations to assess the possibility of using mmW for communication systems in metropolitan railway tunnels.

This analysis presents some results regarding the path loss and the fading, power-delay profile (PDP), and angle of arrival (AoA) along a tunnel, taking into account horizontal and vertical polarization in the receiving and transmitting antennas.

This document is organized as follows: firstly, in Section 2, a theoretical attenuation modal model and the 3D RT technique used by the simulator are explained; secondly, Section 3 describes *Raylway* simulation tool and the parameters configured for this experiment in the real environment and in the simulator; afterwards, in Section 4, all the results are enumerated: path loss model and K factor in Section 4.1 and PDP and AoA in Section 4.2; finally, Section 5 presents the conclusion obtained from all this work.

2. Modeling and Simulation of Guided Propagation in Tunnels

In the past, the modal theory has been widely applied to study the propagation in tunnels due to it provides suitable results. However, this method does not take into account the effect of arbitrary geometries in walls, roughness, discontinuities, among others. For that reason, nowadays, RT methods are employed to obtain more accurate propagation models [13].

2.1. Modal Analysis. Modal analysis is a classical technique for studying propagation channel in tunnels where there is waveguide effect. It is based on the concept that the signal attenuation in this kind of scenarios depends on the electromagnetic modes propagating within the tunnel. As the cross-section area of the tunnel is quite large in comparison to the signal wavelength, there are many modes propagating through this channel. Nevertheless, the modes suffer gradual extinction as they travel along the environment up to the

breakpoint, Z_{NF} , where the modes are sufficiently attenuated and it can be considered that only the first mode propagates.

$$Z_{\text{NF}} \approx \max\left(\frac{a^2}{\lambda}, \frac{b^2}{\lambda}\right), \quad (1)$$

where a and b are the horizontal and vertical dimension of the tunnel, respectively, and λ is the signal wavelength.

These two regions are defined as near-field and far-field regions. On the one hand, the near-field region represents the zone where the field amplitude suffers strong fading and fast losses obtained from the contribution of many rays propagating from different grazing angles with high losses. On the other hand, the far-field region is where the relation between the first mode and the rest is high enough to neglect the effect of the other modes.

As [14] explains in detail, the energy contained in the transmitted signal propagating through the tunnel is divided into several modes. Each of them is attenuated following different decay. The overall path loss can be simplified by considering that each mode has an independent power from the others. Therefore, the total received power is approximately the sum of all modes' power. This supposition is based on the fact that modes are closely orthogonal.

Assuming this situation, the loss expression of each mode can be approximated for horizontal and vertical polarization, $\alpha(m, n)^{h,v}$, considering the tunnel as a rectangular waveguide.

$$\alpha(m, n)^v = 4.343\lambda^2 \left(\frac{m^2}{a^3 \sqrt{\epsilon_{r_1} - 1}} + \frac{n^2 \epsilon_{r_2}}{b^3 \sqrt{\epsilon_{r_2} - 1}} \right), \quad (2)$$

$$\alpha(m, n)^h = 4.343\lambda^2 \left(\frac{m^2 \epsilon_{r_1}}{a^3 \sqrt{\epsilon_{r_1} - 1}} + \frac{n^2}{b^3 \sqrt{\epsilon_{r_2} - 1}} \right),$$

where $\alpha(m, n)^{v,h}$ are the attenuation of each mode in dB/km in vertical (v) and horizontal (h) polarization for the m, n th mode; ϵ_{r_1, r_2} are the relative permittivity of the vertical and horizontal walls, respectively. This model can be also applied to arched tunnels by adjusting the cross-section dimensions [15].

As the equations in (2) show, tunnels dimensions are directly related to the attenuation that every mode suffers. Thus, the greater the tunnel cross-section is, the smaller the attenuation experienced by the modes is. This is because losses are inversely proportional to the cube of tunnels height and width.

With this propagation constant, the overall attenuation for both polarization directions, $L_{mn}^{v,h}$, at a certain distance, (z), considering losses as the rms contribution of modes for both polarization directions is the following:

$$L_{mn}^v(z) = 10 \log_{10} \left[\sum_{n=1}^M \sum_{m=1}^N 10^{(10 \log_{10}(z) + \alpha(m, n)^v)/10} \right], \quad (3)$$

$$L_{mn}^h(z) = 10 \log_{10} \left[\sum_{n=1}^M \sum_{m=1}^N 10^{(10 \log_{10}(z) + \alpha(m, n)^h)/10} \right],$$

where M and N are the last modes taken into account.

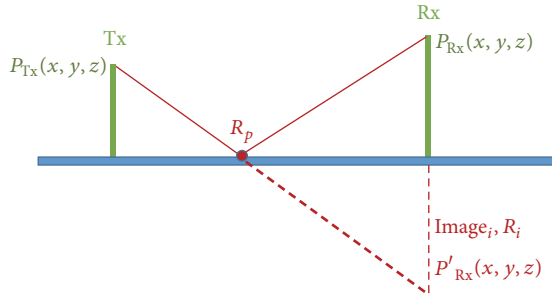


FIGURE 1: The image method. R_i with respect to the ground plane.

In addition to this, losses are directly proportional to the square of the order of the modes, so that higher modes experience stronger attenuation. In fact, we can consider that, from a certain distance, all high order modes have been extinguished and only the fundamentals remain.

However, the modal propagation model does not take into account tilt losses, which are more important in semicircular tunnels and must be adjusted carefully for each tunnel, or wall roughness in tunnels, which might produce scattering of the signal. That is why simulations using RT technique are performed to obtain more accurate results.

2.2. Ray Tracing Technique. This simulator uses the novel technique of 3D ray tracing which is based on a geometrical optics method to compute the propagation channel of the modeled environment. It is an accurate and versatile propagation prediction tool for different kind of scenarios [16]. It uses a deterministic channel model which requires an exact knowledge of the geometrical and electromagnetic description of the environment. For that reason, the accuracy of RT comes up with a high computational complexity, which directly scales with the number of propagation paths considered. Nevertheless, it has great advantages as, on the one hand, it allows really detailed modeling, and, on the other hand, with this technique, it is possible to calculate wideband information such as PDP or AoA of the rays.

Tunnels are modeled as a triangular solid mesh made of different materials whose dielectric properties are defined according to the carrier frequency. As this is a 3D RT, reflections on the ceiling and ground are taken into account. This provides more accurate prediction results compared with conventional 2D models.

Using the images method, reflections are calculated in order to obtain the propagation paths. This method consists of basically converting an electric field into an equivalent one easier to compute. In certain cases, it is possible to replace a conductor with one or more point loads. Thus, conductor surfaces are replaced by equipotential surfaces with equivalent potentials.

As Figure 1 shows, having the location of Tx and Rx, the reflection point, R_p , coincides with the intersection between the obstacle and the segment joining the Tx with the image of the receiver, R_i . Therefore, the ray follows a straight line from Tx to R_p and, then, another straight line from R_p to Rx. It is possible to extend this method to obtain the paths with

multiple reflections. Finally, the received signal, E_r , is the sum of all the rays that arrived at Rx, as follows:

$$E_r = \left| \sum_i E_i(d = d_{rx}) \right|, \quad (4)$$

$$E_i(d) = E_0 \rho_{tx} \rho_{rx} L_i(d) \prod_p^N [\Gamma(\phi_{pi}) T(\phi_{pi})] e^{-j2\pi d/\lambda},$$

where $E_i(d)$ is the i th ray electric field along the distance; d_{rx} is the distance between the transmitter and the receiver; E_0 is the amplitude of the electromagnetic field; ρ_{tx} and ρ_{rx} are the radiation pattern of the transmitter and receiver antenna, respectively; $L_i(d)$ is the path losses for i th ray component at a distance d ; $\Gamma(\phi_{ji})$ and $T(\phi_{pi})$ are the reflection and transmission coefficient of the p th reflection of the i th component, respectively; N is the maximum reflections taken into account; and $e^{-j2\pi d/\lambda}$ is the phase factor due to the travelled distance.

Besides, this simulator calculates the power-delay profile which is a temporal representation of the pulse widening. The instantaneous impulse response [17], $h(t, \tau)$, is function of the time, t , and the propagation delay, τ . The power-delay profile, PDP(τ), is described by (5) when the channel satisfies the wide sense stationary uncorrelated scattering assumption [18].

$$\text{PDP}(\tau) = \langle |h(\tau, t)|^2 \rangle. \quad (5)$$

Lastly, the angle of arrival is a method for obtaining the propagation direction of a radio-frequency wave incident on a virtual array antenna. The direction is determined by measuring the received signal in each of the elements of the virtual array. This difference in phase is measured by receiver nodes R, A_1 , as follows:

$$\Delta\varphi = \frac{2\pi}{\lambda} (d_{RA_2} + d_{A_1A_2} + d_{TA_1} - d_{TR}), \quad (6)$$

where R is the receiver position with its separated virtual elements A_1 and A_2 and T represents the position of the transmitter.

Hence, the use of 3D-RT technique allows the detailed study of the behavior of wideband channel.

3. Simulation and Measurement Set-Up

3.1. Simulation Tool. Simulations are performed using *Raylaw: Radio Propagation Simulator for Tunnels* tool, which calculates the radio signal propagation along different tunnel environments. The software, developed in Java and Matlab, allows the user to design and set up the tunnel in order to analyze the propagation in a specific environment. Correspondingly, *Raylaw* software brings the received power, the power-delay profile, and the angle of arrival.

This simulator allows users to set up several parameters in order to obtain results according to the tunnel under study:

- (i) tunnel: definition of the different cross-section types plus their shape and the longitudinal section and wall material properties;

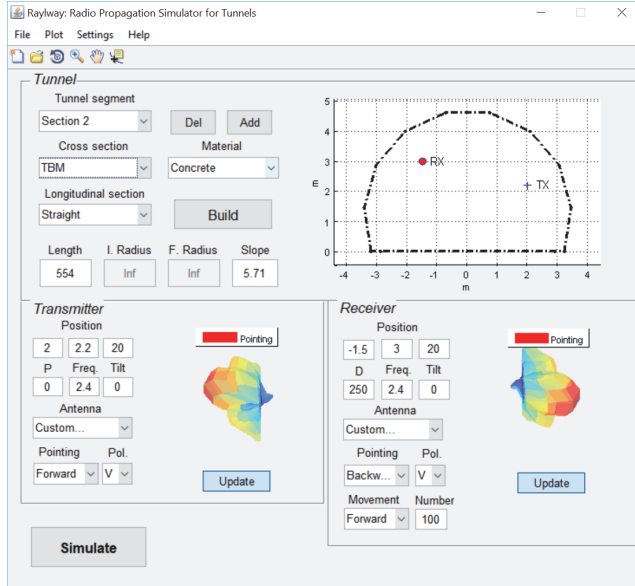


FIGURE 2: Simulator user interface with set-up parameters.

- (ii) transmitter: initial fixed position, frequency, and transmitted power;
- (iii) receiver: initial position, frequency, and distance travelled;
- (iv) antennas: radiation pattern of each antenna, polarization, and relative position between them;
- (v) simulation settings: number of simulation points, maximum number of each ray reflections, and possibility of enabling diffraction.

3.2. Simulation Set-Up. *Raylway* user interface is presented in Figure 2 where the set-up parameters are shown, in this case, for vertical polarization; however, except the polarization, the same values are maintained for the horizontal polarization. The resulting set-up simulation scenario is shown in Figure 4.

3.3. Measurement Set-Up. In this section, the measurement set-up in a realistic subway tunnel is explained in detail.

This experiment was conducted in a subway tunnel of Metro de Madrid. Figure 3(b) illustrates the scenario with its more important elements. The set-up parameters are enumerated in Table 1.

On the one hand, the transmitter (Tx) is situated in a fixed position between one station and the tunnel; on the other hand, the moving receiver (Rx) module is located on the windshield of the train. The same antenna model is used in the Tx and Rx equipment. It is a horn antenna of Vector Telecom with model number VT260SGAH15 [19] which covers the frequency range from 21.7 GHz to 33 GHz. Its radiation pattern provided at 23.96 GHz is shown in Figure 5. The gain is a 15.2 dBi and the half power beamwidth is 28.3° in *E*-plane and 27.9° in *H*-plane.

The tunnel has an arched type tunnel which can be approximately modeled as an equivalent rectangular cross-section since there is a slight adaptation of the dimensions,

TABLE 1: Set-up parameters.

Frequency	24.2 GHz
Transmitted power	5.4 dBm
Tx signal	Continuous wave
Tx and Rx antenna	Horn antenna, 15.2 dBi
HPBW antenna	<i>E</i> -plane 28.3° <i>H</i> -plane 27.9°
Antenna polarization	Horizontal and vertical
Tunnel cross-section	Arched
Tunnel dimensions	6.9 m × 4.9 m
Train speed	5 km/h

according to [15]. To apply the modal propagation model described in Section 2.1, in this case, the dimensions are 6.9 m × 4.9 m with a radius of 2.2 m, as Figure 3(a) shows. The assessed route follows a straight line of 350 m with a minor slope of 5.7‰. The point 0 represents where the Tx is situated.

This train moves along the railway up to 350 m at a constant speed of 5 km/h.

4. Results

In this section, both modal analyses and RT technique together with measurement conducted in a real metropolitan railway tunnel are applied with the aim of assessing the propagation in this particular environment at 24 GHz band.

The analysis is focused on the path loss model, fast-fading, power-delay profile, and angle of arrival.

4.1. Narrowband Analysis. This section provides a comparison between measurements, simulation, and modal propagation model for vertical and horizontal polarization. For that purpose, two experiments were performed: the first one with vertical polarization in both antennas and the second one with horizontal polarization. The train follows the exact same route in both experiments; likewise, two simulations were performed with the different polarization directions; and, finally, the theoretical modal losses are shown in order to compare these different approaches.

4.1.1. Path Loss Model. The attenuation suffered by a signal can be described through a path loss model defined by (7). The main parameters are derived from the following measurements conducted in a real environment:

$$A(d) = A(d_0) + 10n \log\left(\frac{d}{d_0}\right) + \chi_\sigma, \quad (7)$$

where $A(d_0)$ is attenuation in a reference distance d_0 , n represents the loss exponent, and χ_σ denotes a zero-mean random variable of standard deviation σ which follows a Gaussian distribution.

Figure 6 presents the received power of the empirical data, the simulation result, the theoretical modal model, and the resulting path loss model for the vertical, Figure 6(a), and horizontal, Figure 6(b), experiments, respectively.

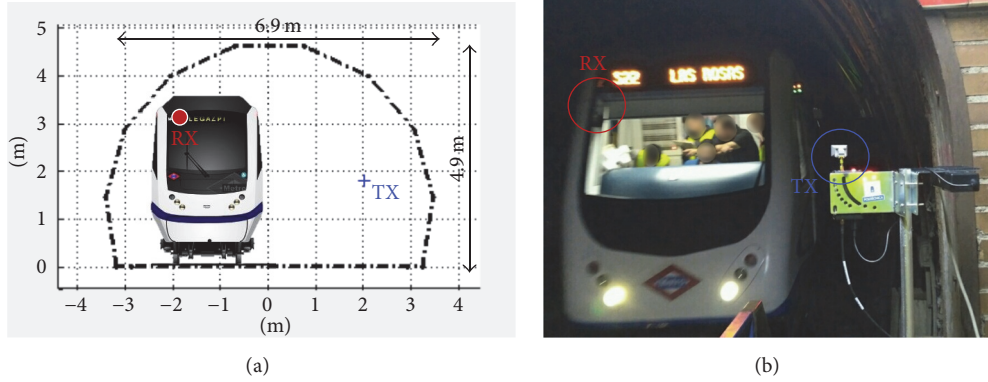


FIGURE 3: (a) Tunnel cross-section dimensions and shape. (b) Measurement scenario: fixed position of Tx at the beginning of the tunnel and moving Rx at the windshield of the train.

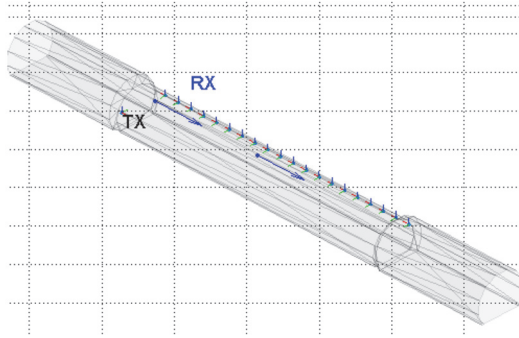


FIGURE 4: Simulation set-up scenario with fixed Tx (in black) and moving Rx (in blue).

Since the antennas are highly directive, as Figure 5 shows, the losses caused by the misalignment of the antenna are very high for distances lower than 20 m. In addition to that, RT simulations have a strong dependency of the number of reflections for short distances. Hence, the simulation results are not accurate and the first 20 m has been removed from Figure 6.

In both experiments, the measurements expose a loss exponent, n , equal to 1.3 approximately, which is lower than the decay of the free space. Besides, as [20, 21] explains, regardless the type of tunnel, loss exponents are always lower than the free space. This is due to waveguide effect produced in tunnels.

The curve obtained from the modal analysis presents a similar attenuation since the loss exponents are 1 for vertical and 1.1 for horizontal polarization. This shows a significant effect of the modal propagation. Likewise, simulation results are slightly greater than the one acquired by the measurements since the loss exponent is 1.8 for vertical and 1.9 for horizontal polarization. These results are summarized in Table 2.

The differences between models may be produced because, on the one hand, in the modal model just the losses caused by the reflections are taken into account, and, on the other hand, in the case of the RT simulations, the maximum

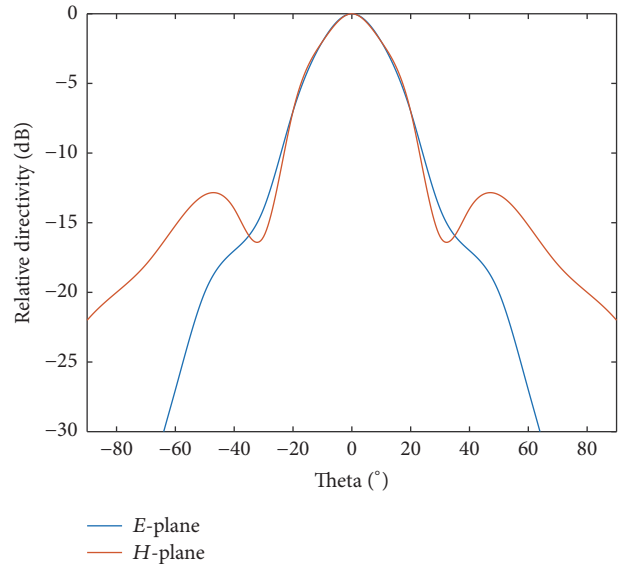


FIGURE 5: Horn antenna radiation pattern.

TABLE 2: Path loss model parameters at the vertical and horizontal polarization directions.

	Vertical	Horizontal
Ref. attenuation, $A(d_0)$	64.8 dB	62.9 dB
Measurement n	1.28	1.29
Simulation n	1.8	1.9
Modal propagation model n	1	1.1
Measurement χ_σ	1.4 dB	1.3 dB
Simulation χ_σ	1.2 dB	0.9 dB

The attenuation is at the reference point, d_0 , of 20 m. $A(d_0)$ is referred to the parameters in (7), as n and χ_σ .

number of reflections used is limited to six which seems to be not enough to calculate a more accurate model; nevertheless, after some distance, the results converge when the reflections are high enough, as Figure 7 shows.

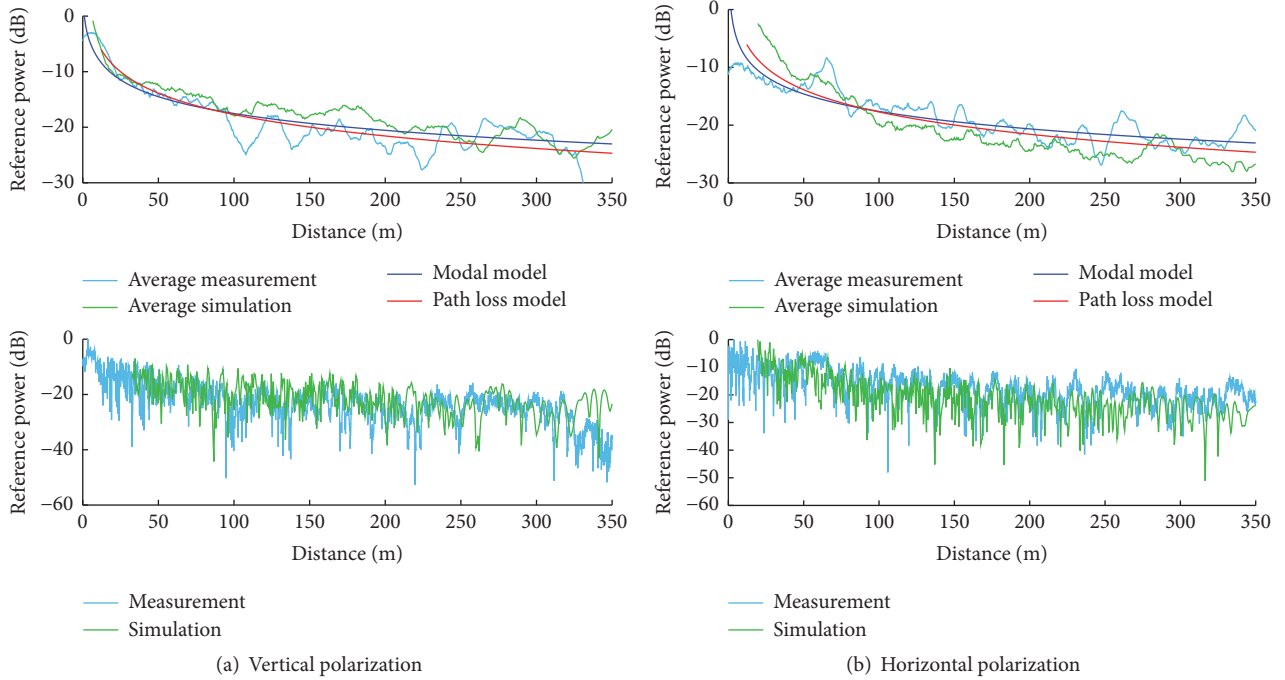


FIGURE 6: Comparison between measurements, simulation, and modal model for vertical and horizontal polarization.

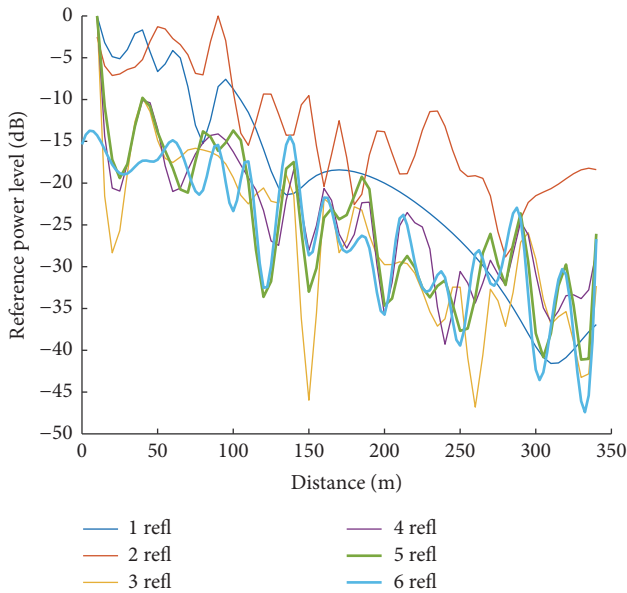


FIGURE 7: RT Simulation results for different number of each ray's reflections.

Nevertheless, in all the cases, the loss exponents are lower than those in the free space which show a clear waveguide effect. This is because the electromagnetic waves are repeatedly reflected in the tunnel's walls. As concrete is made of conductor materials (among others) the reflection coefficient is high. For that reason, the waves are confined to the dielectric by almost total internal reflection at its surface.

At mmW bands, a large number of modes are propagated through the tunnel. Particularly at 24.2 GHz, according to rectangular waveguide theory cut-off frequencies, modes up to m and n equal to 1246 and 1877, respectively, travel down the tunnel.

For that reason, the breakpoint, where most of them are sufficiently extinguished, is located at a few hundred meters in lower frequencies (from 1 to 6 GHz) [14]. However, at 24.2 GHz, it is at 8 km which means that theoretically the route is fully situated in the waveguide region.

The polarization seems to be independent of the loss exponent since it does not show a substantial difference in any of the cases. As Table 2 shows, this also holds true for the shadowing whose standard deviation is closely equal in both polarization directions.

The effect of the slope reveals an interesting difference in both polarization directions. There is a slope of 5.7%. Thus, focusing on the average of the last 50 m where this slope has its major effect, there are greater losses in vertical polarization. This result is noticed in the simulations and in the measurements. It may be due to, firstly, the general misalignment of both antennas, which is analyzed in Section 4.2, and, secondly, the fact that this effect is more notable in vertical polarization since these antennas present higher directivity in elevation than in azimuth.

Regarding the reference attenuation, $A(d_0)$, there is a slight difference between polarization directions. In the case of horizontal polarization, there are 2 dB more than in vertical. This is related to the tunnel dimensions that are directly connected to the effect of polarization in the antennas. When tunnel presents larger width than its height, higher reflection coefficients appear in vertical polarization. Lower attenuation

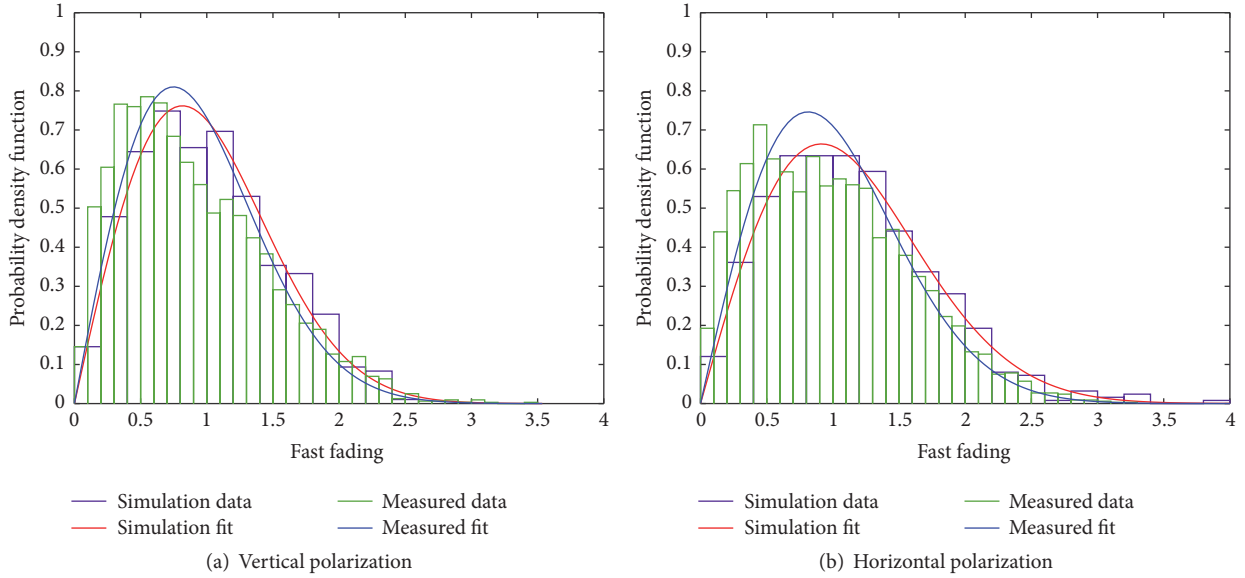


FIGURE 8: Comparison between measurements and simulation of the fast-fading probability density function.

comes out for the case of horizontal polarization. This effect is more significant in short distances. As [22] explains, in tunnels where there is a perfectly square cross-section, the result of vertical and horizontal polarization will be exactly the same.

4.1.2. Fast Fading. In this section, an analysis of the fast fading is shown. The results for vertical and horizontal polarization are described in Figure 8. A comparison between the measurements and simulations are made.

Rician distribution, $P_r(r)$, is a statistical model which better describes the fast-fading effect in an environment where there are LoS conditions.

$$P_r(r) = \frac{r}{\sigma^2} e^{-(r^2+A^2)/2\sigma^2} I_0 \frac{rA}{\sigma^2}, \quad (8)$$

where r is a random variable; σ is the standard deviation; and K factor, represented in (9), is the relation between LoS component, A , and multipath component.

$$K = 10 \log \left(\frac{A^2}{2\sigma^2} \right). \quad (9)$$

At this frequency, as Table 3 enumerates, the channel varies considerably fast independently of the experiment since the wavelength is small, 12.4 mm.

As Figure 6 shows, there are peaks up to 25 dB of attenuation in both cases. Horizontal polarization shows greater immunity to the shadowing, despite an insignificant impact on the fast fading compared to the vertical polarization.

Nevertheless, overall, fast fading has a major effect on the signal, as Figure 8 shows. This occurs when the coherence time of the channel is small relatively to the delay requirement of the application. In this case, the amplitude and phase change imposed by the channel vary considerably over the period of use.

TABLE 3: Fast-fading modeled with a Rician distribution at the vertical and horizontal polarization directions.

	Vertical	Horizontal
K factor measurements	2.62 dB	2.62 dB
K factor simulation	2.79 dB	2.62 dB
Std measurements	0.55	0.59
Std simulation	0.52	0.61

Regarding the K factor, the three scenarios present similar results. The relation between LoS and the multipath component is very low. This is because, as it was described in previous sections, the waveguide effect allows the propagation of a high number of modes at this frequency. As a result, the received signal is essential for not only the LoS component, but also the sum of all the reflected signals along the tunnel.

4.2. Wideband Analysis. This RT based simulator is used to acquire PDPs and AoAs whose information is helpful to understand the wideband channel. In this particular case, the data obtained from the measurements in narrowband are used to parametrize the needed values in the simulator in the wideband analysis.

4.2.1. Power-Delay Profile. The PDPs, in Figure 9(a), reveal that the energy is almost equally divided between LoS and the reflections since the power of these rays has slightly lower power than the one coming from the direct path. This is fully coherent with K factor resulting from the Rician distribution obtained in Section 4.1.2.

Besides, there is a clear decrease in the delay spread when the distance between Tx and Rx raises. This is connected with the great attenuation of the higher modes along the tunnel.

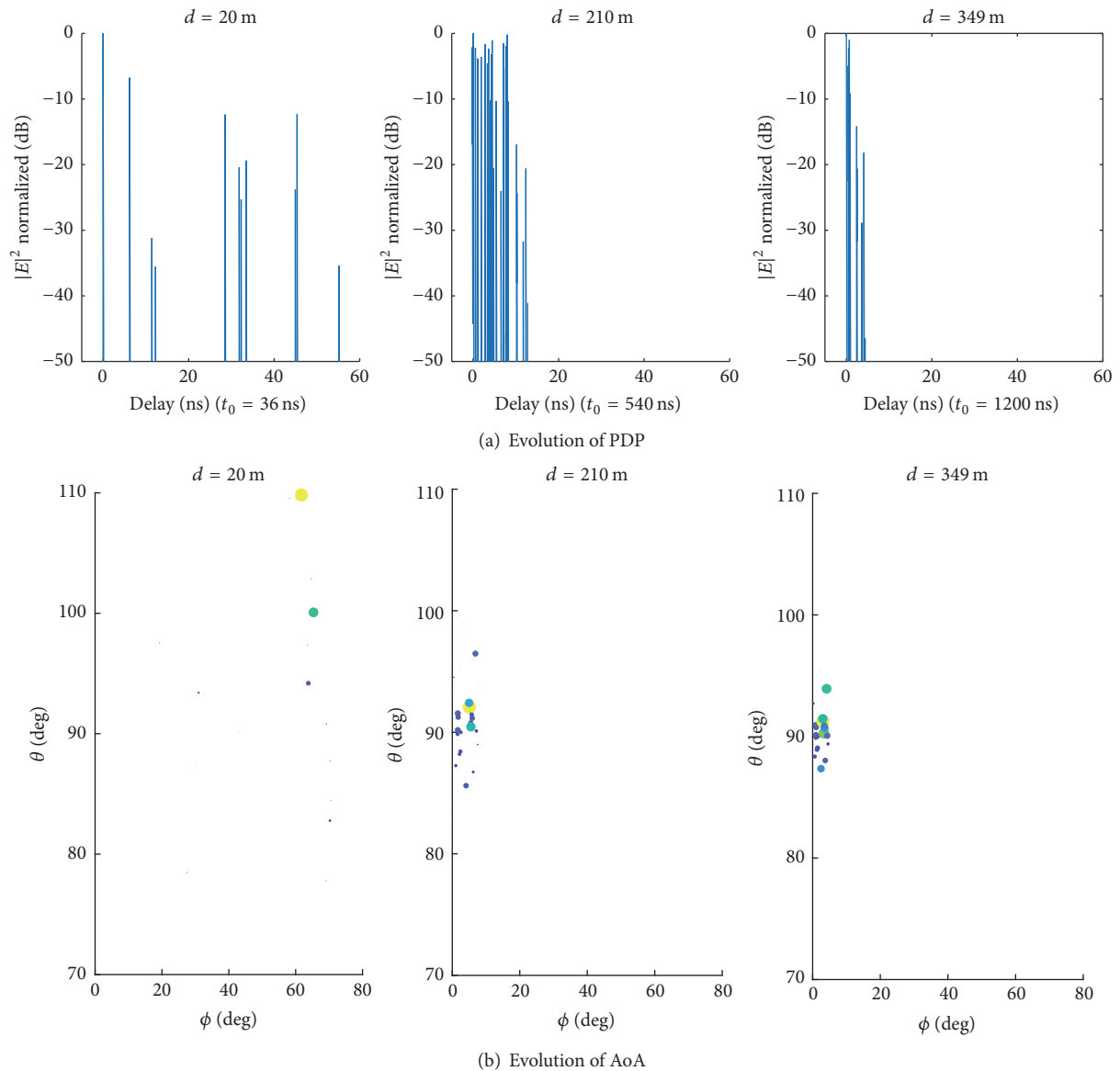


FIGURE 9: Simulation results for (a) PDP and (b) AoA along the distance.

In short distances, as there is an extensive spread of the pulse, signals may be damaged by intersymbol interference.

4.2.2. Angle of Arrival. The AoA, in Figure 9(b), shows also the decrease in the delay spread as Rx moves away from Tx. There is no ray coming from the negative axis of ϕ since the horn antenna is directive and the front-to-back ratio is very high, as Figure 5 shows. Besides, all the rays come from the right side of the Rx, which is reasonable as there is misalignment of the antennas imposed by the set-up itself.

On the other side, when the antennas are close, most of the signals arrive from the back side of the antenna, but, when the antennas are sufficiently separated, the different rays are reduced until all the energy is fully concentrated in a single ray.

Considering the shape of the PDP obtained from simulations and the AoA of the rays, it can be assumed that the Doppler spectrum follows an asymmetric Jakes type [23]. It will change from moderate to strong asymmetry when the distance to the transmitter increases, according to [24]. The maximum Doppler deviation for this frequency, considering a 120 km/h speed of trains, would be ± 9.68 kHz.

5. Conclusion

In this paper, a narrowband and a wideband study have been performed for mmW band propagation in subway tunnels on metropolitan railways.

The narrowband analysis takes into account several approaches: measurements, simulations, and a modal propagation model. By combining these techniques, an accurate

path loss model is obtained. It is clear that there is a considerable lower loss exponent in comparison to the Friis formula since the measurements show a loss exponent of 1.3 in the tunnel. Regarding the simulations, although some limitations have been found when the maximum reflections of each ray are not enough, this inaccuracy is gradually reduced in accordance with the distance as the modes are becoming weaker and, as a result, fewer rays are necessary to represent more precisely the path loss.

The wideband analysis, based on the PDP and the AoA, reveals that the delay spread decreases as Rx moves away from Tx. This is an important result which, once again, highlights that higher modes extinguish faster than the lower ones. For that reason, the behavior of wideband channel improves with the distance to the transmitter.

Finally, an important remark is that there is the absence of published measurement on propagation at mmW frequencies in real subway tunnels, and this paper validates the possibility of using mmW frequency bands for communications in metropolitan railway tunnels.

Conflicts of Interest

The authors declare that there are no conflicts of interest regarding the publication of this paper.

Acknowledgments

This work was developed under the framework of ENABLING 5G TEC2014-55735-C3-2-R funded by the Spanish Ministry of Economy and Competitiveness and also funded by the Chinese Strategic International Cooperative Project of National key R&D Plan, 2016YFE0200200.

References

- [1] S. Chen, J. Hu, Y. Shi et al., "Vehicle-to-everything (v2x) services supported by LTE-based systems and 5G," *IEEE Communications Standards Magazine*, vol. 1, no. 2, pp. 70–76, 2017.
- [2] J. Moreno, J. Riera, L. De Haro, and C. Rodriguez, "A survey on future railway radio communications services: challenges and opportunities," *IEEE Communications Magazine*, vol. 53, no. 10, pp. 62–68, 2015.
- [3] A. Gonzalez-Plaza, J. Moreno, I. Val et al., "5G communications in high speed and metropolitan railways," in *Proceedings of the 11th European Conference on Antennas and Propagation, EUCAP 2017*, pp. 658–660, France, March 2017.
- [4] L. Zhang, A. Gonzalez-Plaza, J. R. Fernandez et al., "Propagation measurements and modelling inside trains at 900 MHz, 2.4 and 5.8GHz," in *Proceedings of the 11th European Conference on Antennas and Propagation, EUCAP 2017*, pp. 2895–2898, France, March 2017.
- [5] A. Arriola, P. M. Rodriguez, I. Val et al., "Characterization of an Outdoor-to-Indoor wireless link in metro environments at 2.6 GHz," in *Proceedings of the 15th International Conference on ITS Telecommunications, ITST 2017*, Poland, May 2017.
- [6] T. Rosowski, "5G spectrum scenarios, requirements and technical aspects for bands above 6 GHz, 2016," https://metis-ii.5g-ppp.eu/wp-content/uploads/deliverables/METIS-II_D3.1.V1.0.pdf.
- [7] J. Barrett, "Global mobile Suppliers Association, 2017," <https://gsacom.com/5g-spectrum-bands/>.
- [8] X. Yang and Y. Lu, "Propagation characteristics of millimeter wave in circular tunnels," in *Proceedings of the 2006 7th International Symposium on Antennas, Propagation & EM Theory*, pp. 1–5, Guilin, China, October 2006.
- [9] S.-W. Choi, H.-S. Chung, D.-S. Cho et al., "Performance evaluation of millimeter-wave-based communication system in tunnels," in *Proceedings of the IEEE Globecom Workshops, GC Wkshps 2015*, USA, December 2015.
- [10] W. Hui, Z. Guoxin, and J. Minghua, "The measurements and simulations of millimeter wave propagation at 38ghz in circular subway tunnels," in *Proceedings of the 2008 China-Japan Joint Microwave Conference, CJMW 2008*, pp. 51–54, China, September 2008.
- [11] N. Prediger and A. Plattner, "Propagation measurements at 60 GHz in railroad tunnels," in *Proceedings of the IEEE/MTT-S International Microwave Symposium - MTT '94*, pp. 1085–1087, San Diego, CA, USA.
- [12] J. Antes, F. Boes, T. Messinger et al., "Multi-gigabit millimeter-wave wireless communication in realistic transmission environments," *IEEE Transactions on Terahertz Science and Technology*, vol. 5, no. 6, pp. 1078–1087, 2015.
- [13] C. Zhou, "Ray tracing and modal methods for modeling radio propagation in tunnels with rough walls," *IEEE Transactions on Antennas and Propagation*, vol. 65, no. 5, pp. 2624–2634, 2017.
- [14] C. Briso-Rodriguez, J. M. Cruz, and J. I. Alonso, "Measurements and modeling of distributed antenna systems in railway tunnels," *IEEE Transactions on Vehicular Technology*, vol. 56, no. 5, pp. 2870–2879, 2007.
- [15] C.-S. Zhang and L.-F. Guo, "Research on propagation characteristics of electromagnetic wave in tunnels with arbitrary cross sections," in *Proceedings of the 2010 2nd International Conference on Future Computer and Communication, ICFCC 2010*, pp. V122–V125, China, May 2010.
- [16] C. Zhou and R. Jacksha, "Modeling and measurement of radio propagation in tunnel environments," *IEEE Antennas and Wireless Propagation Letters*, vol. 16, pp. 141–144, 2017.
- [17] M. Jia and J. Zhao, "A novel method to predict the wideband characteristics of MMW propagation in tunnels," in *Proceedings of the 7th International Conference on Wireless Communications, Networking and Mobile Computing, WiCOM 2011*, China, September 2011.
- [18] I. Val, A. Arriola, P. M. Rodriguez et al., "Wireless channel measurements and modeling for TCMS communications in metro environments," in *Proceedings of the 11th European Conference on Antennas and Propagation, EUCAP 2017*, pp. 108–112, France, March 2017.
- [19] Vector Telecom, "A global supplier of microwave components, assemblies and antenna systems, 2017," <http://www.vectortele.com/>.
- [20] K. Guan, B. Ai, Z. Zhong et al., "Measurements and analysis of large-scale fading characteristics in curved subway tunnels at 920 MHz, 2400 MHz, and 5705 MHz," *IEEE Transactions on Intelligent Transportation Systems*, vol. 16, no. 5, pp. 2393–2405, 2015.
- [21] A. Hrovat, G. Kandus, and T. Javornik, "A survey of radio propagation modeling for tunnels," *IEEE Communications Surveys & Tutorials*, vol. 16, no. 2, pp. 658–669, 2014.
- [22] S. Bashir, "Effect of antenna position and polarization on UWB propagation channel in underground mines and tunnels," *IEEE*

Transactions on Antennas and Propagation, vol. 62, no. 9, pp. 4771–4779, 2014.

- [23] X. Zhao, J. Kivinen, P. Vainikainen, and K. Skog, “Characterization of doppler spectra for mobile communications at 5.3 GHz,” *IEEE Transactions on Vehicular Technology*, vol. 52, no. 1, pp. 14–23, 2003.
- [24] X. Chen, Y. Pan, Y. Wu, and G. Zheng, “Research on Doppler spread of multipath channel in subway tunnel,” in *Proceedings of the 2014 IEEE International Conference on Communication Problem-Solving, ICCP 2014*, pp. 56–59, China, December 2014.

Research Article

Modeling and Analysis of Safety Messages Propagation in Platoon-Based Vehicular Cyber-Physical Systems

Liqiang Qiao,¹ Yan Shi ,¹ Shanzhi Chen,² and Wei Gao¹

¹State Key Laboratory of Networking and Switching Technology, Beijing University of Posts and Telecommunications, Beijing 100876, China

²State Key Laboratory of Wireless Mobile Communications, China Academy of Telecommunications Technology, Beijing 100083, China

Correspondence should be addressed to Yan Shi; shiyan@bupt.edu.cn

Received 3 November 2017; Accepted 10 January 2018; Published 8 February 2018

Academic Editor: Hongwei Wang

Copyright © 2018 Liqiang Qiao et al. This is an open access article distributed under the Creative Commons Attribution License, which permits unrestricted use, distribution, and reproduction in any medium, provided the original work is properly cited.

Safety messages propagation is the major task for Vehicular Cyber-Physical Systems in order to improve the safety of roads and passengers. However, reducing traffic and car accidents can only be achieved by disseminating safety messages in a timely manner with high reliability. Although mathematical modeling of the delay of safety messages is extremely beneficial, analyzing the safety messages propagation is considerably complex due to the high dynamics of vehicles. Moreover, most previous works assume vehicles drive independently and the interaction between vehicles is not taken into consideration. In this paper, we proposed an analytical model to describe the performance of safety messages propagation in the VCPSs under platoon-based driving pattern. Infrastructure-less and RSU-supported scenarios are evaluated independently. The analytical model also takes into account different transmission situations and various system parameters, such as communication range, traffic flow, and platoon size. The effectiveness of the analytical model is verified through simulation and the impacts of different parameters on the expected transmission delay are investigated. The results will help determine the system design parameters to satisfy the delay requirement for safety applications in VCPSs.

1. Introduction

Vehicular Cyber-Physical Systems (VCPSs), which take advantage of the latest advances in communication, computing, sensing, control, and so on, have attracted the attention of many researchers, for the great potential of providing different applications, such as safety-related services, traffic information services, and entertainment services [1–5]. In a typical VCPS, moving vehicles are all equipped with various sensors to collect the up-to-date information about the road and disseminate the collected information to all neighbor vehicles in order to avoid the traffic jam, reduce car accidents, and save fuel consumption [6]. Generally, a platoon-based VCPS consists of two main processes: the platoon mobility process which describes the platoon mobility pattern under a control strategy and the communication process that generalizes the communication request of VCPSs applications [7]. VCPSs can support both ad hoc and infrastructure-based communications [8]. Particularly, vehicles on the road can

communicate with each other through a direct and indirect multihop ad hoc connection. In addition, these vehicles can also communicate with roadside units (RSUs) deployed in the road, which provide Internet access and real-time data services to passing vehicles.

Among the vast array of potential applications, safety messages propagation has been the major task of VCPSs. The majority of the VCPSs safety applications require that each vehicle broadcasts safety messages to all the surrounding vehicles. There are two main types of safety messages broadcast by each vehicle, namely, beacon and event-driven message [9, 10]. The former is automatically sent by each vehicle at regular intervals to inform others about its current position, speed, and direction of movement. The latter is broadcast by certain vehicles only in case of an unexpected event. When on-board sensors detect an accident or a sudden brake, the vehicle immediately generates an emergency message and broadcasts it to the following vehicles to notify other drivers before they reach the potential danger zone. A relatively small

reduction in the driver's reaction time may potentially avoid the trigger of an accident. Thus, message transmission delay is a main quality-of-service (QoS) metric for safety application in VCPSs. However, data communication in VCPSs is a challenging task due to the highly dynamic network topology and intermittent connectivity caused by the high mobility and speed of vehicles [11–14].

Recently, several works have been conducted to study the safety messages propagation in VCPSs [15–18]. Zhou et al. [15] proposed an analytical model to investigate the safety message propagation process and derived the probability of delivering safety messages to all neighbor vehicles for different traffic condition. Wang et al. [16] derived a mathematical model to describe the relationship between the average delay and the deployment distance between two neighbor RSUs. In [17], the authors analyzed the safety messages delivery delay with general store-carry-forward mechanism and decelerating store-carry-forward mechanism, respectively. Li et al. [18] analyzed the delay of multihop safety message broadcast by taking propagation distance, distribution of vehicles, vehicle density, and minimum safe distance between vehicles into consideration. However, these theoretical analyses are useful to understand the safety message propagation delay in VCPSs. The main limitation of these works is that they usually assume vehicles drive in free traffic state, that is, each vehicle moves independently at constant velocity, and the interaction between vehicles is seldom taken into consideration.

In practice, vehicles that move in the same direction with close space can naturally be grouped into a platoon. Platoon-based driving pattern in highway is regarded as a promising driving manner. To the best of our knowledge, there is no equivalent investigation on the performance of safety messages propagation in the VCPSs under platoon-based driving pattern. Therefore, the main purpose of this work is to analyze and provide quantitative insights into the expected transmission delay of safety messages based on platoon driving pattern. The major contributions of this paper are summarized as follows:

- (i) We develop an analytical model for safety messages propagation in a dynamic network formed over vehicles traveling in opposing direction. The model captures the platoon mobility characteristics of vehicles. Under the model, we derive the expected transmission delay of safety messages under infrastructure-less and RSU-supported scenarios.
- (ii) The analytical model takes into account different transmission cases and various system parameters, such as communication range, traffic flow, and platoon size. The effectiveness of the mathematical model is verified, and the impacts of different parameters on the expected transmission delay are investigated through simulation results.
- (iii) The derived mathematical model can be used to estimate the safety message transmission delay, which will help determine the system design parameters to satisfy the delay requirement for safety applications in VCPSs.

The rest of the paper is organized as follows: The scenario and necessary assumptions are introduced in Section 3. The analysis of safety messages propagation delay in an infrastructure-less scenario is derived in Section 4. With the help of RSUs, the delay of safety messages propagation will be discussed in Section 5. Numerical and simulation results are shown in Section 6. The last section is for a brief summary.

2. Related Works

In the literature, several works have been conducted on how to improve the communication quality of safety messages propagation in various aspects, including the network connectivity, medium access control (MAC), and routing protocols. Network connectivity is a fundamental requirement of safety messages propagation in VCPSs. The authors in [19] developed an analytical model with a general radio channel to fully characterise the access probability and connectivity probability in a vehicular relay network. The empirical studies [20, 21] have investigated the instantaneous network connectivity and the impacts of vehicles mobility on the connectivity. Efficient and scalable medium access control (MAC) protocol is crucial to guarantee the reliable broadcast of safety messages in VCPSs. A MAC protocol named VeMAC is proposed in [22] which supports a reliable one-hop broadcast service for safety applications in VCPSs. They also analyzed the total delivery delay of VeMAC for periodic and event-driven safety messages. Lyu et al. [23] designed a novel time slot-sharing MAC, named SS-MAC, to support diverse beacon rates for safety applications in VCPSs. Suthaputchakun et al. [24] introduced a mini-distributed interframe (DIFS) in the MAC protocol to give the safety message a higher access priority and selected the farthest possible vehicle to perform forwarding to increase the dissemination speed by reducing the number of forwarding hops.

From the perspective of routing, an efficient broadcast protocol called Density-aware Emergency message Extension Protocol (DEEP) is proposed in [25]. Different vehicles are given different forwarding priorities by segmenting roads into multiple blocks according to vehicle density. Binary partition approach is used in the forward node selection process to improve the efficiency of broadcast by reducing the delay incurred before choosing the relay node in each hop in [26]. Wu et al. [27] used fuzzy logic algorithm to choose the best relay node by taking intervehicle distance, vehicle velocity, and link quality into account. To lower safety message transmission delay and reduce message redundancy, Bi et al. [28] utilized iterative partition, mini-slot, and black-burst to quickly select forwarding node. Although these works are useful to improve the performance of safety messages propagation, they mainly focus on the design of broadcast protocol, so as to make safety messages be received by other relevance vehicles with low dissemination delay and high reliability.

Other works have developed analytical models studying safety messages propagation in VCPS. In [29], Abboud and Zhuang developed a mathematical model to compute the total delay in emergency message broadcasting based on the traffic flow theory for three traffic flow levels (high,

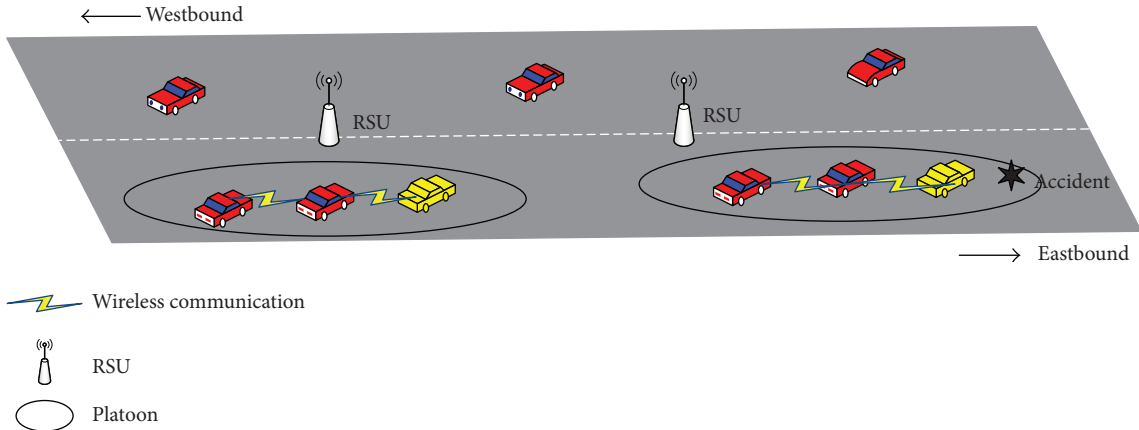


FIGURE 1: Network scenario.

medium, and low). The impact of two different network parameters on the communication delay in infrastructure-less highway scenarios was studied in [30]. A time/location-critical framework for emergency message dissemination is proposed in [31]. Nevertheless, the literatures [29–31] only took into account the delivery delay in a highway scenario without RSUs. In [32], the maximum message delivery delay from a vehicle to the nearest RSU was estimated. They also derived the minimum number of RSUs required to cover a straight road. The probability of a rear-end collision between two vehicles that travel in the same direction when a sudden event occurs is derived in [33]. However, the literatures [32, 33] consider the unidirectional scenario that the vehicle only moves in one direction, so the message delivery process cannot get the help from the vehicles moving in the reverse direction. The improvement in the rehealing delay when a number of RSUs are deployed was investigated in [34, 35], and the results show the rehealing time is significantly reduced in the presence of RSUs. Jia et al. [7] proposed a novel architecture for platoon VCPs and derived the intraplatoon and interplatoon spacing in the steady state. Our paper is based on the results of intraplatoon and interplatoon spacing derived in [7]. We investigated the expected transmission delay of safety messages under different scenarios. In addition, we also discussed the benefits of RSU deployed at fixed interval to enable relaying of information when there is severe disconnection between vehicles.

3. System Model

This section describes our system model with necessary assumptions in terms of the network scenario, distribution of traffic flow, and vehicle mobility model, for tractability in establishing the analytical model.

3.1. Network Scenario. In this paper, we consider a straight two-lane highway that goes in opposite directions (i.e., the eastbound and the westbound directions) shown in Figure 1. We assume that all vehicles are equipped with storage, computation, and communication capabilities. Thus, vehicles can quickly and accurately collect the real-time information

about the status of the road and notify neighboring vehicles of potential dangerous events. The communication radius of each vehicle is denoted by R within which reliable V2V communication is guaranteed. Vehicles that move in the same direction and within each other's communication range will form a platoon. The foremost vehicle in a platoon is the platoon leader which is responsible for creating and managing the platoon. The platoon tail is located at the end of a platoon and is responsible for communicating with the following platoon leader. All vehicles in the same platoon can directly communicate with each other. As shown in Figure 1, the vehicles in the same circle belong to the same platoon and the foremost vehicle (e.g., the yellow one) is the platoon leader. When an accident occurs, the vehicle first passing the accident location is referred to as the source node Src which immediately generates a safety message containing the traffic condition and broadcasts it to the succeeding vehicles traveling in the same direction. The safety message can be delivered to the tail of the platoon through the direct wireless communication. However, the target vehicle Dst (the leader of the following platoon) is not within the platoon tail's communication range. For such a scenario, the message can be stored and forwarded to a vehicle that travels in the opposite direction. Then, the relay node can forward the message until it enters the communication range of the target node. The average safety message delivery delay is the time from the instant when it is issued to the instant when the target node Dst has received it. Therefore, the problem considered in this paper is to develop a mathematical model to calculate the average information delivery delay.

3.2. Distribution of Traffic Flow. In this paper, we adopt the statistics of time headway as the fundamental parameter to describe the traffic flow distribution. Time headway is defined as the elapsed time of the passage of identical points on two consecutive vehicles [36]. So far numerous probability density distribution models have been proposed to fit the empirical distributions of time headway, including normal distribution, exponential distribution, gamma distribution, and log-normal distribution [37–40]. The exponential distribution is widely accepted as a very good model for relative

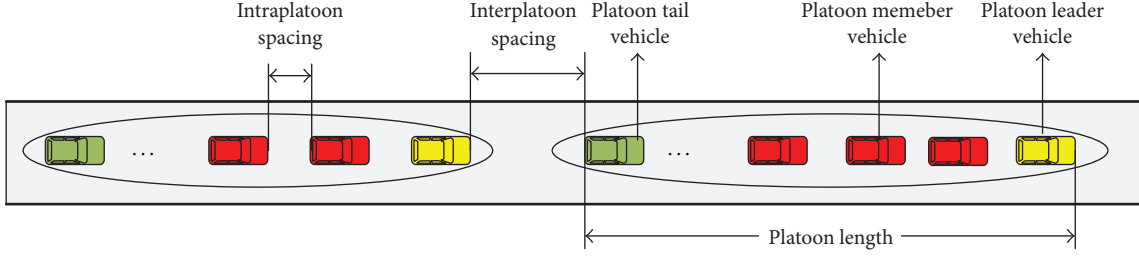


FIGURE 2: An illustrative example of platoon parameters.

long headway. However, it fails to describe the smaller variability in the headways observed in groups of vehicles that follow each other [41]. Through statistical analysis of empirical vehicle trajectory data collected from highways, the authors of [42] found that the log-normal distribution model is a good fit for the interarrival time of traffic during day-time hours. It is also confirmed in [37] that log-normal distribution fits well the intermediate traffic demand level. Therefore, we assume that the time headway has a log-normal distribution, which is expressed as

$$f_{T_h}(t_h, \mu, \sigma, \tau) = \frac{1}{\sqrt{2\pi\sigma}(t_h - \tau)} \exp\left(-\frac{(\log(t_h - \tau) - \mu)^2}{2\sigma^2}\right), \quad (1)$$

$$t_h > \tau,$$

where t_h represents the possible value of the time headway, τ represents the minimum value of the time headway, μ is the scale parameter, and σ is the shape parameter. Therefore, the mean and variance of time headway can be calculated as

$$\begin{aligned} \mu(T_h) &= \tau + e^{\mu + (1/2)\sigma^2}, \\ \sigma^2(T_h) &= e^{2\mu + \sigma^2} (e^{\sigma^2} - 1). \end{aligned} \quad (2)$$

3.3. Vehicle Mobility Model. Car-following model, which falls into the category of microscopic level description, is the most common vehicle mobility model to describe the interaction among adjacent vehicles in the same platoon. In a car-following model, the behavior of each driver is described in relation to the vehicle ahead. A typical car-following model, known as Intelligent Driver Model (IDM) [43], is applied in this paper. According to IDM, acceleration of a following vehicle can be expressed as follows:

$$a_{fv}(t) = a \left[1 - \left(\frac{v_{fv}(t)}{v_0} \right)^4 - \left(\frac{s^*(v_{fv}(t), \Delta v(t))}{s(t)} \right)^2 \right], \quad (3)$$

where v represents the velocity of the following vehicle, the gap to the preceding vehicle is s , and velocity difference between the following and preceding vehicle is Δv . Subscript fv denotes the following vehicle. In (3), the instantaneous

acceleration consists of a free acceleration $a[1 - (v_{fv}(t)/v_0)^4]$ to achieve the desired speed v_0 and an interaction deceleration $-a(s^*(v_{fv}(t), \Delta v(t))/s(t))^2$ based on the existing gap and the desired minimum gap between the subject and preceding vehicles. The desired minimum gap is as follows:

$$s^*(v_{fv}(t), \Delta v(t)) = s_0 + T_0 v_{fv}(t) + \frac{v_{fv}(t) \Delta v(t)}{2\sqrt{ab}}, \quad (4)$$

where s_0 and T_0 represent the minimum intraplatoon spacing and the desired time headway, respectively, and a and b represent maximum acceleration and desired deceleration.

4. Delay Analysis of Safety Messages under Infrastructure-Less Scenario

In this section, we first present platoon analysis, and then, based on the communication scenario shown in Figure 1, we study the average delay of safety message propagation under two different situations: the best-case where the source node can immediately relay the information to a westbound car and the worst-case where no westbound vehicles are located in the communication range of the source node, respectively.

4.1. Platoon Analysis

4.1.1. Intraplatoon Spacing. Following the illustrative example presented in Figure 2, the intraplatoon spacing between two adjacent vehicles in the same platoon is denoted by S_{intra} . According to (3) and (4), the intraplatoon spacing is

$$S_{\text{intra}} = \frac{s_0 + T_0 v_{fv}(t) + v_{fv}(t) \Delta v(t) / 2\sqrt{ab}}{\sqrt{1 - (v_{fv}(t)/v_0)^4 - a_{fv}(t)/a}}. \quad (5)$$

In this paper, we consider that all vehicles in the scenario run at the same velocity in the steady state [44], where $a_{fv} = 0$ and $\Delta v(t) = 0$. Let v_{stb} and S_{stb} be the velocity and intraplatoon spacing in the steady state, respectively; then, the intraplatoon spacing can be rewritten as [44]

$$S_{\text{intra}} = S_{\text{stb}} = \frac{s_0 + v_{\text{stb}} T_0}{\sqrt{1 - (v_{\text{stb}}/v_0)^4}}. \quad (6)$$

4.1.2. Interplatoon Spacing. Similar to intraplatoon spacing, the gap between the tail of the leading platoon and the

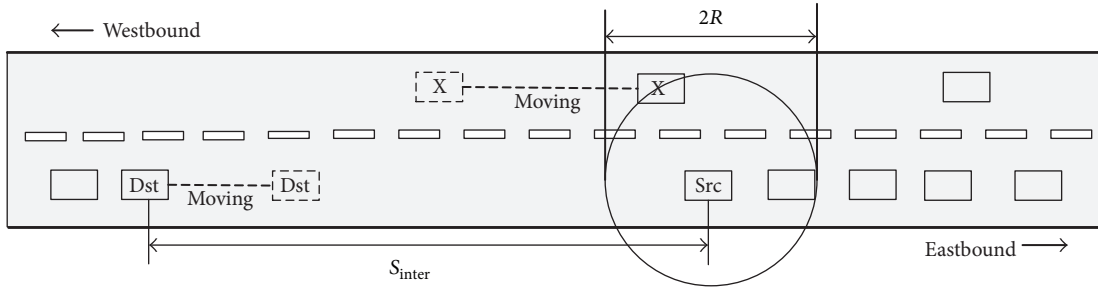


FIGURE 3: Best-case scenario.

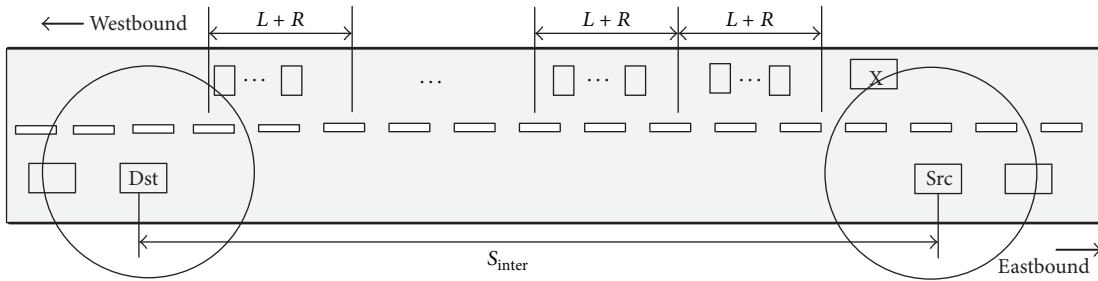


FIGURE 4: Case 1.

leader of the following platoon is referred to as interplatoon spacing, which is represented by S_{inter} . Under the assumption that all platoons have the same platoon size n and the same IDM parameters, the probability density function of the interplatoon spacing is derived in [7]

$$f_{S_{\text{inter}}}(x) = \frac{1}{\sqrt{2\pi}\sigma_D x} \exp\left(-\frac{(\log(x) - \mu_D)^2}{2\sigma_D^2}\right), \quad (7)$$

$x > 0,$

where the scale parameter μ_D and the shape parameter σ_D are given by

$$\sigma_D^2 = \log\left(\frac{\sigma^2(T_h)}{n(\mu(T_h) - \tau)^2} + 1\right), \quad (8)$$

$$\mu_D = \log(nv_{\text{stb}}(\mu(T_h) - \tau)) - \frac{\sigma_D^2}{2}.$$

4.2. Delay Analysis of Safety Messages Propagation. Without loss of generality, we assume the source node Src is located in the end of a platoon and has to deliver safety message to the vehicle Dst which is the following platoon leader. Because the distance between the source node Src and the target node Dst is out of the communication range, the vehicle Dst cannot receive the safety message directly. The message waits on the source node Src until the gap is filled by westbound vehicles. The expected transmission delay of safety message from Src to Dst is denoted by $E[T]$. In order to relay the message, the source node Src could run into one of the following cases.

4.2.1. Best-Case Scenario. As shown in Figure 3, the source node Src can immediately relay the safety message to a westbound vehicle X as the relay node which is the closet vehicle to the target node Dst. Let $f(x)$ denote the probability density function of the position of X. According to [7], the probability density function $f(x)$ is

$$f(x) = \frac{1}{e^{\mu_D} + L}, \quad (9)$$

where L represents the platoon length and is calculated by $L \approx n\tau v_{\text{stb}}$. Thus, the probability of this case is given by

$$\begin{aligned} p_1 &= P\{-R < x < R, S_{\text{inter}} > R\} \\ &= \int_{-R}^R \frac{1}{e^{\mu_D} + L} dx \int_R^{+\infty} f_{S_{\text{inter}}}(y) dy \\ &= \frac{2R}{e^{\mu_D} + L} \Phi\left(\frac{\mu_D - \log R}{\sigma_D}\right). \end{aligned} \quad (10)$$

Once the safety message arrives at the first relay node X, there can be two possible subcases.

Case 1. In this case, the relay node X is spatially connected to the target node Dst as illustrated in Figure 4. That is to say, the safety message can be continuously forwarded by each platoon leader and eventually received by the Dst. In order to calculate the probability of this event, we discrete the westbound roadway segment $S_{\text{inter}} - R$ into multiple cells, each of size $L + R$. The number of cells is $m = \lceil (S_{\text{inter}} - R)/(L + R) \rceil$. We consider a cell to be occupied if one or more platoon leaders are positioned within that cell. The probability of each

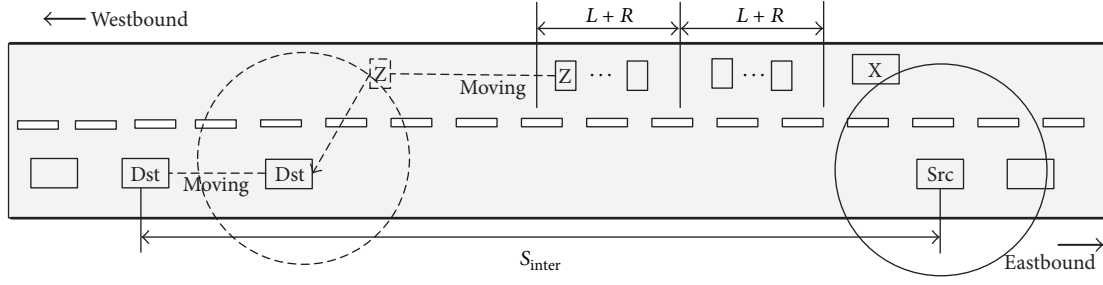


FIGURE 5: Case 2.

cell being occupied by at least one platoon leader is calculated by

$$p_w = P(0 < S_{\text{inter}} < R) = \int_0^R f_{S_{\text{inter}}}(x) dx \quad (11)$$

$$= \Phi\left(\frac{\log R - \mu_D}{\sigma_D}\right).$$

Case 1 happens when all of the m adjacent cells are occupied and the probability of this event is $p_{10} = p_w^m$. Because the speed of wireless communication is much faster than that of the vehicle, we ignore the delay caused by direct wireless transmission between two vehicles. Thus, the corresponding expected transmission delay $E[T_{10}] \approx 0$.

Case 2. As shown in Figure 5, not all of the m cells are occupied. The safety message can only be forwarded by X

between adjacent cells where platoon leaders are located. The last forwarder is vehicle Z which carries the message until it comes into contact with the target node Dst. The probability of Case 2 is simply the complement of p_{10} and is given by $p_{11} = 1 - p_{10}$. Let $E[d]$ denote the expected distance traversed by adjacent cells, which can be calculated by

$$E[d] = (L + R) \frac{1}{m} \sum_{i=1}^m i p_w^i \quad (12)$$

$$= (L + R) \left[\frac{p_w (1 - p_w^m)}{m (1 - p_w)^2} - \frac{p_w^{m+1}}{1 - p_w} \right].$$

The safety message transmission delay is the time that the relay node Z has to carry the message until it comes into Dst's communication range. Let $E[T_{11}]$ denote the expected transmission delay of this case, which can be calculated by

$$E[T_{11}] = \frac{E[S_{\text{inter}}] - R - (1 - p_w) E[d]}{2v_{\text{stb}}} = \frac{e^{\mu_D + (1/2)\sigma_D^2} - R - (L + R) [p_w (1 - p_w^m) / m (1 - p_w) - p_w^{m+1}]}{2v_{\text{stb}}}. \quad (13)$$

Given all the given cases, we have

$$E[T_1] = p_{10} E[T_{10}] + p_{11} E[T_{11}]. \quad (14)$$

4.2.2. Worst-Case Scenario. In this case, the source node Src cannot immediately relay the message to a westbound vehicle. The probability that this case happens can be calculated:

$$p_2 = 1 - p_1. \quad (15)$$

This case can be further divided into the following two subcases.

Case 3. No westbound vehicles are located within the communication range of the source node Src and other nodes in the same platoon, as shown in Figure 6. Let p_{20} represent the probability that this case happens. We have

$$p_{20} = P(S_{\text{inter}} > L) = \int_L^{+\infty} f_{S_{\text{inter}}}(x) dx \quad (16)$$

$$= \Phi\left(\frac{\mu_D - \log L}{\sigma_D}\right).$$

In this case, the safety message is carried by the platoon leader in the same platoon until it comes into contact with a westbound vehicle, which will further forward the information to the target node Dst. We assume that the platoon leader is statistically located in the center of interplatoon spacing. Thus, the westbound vehicle closest to the source node Src is at least $E[S_{\text{inter}}] + L + (1/2)E[S_{\text{inter}}]$ away from the target node Dst. The expected transmission delay $E[T_{20}]$ is calculated by

$$E[T_{20}] = \frac{E[S_{\text{inter}}] + L + (1/2) E[S_{\text{inter}}]}{2v_{\text{stb}}} \quad (17)$$

$$= \frac{L + (3/2) e^{\mu_D + (1/2)\sigma_D^2}}{2v_{\text{stb}}}.$$

Case 4. As shown in Figure 7, there is no relay node traveling in the westbound direction within the communication range of the source node Src, but there is one or more westbound vehicles within the communication range of a node other

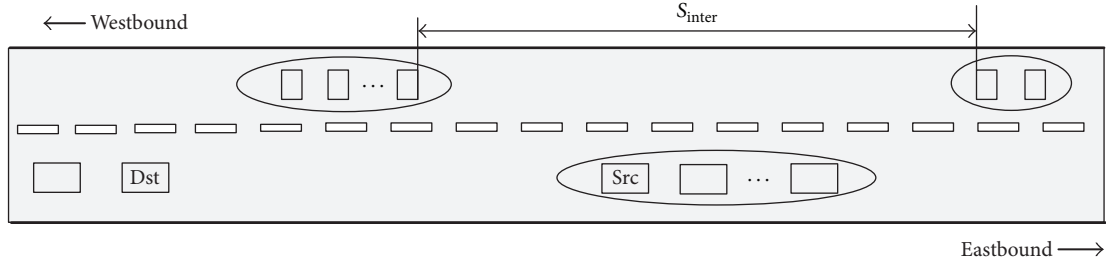


FIGURE 6: Case 3.

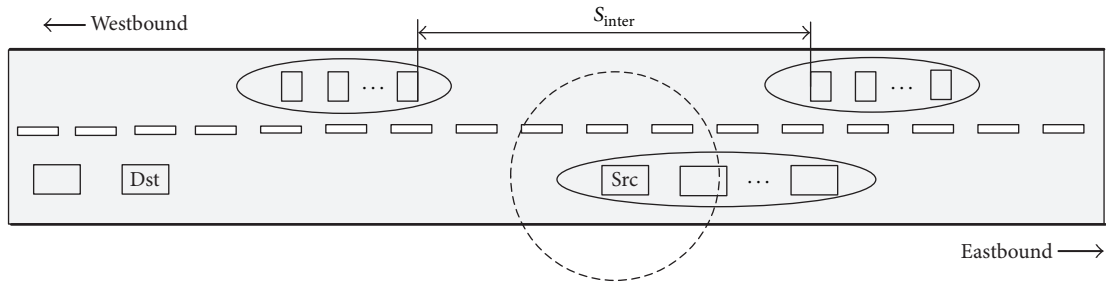


FIGURE 7: Case 4.

than the source node Src in the same platoon. This case happens with the following probability:

$$p_{21} = 1 - p_{20} = \Phi\left(\frac{\log L - \mu_D}{\sigma_D}\right). \quad (18)$$

Since the closest westbound vehicle to the source is at most $E[S_{\text{inter}}] + L + R$ away from the target node Dst, the delivery delay can be approximately calculated as

$$E[T_{21}] = \frac{E[S_{\text{inter}}] + L + R}{2v_{\text{stb}}} = \frac{e^{\mu_D + (1/2)\sigma_D^2} + L + R}{2v_{\text{stb}}}. \quad (19)$$

Under the worst-case scenario, the expected transmission delay $E[T_2]$ is

$$E[T_2] = p_{20}E[T_{20}] + p_{21}E[T_{21}]. \quad (20)$$

Consequently, the total expected transmission delay $E[T]$ is

$$E[T] = p_1E[T_1] + p_2E[T_2]. \quad (21)$$

5. Delay Analysis of Safety Messages with RSU Supported

In this section, we present the analytical model to describe the delay of safety messages transmission with RSU-supported VCPSS. RUSs usually have larger communication range due to the availability of power source and more powerful devices. Thus, they are capable of quickly disseminating a message to most of vehicles in a region of VCPSSs. We consider the most critical scenario where RSUs are deployed at fixed

interval of D_u to enable relaying of information when there is severe disconnection between vehicles. Thus, the probability of finding an RSU is a uniformly distributed random variable in $[0, D_u]$:

$$f_{\text{RSU}}(r) = \begin{cases} \frac{1}{D_u} & 0 < r < D_u \\ 0 & \text{others.} \end{cases} \quad (22)$$

Working with the analytical model in Section 4, we determine which communication scenarios can benefit from the presence of RSUs. Best-case and worst-case are evaluated independently, as each leads to a different set of benefits.

5.1. Best-Case Scenario. In this case, as shown in Figure 3, the source node Src can immediately relay the safety message to a westbound vehicle X. The improvements are obtained when an RSU is deployed in a way where it can forward the safety message from X to the destination node Dst. Let R_u represent the communication range of an RSU. We consider the case where the vehicles Dst and X reach a distance of $2R_u$ from one another where an RSU can act as a relay node between the two vehicles. If no RSUs were present, the two vehicles have to travel a distance of $2R_u - R$ to be able to communicate with each other. We see a range of positions where an RSU can be deployed as shown in Figure 8. The most favorable position for the RSU is in front of vehicle Dst by R_u where the travel distance reduction is highest ($2R_u - R$) and vehicles can communicate immediately. No improvements can be obtained when the RSU is on top of either vehicle Dst or X. Let z denote the distance from the RSU to the vehicle Dst. We observe that the reduction in travel distance increases

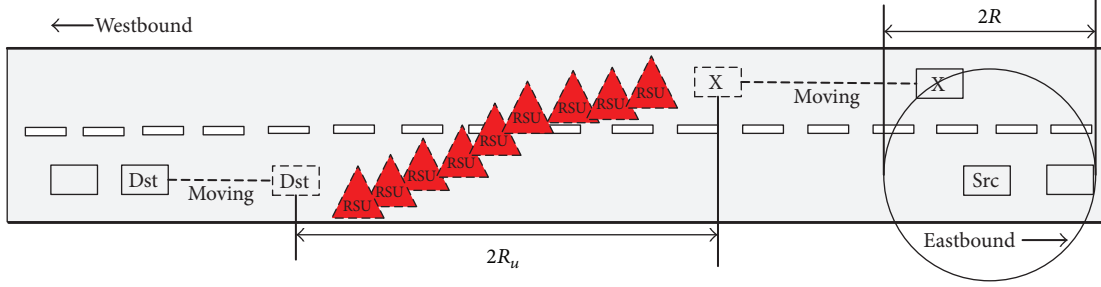


FIGURE 8: Favorable positions for RSUs.

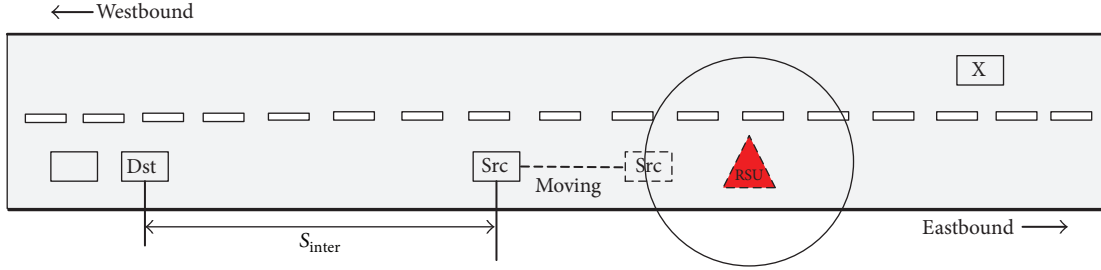


FIGURE 9: RSU acting as a relay node in worst-case.

linearly from $z = 0$ to R_u and decreases linearly from R_u to $2R_u$. The travel distance reduction, $G(z)$, is given by

$$G(z) = \begin{cases} \left(2 - \frac{R}{R_u}\right)z & 0 < z < R_u \\ -\left(2 - \frac{R}{R_u}\right)z + 2(2R_u - R) & R_u < z < 2R_u. \end{cases} \quad (23)$$

Therefore, the mean reduction in travel distance is given by

$$E[L] = \int_0^{2R_u} G(z) f_{\text{RSU}}(z) dz = \frac{R_u(2R_u - R)}{D_u}. \quad (24)$$

With the presence of an RSU acting as a relay node, the delay of safety message transmission $E[T'_1]$ is

$$E[T'_1] = \frac{E[S_{\text{inter}}] - R - E[L] - (1 - p_w)E[d]}{2v_{\text{stb}}}. \quad (25)$$

5.2. Worst-Case Scenario. In this case, the source node Src does not have any vehicles traveling on the opposite direction within its communication range to relay the safety message. With the presence of RSUs, a new scenario where an RSU act as a relay node becomes possible. This is shown in Figure 9. The source node Src can first deliver the safety message to the RSU. The destination node Dst receives the message from the RSU when it comes into the communication range of the RSU. This case happens when the delay for the destination node Dst to get the message from the RSU is smaller than the delay to forward the message to a vehicle traveling on the opposite direction. The source node Src is at most $(D_u - 2R_u)/2$ away

from an RSU. Let p_r represent the probability of an RSU acting as a relay node

$$\begin{aligned} p_r &= P \left[\frac{S_{\text{inter}} + L + (1/2)S_{\text{inter}}}{2v_{\text{stb}}} > \frac{S_{\text{inter}} + (1/2)D_u - R_u}{v_{\text{stb}}} \right] \\ &= \int_{-\infty}^{2(L+2R_u-D_u)} f_{S_{\text{inter}}}(x) dx \\ &= \Phi \left(\frac{\log(2(L + 2R_u - D_u)) - \mu_D}{\sigma_D} \right). \end{aligned} \quad (26)$$

The delay of safety message transmission $E[T'_{20}]$ in this scenario is

$$\begin{aligned} E[T'_{20}] &= \frac{E[S_{\text{inter}}] + (1/2)D_u - R_u}{v_{\text{stb}}} \\ &= \frac{e^{\mu_D + (1/2)\sigma_D^2} + (1/2)D_u - R_u}{v_{\text{stb}}}. \end{aligned} \quad (27)$$

If the above scenario does not occur, the delay of safety message transmission is sum of two components: the source node Src has to wait for an opposite-lane vehicle Z and Z comes into the communication range of Dst.

Thus, under the worst-case scenario with RSU-support, the expected transmission delay $E[T'_2]$ is

$$E[T'_2] = p_r E[T'_{20}] + (1 - p_r) E[T'_{21}], \quad (28)$$

where $E[T'_{21}]$ is the previous worst-case expected transmission delay.

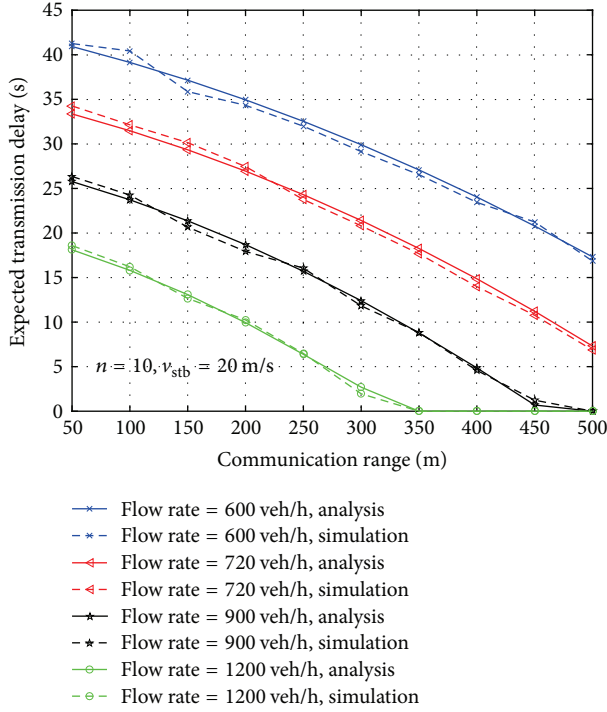


FIGURE 10: Impact of the communication range on the expected transmission delay ($n = 10, v_{\text{stb}} = 20 \text{ m/s}$).

Given all cases, the expected transmission delay $E[T']$ with RSU supported is

$$E[T'] = p_1 E[T'_1] + (1 - p_1) E[T'_2]. \quad (29)$$

6. Numerical and Simulation Results

In this section, we verify the effectiveness of the analytical model through simulation results and investigate the impacts of different parameters on the expected transmission delay, respectively, including the communication range of a vehicle (i.e., R), the platoon size (i.e., n), and the steady velocity (i.e., v_{stb}). To perform the simulation experiments, we have developed a MATLAB simulator. In the simulation experiments, vehicles are generated at the beginning of each road at time intervals obtained from a log-normal random number generator. Vehicles move at a constant speed in steady state and there is no overtaking. The value of σ is set to 0.4 like in [7], which normally does not vary much over different traffic flow levels. The minimum value of headway time is $\tau = 1 \text{ s}$. By setting different value of μ , we can simulate the traffic scenarios with various traffic flow rates.

6.1. Impact of Communication Range of Vehicle. We now study how different communication ranges impact the expected transmission delay $E[T]$. Given the platoon size $n = 10$ and steady velocity $v_{\text{stb}} = 20 \text{ m/s}$, we show the expected transmission delay of safety message when the communication range R varies from 50 m to 500 m under various traffic flow conditions in Figure 10. We can observe that the simulation results and the analytical results fit very well for all

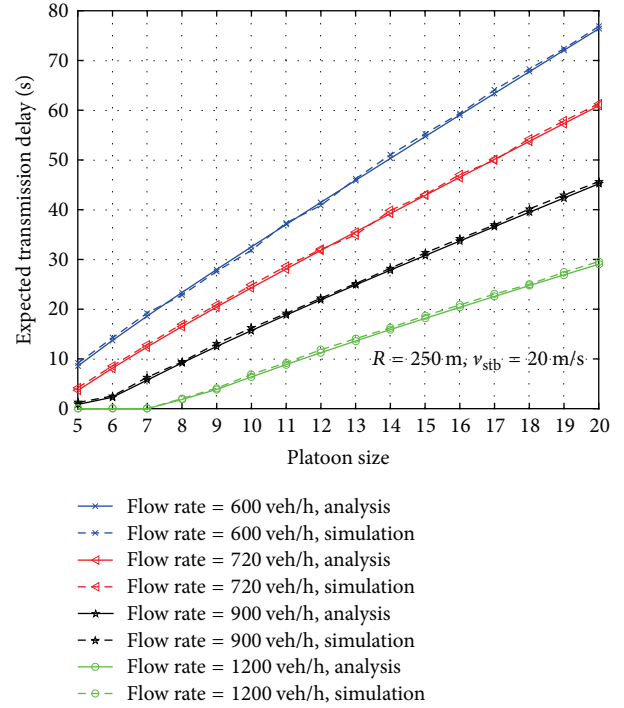


FIGURE 11: Impact of the size of platoon on the expected transmission delay ($R = 250 \text{ m}, v_{\text{stb}} = 20 \text{ m/s}$).

cases of traffic flow rates, which means the analytical model is effective. It is easy to see that the expected transmission delay of safety message decreases as the communication range R increases. Particularly, when the traffic flow rate is 1200 veh/h, the expected transmission delay $E[T]$ decreases from 18 s to 0 s as the communication range increases from 50 m to 350 m. That is to say, the safety message can be directly transmitted from the succeeding tail of platoon to the following platoon header when the communication range is 350 m. Even in sparse scenario (i.e., 600 veh/h), the expected transmission delay still significantly decreases as R increases. This is mainly due to the fact that R can significantly enhance the network connectivity. There are more high probabilities that two vehicles are connected and forward the message to each other when the communication range increases. As expected, for a given value of communication range R (i.e., 250 m), it also takes less time to forward a safety message to the following platoon header in the dense traffic condition. This is because as the traffic flow rate increases, the interplatoon spacing gets smaller.

6.2. Impact of Platoon Size. To study the impact of platoon size on the expected transmission delay, we fix the communication range $R = 250 \text{ m}$ and the steady velocity $v_{\text{stb}} = 20 \text{ m/s}$, respectively. Figure 11 shows the expected transmission delay $E[T]$ under different traffic flow rates. It is seen that simulation results are very close to the analytical results. Moreover, with an increasing platoon size, the expected transmission delay increases in various traffic flow conditions. The graph shows that, for the traffic flow rate of 720 veh/h, the expected transmission delay increases from 4 s to 61 s as the platoon

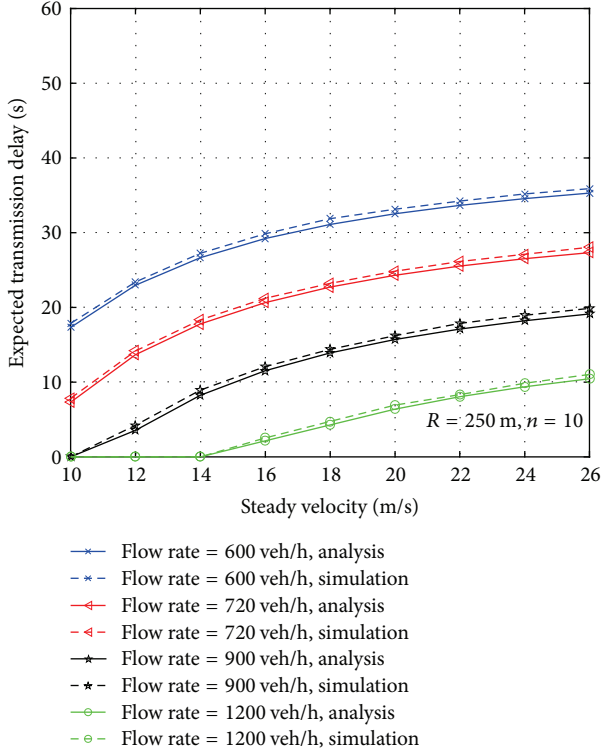


FIGURE 12: Impact of the steady velocity on the expected transmission delay ($R = 250$ m, $n = 10$).

size increases from 5 to 26. A similar phenomenon is also observed in other traffic flow rates. This is due to the fact that the interplatoon spacing is enlarged when the platoon size increases. As a result, the possible distance traversed during store-carry-forwarding process will be maximized.

6.3. Impact of Steady Velocity. Figure 12 plots the expected transmission delay $E[T]$ against the steady velocity of vehicles in various traffic flow rates, where $R = 250$ m and $n = 10$. Similar to the effect of platoon size, the expected transmission delay slowly increases with the increase of steady velocity. For the traffic flow rate of 1200 veh/h, we notice that there is no transmission delay when $v_{\text{stb}} \leq 14$ m/s, and the transmission delay is less than 10 s when the steady velocity reaches 26 m/s. That is because increasing steady velocity results in large interplatoon spacing for a given traffic flow rate.

6.4. The Benefits on the Expected Transmission Delay with RSU Supported. First, we investigate the two main components of the expected transmission delay $E[T']$ with RSU supported. We conduct the simulation under different flow rate conditions, where the value of RSU deployment interval D_u is set to 1 km and the communication range of RSU is set to 400 m.

Figure 13 shows the analytical and simulation results for the best-case and worst-case scenario with RSU supported, for traffic flow rate ranging from 300 to 900 veh/h. We observe a very good match between the predictions of our analytical model and the output of the simulations. The results clearly show that the expected transmission delay of both best-

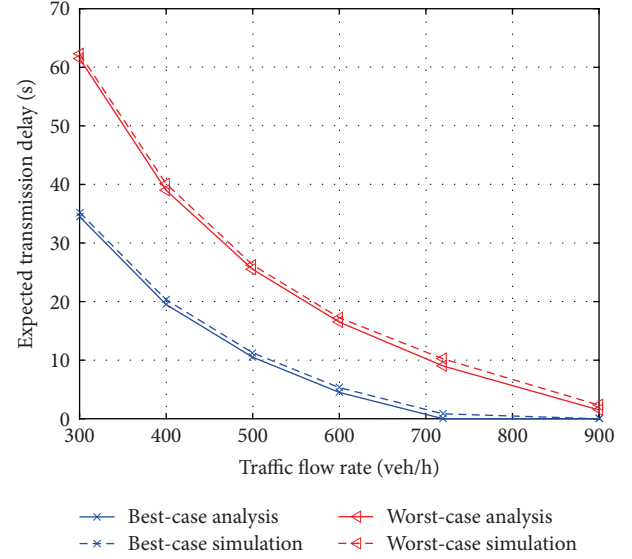


FIGURE 13: The expected transmission delay of best-case and worst-case with RSU supported ($D_u = 1000$ m, $R_u = 400$ m).

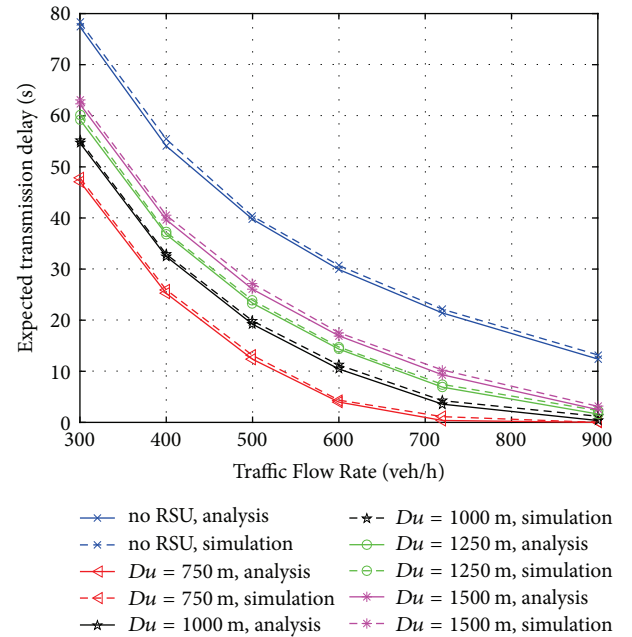


FIGURE 14: The expected transmission delay with RSU supported under different deployment interval.

and worst-case scenarios decreases as the traffic flow rate increases. When the traffic flow rate is below 600 veh/h, the network is essentially disconnected, and the likelihood of being in the presence of a worst-case scenario is high. As the traffic flow rate increases, the networks are largely connected, and the safety messages are more likely propagated under the best-case scenario, which gives a lower penalty in expected transmission delay.

The expected transmission delay $E[T']$ under different deployment intervals is shown in Figure 14. It is easy to

see that the delay of safety message propagation can be reduced obviously with the help of RSUs. When the traffic flow rate is 300 veh/h, the expected transmission delay decreases almost 45% by a regular space 750 m deployment of RSUs. There is still 22% reduction when the deployment interval increases to 1500 m. On the other hand, the safety message propagation can be done almost instantly when the traffic flow rate reaches 700 veh/h with RSU supported. That indicates sufficient number of RSUs can significantly reduce the expected transmission delay of safety messages. However, with too many RSUs, it would also incur high installation cost and maintenance cost of these RSUs.

7. Conclusions

The message transmission delay is a main QoS metric for safety application in VCPSSs. In this paper, we developed an analytical model to analyze the safety message transmission delay in both infrastructure-less and RSU-supported scenarios. The vehicles are assumed to move based on Intelligent Driver Model. The analytical model takes into account different transmission cases and various system parameters, such as communication range, traffic flow, and platoon size. We conducted extensive simulation to validate the effectiveness of the analytical model. The results will help determine the system design parameters to satisfy the delay requirement for safety applications in VCPSSs.

Conflicts of Interest

The authors declare that there are no conflicts of interest regarding the publication of this paper.

Acknowledgments

This work was supported in part by the National Natural Science Foundation Projects under Grant 61731004, the National Science and Technology Major Projects of China under Grant 2017ZX03001014, and the National Science Fund for Distinguished Young Scholars under Grant 61425012.

References

- [1] D. Jia, K. Lu, J. Wang, X. Zhang, and X. Shen, "A survey on platoon-based vehicular cyber-physical systems," *IEEE Communications Surveys & Tutorials*, vol. 18, no. 1, pp. 263–284, 2016.
- [2] K. Liu, V. C. S. Lee, J. K.-Y. Ng, J. Chen, and S. H. Son, "Temporal data dissemination in vehicular cyber-physical systems," *IEEE Transactions on Intelligent Transportation Systems*, vol. 15, no. 6, article no. A6, pp. 2419–2431, 2014.
- [3] O. Kaiwartya, A. H. Abdullah, Y. Cao et al., "Internet of vehicles: motivation, layered architecture, network model, challenges and future aspects," *IEEE Access*, vol. 4, no. 99, pp. 5356–5373, 2016.
- [4] J. Wan, D. Zhang, S. Zhao, L. T. Yang, and J. Lloret, "Context-aware vehicular cyber-physical systems with cloud support: architecture, challenges, and solutions," *IEEE Communications Magazine*, vol. 52, no. 8, pp. 106–113, 2014.
- [5] S. Chen, J. Hu, Y. Shi et al., "Vehicle-to-everything (v2x) services supported by LTE-based systems and 5G," *IEEE Communications Standards Magazine*, vol. 1, no. 2, pp. 70–76, 2017.
- [6] Y. Wang, J. Zheng, and N. Mitton, "Delivery delay analysis for roadside unit deployment in intermittently connected VANETs," in *Proceedings of the 2014 IEEE Global Communications Conference, GLOBECOM 2014*, pp. 155–161, December 2014.
- [7] D. Jia, K. Lu, and J. Wang, "On the network connectivity of platoon-based vehicular cyber-physical systems," *Transportation Research Part C: Emerging Technologies*, vol. 40, pp. 215–230, 2014.
- [8] S. Chen, J. Hu, Y. Shi, and L. Zhao, "LTE-V: a TD-LTE-based V2X solution for future vehicular network," *IEEE Internet of Things Journal*, vol. 3, pp. 997–1005, 2016.
- [9] H. A. Omar, N. Lu, and W. Zhuang, "Wireless access technologies for vehicular network safety applications," *IEEE Network*, vol. 30, no. 4, pp. 22–26, 2016.
- [10] H. P. Luong, M. Panda, H. Le Vu, and Q. B. Vo, "Analysis of multi-hop probabilistic forwarding for vehicular safety applications on highways," *IEEE Transactions on Mobile Computing*, vol. 16, no. 4, pp. 918–933, 2017.
- [11] C. Shao, S. Leng, Y. Zhang, A. Vinel, and M. Jonsson, "Performance analysis of connectivity probability and connectivity-aware MAC protocol design for platoon-based VANETs," *IEEE Transactions on Vehicular Technology*, vol. 64, no. 12, pp. 5596–5609, 2015.
- [12] J. He, L. Cai, J. Pan, and P. Cheng, "Delay analysis and routing for two-dimensional VANETs using carry-and-forward mechanism," *IEEE Transactions on Mobile Computing*, vol. 16, no. 7, pp. 1830–1841, 2017.
- [13] Y. Wang, Y. Liu, J. Zhang, H. Ye, and Z. Tan, "Cooperative store-carry-forward scheme for intermittently connected vehicular networks," *IEEE Transactions on Vehicular Technology*, vol. 66, no. 1, pp. 777–784, 2017.
- [14] Y. Huo, W. Dong, J. Qian, and T. Jing, "Coalition game-based secure and effective clustering communication in vehicular cyber-physical system (VCPS)," *Sensors*, vol. 17, no. 3, article no. 475, pp. 1–23, 2017.
- [15] H. Zhou, S. Xu, D. Ren, C. Huang, and H. Zhang, "Analysis of event-driven warning message propagation in vehicular Ad Hoc networks," *Ad Hoc Networks*, vol. 55, pp. 87–96, 2017.
- [16] Y. Wang, J. Zheng, and N. Mitton, "Delivery Delay analysis for roadside unit deployment in vehicular ad hoc networks with intermittent connectivity," *IEEE Transactions on Vehicular Technology*, vol. 65, no. 10, pp. 8591–8602, 2016.
- [17] B. Pan and H. Wu, "Analysis of safety messages delivery in vehicular networks with interconnected roadside units," *IEEE Access*, vol. 5, pp. 24873–24883, 2017.
- [18] X. Li, B.-J. Hu, H. Chen, B. Li, H. Teng, and M. Cui, "Multi-hop delay reduction for safety-related message broadcasting in vehicle-to-vehicle communications," *IET Communications*, vol. 9, no. 3, pp. 404–411, 2015.
- [19] S. C. Ng, W. Zhang, Y. Zhang, Y. Yang, and G. Mao, "Analysis of access and connectivity probabilities in vehicular relay networks," *IEEE Journal on Selected Areas in Communications*, vol. 29, no. 1, pp. 140–150, 2011.
- [20] D. Naboulsi and M. Fiore, "Characterizing the instantaneous connectivity of large-scale urban vehicular networks," *IEEE Transactions on Mobile Computing*, vol. 16, no. 5, pp. 1272–1286, 2017.

- [21] X. Hou, Y. Li, D. Jin, D. O. Wu, and S. Chen, "Modeling the impact of mobility on the connectivity of vehicular networks in large-scale urban environments," *IEEE Transactions on Vehicular Technology*, vol. 65, no. 4, pp. 2753–2758, 2016.
- [22] H. A. Omar, W. Zhuang, A. Abdrabou, and L. Li, "Performance evaluation of VeMAC supporting safety applications in vehicular networks," *IEEE Transactions on Emerging Topics in Computing*, vol. 1, no. 1, pp. 69–83, 2013.
- [23] F. Lyu, H. Zhu, H. Zhou et al., "SS-MAC: a novel time slot-sharing MAC for safety messages broadcasting in VANETs," *IEEE Transactions on Vehicular Technology*, pp. 1-1, 2017.
- [24] C. Suthaputthakun, M. Dianati, and Z. Sun, "Trinary partitioned black-burst-based broadcast protocol for time-critical emergency message dissemination in VANETs," *IEEE Transactions on Vehicular Technology*, vol. 63, no. 6, pp. 2926–2940, 2014.
- [25] M.-C. Chuang and M. C. Chen, "DEEP: density-aware emergency message extension protocol for VANETs," *IEEE Transactions on Wireless Communications*, vol. 12, no. 10, pp. 4983–4993, 2013.
- [26] J. Sahoo, E. H.-K. Wu, P. K. Sahu, and M. Gerla, "Binary-partition-assisted MAC-layer broadcast for emergency message dissemination in VANETs," *IEEE Transactions on Intelligent Transportation Systems*, vol. 12, no. 3, pp. 757–770, 2011.
- [27] C. Wu, S. Ohzahata, Y. Ji, and T. Kato, "Joint fuzzy relays and network-coding-based forwarding for multihop broadcasting in vanets," *IEEE Transactions on Intelligent Transportation Systems*, vol. 16, no. 3, pp. 1415–1427, 2015.
- [28] Y. Bi, H. Shan, X. S. Shen, N. Wang, and H. Zhao, "A multihop broadcast protocol for emergency message dissemination in urban vehicular ad hoc networks," *IEEE Transactions on Intelligent Transportation Systems*, vol. 17, no. 3, pp. 736–750, 2016.
- [29] K. Abboud and W. Zhuang, "Modeling and analysis for emergency messaging delay in vehicular ad hoc networks," in *Proceedings of the IEEE Global Telecommunications Conference (GLOBECOM '09)*, pp. 1–6, Honolulu, Hawaii, USA, December 2009.
- [30] A. B. Reis, S. Sargento, and O. K. Tonguz, "Parameters that affect safety message delay in sparse infrastructure-less vehicular networks," in *Proceedings of the 2014 1st IEEE International Conference on Communications, ICC 2014*, pp. 2568–2574, June 2014.
- [31] Y. Zhuang, J. Pan, Y. Luo, and L. Cai, "Time and location-critical emergency message dissemination for vehicular Ad-hoc networks," *IEEE Journal on Selected Areas in Communications*, vol. 29, no. 1, pp. 187–196, 2011.
- [32] A. Abdrabou and W. Zhuang, "Probabilistic delay control and road side unit placement for vehicular ad hoc networks with disrupted connectivity," *IEEE Journal on Selected Areas in Communications*, vol. 29, no. 1, pp. 129–139, 2011.
- [33] S.-I. Sou, "Modeling emergency messaging for car accident over dichotomized headway model in vehicular ad-hoc networks," *IEEE Transactions on Communications*, vol. 61, no. 2, pp. 802–812, 2013.
- [34] S.-I. Sou and O. K. Tonguz, "Enhancing VANET connectivity through roadside units on highways," *IEEE Transactions on Vehicular Technology*, vol. 60, no. 8, pp. 3586–3602, 2011.
- [35] A. B. Reis, S. Sargento, F. Neves, and O. K. Tonguz, "Deploying roadside units in sparse vehicular networks: what really works and what does not," *IEEE Transactions on Vehicular Technology*, vol. 63, no. 6, pp. 2794–2806, 2014.
- [36] A. D. May, *Traffic Flow Fundamentals*, Prentice-Hall, 1990.
- [37] D.-H. Ha, M. Aron, and S. Cohen, "Time headway variable and probabilistic modeling," *Transportation Research Part C: Emerging Technologies*, vol. 25, pp. 181–201, 2012.
- [38] G. Yan and S. Olariu, "A probabilistic analysis of link duration in vehicular Ad Hoc networks," *IEEE Transactions on Intelligent Transportation Systems*, vol. 12, no. 4, pp. 1227–1236, 2011.
- [39] K. Abboud and W. Zhuang, "Stochastic analysis of a single-hop communication link in vehicular ad hoc networks," *IEEE Intelligent Transportation Systems Magazine*, vol. 15, no. 5, pp. 2297–2307, 2014.
- [40] L. Cheng and S. Panichpapiboon, "Effects of intervehicle spacing distributions on connectivity of VANET: a case study from measured highway traffic," *IEEE Communications Magazine*, vol. 50, no. 10, pp. 90–97, 2012.
- [41] J. S. Baras, A. J. Dorsey, and W. S. Levine, "Estimation of traffic platoon structure from headway statistics," *IEEE Transactions on Automatic Control*, vol. 24, no. 4, pp. 553–559, 1979.
- [42] N. Wisitpongphan, F. Bai, P. Mudalige, V. Sadekar, and O. Tonguz, "Routing in sparse vehicular ad hoc wireless networks," *IEEE Journal on Selected Areas in Communications*, vol. 25, no. 8, pp. 1538–1556, 2007.
- [43] M. Treiber, A. Hennecke, and D. Helbing, "Congested traffic states in empirical observations and microscopic simulations," *Physical Review E: Statistical, Nonlinear, and Soft Matter Physics*, vol. 62, no. 2, pp. 1805–1824, 2000.
- [44] D. Jia, K. Lu, and J. Wang, "A disturbance-adaptive design for VANET-enabled vehicle platoon," *IEEE Transactions on Vehicular Technology*, vol. 63, no. 2, pp. 527–539, 2014.

Research Article

A Road Layout Based Broadcast Mechanism for Urban Vehicular Ad Hoc Networks

Yoonyoung Sung  and Meejeong Lee 

Department of Computer Science and Engineering, Ewha Womans University, Daehyun-dong 11-1, Seoul, Republic of Korea

Correspondence should be addressed to Meejeong Lee; lmj@ewha.ac.kr

Received 18 September 2017; Accepted 2 January 2018; Published 30 January 2018

Academic Editor: Hongwei Wang

Copyright © 2018 Yoonyoung Sung and Meejeong Lee. This is an open access article distributed under the Creative Commons Attribution License, which permits unrestricted use, distribution, and reproduction in any medium, provided the original work is properly cited.

Safety services of Vehicular Ad Hoc Network (VANET) require reliable broadcasts. We propose a reliable broadcast mechanism for urban roads called VANET Broadcasting for Urban areas based on Road Layout (VBURL), which tries to minimize the dependency on information that may become inaccurate to maximize the efficiency of broadcast. Specifically, the proposed mechanism takes into account the road layout information accessible from the digital map and only the real-time information obtained from the broadcast messages or beacons. VBURL basically makes the vehicle that is farthest from the current forwarding vehicle take the role of next forwarding vehicle and, if possible, makes an additional broadcast happen at the intersections where the effect of signal attenuation caused by the road side obstacles is low in order to have prompt and reliable dissemination of safety messages towards all roads connected to the intersections. The simulation results verified that VBURL achieves the same high performance as that of the compared legacy schemes in terms of reliability with much higher efficiency. Even though the message reception delay of VBURL is slightly longer than those of compared schemes, it is far less significant to impair the original purpose of safety message.

1. Introduction

The Vehicular Ad Hoc Network (VANET) consists of vehicles that use mobile communications and enables communication between vehicles or between vehicles and fixed infrastructure along the road. The road condition and traffic information collected through various sensors installed in vehicles and on road side units are transmitted in real time through VANET. The IEEE 802.11p standard and the IEEE 1609 working group defined technologies for Wireless Access in Vehicular Environments (WAVE) [1, 2]. In particular, 802.11p defines the MAC and PHY layers, and 1609.4 defines multichannel operation. For multichannel operation, it is specified to use the control channel (CCH) for safety services, as well as system control such as beacons, and the service channels (SCHs) for general commercial services. The Synchronization Interval (SI) of 100 ms is divided into an equal length of a CCH interval and an SCH interval.

VANET enables the provision of services to improve passenger safety and traffic flow through the propagation of information on dangerous situations and the detection of

traffic congestion, as well as various services for passenger conveniences and entertainment, such as games, chatting, and data sharing between vehicles [3]. Among these various prospective VANET services, safety related services are expected to be the foremost and representative applications. In particular with the upcoming deployment of autonomous vehicles, the importance of safety service becomes more critical. When a traffic accident occurs or obstacles fall on the road, a safety message is broadcast to encourage deceleration or rerouting to a bypass. Generically, the safety services require reliable broadcasting, and extensive studies have been actively conducted regarding this subject.

Various mechanisms have been proposed to make up for 802.11p for the provision of reliable broadcasts [4–19]. In [4–8] the authors proposed extensions of 802.11p to avoid the collisions caused by the hidden terminal. On the other hand [9–16] proposed the acknowledgment schemes for 802.11p to check the reception of broadcast message at the target vehicles and to have the rebroadcast be made if it is needed in order to guarantee the reliable broadcast. In particular, [17–19] focus on the reliable broadcast in urban environments

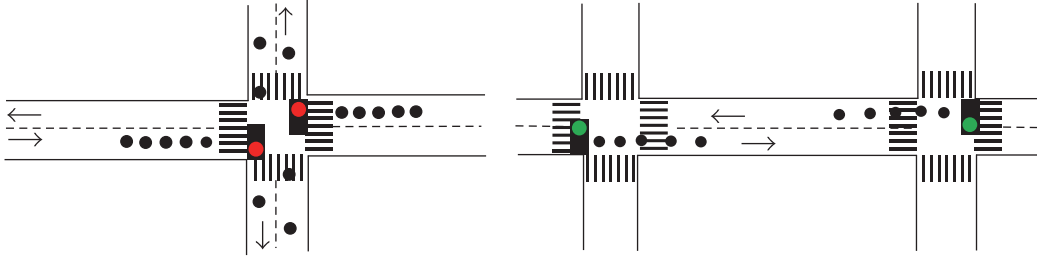


FIGURE 1: Characteristics of urban roads, formation of concentrated vehicle groups due to red light of traffic signals.

and address the problem of broadcast inefficiency in addition to the reliability. Broadcast efficiency is critical in urban environments where the traffic density is relatively high. However, there are some limitations in dealing with the broadcast inefficiency problem at the MAC layer by fully reflecting the characteristics of urban roads.

Differing from [4–19], [20, 21] proposed reliable broadcast mechanisms for VANET to be implemented above the MAC layer, that is, 802.11p. Their common design objectives are to reduce the number of broadcast forwarding attempts by selecting vehicles that can forward the message to the largest possible number of vehicles that have not received the message yet to optimize the broadcast efficiency. Both [20, 21] leverage the location information of neighboring vehicles which has been conveyed through the periodic beacons in order to determine the optimal forwarding vehicles. To this end, the location information is conveyed through the beacons that are periodically exchanged over the CCH of 802.11p and is kept on hold during a certain holding time.

However, the effect of traffic concentration due to the red light of traffic signals, as shown in Figure 1, is not considered carefully in [20, 21]. With the traffic concentration, frequent exchanges of beacons may cause congestion in CCH, which leads to the collisions and losses of beacons as well as the safety service messages. On the other hand, increasing the beacon exchanging interval to avoid such congestion also lowers the accuracy of the information provided by the beacons. References [20, 21] also implicitly judge the message reception status of neighboring vehicles based on their location information and reflect it to their forwarding vehicle decisions. Around the intersections, though, the implicit judgement on the message reception status frequently turns out to be incorrect due to the signal attenuation by the surrounding buildings. In particular, the inaccuracy of information about the neighboring vehicles may aggravate the broadcast inefficiency more seriously by causing unnecessary broadcast or broadcast message collisions when traffic is heavily concentrated. With the traffic signals and intersections, usually the vehicles with the broadcast message and the vehicles that have not received the message yet meet across one another in groups. With the incorrect information about the neighboring vehicles, wrong and/or the same forwarding priority values are assigned among the neighboring vehicles, resulting in unnecessary broadcasts or broadcast message collisions which wastes the CCH resources and causes serious efficiency deterioration. Therefore, the legacy schemes that

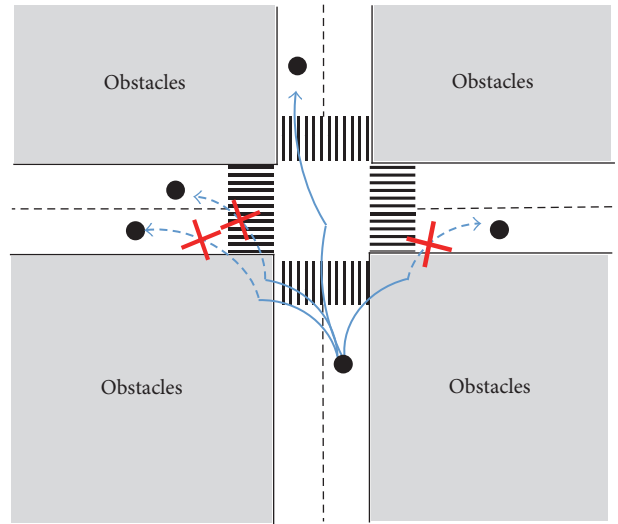


FIGURE 2: Intersection with no vehicle and with significant signal attenuation due to obstacles.

leverages the non-real-time information and the implicit judgement about the message reception status of neighboring vehicles without careful considerations about the characteristics of urban roads need to be reconsidered.

Similar to [20, 21], [22] and a recent work [23] also proposed the broadcast mechanisms for urban roads that is supposed to be implemented above the MAC layer. In [22, 23], differing from [20, 21], the road layout information instead of the holding information from beacons is leveraged to minimize the vulnerability to the inaccuracy of information utilized in the forwarding vehicle decisions. The reliability, though, cannot be assured by the works in [22, 23]. For instance, in both [22, 23], a vehicle that enters a road segment where the broadcast is just completed cannot receive the broadcast message. In particular, [23] focuses on the broadcast efficiency to eliminate or minimize the redundant broadcast. The delay for broadcast message dissemination, though, may become extraordinarily long in [23] if no vehicle exists at some or many of the intersections and the signal attenuation by surrounding obstacles prohibits the propagation of the broadcast message crossing over those intersections to reach the road segments at the other side of the intersection, as shown in Figure 2.

As the diverse applications of the Intelligent Transportation System (ITS) are expected along with the development of

VANETs, maximizing the usage efficiency of limited wireless resources is emerging as a critical issue. To this end, studies are conducted on dynamic and flexible utilization of wireless channels based on the real-time usage information [24–27]. Under this paradigm, lowering the utilization of CCH becomes also helpful in enhancing the chances to accommodate additional useful services in SCH by leveraging the leisurely utilized CCH resources. Note that CCH is assigned for the safety message dissemination as well as for the transmission of control messages such as beacons. In order to optimize the efficiency of CCH, therefore, not only the elimination of factors that demand the frequent beacon exchanges but also the maximization of broadcast efficiency of safety message dissemination is necessary.

In this paper, hence, we propose a safety message broadcasting scheme named “VANET Broadcasting for Urban areas based on Road Layout (VBURL)” that enhances the efficiency of safety message broadcast by minimizing the possibility of falsely selecting a forwarding vehicle based on the incorrect information while having little dependency on the beacon interval as well. VBURL is the extension of the work proposed by the authors in [22] to remedy its reliability weakness. Instead of leveraging non-real-time holding information from the periodic beacons or implicit judgement about the message reception status of neighboring vehicles, VBURL takes into account the road layout information accessible from the digital map similar to [22, 23], which is common and available already through the Digital Multimedia Broadcasting (DMB) networks. The performance of VBURL is, therefore, much less vulnerable to the beacon cycles as well as to the usual urban road characteristics such as high traffic density, frequent traffic signals and intersections, and traffic concentration.

Note that the urban roads consist of intersections and the roads interconnecting them. In VBURL, different forwarding strategies are applied depending on whether there is an intersection within the transmission range of a vehicle that receives the broadcast message and is supposed to determine whether to take the role of message forwarding. It is assumed that the signal attenuation caused by obstacles along the road sides is not significant on the straight roads between intersections, and thus, VBURL simply makes the vehicle that is farthest from the current forwarding vehicle perform the rebroadcast on the straight roads for rapid and efficient broadcasting. Meanwhile, for the message dissemination around the intersections, VBURL makes an additional broadcast happen at the intersections in addition to the one made by the farthest vehicle as long as there exists a vehicle hearing the broadcast at the intersection or else at least there exist one or more vehicles that are moving toward the intersection with that intersection within their transmission range. Since the effect of signal attenuation caused by the road side obstacles is low inside of the intersections, it enables the prompt and reliable dissemination of safety message toward all roads connected to the intersections.

This paper is organized as follows. After the introduction in Section 1, Section 2 examines the related studies. VBURL is explained in detail in Section 3. Section 4 describes the simulation to compare the performance of VBURL with that

of two representative legacy schemes and analyzes the results of simulation. Finally, Section 5 provides a conclusion.

2. Related Work

In this section, existing studies that implement the efficiency of reliable broadcasting on urban roads on top of the plain 802.11p, similar to VBURL, are examined [20, 21, 23]. These schemes commonly use the Connected Dominating Sets (CDS) [28] as the virtual backbone network for broadcasting. If a correct CDS can be set up, the broadcast dissemination to entire network is possible solely by the broadcast relays of vehicles included in the CDS. These schemes, hence, strive to suppress unnecessary transmissions by non-CDS vehicles in order to maximize the efficiency. References [20, 21] leverage the holding information obtained from the beacons such as the location of neighboring vehicles to determine the CDS, whereas the road layout information is utilized in [23].

2.1. Acknowledged Parameter-Less Broadcast in Static to High Mobile (ABSM). ABSM uses the Neighbor Elimination Scheme (NES) as proposed in [28, 29] as well as CDS vehicle information to determine the broadcast-forwarding vehicle [20]. In ABSM, the vehicles implicitly decide the message reception status of their neighboring vehicles by considering the distance between the forwarding vehicle and the neighboring vehicle leveraging the location information of neighboring vehicle obtained from the beacon. Each vehicle manages neighboring vehicle lists of R and N , and the neighboring vehicles that are believed to have received the message are compiled in list R and the other vehicles are placed on the list N . Upon receiving the message, each vehicle sets the broadcast timer for deciding the next forwarding vehicle. In ABSM, the broadcast timer value, which determines the forwarding vehicle, is set combining two factors: (1) whether the vehicle is in the CDS, and (2) the number of neighboring vehicles that have not received the message, that is, $|N|$. A CDS vehicle sets the timer to be inversely proportional to the number of neighboring vehicles that have not received the message. For the timer value of non-CDS vehicles, a constant value of ‘maximum waiting time’ is added to that of CDS vehicle so that the timer of CDS vehicle always expires first before that of non-CDS vehicle when they have the same number of neighboring vehicles that have not received message. The vehicle whose timer has expired performs a broadcast and the other vehicles that receive the duplicate broadcast release their broadcast timer.

Furthermore, message reception is indicated in the beacon so that, when a new vehicle with no message appears as a neighboring vehicle, it can be detected and the message can be sent to the new neighbor. ABSM updates the lists R and N through the broadcast message reception and the beacon exchange. Broadcast is repeated until no neighboring vehicles exist in the list N so that the reliability of message transmission to the entire network can be guaranteed.

In ABSM, not only the CDS virtual backbone network set up but also the broadcast timer setting is determined based on the holding information conveyed by the beacons. In order for ABSM to operate efficiently, the real-time locations of

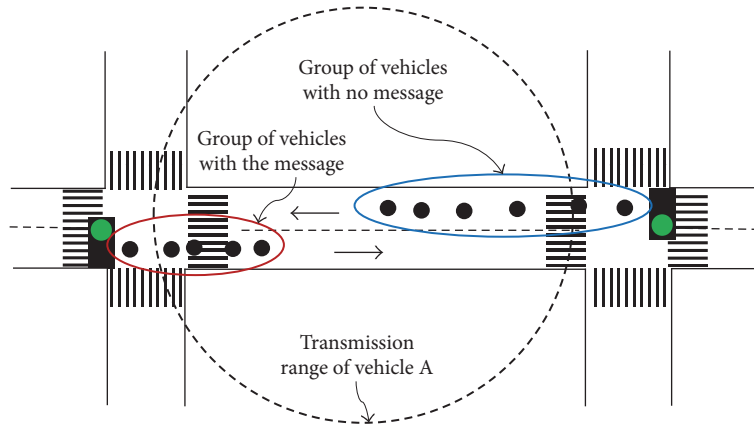


FIGURE 3: Example of a general situation where vehicles with no message are discovered through a beacon.

neighboring vehicles and positional relationships must be accurately identified. On urban roads, which have frequent intersections and high vehicle densities, however, the beacon may not be received properly due to signal attenuation or a collision, and thus, the locations of neighboring vehicles may not be accurately identified or actual neighbors may not be recognized as neighbors (or vice versa), lowering the broadcast performance of ABSM.

Especially, with the traffic concentration at the red traffic light, it is more likely that there exist multiple vehicles with the same number of neighboring vehicles that have not received the broadcast message, resulting in a broadcast collision. Broadcast collision degrades the performance of ABSM by causing additional broadcasts. In particular, many such broadcast collisions can occur in a series of attempted broadcasts when vehicles with no message are discovered by a beacon. Figure 3 shows the situation where vehicles with no message are discovered by a beacon. Due to the traffic concentration phenomenon of urban roads, vehicles with the message and vehicles with no message frequently approach each other in groups. Note that the discovery of neighbors and the confirmation of message possession can be verified only through beacons, and the beacons of different vehicles are not synchronized. When the first beacon from a vehicle in the group with no message is generated, multiple vehicles in the group with the message recognize it simultaneously and set the broadcast waiting timer accordingly. In this case, the same waiting time is set for all the vehicles with the same CDS status, and this results in simultaneous broadcasts. In case the broadcast waiting time of ABSM is shorter than the beacon cycle, a “broadcast and then collision” incident occurs repeatedly whenever each vehicle in the group with no message generates a beacon.

Furthermore, ABSM may incorrectly judge the message reception status of neighboring vehicles. ABSM implicitly determines the message reception status of neighbors by considering the distance between a neighbor and a message-forwarding vehicle without considering the signal attenuation by obstacles. This may, however, turn out to be a false guess. In particular, as shown in Figure 4, the reception status of neighbors cannot be accurately guessed near an

intersection. The broadcast of the forwarding vehicle may not be delivered to the vehicles on roads R1 and R2, which are close to the intersection, due to signal attenuation. However, vehicle A thinks that its neighboring vehicles on roads R1 and R2 have received the message by only considering the distance between the neighbors and a message-forwarding vehicle. This incorrect judgement affects the determination of the optimum forwarding vehicle.

2.2. Receiver Consensus (ReC). ReC is proposed to improve the speed of message delivery as well as the broadcast efficiency [21]. As with ABSM, ReC also constructs a CDS virtual backbone network for broadcast delivery. While ABSM determines the priority of forwarding vehicles according to the combined factors, that is, the number of neighboring vehicles that have not received the message and whether the vehicle is a CDS vehicle or not, ReC definitively gives higher priorities to CDS vehicles than to non-CDS vehicles. The broadcast priorities among the vehicles with the same CDS status are determined based on the ideal location, which is the average location of neighboring vehicles that have not received the broadcast message. The first time slot is assigned to the first priority vehicle for immediate broadcast with no delay. Furthermore, the n th time slot is assigned to the vehicle of n th priority, and the broadcast is carried out if no broadcast is heard in the previous time slots before the expiration of its own broadcast timer. Since CDS status of neighboring vehicle is also reflected in the decision of forwarding vehicle in ReC, CDS information is indicated in the beacon together with the location of vehicle.

ReC manages neighbors with three lists by adding list P to lists R and N , which are also used in ABSM. ReC is similar to ABSM in that neighbors are classified (lists P and N) by judging message reception status based on the locations of neighbors informed by the beacons and the location of the current forwarding vehicle. A vehicle in P is moved to R only when message reception is explicitly confirmed by a beacon. For each vehicle, the beacon cycle is divided by $|R| + |P|$ time slots. The forwarding vehicle that has performed broadcast moves its neighbors in list N to list P , and the vehicles that

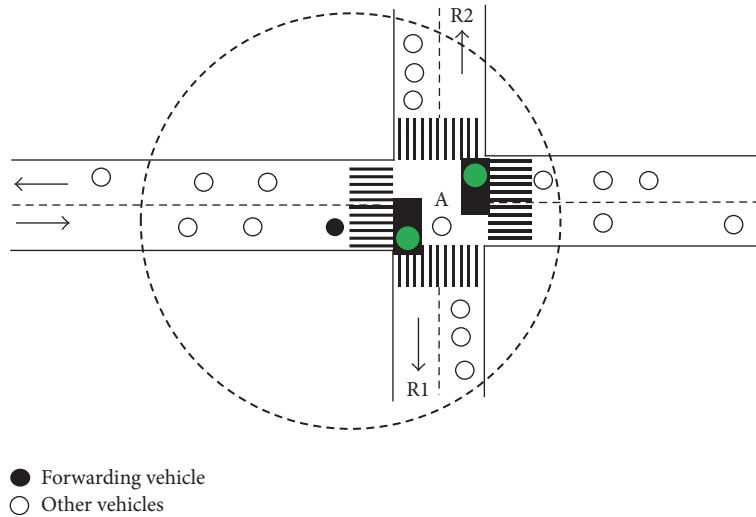


FIGURE 4: Example of a broadcast near an intersection.

have received message repeat this process until there is no vehicle in list N , thus ensuring message dissemination to the entire network.

As with ABSM, however, the inaccuracy of beacon information due to the signal attenuation around the intersection or beacon collisions as well as non-real-time characteristics of holding information may result in suboptimal selection of forwarding vehicle.

2.3. Broadcast Protocol with Road Network Topology (BRNT). Differing from ABSM and ReC, BRNT configures a CDS consisting of the road segments connecting the intersections instead of the individual vehicles [23]. Upon receiving a broadcast message, the broadcast timer of a vehicle is set according to where they are located so that the vehicles located at the intersections are assigned with the highest forwarding priority among the vehicles that receive the broadcast message, then the vehicles on the CDS road segments, and finally the ones on the other road segments. Specifically, the broadcast timer of the vehicles on a higher forwarding priority road segments is set with a shorter timer expiration value, and a vehicle forwards the broadcast message upon the expiration of its timer while the vehicles receiving the duplicate message cancel their message forwarding. The broadcast timer is further tuned so that the farther vehicle from the current forwarding vehicle is assigned with the higher forwarding priority on the same road segment.

If there exist one or more vehicles at every intersection or the signal attenuation at intersections is not significant so that all CDS road segments are connected by the intersections, BRNT could work optimally in terms of both delay and efficiency since the message is disseminated via the CDS road segments which have the shortest waiting time for forwarding, with no duplicate transmissions. As the ratio of intersections with no vehicle or with nonnegligible signal attenuation gets higher, though, the broadcast dissemination delay could get very long since not only some of the road segments connected to those intersection can only receive the message via a detouring path but also the broadcast

message may have to be disseminated via the non-CDS road segments, which requires longer forwarding delay than the CDS road segments, due to the incomplete connectivity of CDS road segments. Note that chance of having broadcast at the intersection is higher in the proposed VBURL than in BRNT since intersection broadcast cannot happen in BRNT if there is no vehicle at the intersection at the point of broadcast message reception, whereas VBURL may have the vehicle moving toward the intersection perform the intersection broadcast even in the case where no vehicle exists at the intersection at the point of broadcast message reception. Furthermore, no mechanism is provided to ensure the delivery of broadcast message to a vehicle that newly appears or missed the broadcast due to some signal interference on the road segment where the message broadcast has been completed once.

3. VANET Broadcasting for Urban Areas Based on Road Layout

Safety service aims to alert the occurrence of a traffic accident or the falling of obstacles on the road through broadcasts to all vehicles near the point of accident so that they can decelerate or reroute to a bypass. The purpose of the proposed VBURL is to improve the efficiency while ensuring the reliability of safety message broadcasting by considering the environmental characteristics of urban roads such as a high vehicle density, as well as frequent intersections and traffic signals. VBURL attempts to take appropriate broadcast dissemination in consideration of the road layout without depending on neighboring vehicle information which is identified through a beacon. On straight roads between intersections, where the effect of signal attenuation by obstacles is low, it allows the vehicle located farthest from the current forwarding vehicle perform the next broadcast forwarding in order to deliver the message to the largest possible number of vehicles similar to the Contention Based Forwarding (CBF) [30]. Meanwhile, to facilitate the message dissemination around the intersections, VBURL makes an additional broadcast happen

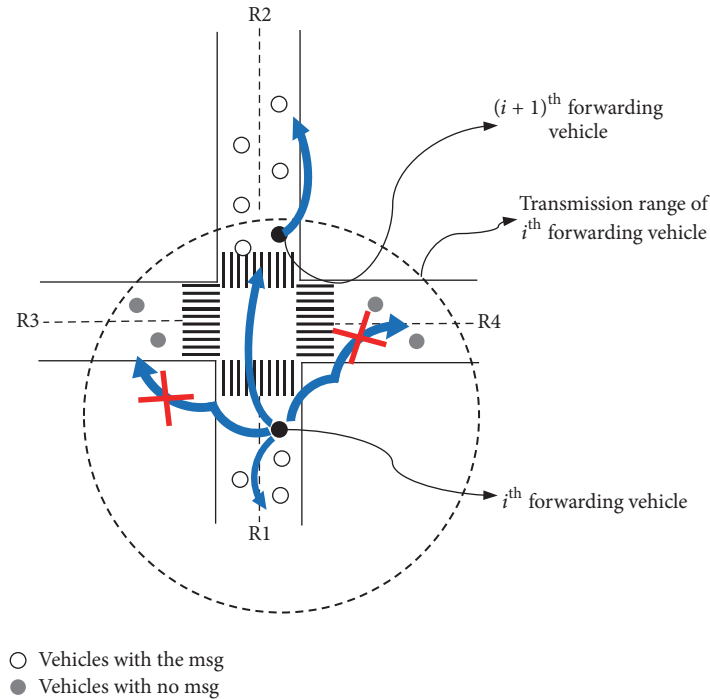


FIGURE 5: Broadcasting near an intersection.

at the intersections in addition to the one made by the farthest vehicle as long as there exists a vehicle hearing the broadcast at the intersection or else there exist one or more vehicles that are moving toward the intersection with that intersection within their transmission range. Since the effect of signal attenuation caused by the road side obstacles is low inside of the intersections, it facilitates the prompt and reliable dissemination of safety message toward all roads connected to the intersections. Furthermore, in order to achieve reliability, a rebroadcast is performed if broadcast dissemination of the next forwarding vehicle is not heard or a neighboring vehicle that has not received the message is discovered by a beacon. In Section 3.1, the safety message broadcasting method of VBURL is explained. The rebroadcasting method for the reliability in safety message dissemination is explained in Section 3.2.

3.1. Broadcasting of Safety Message. When a vehicle receives a new safety message that is required to be broadcast, it determines the forwarding method depending on the existence of an intersection within its transmission range. First, the forwarding method of a vehicle that has no intersection within its transmission range is described. The forwarding method when there is an intersection within the transmission range is then described.

3.1.1. Broadcasting with No Intersection. The vehicle that has received a new safety message saves it in the broadcast message buffer and maintains it until the expiration of message life time. In addition, it uses the Forwarding Timer (FT) to determine the next forwarding vehicle for continuous dissemination of the message. Similar to CBF, every vehicle receiving the safety message sets its FT in inverse proportion

to its distance from the current forwarding vehicle using the location information of forwarding vehicle conveyed in the message, and the vehicle whose timer expires before hearing others' broadcast performs the broadcast. As a result, the farthest vehicle from the current forwarding vehicle takes the role of message-forwarding vehicle. On a straight road where the effect of obstacles is relatively little, broadcasting by the vehicle that is farthest from the message-forwarding vehicle potentially disseminates the message to the largest possible number of vehicles that have not received the message.

If the received safety message is already stored in the buffer, it will be labeled as a duplicate message. When a vehicle receives a duplicate of the message for which the FT is running, it means that another vehicle already has taken the role of the next forwarding vehicle. In this case, the FT is released to avoid unnecessary duplicate broadcasts.

3.1.2. Broadcasting with an Intersection. Near an intersection, due to the effect of obstacles such as buildings around the intersection, there can be roads where message dissemination is impossible through the simple broadcasting by a vehicle whose FT expires first. For instance, the vehicles on roads R3 and R4 in Figure 5 cannot receive the message forwarded by the vehicles that are selected according to the FT expiration because of the signal attenuation due to the buildings around the intersection. On the other hand, as shown in Figure 6, the center of an intersection is least vulnerable to the signal attenuation by surrounding obstacles. In this paper, it is defined as the "intersection area." To facilitate prompt and reliable broadcast message dissemination to all roads adjacent to an intersection, hence, VBURL maximizes the chance of broadcast occurring within the intersection area by having not only the vehicle in the intersection area but also the vehicle

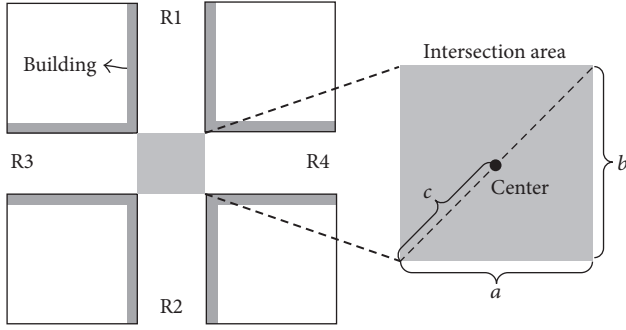


FIGURE 6: Intersection area.

moving toward the intersection, in case there is no vehicle in the area at the point of broadcast message reception, perform the intersection area broadcast forwarding. Specifically, VBURL makes the first vehicle that arrives at the intersection perform the intersection area broadcast forwarding in case there is no vehicle at the intersection at the point of broadcast message reception but there exist one or more vehicles moving toward the intersection with that intersection within their transmission range.

In order to do this, the vehicles that have the intersection in their transmission range (groups (1) and (2) in Figure 7) and the vehicles that are already located within the intersection area (group (3) in Figure 7) set the Intersection Forwarding Timer (IFT) according to (1) in addition to the FT. The vehicles in the intersection area, group (3), set their IFT in proportion to their distance from the center of intersection,

$$\text{IFT} = \begin{cases} \text{IFT}_{\text{time.out}} = \text{MaxWT} \times \frac{D_{\text{vehicle.to.center}}}{c}, & \text{if intersection vehicle} \\ \text{IFT}_{\text{max}}, & \text{if intersection within TR and approaching intersestion.} \end{cases} \quad (1)$$

- (i) IFT_{max} is maximum timer value that is large enough not to expire until the vehicle enters the intersection;
- (ii) MaxWT is maximum waiting time;
- (iii) $D_{\text{vehicle.to.center}}$ is distance from the center of intersection to the vehicle;
- (iv) c is half of the diagonal length of the intersection area (see Figure 6).

3.2. Rebroadcast of Safety Messages. For reliable broadcasting, the safety message must be rebroadcast in case the safety message fails to be disseminated to the next forwarding vehicle. For this purpose, it must be possible for the current forwarding vehicle to confirm the reception of a safety message by the next forwarding vehicle. There are largely two methods of confirming the receipt of a safety message: explicit acknowledgment, which requires the exchange of a control message, and implicit acknowledgment, which regards the broadcast of safety message by the next forwarding vehicle

so that the vehicle closer to the center of intersection where the effect of signal attenuation by surrounding buildings is the least will take the role of broadcasting before others. On the other hand, the vehicles moving toward the intersection, such as groups (1) and (2), set their IFT to the maximum value that is large enough not to expire until they reach the intersection (IFT_{max}). Upon the arrival at the intersection, if they have not heard the broadcast from the intersection area yet, they reset their IFT to $\text{IFT}_{\text{time.out}}$. Consequently, when there are vehicles in the intersection area, the vehicle that is closest to the center of the intersection area takes charge of broadcasting within the intersection area, whereas, if there is no vehicle in the intersection area, the vehicle that arrives at the intersection first takes charge of it.

The goal of IFT is to facilitate the dissemination of broadcast message to all roads adjacent to the intersection. Thus, it is released only when a duplicate broadcast from the intersection area is heard. The FT and IFT may be running simultaneously at a vehicle for a specific safety message, and whichever that expires first makes the broadcast be performed. If the FT expires first and the vehicle is in the intersection area, it means that broadcast is already occurring in the intersection area due to the FT expiration, and the IFT is released to prevent an unnecessary duplicate broadcast. On the other hand, if the vehicle is still on its way to the intersection upon the broadcasting caused by the FT expiration, broadcast within the intersection area is still necessary and the running IFT is maintained. If the FT is running in the vehicle when the IFT expires, the FT is always released to prevent unnecessary duplicate broadcasts:

as the reception confirmation message and considers that all vehicles located between itself and the next forwarding vehicle have received the safety message [9–13]. In VBURL, the implicit acknowledgment is deployed for the efficient use of limited wireless resources considering the VANET environments, similarly to the method used in other studies [9, 12, 13]. In general, when the implicit acknowledgment method is used, if the broadcast of the next forwarding vehicle is not heard within a certain amount of time after broadcasting, rebroadcasts are performed repeatedly for a maximum count. In addition, if the vehicle with an effective safety message discovers a neighbor that has not received the message after the broadcast has been completed, it makes an additional broadcast to improve reliability.

3.2.1. Rebroadcast of a Forwarding Vehicle. When the vehicle that has broadcast a safety message receives it redundantly from another vehicle, it assumes that successful progress of continuous message dissemination is made by next forwarding vehicles. Otherwise, the vehicle determines that the dissemination of broadcast has stopped and performs a rebroadcast. For this purpose, every forwarding vehicle sets the

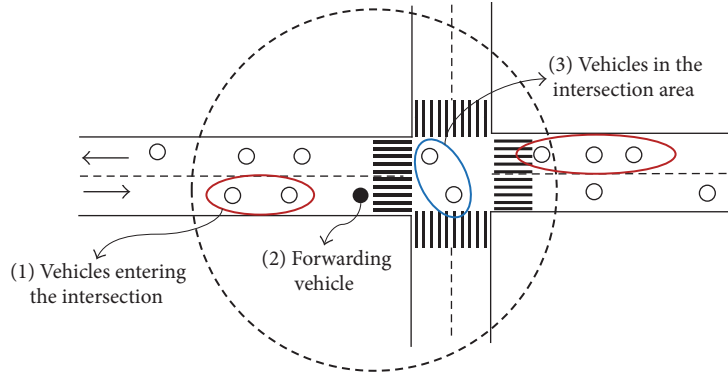


FIGURE 7: Target vehicles of IFT setting for broadcasting in the intersection area.

Rebroadcast Timer (RT) after broadcasting a message. In the study [9], if a vehicle that has performed broadcast receives a broadcast from the next forwarding vehicle, it assumes that all neighboring vehicles between the two forwarding vehicles have received the message. However, this may not be a valid assumption if there are roads where broadcast dissemination is not smooth due to signal attenuation by obstacles. In particular, around the intersection, receiving a broadcast from the next forwarding vehicle that comes from a certain road may not mean successful progress of broadcast dissemination toward every road adjacent to the intersection. Consequently, in VBURL, the vehicle that has performed broadcast in the intersection area sets the Intersection Rebroadcast Timer (IRT) to verify that the message has been delivered to all roads adjacent to the intersection while the forwarding vehicle that has performed broadcast with no intersection within its transmission range sets the RT. Receiving a duplicate message for which the RT is running means that the next forwarding vehicle has successfully received the message that the vehicle has broadcast. Thus, the vehicle considers that its responsibility for message dissemination has been transferred to the next forwarding vehicle and releases the RT. On the other hand, the IRT is released after receiving the duplicate message from all roads adjacent to the intersection where neighbor vehicles exist, because the purpose of IRT is to confirm that the message has been disseminated to all roads adjacent to the intersection. For the purpose of figuring out the roads where neighboring vehicles exist and for this purpose only, VBURL leverages the holding information which has been obtained from the periodic beacons.

To avoid early expiration, RT and IRT are defined according to (2) considering the time over which the safety message has been disseminated to the transmission range and the delay until the safety message returns by broadcasting after the broadcast waiting time of the next forwarding vehicle. RT or IRT expires when there is a road where message dissemination has not been confirmed. Therefore, when RT or IRT expires, the forwarding vehicle rebroadcasts the same message and sets the timer again to wait until message reception is confirmed from all roads to which the broadcast must be disseminated. These timers can be reset for the maximum

number set by the system so as to repeat the rebroadcast process as needed:

$$RT_{\text{timeout}} = \text{MaxWT} + 2 \times \text{MaxPT}. \quad (2)$$

- (i) MaxWT is maximum waiting time;
- (ii) MaxPT is maximum dissemination delay of the broadcast message, which is the time until the message is disseminated to the transmission range.

3.2.2. Rebroadcast for the New Neighboring Vehicles with No Message. Neighboring vehicles that have not received a broadcast of the safety message may appear for various reasons, such as collision, radio interference, and the entrance of a new vehicle. In this case, an additional broadcast must be performed to deliver the safety message to the vehicle with no message. The Neighbor Forwarding Timer (NFT) is used for this purpose. The NFT is set when none of FT, IFT, RT, and IRT is running for a valid safety message, and the message is not specified in the received message list in the beacon of a neighbor. The purpose of NFT is to avoid the collision of broadcasts or unnecessary broadcasts by deciding the optimum vehicle that will take the broadcasting role when multiple vehicles with the message discover a vehicle with no message simultaneously in a geographically close area. For this purpose, among the vehicles that have the message and have received a beacon from a vehicle with no message, VBURL makes the vehicle closest to the vehicle with no message perform the broadcast of safety message. Considering that usually the vehicles with no message and the vehicles with the message encounter each other in groups on urban roads due to the traffic signals as shown in Figure 3, if a vehicle closest to the vehicle with no message takes charge of message delivery, it can deliver the message to more vehicles with no message through one broadcast. Specifically, the values of the NFT are set by (3). The distance among the vehicles with the message may be quite small due to vehicle concentration upon the wait traffic signal. To prevent unnecessary broadcasts, VBURL makes the difference in NFT

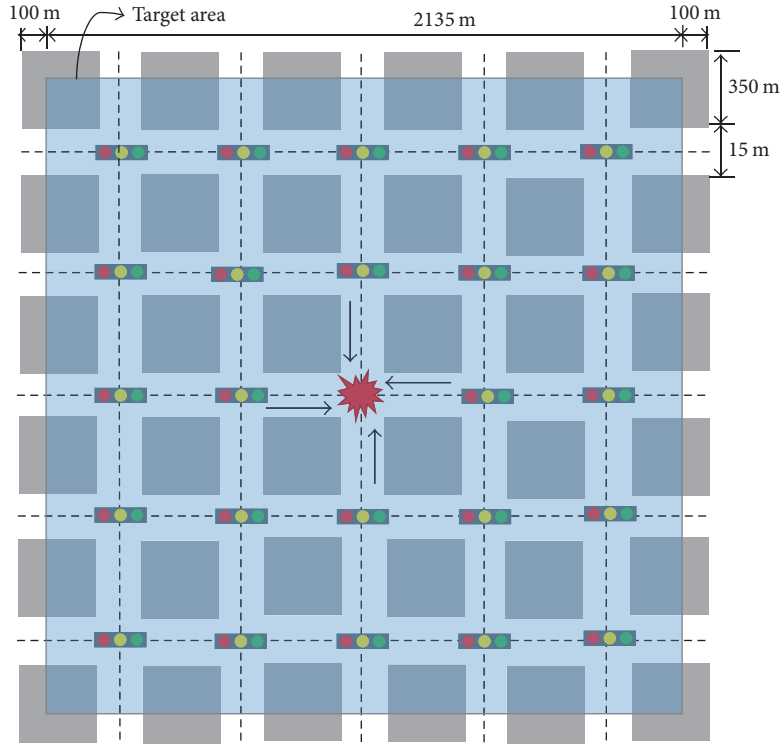


FIGURE 8: Urban road layout for simulation.

values set by vehicles with the message be greater than the propagation delay by increasing MaxWT n times in NFT value calculation. As with the FT, unnecessary duplicate broadcasts are avoided by releasing the NFT when a vehicle running the NFT receives a duplicate broadcast, that is, when the message has been delivered by another forwarding vehicle. NFT may also be released if it is confirmed through the beacons that have been received during the running of NFT that all neighbors have received the message:

$$\text{NFT}_{\text{timeout}} = n \times \text{MaxWT} \times \frac{D}{\text{TR}}. \quad (3)$$

- (i) MaxWT is maximum waiting time;
- (ii) D is distance between a vehicle with a message and a vehicle with no message;
- (iii) TR is transmission range.

The broadcasting and rebroadcasting mechanisms of VBURL are illustrated in pseudocodes in Algorithm 1.

4. Performance Evaluation

A simulation is conducted using OPNET to compare the performance of VBURL with ABSM and ReC, which are the legacy schemes implementing the reliable broadcast for urban roads on top of IEEE 802.11p. The simulation environments are first explained in Section 4.1. In Section 4.2, the numerical results of simulation are then presented.

4.1. Simulation Environments. The urban roads used in the experiment are bidirectional one-lane roads where 25 intersections are located at intervals of 350 m as shown in Figure 8. It is assumed that 10–20 m high buildings are located along the road and the signal attenuation by the surrounding buildings is implemented using the knife-edge model [31].

At the beginning of the simulation, vehicles running at random speeds start one by one at fixed intervals at each of the 20 entrances in the simulation network roads and are directed to run straight along the road. The vehicle arriving at the end of the road exits the simulation network, and a new vehicle instead starts on the lane of the opposite direction to maintain a constant vehicle density on the simulation network roads. Each intersection has signal lights, and the vehicles repetitively drive/wait according to the signals. All of the signal lights on the east-west roads turn to driving (waiting) signals simultaneously, and all of the signal lights on the south-north roads turn to waiting (driving) signal simultaneously. The vehicles are set to stop at 4 m intervals at the waiting signal of intersections considering the average body length of vehicles.

As shown in Figure 8, the accident point is at the center of the simulation network, and it is assumed that the safety message is first broadcast from the accident point. The east-west and south-north roads, excluding 100 m on each edge, are set as the target area (shaded area in Figure 8) to which the safety message must be broadcast. Furthermore, the vehicles in the target area when the safety message is broadcast for the first time are assumed to be the target vehicles that are considered in the message reception ratio. The safety message

```

Reception of a broadcast message
If (new message)
    Save the message
    Set FT
    If (intersection vehicle)
        Set IFT = IFTtime.out
    Else if (intersection within TR && approaching intersection)
        Set IFT = IFTmax
    Else
        If (FT is running)
            Cancel FT
        If (IFT is running)
            If (implicit ACK from all branches where neighbors exist || msg from intersection vehicle)
                Cancel IFT
            Else
                Keep waiting implicit ACK
        If (RT is running)
            Cancel RT
        If (IRT is running)
            If (implicit ACK from all branches where neighbors exist)
                Cancel IRT
            Else
                Keep waiting implicit ACK
        If (NFT is running)
            Cancel NFT
Timer expiration
If (FT || NFT)
    Broadcast the message
    If (intersection vehicle)
        Set IRT = RTtime.out
    Else
        Set RT = RTtime.out
    Wait for implicit ACK
Else if (IFT)
    Broadcast the message
    Set IRT = RTtime.out
    If (FT is running)
        Cancel FT
Else if (RT || IRT)
    If (num. of rebroadcast by RT or IRT less than maximum)
        Broadcast the message
        Num. of rebroadcast by RT or IRT ++
        Set RT or IRT = RTtime.out
        Wait for implicit ACK
Arrival at intersection zone
If (IRT is running)
    Reset IFT = IFTtime.out
Meet new neighbor vehicles without message
If (FT, IFT, RT, and IRT are NOT running)
    Set NFT

```

ALGORITHM 1: Pseudocode of VBURL.

size is 100 bytes, and the life time of the safety message is set to 100 seconds.

Both ABSM and ReC use the location information of neighboring vehicles transmitted through beacons, and when the beacon cycle increases, the accuracy of neighboring vehicles' location information decreases. Furthermore, all of the three compared schemes discover the neighboring vehicles

with no message by exchanging the received safety message identifier through beacons. Thus, when the beacon cycle is short, the broadcast dissemination attempts for the vehicles with no message are made frequently. In this experiment, therefore, beacon exchange cycle, which is an important parameter that can affect the performance, is increased to 0.5, 1.0, 3.0, 5.0, 7.0, and 10.0 seconds.

TABLE 1: Simulation Parameters.

Simulation parameters	Values
Transmit power	0.005 W
Min. frequency	5885 MHz
Data rate	6 Mbps
Channel bandwidth	10 MHz
Transmission range	300 m
Network dimensions	Target area, 2,135 m × 2,135 m, 1 lane in 2 directions
Vehicle velocity	20–30 km/h (congestion scenario) 40–50 km/h (smooth scenario)
Vehicle density	4000 vehicles, 86.4 vehicles/km (congestion scenario) 2000 vehicles, 43.2 vehicles/km (smooth scenario)
Beacon interval	(0.5, 1.0, 3.0, 5.0, 7.0, 10.0) seconds
Beacon hold time	(1.5, 3.0, 9.0, 15.0, 21.0, 30.0) seconds

The driving speed on urban roads is generally slower than on the express or freeways due to a high vehicle density and frequent intersections. Furthermore, it is usual to have higher traffic density during the commuting hours due to a large number of inflowing vehicles. In this experiment, two scenarios of traffic flow are assumed: a case of rush hours, such as commuting hours, during which vehicles are congested (hereinafter referred to as the “congestion scenario”), and a case of noncommuting hours, during which the traffic flow is relatively smooth (hereinafter referred to as the “smooth scenario”). For the congestion scenario, longer traffic signal cycles are set to reflect the reality. Specifically, for the congestion scenario, 200 vehicles running at random speeds between 20 and 30 km/h start at 1.5 sec intervals at each road entrance (a total of 4000 vehicles, i.e., traffic density of 86.4 vehicles/km), and the waiting/driving signal duration is set to 25 seconds. For the smooth scenario, 100 vehicles running at random speeds between 40 and 50 km/h start at 2 sec intervals at each road entrance (a total of 2000 vehicles, i.e., traffic density of 43.2 vehicles/km), and the signal changes at intervals of 15 seconds.

In this experiment, the MaxWT value is set to 0.1 sec, which is used to set the FT ($FT_{\text{timeout}} = \text{MaxWT} \times (1 - D/TR)$), IFT, RT, and IRT in VBURL, and the MaxPT used to set the RT and IRT is set to 0.003 sec. For the NFT, n is set to 10 for the maximum waiting time of 1 sec. The parameter for broadcast in ABSM is set to $W = 0.25$ sec according to [20]. The maximum waiting time used to set the waiting time in ReC is set as the beacon cycle according to [21]. Table 1 outlines the major simulation parameters used in this experiment and their values.

The performance measurement values collected for performance evaluation are as follows. All the measurement values are averages of the measurements for 10 broadcasts.

- (1) Message reception ratio: this is the ratio of vehicles that have received the message before expiration of the life time of the message among all the target

vehicles. It is used to evaluate the reliability of a broadcast scheme.

- (2) Number of receiving vehicles per broadcast: this is the number of receiving vehicles per broadcast forwarding. It is used to evaluate the efficiency of a broadcast scheme.
- (3) End to end delay: this is the time elapsed until a target vehicle receives a message after the message is first generated. It is used to evaluate the rapidity of a broadcast scheme.

4.2. Simulation Results. The performances of three schemes are compared in terms of reliability, efficiency, and rapidity, respectively.

4.2.1. Reliability. All the three compared schemes show a 99% or higher reception rate in all beacon cycles of the congestion and smooth scenarios. VBURL, ABSM, and ReC ensure broadcast reliability by performing rebroadcast whenever a vehicle that has not received the message is found. The reception rate does not reach 100%, though, because there are vehicles moving to exit the road on each edge of the target area and exit the simulation network before receiving the message. Because these vehicles are moving farther away from the accident point, there is no safety problem even if they do not receive the message. It is only that they could not take the helpful role to forward safety messages to vehicles beyond the target area.

4.2.2. Broadcasting Efficiency. Figure 9 shows the ratio of vehicles that receive the message against the broadcast count, which signifies the efficiency of a broadcast scheme. The efficiency of VBURL is 2–100 times higher than that of the ABSM and ReC. In particular, the difference is greater in the congestion scenario where the loss of the beacons and traffic concentration are more significant. The beacon inaccuracy caused by the loss of the beacons aggravates the performance of ABSM and ReC whose forwarding vehicle is determined based on the location information provided by the beacons. On the other hand, the performance of VBURL is intact regardless of the loss of beacons in the congestion scenario since it mainly uses the real-time or semistatic information in its forwarding decision. Furthermore, the efficiency of VBURL even becomes better in the congestion scenario because the number of neighboring vehicles included in the transmission range of a forwarding vehicle is larger.

The efficiency of VBURL decreases slightly as the beacon exchange cycle is lengthened in both of the scenarios. It is because, for the intersection broadcast, VBURL also utilizes holding information from the beacons to determine the roads on which neighboring vehicles exist. As the beacon cycle increases, the beacon information holding time also increases, and, as a result, a road with no neighboring vehicle anymore actually tends not to be recognized early enough, causing unnecessary rebroadcasts. Furthermore, for higher vehicle speed, the information accuracy becomes more sensitive to the beacon cycle. Thus, the broadcast efficiency

TABLE 2: Number of broadcasts due to the reception of a safety message (A) and the number of broadcasts due to the discovery of a vehicle with no message by a beacon (B).

(a) Congestion scenario								
Beacon cycle	VBURL		ABSM		ReC			
	(A)	(B)	(A)	(B)	(A)	(B)	(A)	(B)
0.5	175.6	9.7	192.1	21148.1	573.9	9321.7		
1.0	190.5	8.9	219.5	21727.2	371.8	1854.8		
3.0	181.8	7.3	267.4	24039.6	796.7	1581.6		
5.0	182.2	7.9	271.7	16707.0	751.6	875.3		
7.0	193.7	8.3	305.4	11911.1	757.0	674.0		
10.0	206.3	10.5	376.6	10384.6	754.3	346.8		

(b) Smooth scenario								
Beacon cycle	VBURL		ABSM		ReC			
	(A)	(B)	(A)	(B)	(A)	(B)	(A)	(B)
0.5	155.1	3.6	174.8	2434.8	334.5	1692.7		
1.0	157.7	3.1	190.2	2979.2	253.9	299.2		
3.0	166.8	4	217.1	1831.2	227.5	135.4		
5.0	175.2	4	249.3	1544.4	244.8	119.5		
7.0	166.6	5.1	260.4	1318.0	287.1	97.3		
10.0	194.8	5.4	271.5	1344.3	451.3	95.0		

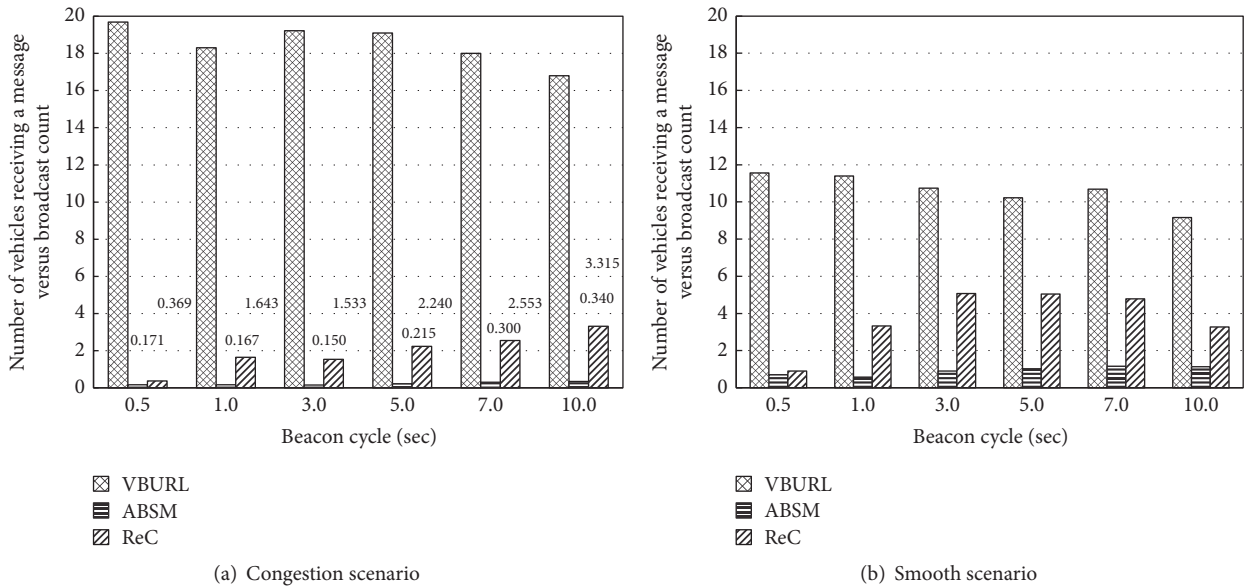


FIGURE 9: Broadcast efficiency.

decreases slightly in the 7 sec or longer beacon cycles in the congestion scenario and in 3 sec or longer beacon cycles in the smooth scenario in VBURL.

ABSM has the lowest efficiency among the compared schemes due to its great inefficiency in the broadcast when a new neighbor with no message is found as shown in Table 2. In the case of ABSM, the efficiency increases slightly in both congestion and smooth scenarios as the beacon cycle lengthens since the efficiency of ABSM is mainly determined by the efficiency of rebroadcast upon the discovery of with-no-message neighbors, for which the efficiency is better with the

longer beacon cycle as shown in Table 2. On the other hand, in the case of ReC, as the beacon cycle becomes longer, the efficiency increases in the congestion scenario whereas the efficiency increases first and then decreases in the smooth scenario. It is because, in ReC, the effect of an efficiency decrement due to the inaccuracy of location information resulting from the long beacon cycle is more prominent in the smooth scenario where the difference in beacon accuracy by the beacon cycle is greater due to the faster speed of vehicles.

Specifically, the message broadcast is attempted when (1) the vehicle receives a new safety message or (2) neighboring

vehicles with no message are detected by the beacons. Table 2 shows the number of broadcasts occurred during the entire simulation according to by which incident the broadcast is attempted. In VBURL, the least number of broadcasts are incurred on both of the incident (1) and (2) in all beacon cycles of the congestion and smooth scenarios. In particular, In VBURL, the broadcasts are performed mainly by receiving a new safety message. On the contrary, in ReC, more broadcasts are incurred by the detection of a vehicle with no message for relatively short beacon cycles. Furthermore, in ABSM even for all lengths of beacon cycles most of the broadcasts are caused by the incident (2).

The difference between VBURL and the two compared legacy schemes is particularly prominent in (2). Due to the characteristics of urban roads, vehicles with a message and vehicles with no message often encounter each other in groups. When one of the vehicles in the with-no-message group issues a beacon, multiple vehicles in the with-the-message group may receive this beacon and the process to determine the next forwarding vehicle starts immediately. In case of ABSM, all CDS (similarly all non-CDS) vehicles with the message are assigned the same broadcast priority upon receiving the beacon and perform the broadcast simultaneously resulting in broadcast collisions. Moreover, since the beacon generation times of vehicles are not synchronized, in the worst case, whenever a beacon is issued from a vehicle in the with-no-message group, the vehicles in the with-the-message group may attempt to broadcast and cause a collision. In ReC, broadcast priority is assigned in the order of proximity to the vehicle with no message, instead of simply reflecting the number of neighbors with no message as with ABSM (which is one for all the vehicles in the with-the-message group that hears the beacon from a with-no-message vehicle). Therefore, ReC has a lower possibility of the same broadcast priority among the vehicles in with-the-message group. However, a similar problem to ABSM may still occur due to the inaccuracy of beacon information caused by the loss of a beacon due to collisions in traffic concentration.

The size of a vehicle group tends to be larger in an environment with high vehicle density and worsens the situation. Thus, in VBURL, ABSM, and ReC, the number of broadcasts due to the discovery of a vehicle with no message in the congestion scenario is approximately 2 times, 9.2 times, and 2.1 times larger than in the smooth scenario, respectively. Both ABSM and ReC have a decreased chance of performing broadcast by discovering the vehicles with no message as the beacon cycle is lengthened. As a result, the number of broadcasts owing to the discovery of vehicles with no message decreases as the beacon cycle gets longer in Table 2.

VBURL incurs the smallest number of broadcasts resulting from the reception of a safety message even though the difference among the schemes is not as large as the difference in terms of the number of broadcasts resulting from the discovery of vehicles with no message. In all three schemes, the number of broadcasts resulting from the reception of a safety message is around 1.1–1.5 times larger in congestion scenario than in the smooth scenario. It is because the loss of a beacon due to a beacon collision causes the inaccuracy of beacon information in the environment with high vehicle density

resulting in decision of suboptimal forwarding vehicle and/or rebroadcast. The performance difference depending on the traffic density scenario is the least in VBURL though since it is the least dependent on the holding information obtained from beacons; that is, the utilization of holding information is limited to the rebroadcast decision at the intersections.

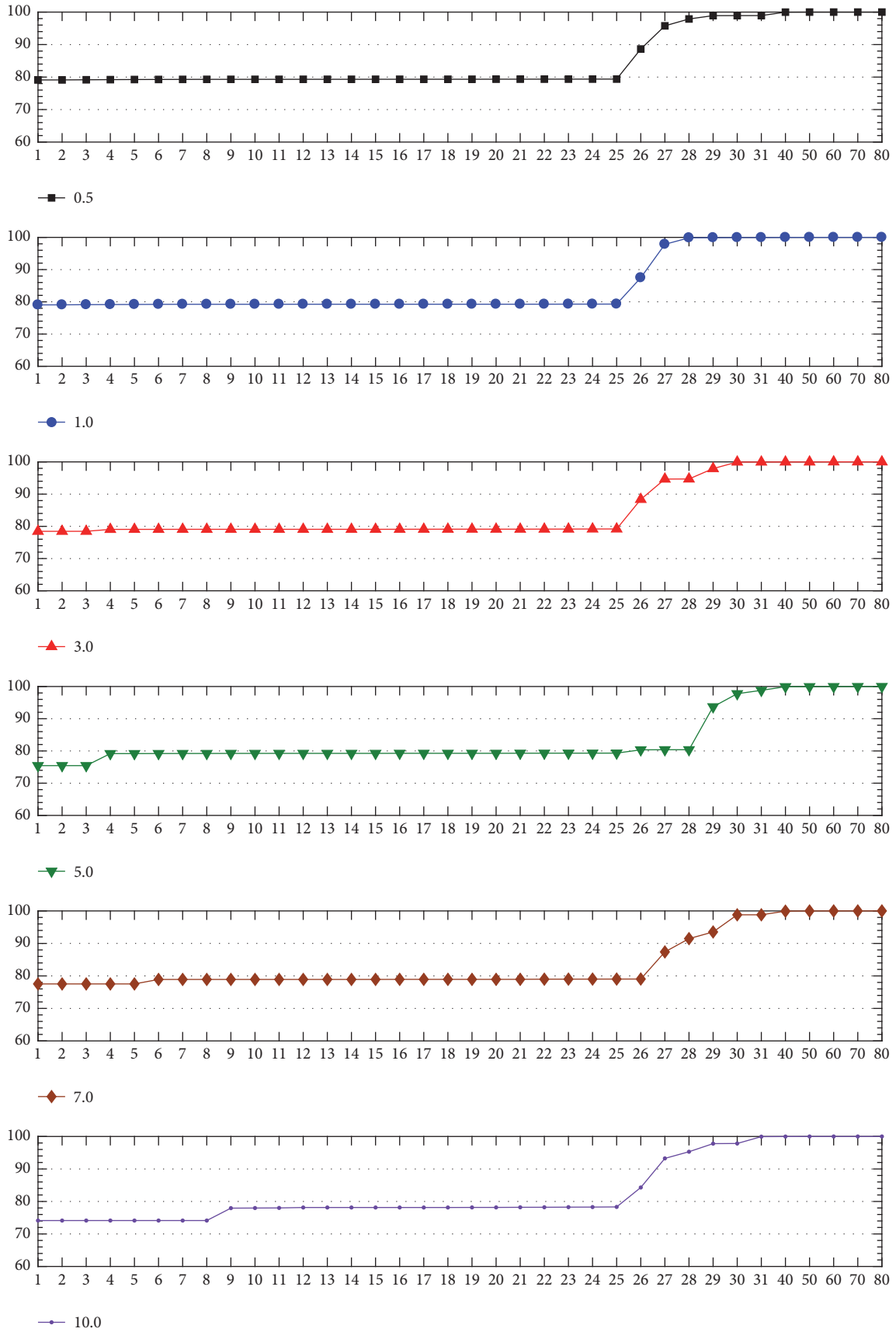
In VBURL, the number of broadcast attempts upon receiving a new safety message slightly increases as the beacon cycle is lengthened. It is because, as the beacon cycle lengthens, a road with no neighboring vehicle anymore actually tends not to be recognized early enough, causing unnecessary rebroadcasts.

The number of broadcasts by the reception of a new safety message is the largest in ReC, which is the most dependent on the accuracy of location information provided by beacons. In ReC, if the beacon cycle is too short, not only the loss of the beacons due to collisions increases, but also more frequent broadcasts occur because the broadcast waiting time becomes shorter (note that the maximum waiting time is set as the beacon cycle in ReC). Note that difference in waiting time among the vehicles as well as the length of waiting time becomes smaller as the maximum waiting time becomes shorter and vehicle density becomes higher, leading to higher chance of unnecessary broadcasts. On the other hand, when the beacon cycle becomes too long, not only the inaccuracy of location information obtained from beacon increases, but also the number of vehicles considered as neighbors increases, both of which lead to the degradation in efficiency. As a result, in ReC, the number of broadcasts initiated by the reception of a new safety message first decreases as the beacon cycle became longer, then it starts to increase when the beacon cycle rises above a certain value.

In the case of ABSM, the number of broadcast attempts upon receiving a new safety message increases as the beacon cycle is lengthened. For ABSM, not only the beacon inaccuracy increases as the beacon cycle is lengthened but also the average number of neighboring vehicles tends to increase due to the increase in beacon hold time. If the number of vehicles regarded as neighbors increases, the broadcast waiting time becomes shorter and tends to be similar among vehicles in ABSM, thus increasing the chance of unnecessary broadcasts or collisions.

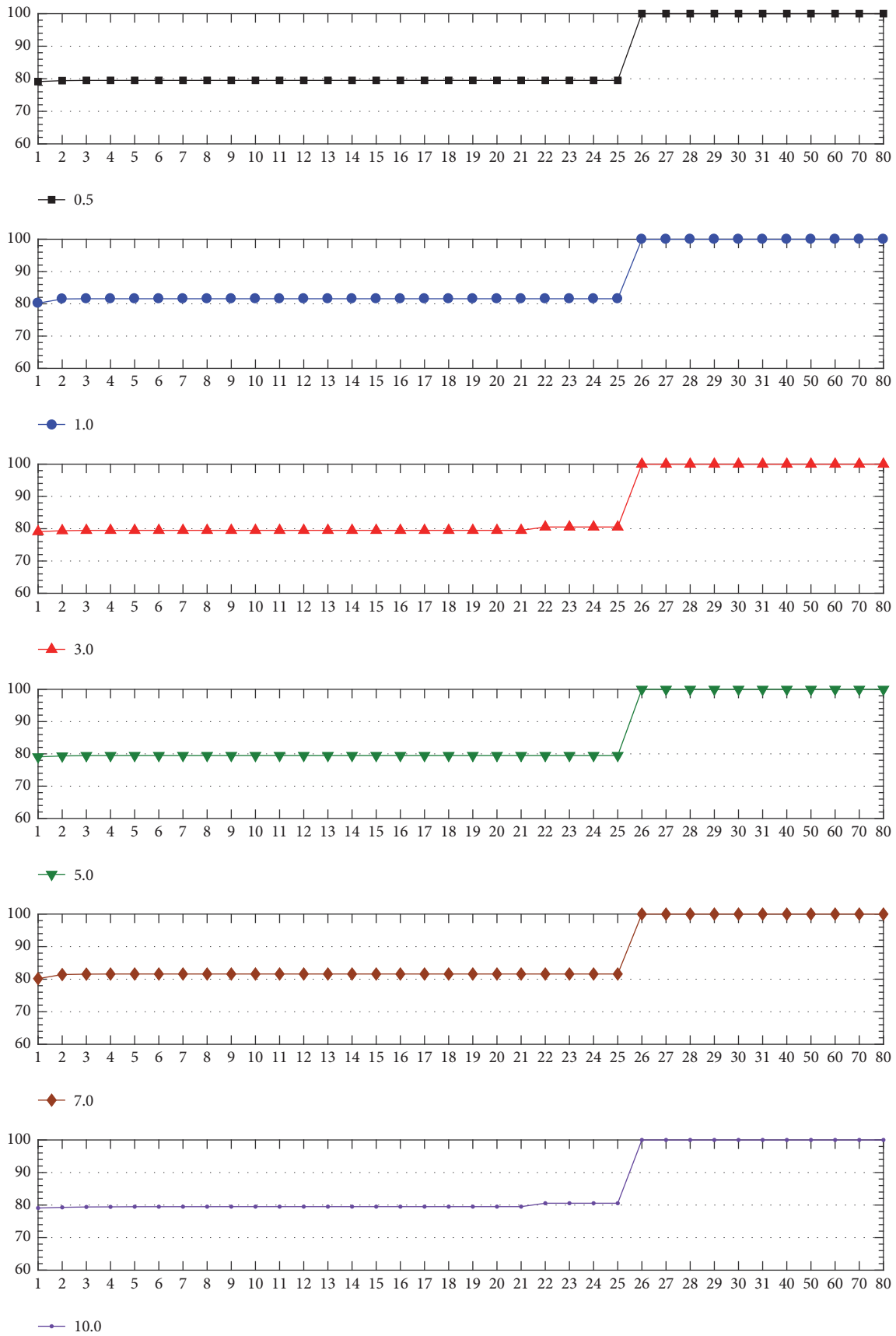
4.2.3. Latency. Figure 10 shows the transient behavior in the changing ratio of vehicles receiving the message over time in the congestion and smooth scenarios, respectively. In both congestion and smooth scenarios of all the three schemes, at least 99% of vehicles receive the message after an interval that is slightly longer than the traffic signal waiting time after the first broadcast. It is because when one interval of signal waiting time passes after the first broadcast, it is highly likely that a vehicle with a message has passed every intersection. As a result, the possibility of message dissemination to most of the roads in the simulation network is high.

The percentage of vehicles receiving a message within one second after the first broadcast in the smooth scenario (Figures 10(d), 10(e), and 10(f)) is lower than in the congestion scenario (Figures 10(a), 10(b), and 10(c)). It is because the vehicle density of the smooth scenario is lower than that of the



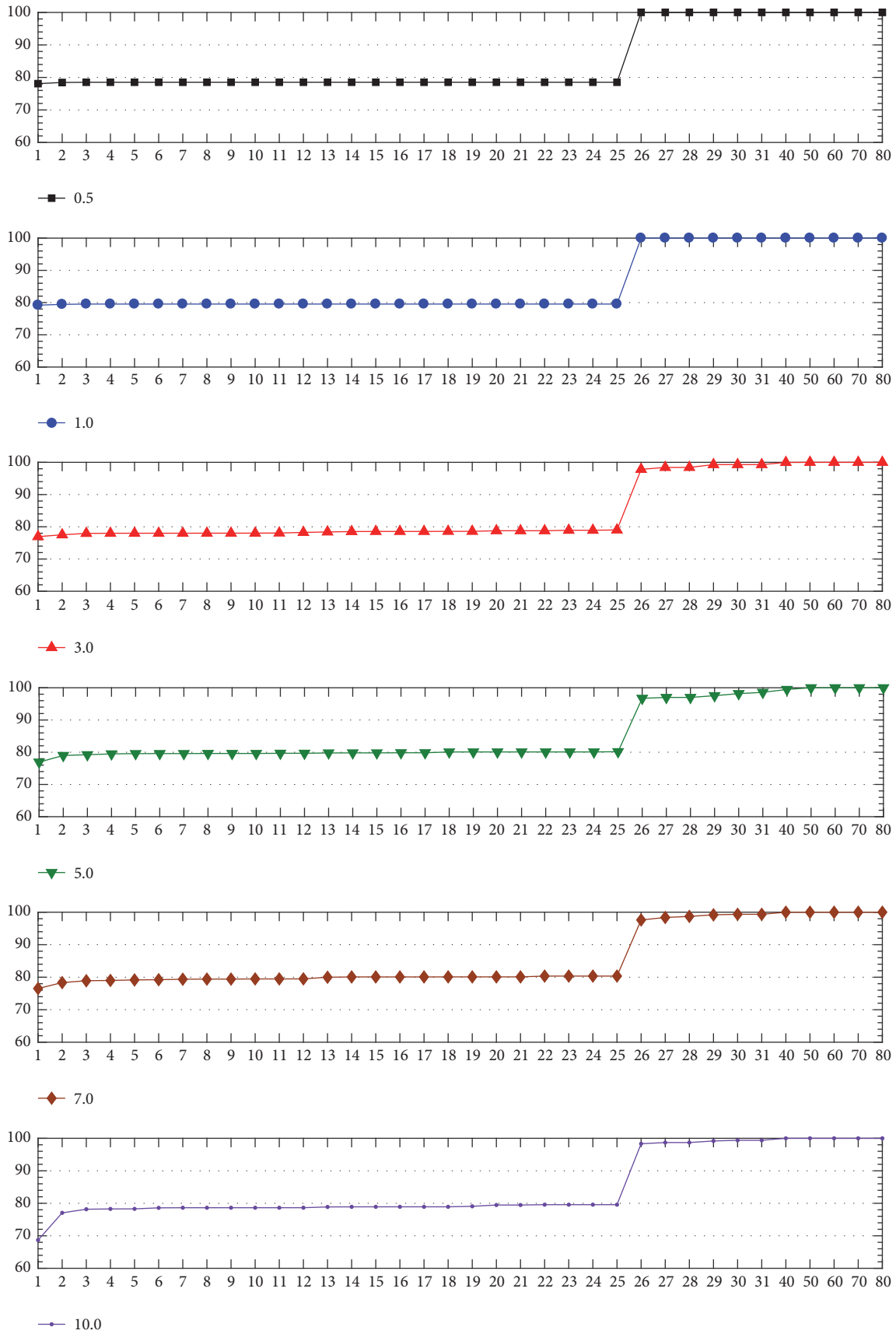
(a) Congestion scenarios: VBURL (x axis: time (sec), y axis: percentage of vehicle receiving the message)

FIGURE 10: Continued.



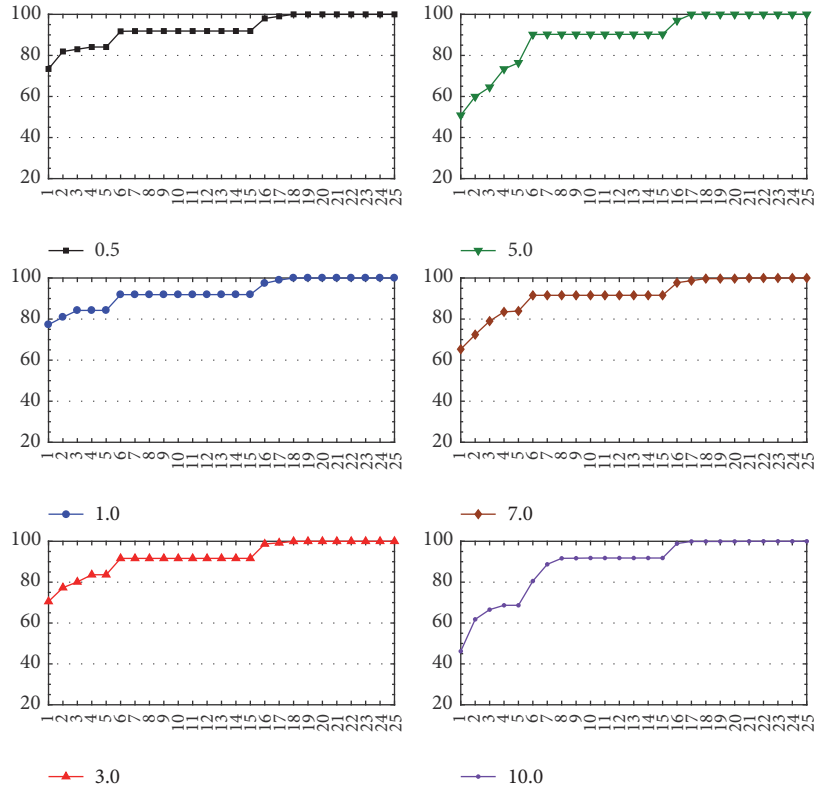
(b) Congestion scenarios: ABSM (x axis: time (sec), y axis: percentage of vehicle receiving the message)

FIGURE 10: Continued.

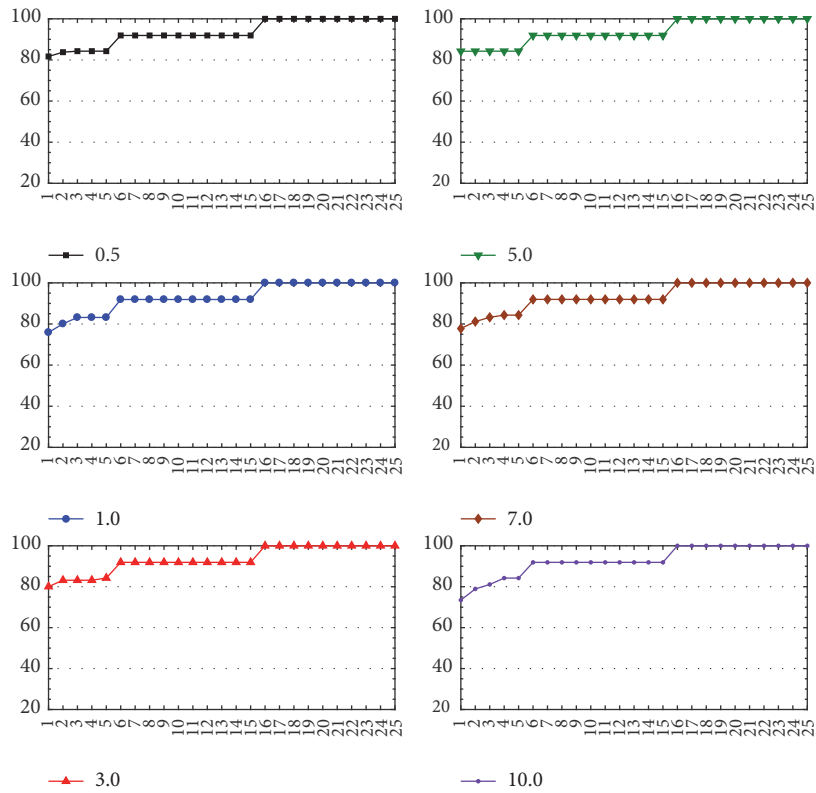


(c) Congestion scenarios: ReC (x axis: time (sec), y axis: percentage of vehicle receiving the message)

FIGURE 10: Continued.



(d) Smooth scenarios: VBURL (x axis: time (sec), y axis: percentage of vehicle receiving the message)



(e) Smooth scenarios: ABSM (x axis: time (sec), y axis: percentage of vehicle receiving the message)

FIGURE 10: Continued.

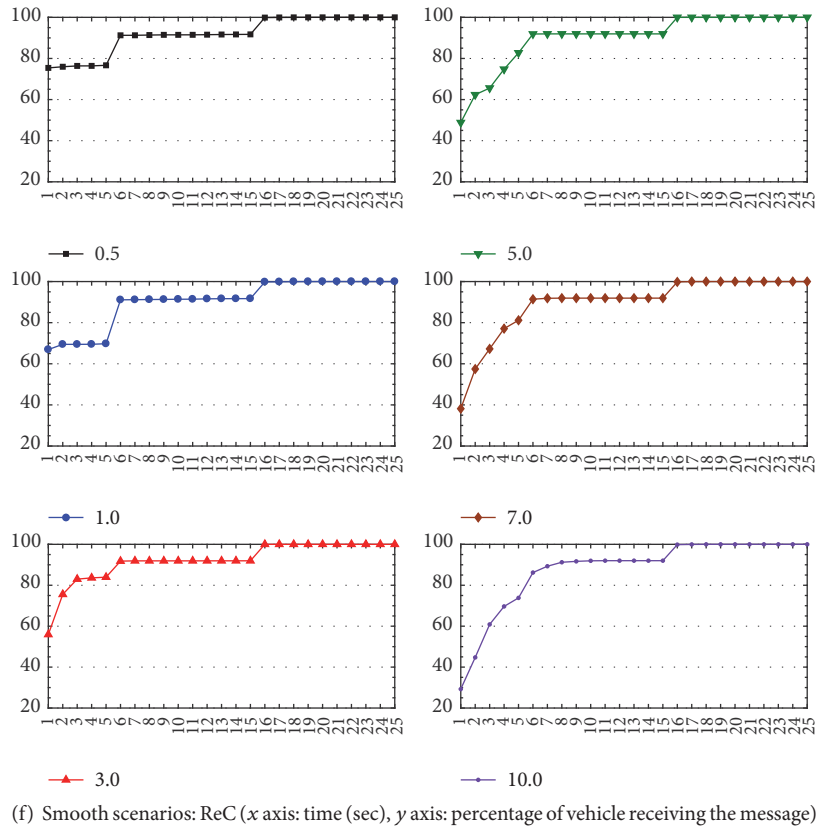


FIGURE 10: Delay of message reception.

congestion scenario and has a higher possibility of suspension of message dissemination. The suspended broadcast could be resumed when a vehicle with no message is discovered by a vehicle with the message through a beacon, and the time required to discover a vehicle with no message tends to increase as the beacon cycle becomes longer. Thus, in all of the three compared schemes, the percentage of vehicles receiving a message within one second tends to decrease as the beacon cycle is lengthened.

Meanwhile, ABSM has a slightly higher percentage of message reception within one second compared to VBURL and ReC. This is not only because waiting time of ABSM tends to be shorter than the other two schemes, but also at the cost of very low efficiency and large number of broadcasts as shown in Figure 9 and Table 2. For the percentage of message reception within one second, ReC is the lowest in all cycles except for the case of 0.5 sec beacon cycle. The reason for this is that as the beacon cycle becomes longer, beacon inaccuracy becomes greater, causing as a result more broadcast collisions or longer delay due to no forwarding vehicle with the first priority.

In the congestion scenario (Figures 10(a), 10(b), and 10(c)), all vehicles in ABSM receive messages before 30 seconds, while VBURL and ReC have few vehicles that receive messages after 30 seconds. For the vehicles whose delay of message reception is more than 30 seconds in VBURL, (1) the distance to the accident point when the message is first issued, (2) the ratio of the distance travelled before reception

of message and the original distance when the message is first issued, and (3) the message reception delay is measured in order to check how critical the delay could be to the quality of application. As shown in Figure 11, the vehicles with longer delay of reception tend to be farther away from the accident point when the message is first issued. Even though it takes longer than 30 seconds to receive the message, they receive it at least one intersection ahead of the accident point and, on average, around three or more intersections away from the accident point, that is, way ahead of reaching the accident point. Since they were far from the accident, taking longer time in receiving the message is not critical to the purpose of application. Even in the case where the reception delay is long, the message is received with a sufficient distance to be able to respond to the accident by decelerating or rerouting to a bypass. In our experiments, the vehicle that receives a message the latest receives the message at 77.5 seconds after the broadcast starts, and it is still around 3.8 intersections away from the accident point when the message is received.

Figure 12 shows the average message reception delay for varying beacon cycles. In all cases, the difference in average reception time among VBURL, ABSM, and ReC is less than 1.5 seconds, and the movement distance corresponding to this time is 8–21 m depending on the vehicle speed. Therefore, it does not result in a significant difference that would affect the safety service quality on urban roads where the vehicle density and congestion are high and the speed is low. The factors that have the greatest effect on the average reception

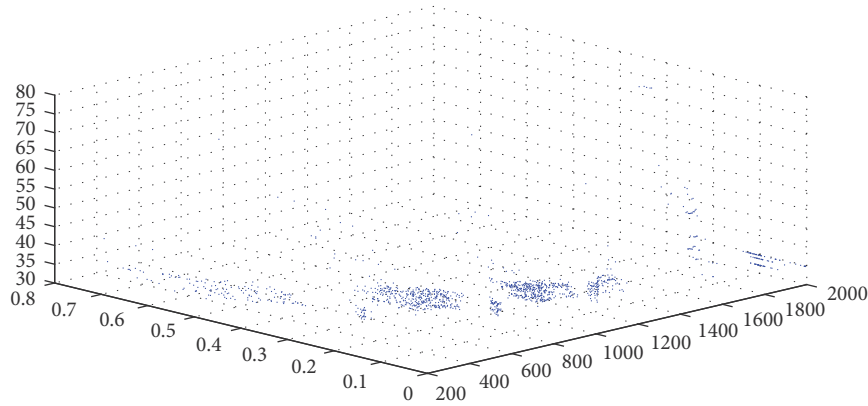


FIGURE 11: Safety message delivery QoS for vehicles receiving messages 30 seconds after the first broadcast.

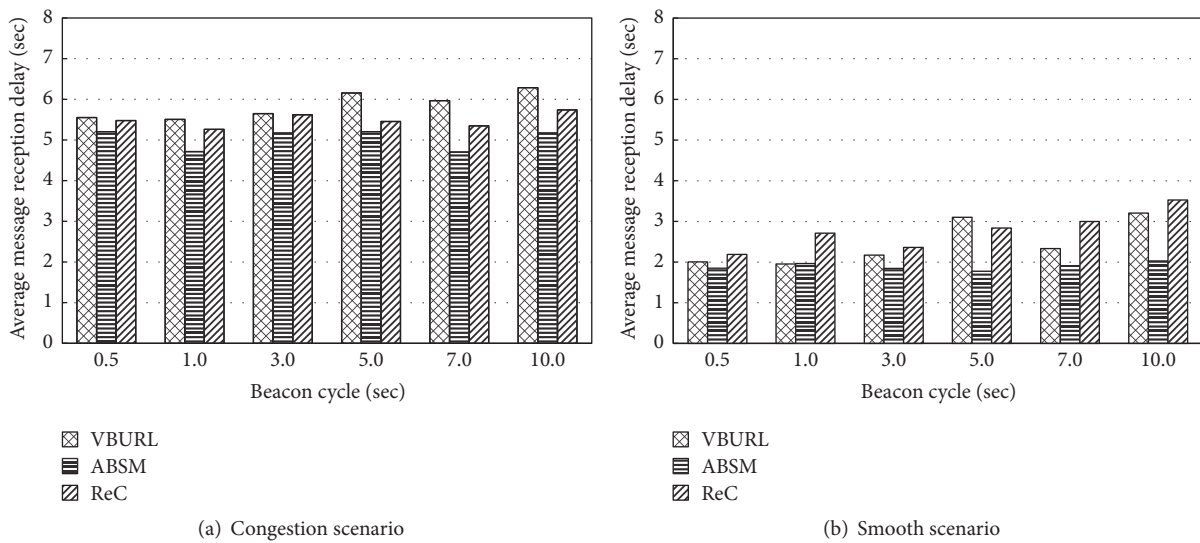


FIGURE 12: Average message reception delay.

delay are length of traffic signals and vehicle speed. The average reception delay of the congestion scenario (5-6 sec), where traffic signal cycle is longer and vehicle speed is slow due to high vehicle density and traffic congestion, is longer by 2.8–3.4 sec than in the smooth scenario (2-3 sec).

VBURL and ReC show a trend of slightly increasing average reception delay as the beacon cycle is lengthened, because it takes longer to discover a vehicle with no message. According to the way how the broadcast waiting time is set, VBURL tends to have a longer broadcast waiting time than ABSM and ReC. As a result, in most of the cases, the average reception delay of VBURL is slightly longer than those of the compared schemes. In the case of ReC, the message reception delay tends to be higher when the vehicle density is high and the beacon cycle is long. It is because the information inaccuracy increases as the vehicle density and/or the beacon cycle increase, and as a result, multiple forwarding vehicles with the highest priority may exist resulting in collisions or broadcast delay increases due to the lack of a vehicle with the highest priority. In the smooth scenario, where the vehicle speed is high and the inaccuracy of location information

tends to be higher, there are cases where the average reception delay of ReC is longer than that of VBURL. In the case of ABSM, the average reception delay is the shortest among the compared schemes for all beacon cycles. The waiting time of ABSM tends to be very short due to too many rebroadcasts meaning extremely low efficiency, as shown in Figure 9 and Table 2.

5. Conclusions

A broadcast message dissemination scheme with minimal beacon dependency is proposed considering the characteristics of urban roads such as frequent intersections, high vehicle density, and traffic concentration due to frequent traffic signals. The proposed VBURL selects the forwarding vehicle only using its location and the location of the current forwarding vehicle which is conveyed in the received message, that is, real-time information, and by leveraging the road layout information which is available from the digital map obtained through the DMB network. On urban roads, the intersections and the roads connecting the intersections are

repeated. On a straight road, the vehicle that is farthest from the current forwarding vehicle simply performs broadcast forwarding for rapid and efficient broadcast dissemination. In intersections, however, where signal attenuation is more serious due to surrounding obstacles such as buildings, the vehicle located in the intersection area that is free from such influence performs additional broadcasts in order to facilitate broadcast dissemination to all the roads adjacent to the intersection. The beacon only serves a supplementary role to deliver a safety message to the vehicles that have not received the message, which are newly entering an area where the broadcast has been completed. For performance evaluation, the percentage of vehicles receiving messages, the number of vehicles receiving the message per broadcast, and the message reception delay are measured for various beacon cycles in the congestion/smooth scenarios. All of the three compared schemes, VBURL, ABSM, and ReC, show reliabilities close to 100%, but the broadcast efficiency of VBURL is 2–100 times higher than that of ABSM and ReC for all beacon cycles in both of the congestion and smooth scenarios. Difference in efficiency between VBURL and the compared schemes is greater in congestion scenario for which the traffic concentration as well as the loss of beacons is more serious. In particular, the broadcasts inefficiency of ABSM and ReC is significant when neighboring vehicles with no message are detected. In terms of message propagation speed, the average message reception delay of VBURL is slightly longer than that of ABSM and ReC. The difference in the average reception delay among the three schemes is, though, less than 1.5 seconds, which would not have a significant effect on quality of service. Furthermore, in VBURL, the vehicles whose message reception delay is long are those located far from the accident point at the time of the first broadcast, and all the vehicles receive the safety message early enough to have sufficient chance to reroute to a bypass before reaching the accident point.

Conflicts of Interest

The authors declare that they have no conflicts of interest.

Acknowledgments

This work was supported by Institute for Information & Communications Technology Promotion (IITP) Grant funded by the Korea government (MSIT) (no. 2015-0-00183, “A Study on Hyper Connected Self-Organizing Network Infrastructure Technologies for IoT Service”).

References

- [1] IEEE P802.11p/D6.01, “Part II: Wireless lan medium access control (MAC) and physical layer (phy) specifications-amendment 7: Wireless access in vehicular environments,” Apr 2009.
- [2] IEEE Std, “IEEE Standard for Wireless Access in Vehicular Environments (WAVE) Multi-Channel Operation,” Sep. 2010.
- [3] M. Nekovee, “Sensor networks on the road: the promises and challenges of vehicular ad hoc networks and vehicular grids,” in *Proceedings of the Workshop on Ubiquitous Computing and e-Research*, May 2005.
- [4] X. Ma, J. Zhang, and T. Wu, “Reliability analysis of one-hop safety-critical broadcast services in VANETs,” *IEEE Transactions on Vehicular Technology*, vol. 60, no. 8, pp. 3933–3946, 2011.
- [5] M. M. I. Taha and Y. M. Y. Hasan, “VANET-DSRC protocol for reliable broadcasting of life safety messages,” in *Proceedings of the ISSPIT 2007 - 2007 IEEE International Symposium on Signal Processing and Information Technology*, pp. 104–109, Egypt, December 2007.
- [6] Y. Li, H. Zhang, Z. Huang, and M. Albert, “Optimal link scheduling for delay-constrained periodic traffic over unreliable wireless links,” in *Proceedings of the 33rd IEEE Conference on Computer Communications, IEEE INFOCOM 2014*, pp. 1465–1473, Canada, May 2014.
- [7] S. Wang, B. Yang, F. Gu, and X. Shi, “A novel reliable broadcast protocol for VANET’s safety applications,” in *Proceedings of the 6th IEEE International Conference on Electronics Information and Emergency Communication, ICEIEC 2016*, pp. 282–286, China, June 2016.
- [8] W. Zhu, D. Gao, C. H. Foh, W. Zhao, and H. Zhang, “A collision avoidance mechanism for emergency message broadcast in urban VANET,” in *Proceedings of the 83rd IEEE Vehicular Technology Conference, VTC Spring 2016*, China, May 2016.
- [9] M. Koubek, S. Rea, and D. Pesch, “Reliable broadcasting for active safety applications in vehicular highway networks,” in *Proceedings of the 2010 IEEE 71st Vehicular Technology Conference, VTC 2010-Spring*, Taiwan, May 2010.
- [10] C. Wu, K. Kumekawa, and T. Kato, “A novel multi-hop broadcast protocol for vehicular safety applications,” *Journal of Information Processing*, vol. 18, pp. 110–124, 2010.
- [11] C. Liu and C. Chigan, “RPB-MD: providing robust message dissemination for vehicular ad hoc networks,” *Ad Hoc Networks*, vol. 10, no. 3, pp. 497–511, 2012.
- [12] S. Biswas, R. Tatchikou, and F. Dion, “Vehicle-to-vehicle wireless communication protocols for enhancing highway traffic safety,” *IEEE Communications Magazine*, vol. 44, no. 1, pp. 74–82, 2006.
- [13] F. Ye, M. Adams, and S. Roy, “V2V wireless communication protocol for rear-end collision avoidance on highways,” in *Proceedings of the IEEE International Conference on Communications Workshops (ICC '08)*, pp. 375–379, Beijing, China, May 2008.
- [14] G. Xiao, H. Zhang, Z. Huang, and Y. Chen, “Decentralized cooperative piggybacking for reliable broadcast in the VANET,” in *Proceedings of the 83rd IEEE Vehicular Technology Conference, VTC Spring 2016*, China, May 2016.
- [15] X. Zhen, J. Wang, P. Wang, X. Wang, and F. Liu, “A sender-initiated adaptive and reliable broadcast scheme for VANET safety message,” in *Proceedings of the 2012 4th International Symposium on Information Science and Engineering, ISISE 2012*, pp. 329–334, China, December 2012.
- [16] X. Ma, J. Zhang, X. Yin, and K. S. Trivedi, “Design and analysis of a robust broadcast scheme for VANET safety-related services,” *IEEE Transactions on Vehicular Technology*, vol. 61, no. 1, pp. 46–61, 2012.
- [17] N. Wisitpongphan, O. K. Tonguz, J. S. Parikh, P. Mudalige, F. Bai, and V. Sadekar, “Broadcast storm mitigation techniques in vehicular ad hoc networks,” *IEEE Wireless Communications Magazine*, vol. 14, no. 6, pp. 84–94, 2007.
- [18] G. Korkmaz, E. Ekici, and F. Ozguner, “Black-burst-based multihop broadcast protocols for vehicular networks,” *IEEE*

- Transactions on Vehicular Technology*, vol. 56, no. 5, pp. 3159–3167, 2007.
- [19] Y. Bi, H. Shan, X. S. Shen, N. Wang, and H. Zhao, “A multi-hop broadcast protocol for emergency message dissemination in urban vehicular ad hoc networks,” *IEEE Transactions on Intelligent Transportation Systems*, vol. 17, no. 3, pp. 736–750, 2016.
- [20] F. J. Ros, P. M. Ruiz, and I. Stojmenovic, “Acknowledgment-based broadcast protocol for reliable and efficient data dissemination in vehicular ad hoc networks,” *IEEE Transactions on Mobile Computing*, vol. 11, no. 1, pp. 33–46, 2012.
- [21] J. Liu, Z. Yang, and I. Stojmenovic, “Receiver consensus: on-time warning delivery for vehicular ad-hoc networks,” *IEEE Transactions on Emerging Topics in Computing*, vol. 1, no. 1, pp. 57–68, 2013.
- [22] Y. Sung and M. Lee, “Light-weight reliable broadcast message delivery for vehicular ad-hoc networks,” in *Proceedings of the IEEE 75th Vehicular Technology Conference, VTC Spring 2012*, Japan, June 2012.
- [23] K. Obara, R. Akamatsu, and H. Shigeno, “BRNT: Broadcast protocol with road network topology for urban Vehicular Ad Hoc Networks,” in *Proceedings of the 82nd IEEE Vehicular Technology Conference, VTC Fall 2015*, USA, September 2015.
- [24] S. Eichler, “Performance evaluation of the IEEE 802.11p WAVE communication standard,” in *Proceedings of the 66th IEEE Vehicular Technology Conference (VTC '07-Fall)*, pp. 2199–2203, Baltimore, MD, USA, October 2007.
- [25] V. Nguyen, T. Z. Oo, P. Chuan, and C. S. Hong, “An efficient time slot acquisition on the hybrid TDMA/CSMA multichannel MAC in VANETs,” *IEEE Communications Letters*, vol. 20, no. 5, pp. 970–973, 2016.
- [26] C.-Y. Chang, H.-C. Yen, and D.-J. Deng, “V2V QoS guaranteed channel access in IEEE 802.11p VANETs,” *IEEE Transactions on Dependable and Secure Computing*, vol. 13, no. 1, pp. 5–17, 2016.
- [27] K. A. Hafeez, A. Anpalagan, and L. Zhao, “Optimizing the control channel interval of the dsrc for vehicular safety applications,” *IEEE Transactions on Vehicular Technology*, vol. 65, no. 5, pp. 3377–3388, 2016.
- [28] I. Stojmenovic, M. Seddigh, and J. Zunic, “Dominating sets and neighbor elimination-based broadcasting algorithms in wireless networks,” *IEEE Transactions on Parallel and Distributed Systems*, vol. 13, no. 1, pp. 14–25, 2002.
- [29] W. Peng and X. Lu, “On Reducing Broadcast Redundancy in Ad Hoc Wireless Networks,” *IEEE Trans. Mobile Computing*, vol. 1, no. 2, pp. 111–122, 2002.
- [30] H. Fubler, J. Widmer, M. Kasemann, M. Mauve, and H. Hartenstein, “Contention-based forwarding for mobile ad hoc networks,” *Ad Hoc Networks*, vol. 1, no. 4, pp. 351–369, 2003, Elsevier.
- [31] S. R. Theodore, *Wireless Communications: Principles and Practice*, Prentice Hall, 2nd edition, 2004.